
The University Of Sheffield.

# The Development of Stochastic Based Transport Models to Predict the Advection and Diffusion of Bed-load Sediment

Martina Cecchetto

A thesis submitted for the degree of Doctor of Philosophy

The University of Sheffield
Faculty of Engineering
Department of Civil and Structural Engineering

March, 2017

**Abstract**

Many morphological and environmental problems in rivers are associated with the transport of sediment, in particular with the movement of material along the stream bed. The complex nature of turbulent flow and the variability inherent within granular beds, along with the mutual influence one plays on the other, can only be described using the concepts of probability. It follows that the intermittent motion of bed-load particles can be termed by random variables. The stochasticity of key variables has been recently identified as a source of diffusion, i.e. suggesting that a plume of bed-load grains tends to spread while moving in the main flow direction. In this study the application of a Lagrangian analysis to existing high-frequency measurements of moving natural gravel particles contained in a tracking database helped to identify and scale the diffusive regimes related to different stages of grains' motion. Lagrangian tracking data allowed for an in-depth, study of the stochasticity of the particle step length, i.e. the single longitudinal distance computed by a grain from the entrainment to the deposition. The information on the distributed step lengths is then incorporated into a modified version of the Exner mass balance equation which has been developed to model the experimental advective and diffusive transport observed in long duration flume experiments with graded bed deposits comprised of natural sand and crashed marble gravel that have been previously reported. The modelling results indicate that the relative size of bed roughness, together with the thickness of the mixing surficial layer of the bed, play a major role in dictating the pattern of behaviour of particle motion. As the time-dependent burial depth of grains influences the vertical mixing and therefore the downstream diffusion of particles, concentrating the research only on the surficial motion of particles appears restrictive. In order to attain an insight view of the bed and to overcome the previous experimental limitations in terms of the description of the particle step distribution, a non-intrusive technique has been implemented in an annular flume to track the time history of tracing grains subject to intermittent motion in a bed made of transparent glass beads. In the light of the new information on particle transport, a more general Exner-based model incorporates the idea that tracer particles arriving at position $x$ at time $t$ started their random hops $r$ at many different times. Its application to the latest sediment tracer concentration data has proven to be promising in that convincing detailed descriptions of the observed advective and diffusive behaviour of bed-load transport were obtained.

## Acknowledgements

I would like to thank prof. Simon Tait, Dr. Matteo Tregnaghi and prof. Andrea Marion for the support, their important insights and for providing me with former additional data. A special thank also to Dr. Songdong Shao for providing helpful reviews, and to Dr. Andrew Nichols and Dr. Andrea Bottacin for important contributions to the experimental work and data analysis. Many thanks to Eric Lajeunesse for readily sharing their experimental data. Additional thanks to the students who assisted me in the data processing and during the experiments, in particular Luca Cotterle and Yu Zhang. A special thank to the HYTECH supervisors for critical discussions and to the fellows for constructive suggestions and for sharing together joyful as well as difficult moments. I am very grateful to Righi, my parents and Maia who have supported and accompanied me along this path.

This research received funding from the People Programme (Marie Curie Actions) of the European Union's Seventh Framework Programme under the Initial Training Network (FP7-PEOPLE-2012-ITN) HYTECH 'Hydrodynamic Transport in Ecologically Critical Heterogeneous Interfaces', N.316546.

# Contents

# List of Figures

# List of Tables

# Notations

CDF: cumulative distribution function
$d$: diameter of the moving particle
$d_{50}$: mean bed diameter
$d_T$: tracer particle diameter
$D_b$: volumetric deposition rate per unit stream-bed area
$E_b$: volumetric entrainment rate per unit stream-bed area
$f(X)$: probability distribution of a generic random variable $X$
$F(X)$: cumulative distribution of a generic random variable $X$
$f_t$: tracers concentration
$g$: gravity acceleration
$g_1$: distributive model corrective factor for step length statistics
$I_m$: index of mobility
$k$: step length standard deviation factor
$k_s$: roughness length
Ku: Kurtosis
$L_a$: active layer thickness
$L_x$: longitudinal dimension of the bed investigated area
MSE or S: mean squared error
px: pixel
PDF: probability density function
$q_b$: volumetric bed-load sediment transport rate [$L^3T^{-1}$]
$q_x$: flux of sediment transport in $x$ direction [$L^2T^{-1}$]
$Q$: flow rate
$r$: step length
$R$: scaling corrective factor of truncated distributions
$R_H$: hydraulic radius
Re: Reynolds number
$Re_p$: Reynolds particle number
RI: index of refraction
RMSE or RS: root mean square error
rps: rotation per second
$s_c$: bed channel slope
Sk: Skewness
$u$: flow velocity component in tangential direction
$u_{av}$: tangential flow velocity components
$U$: flow velocity
$u^*$: shear velocity
$v$ or $v_p$: particles' velocity

$V_s$: particle settling velocity
$\gamma$: water specific weight
$\gamma_s$: sediment specific weight
$\gamma_x$: longitudinal diffusive scaling coefficient
$\gamma_y$: lateral diffusive scaling coefficient
$\epsilon$: corrective roughness exponent for step length statistics
$\eta$: bed elevation
$\kappa$: von Kármán constant
$\mu$: water dynamic viscosity
$\nu$: water kinematic viscosity
$\rho$: water density
$\rho_s$: sediment density
$\sigma_b$: standard deviation of bed elevations
$\sigma_g$: standard deviation of grain size distribution
$\tau$: bed shear stress
$\tau^*$: Shields' parameter
$\tau^*_{cr}$: Shields' parameter at the threshold of motion
$\tau^*_r$: Shields' stress capable of transporting a reference value of bed-load slightly above the threshold of motion
$\tau_p$: particle's travelling time
$\omega$: rotational velocity

# Chapter 1

# Introduction and background

The first studies of sediment transport in inland water bodies date back to the nineteenth century with the development of the first large construction works along and across rivers. Scientists and engineers were originally moved by the common interest of understanding the stability of the channel bed and of levees. Because of the potential benefits offered by the proximity of rivers, many towns located along water courses expanded into large cities, which needed to be defended in case of flooding. River banks were then raised, stabilized and controlled to enhance the hydraulic safety of the surrounding land. The channel bed had to be maintained and dredged in order to allow the transit of barges carrying commercial goods from the harbour to the inland. New canals were dredged to open the passage to towns and cities located far from navigable water bodies. Erosion in correspondence with structures such as bridge piers or bed sills had to be kept under control or avoided. All these interventions required a good understanding of the processes involved in shaping the morphology of a river, and the study of sediment transport is one of them.

The morphology of natural alluvial rivers is a direct consequence of sediment transport processes, in particular the mechanisms of sediment motion. Material can be transported in suspension, i.e. supported in the water column and so as defined *suspended load*, or in traction over the river bed where sediment can jump, roll or slide. The latter is defined as *bed-load sediment* and its transport is fundamental in determining the channel morphology. The different types of transport are dependent on the sediment characteristics (the size of material and the supply) and on the river's competence (the capability of the flow to mobilize sediment of a given size) that, once combined together, provide a basis for a classification of alluvial rivers.

Gravel and coarser material such as boulders and cobbles constitute the bottom of mountain and upland valley channels. Transport here occurs as bed-load with partially mobile conditions being common and it is greatly influenced by the bed packing arrangement. In this class of channels, defined as *threshold channels*, morphological changes are slow (e.g. step-pool cascades, alternated bars). In the lower part of the valleys the size of the bed material decreases to fine gravel or sandy gravel. The full mobility of this finer gravel sediment, occurring in significant part as bed-load, characterizes the morphological evolution of the so called *transitional channels*. Braided channels are examples of transitional morphology. When the bed material is formed of sand and finer sediment (clay and silt) which move into suspension, it is the case of *labile channels*, typical of deltaic environments and inland basins. These channels, which can evolve into meanders depending on the channel stability and can host vegetation, are characterized by rapid morphological changes.

Knowing the dynamics of sediment and linking it to the hydraulic conditions allowed rivers to be managed in order to control their flow, to be straighten to facilitate irrigation and transport,

and adjusted in slope to reduce the risk of damaging erosion. One of the main issues identified for channel stability was sediment mobility so that the study of sediment transport was particularly focused on deriving empirical relationship to estimate the bulk volumetric transport rate (Du Bois, 1879; Meyer-Peter and Muller, 1948; Schoklitsch, 1932) or the hydraulic conditions that trigger the initial motion of sediment (Shields, 1936).

Helped by recent advances in measurement and computational technology, researchers started approaching the dynamics of sediment by studying the forces acting on single particles and the fluid velocity near the channel bed. Some addressed aspects of this process in probabilistic terms and tried to link it to the hydrodynamic characteristics of the competent flow (Einstein, 1950; Yang and Sayre, 1971; Grass, 1984). Yet, the former deterministic and empirical relationships were favoured, especially by practising engineers.

It was in the second half of the twentieth century, with the increasing anthropic pressure at the expense of the riverine ecosystem, that the study of sediment transport was encouraged by new applications. The discharge of untreated domestic sewage, the drainage of polluted rainfall run-off from urban areas and the presence of industrial activities along the minor and major river reaches, have contributed to deteriorate the quality of the water ecology in rivers. All this is taking place in streams whose morphological situations are far from the natural conditions. The investigation of the transport of sediment was then diverted to the quality assessment of a water body, in particular to the ecosystem present on its bed.

The river bed constitutes the interface where exchanges between water, sediment and biota take place. Important ecological processes, such as growing roots, deposition of fish eggs, invertebrates' biological functions, are hosted in the surficial permeable sediment layers (Marion et al., 2014). This region of the river bed is the so called the hyporheic zone (Boano et al., 2006) and it performs a fundamental role in interfacial physical and biological processes. This sediment domain provides nutrients, locations for chemical reactions, and shelter for plants, animals and microorganisms. Pollutants carried in water are more likely to associate with the fine sediment matrix which, during low flow regime, can settle on the river's bottom. Here contaminated sediment can be mobilized again by less frequent higher flows or be trapped in bed structures and buried deep inside the river bed. Studying the dynamics of the contaminated sediment is then fundamental for a robust planning of sediment quality investigation and remediation activities.

Within this current framework, the present research in sediment transport also supports the restoration of streams in an attempt to recreate good ecological conditions. The ecological status of the surface water bodies is taken seriously by the European Commission, which promoted in 2000 the Water Framework Directive (WFD), an innovative piece of legislation that aimed to serve as a basis for future EU water legislation. The main aim of this directive is to promote regulation and management control measurements at a catchment scale.

The WFD focuses on attaining good ecological status of the water bodies by indication of control measurements for the water and the sediment compartment. However, the attention given to the sediment compartment in the WFD falls short in comparison to the control measurements proposed for the water compartment (Crane, 2002). For instance, the directive does not distinguish suspended from bedload sediment, and neither specifies the spatial scale of investigation in the assessment of the chemical and biological quality of contaminated sediment. It fails to mention measurements that can be applied to manage eroding soils after a flood event, or the protection of benthic organisms that dwell in sediment deposits. It is therefore desirable to use the existing knowledge and evolving research on sediment transport to attain more appropriate management actions to help surface water bodies attain good ecological status. For instance, being able to predict the motion of a polluted group of sediment, as a function

of the river morphology and the hydraulic conditions, would allow site-specific actions to be implemented to aid the restoration of natural ecological communities.

Regardless of the two centuries of experimental and theoretical studies, our knowledge of sediment transport processes is constantly challenged by the complexity of the phenomenon. This becomes particularly true not only in the natural environment, but also in urban settings. Sediment transported by wastewater can settle in pipes causing clogging issues or become a fertile ground for biochemical reactions. Extreme flood events are more often accompanied by intense sediment transport, which can increase the risk for the urban population, for the sewer system and for the final water body that acts as a receptor for intermittent discharges from a CSO (combined sewer overflow outlet). The flushing of settled sediment from the bottom of an artificial dam to clear the reservoir can produce a change in the outlet reach slope with consecutive triggered erosional and depositional processes of catchment-scale impact.

More challenging the nature of the process, more urgent and necessary its study appears. Understanding the motion of sediment on the bottom of rivers, artificial canals, or pipes, is still of great importance for the conservation of natural water resources.

The next sections will present the study of sediment transport from its origin to the latest findings that accompanied the scientific path followed by researchers in the attempt to acquire a thorough knowledge of fluvial sediment transport process. The successes together with the respective theoretical or empirical limitations will help delineate the conceptual framework this work fits in and from which it develops current knowledge.

## 1.1 The deterministic approach

Early research on sediment transport contains a countless series of empirical and theoretical formulations all aiming to quantifying the bed-load volumetric sediment transport rate, $q_b$, at a single location. Equations combined measurable time-averaged hydraulic parameters of the stream (i.e. water discharge, energy and shear velocity), with sediment characteristics (grain diameter and density) and the geometrical variables of the system (e.g. surface slope, water depth, cross-sectional area) (e.g. Shields, 1936; Schoklitsch, 1934; Engelung and Eggert, 1967; Paintal, 1971; Ackers and White, 1973; Yang, 1984). Most of these formulas are essentially based on the same concept of identifying a hydraulic variable, being it for instance the water discharge (Schoklitsch, 1934), the shear stress (Du Bois, 1879; Paintal, 1971) or the energy expenditure (Ackers and White, 1973; Yang, 1984), whose value needs to be overcome in order to trigger the motion of sediment grains in a stream.

The derivation of a predictive equation generally falls into two principle approaches. A formal or theoretical formulation, that is determined to relate the sediment discharge to the main hydraulic and sedimentological variables, is afterwards verified and calibrated with experimental data (e.g. Schoklitsch, 1950; Meyer-Peter and Muller, 1948). The other approach attempts to describe the key mechanical principles behind sediment transport (e.g. Yalin, 1963) in order to derive a physically-based relation.

One of the first studies on sediment transport can be attributed to du Bois in 1879. In his pioneering work on the River Rhone, du Bois imagined the sediment bed consisting of m different layers. Each layer moves according to the tractive force played by the fluid and the resisting forces between layers. By solving the system of forces a bed-load transport rate can be expressed as follow:

$$q_b = \chi\tau(\tau - \tau_{cr}), \tag{1.1}$$

with $\tau$ being the shear stress, $\tau_{cr}$ the critical shear stress associated to the entrainment and $\chi$ the "characteristic sediment coefficient". The latest parameter derived for a limited set of experimental data is scaled to the mean bed diameter as $\chi = 0.391/d_{50}^{3/4}$.

After du Bois' work, a plethora of equations has appeared. Most of them followed the first approach in linking the sediment discharge to the hydraulic and sedimentological parameters of a stream. One example is offered by the widely used Meyer-Peter and Muller formula (1948). The expression they proposed is a modification of the former work of Meyer-Peter which related the bed-load sediment transport rate to the water discharge $Q$, the bed channel slope $s_c$ and the particle's size $d$. The well-known modified version is:

$$q_b = \frac{\gamma}{\gamma_s - \gamma}\left[\frac{(Q_s/Q)\,(K_s/K_G)^{3/2}\,hs_c - 0.047((\gamma_s-\gamma)/\gamma)d}{(0.25/\gamma)(\gamma/g)^{1/3}}\right]. \tag{1.2}$$

$h$ indicates the water depth, and the two reductive factors $(Q_s/Q)$ and $(K_s/K_G)$ represent respectively the fraction of discharge that is responsible for the movement of particles on the bed, and the reduction in shear stress available to sediment transport due to form resistance dissipation from bedforms. Eq. 1.2 was developed using an extensive number of experiments with uniform and graded material upon which the coefficients were calibrated. It is often used in application for mountain streams, generally for $d > 5$ mm. A dimensionless version simplifies the sediment discharge per unit width relating it to the excess in dimensionless shear stress, i.e. $q_b^* = 8(\tau^* - \tau_{cr}^*)^{3/2}$, with $\tau_{cr}^* = 0.047$.

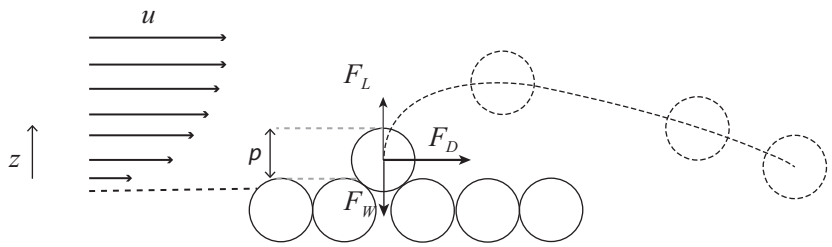


Figure 1.1: System of forces acting on a grain immersed in a flow with mean velocity $u$, namely drag force $F_D$, lift force $F_L$, and grain's submerged weight $F_w$. The protrusion of the target particle, $p$, is sketched too. After Kirchner et al., 1990.

Other researchers attempted a more mechanical approach to address the prediction of sediment motion (second approach). The system of forces acting along the trajectory of a saltating grain was solved in order to derive an estimation of the transport rate (e.g. van Rijn (1984), for $d$ = 200-2000 $\mu$m). The system of forces is depicted in Figure 1.1 and it represents the downward force of the particle's submerged weight, along with the fluid forces, i.e. lift and drag force. Among others, Yalin in 1963 used this mechanical approach when he proposed to calculate the sediment transport rate as the product of the concentration of moving grains per unit area of the bed times the average streamwise velocity of the material. The concentration was assumed to scale with the excess in shear stress, whilst the velocity was derived from the physical description of the saltating grains. Yalin obtained:

$$q_b = \frac{((\gamma_s - \gamma)d)^{3/2}}{\rho^{1/2}} 0.635\psi^{1/2}\left[1 - \frac{1}{as}\ln(1+as)\right], \tag{1.3}$$

where $s = (\psi - \psi_{cr})/\psi_{cr}$, $a = 2.45\psi_{cr}^{1/2}/(\rho_s/\rho)^{2/5}$ and $\psi$ the mobility number expressed as a function of the shear velocity $u^*$. The values of the constants in the above equation are derived

from experimental data.

All these examples of previous equations have one thing in common: they all link the sediment flux to an excess in tractive force (or water discharge or energy in case of other formulations). To do so, they need to define a critical value below which motion does not occur. The most common solution to this problem was presented by Shields in 1936. He addressed the incipient motion condition with a dimensional analysis, assuming that the critical value of shear stress was dependent on five variables, namely the grain size $d$, the water density $\rho$ and viscosity $\nu$, and the grain relative density ($\rho_s$–$\rho$). The Buckingham theorem led him to the identification of two dimensionless groups of parameters:

$$\begin{cases} \tau^* = \frac{\tau}{(\rho_s - \rho) g d} \\ \mathrm{Re}^* = \frac{u^* d}{\nu}. \end{cases} \tag{1.4}$$

The first group $\tau^*$ denotes the ratio of the bed shear stress (fluid drag forces) to the particle's submerged weight, whilst the second one represents the sedimentologic Reynolds Number. A series of experiments allowed Shields to estimate the critical value of dimensionless shear stress associated to different bed sizes corresponding to the incipient motion condition of the bed material. His final curve (Figure 1.2), which has been extensively used in past and present applications, reports a region of constant critical shear parameter for sedimentologic Reynolds Numbers greater than 100, i.e. $\tau^*_{cr} = 0.056$. The simplicity of Shields' benchmark study has brought it to be one of the most popular in the field of hydraulic engineering and fluvial morphology regardless of the uncertainty associated to his method (Buffington, 1999). The criterion used by Shields for the evaluation of the incipient motion condition was from paired measurements of shear stress and bed-load transport rate. Even if the majority of the data was derived with this method, some of it was based on the visual observations of grains' motion in light of the definition of *weak* transport given by Kramer (1932, 1935), i.e. "...several of the smallest particles are in motion, in isolated spots, and in countable numbers.". Preferring one criterion over the other would produce discrepancies and the observed scatter of his data (Buffington, 1999). The sediment material used in the experiments and reported as uniform was actually closely graded. A mixed-size material can generate different mobility and fractional transport which is difficult to describe with a single value of critical shear stress.

Fenton and Abbott in 1977 contended that Shields ignored the effect of the grains' exposure in his definition of incipient motion by attributing the mobility only to the particles' Reynolds number. With their experiments the authors showed that the threshold for the initiation of motion is actually depending on the relative protrusion of the grain over the surrounding material.

The geometry of the bed, especially in graded sediment, appeared therefore as a significant variable in the description of the initiation of motion. Later studies tried to include such variability by introducing "hiding functions" to compensate for the effect induced by a non-uniform sediment mixture. Diplas (1987) argued that a single value of bed diameter was not sufficient to calculate the sediment transport rate for graded material. With a dimensional analysis and experimental data he derived the following hiding function $h_i$ that applies to each size $d_i$ composing the original bed mixture:

$$h_i = \phi_{50}^{\left[(d_i/d_{50})^{0.3214}-1\right]} \left[ \left( \frac{d_i}{d_{50}} \right)^{-0.057} \right]^{(d_i/d_{50})^{0.3214}}, \tag{1.5}$$

with $d_{50}$ the mean bed diameter and $\phi_i$ the normalized shear stress for the grains of class

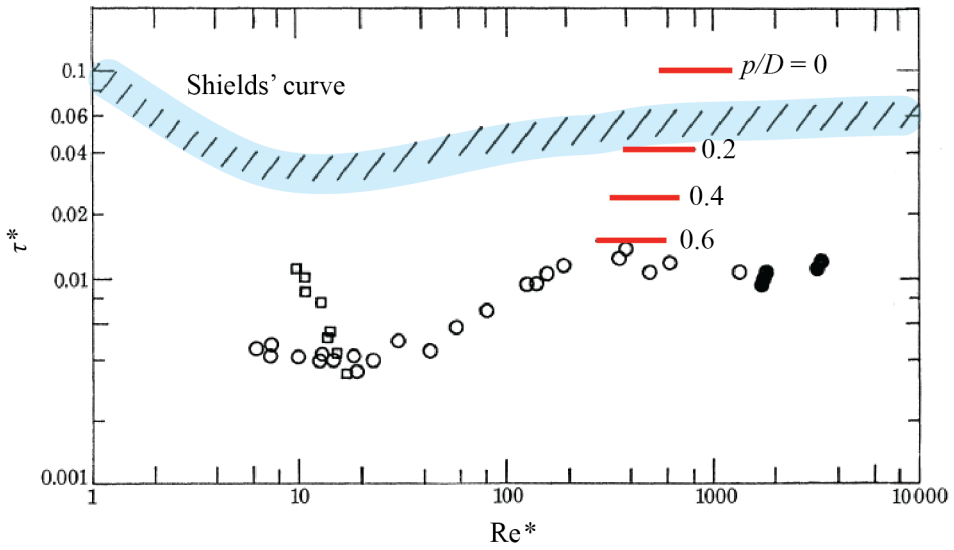


Figure 1.2: Shields' diagram representing the dimensionless shear stress scaled to the Reynolds number. The light blue area indicates the values as derived by Shields in his work (1936) while the red lines denotes the results obtained by Fenton and Abbott (1977) for different degree of grain protrusion ($= p/d$). The circles and the squared markers represent former experimental data re-analysed by Fenton and Abbott for the case of larger grains' protrusion. After Fenton and Abbot (1977).

$i$ defined as the ratio of the Shields stress parameter $\tau_i^*$ over the Shields stress capable of transporting a reference value of bed-load slightly above the threshold of motion, $\tau_{r,i}^*$. In Eq. 1.5 the normalized shear stress refers to the mean bed diameter. The hiding function is used to calculate the fractional volumetric transport rates $q_{bi}$ that compose the total bed-load transport rate $q_b$.

Diplas' work is one of the studies that used the concept of fractional transport rate (Parker et al., 1982; Wilcock, 1997; Wilcock and Crowe, 2002). The approach consisted in dividing the mixed material into grain size ranges $i$ present on the bed in fraction $f_i$, and to formulate a dimensionless transport rate $q_{bi}^*$ as a function of the Shields' stress parameter $\tau_i^*$ calculated for the mean diameter of the size class $i$. The total transport rate was then given as a sum of the fractional rates. These formulations overcome the concept of critical shear stress by considering a reference value of minimum transport rate and the composition of bed material. However they greatly depended on the set of data available to test the model.

The expressions presented so far provide an indication of the range of possible formulations and theoretical approaches that populates the literature on the deterministic description of bedload transport. Researchers have attempted to compare the results of previous formulae to experimental measurements of sediment discharge with few satisfying results (e.g. van Rijn, 1984; Gomez and Church, 1989). Empirical equations owe their validity to the conditions in the experiments where they were based upon. They are restricted to the applicability to well defined sizes of bed material (Meyer-Peter and Muller, 1948) or to certain values of shear stress (Shields, 1936). On the other hand, mechanical deterministic methods based on the description of the physics of particles' motion resulted in the approximation of some variables with constant values, as in the case of van Rijn's saltation length (1984). With a newly collected set of data, new equations would appear or existing ones would be modified to find correspondence in the iterative process of adjusting the constants or adding corrective functions. The proliferation of formulae can be read as an indicator of the complexity denoting bed-load sediment transport.

## 1.2 The stochastic nature of sediment transport

The deterministic approach presented above has proven to be inadequate to predict the measured volumetric transport rate (e.g. van Rijn, 1984; Gomez and Church, 1989). Even if it appears reasonably correct in its experimental and theoretical derivation and it provides simple equations to apply in the field of hydraulic engineering, it fails to match the complex nature of the observed sediment transport. The spatial and temporal variability of the phenomenon has moved researchers towards the development of a different approach.

It was with Einstein in 1942 that the concept of probability was introduced in the scientific research of bed-load sediment transport. He described gravel motion as a succession of alternating streamwise steps and resting periods dominated by the stochasticity nature of the near-bed water velocity. Einstein preferred to relate the number of grains in motion to the probability that water could lift and move a particle downstream instead of using a single representative value of shear stress. He therefore defined the volume of grains likely to be in motion in terms of a dimensionless intensity of sediment transport, $\Phi$, and expressed it as a function of the dimensionless flow intensity exerted on the bed $\Psi$, in the form of $A\Phi = f(B\Psi)$ (Einstein, 1942). In a subsequent work Einstein (1950) updated the former formula to account for the sheltering of small grains in mixed-sized sediment, by the introduction of corrective factors from experimental derivation. His final expression for the probability of motion $p$ was:

$$p = 1 - \left(1/\pi^{1/2}\right) \int_{-(1/7)\Psi_i^{*-2}}^{(1/7)\Psi_i^{*-2}} e^{-t^2} dt = \frac{43.5\Phi_i^*}{1 + 43.5\Phi_i^*}, \tag{1.6}$$

where $\Psi_i^*$ is the corrected flow intensity parameter for non-uniform sized material and $\Phi_i^*$ the intensity of bed-load for particles of size $i$. The application of Eq. 1.6 to a large range of experimental data is presented in Figure 1.3. For individual grain sizes, a higher degree of sheltering of size $i$ corresponds to a larger flow intensity parameter $\Psi^*$ and, from the curve, to a negligible transport rate $\Phi_i^*$.

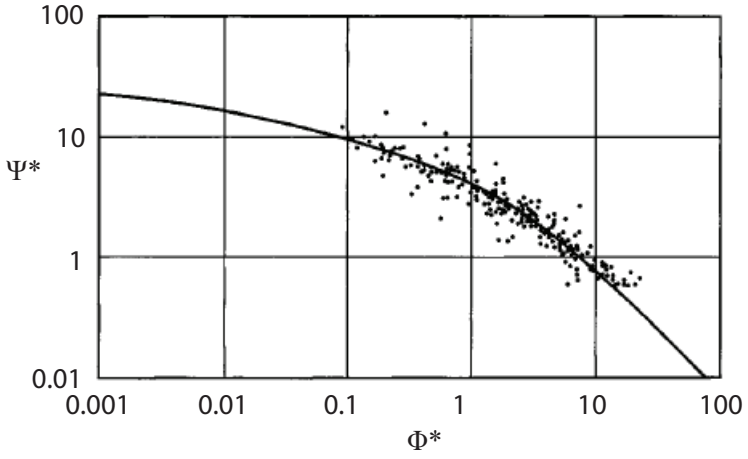


Figure 1.3: Relationship between the flow intensity parameter, $\Psi^*$, and the intensity of bed-load for individual grain sizes $\Phi_i^*$. After Einstein, 1950 (as reported in Ettema and Mutel, 2004).

Einstein's work let the new probabilistic approach begin. Several studies adopted the tools offered by the statistical analysis to address the variability observed in sediment transport. The analytical solution of the system of forces acting on a saltating grain could now include stochastic elements to the solution, such as the randomly located collision point presented by Wiberg and

Smith (1989) or the variability of the bed surface (Paintal, 1971; Kirchner et al. 1990). The experimental measurements of the bed surface, in terms of bed elevations, of grain protrusion and friction angle were better approximated by probability distributions. As the tractive force acting on a grain greatly depends on the relative exposure (Fenton and Abbott, 1977), and since the exposure of a grain varies according to the microtopography of the bed, which in turn is defined as a stochastic variable (Nikora et al, 1998), it follows that the critical shear stress would vary locally too (Kirchner et al., 1990). Transport could then occur for values of shear stress lower than the critical one proposed in literature since the critical shear stress is characterized by a distribution rather than a single value.

Such evidence was obtained by Grass in 1970. He coupled visual observation of grain instability to the instantaneous measurements of longitudinal and vertical flow velocity by means of hydrogen bubble visualisation. He wanted to demonstrate that the initiation of motion is the result of two distributed random variables. The first variable is the critical shear stress a particle is subject to at the instant of instability, and it depends on the bed topography and particles' exposure. The second one is the local instantaneous bed shear stress which distributes accordingly to the local flow turbulence. The initiation of motion is a result of the statistical interaction process between these two distributions and it is more likely to occur when the overlap of the distributions increases. Figure 1.4a reports an extract from the analysis presented by the Grass in his paper.

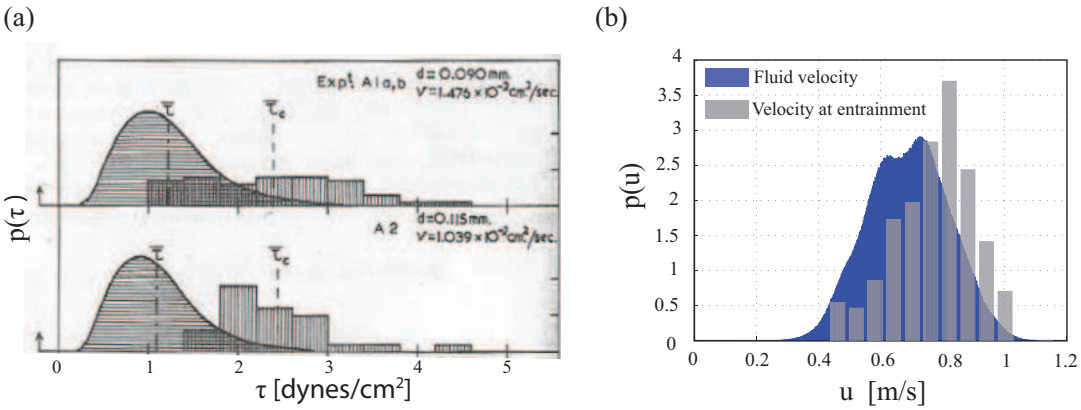


Figure 1.4: (a) Extract from Grass' work representing the two experimentally derived frequency distributions of the bed shear stress $\tau$ (smooth curve) and the critical shear stress measured in correspondence of particles' entrainment $\tau_c$ (histograms). (b) Results from the application of Grass' approach to the instantaneous streamwise fluid velocity at entrainment of gravel grains, after Tregnaghi et al. (2012a).

Further improvement in the description of the initiation of motion was achieved again due to the seminal work of Einstein (1942) with the fluid-mechanic concept of turbulence. The displacement of a particle from its resting position is the result of the pressure gradient that produces drag and lift forces of enough magnitude and duration to overcome a critical threshold. As the system of forces is greatly dependant on the near-bed flow, the instantaneous value of Reynolds shear stress can be expressed in function of the instantaneous turbulence fluctuations of longitudinal and vertical flow velocity, $\tau' = -\rho u' w'$. Within a bursting event, consisting of the cycle of different flow events associated to the sign of the instantaneous velocities fluctuations, only a part of the Reynolds shear stress represents the flux of forward momentum to the bed (Nelson et al., 1995) which is responsible for particles' dislodgment.

The entrainment of sediment is then a random process since it depends on the turbulent nature of the local instantaneous flow field. If the probabilistic nature of the initiation of motion was originally proposed by Einstein (1950), Sutherland (1967) and Grass (1970), it was only with the technological advancement of the last two decades that this concept could be explained (Heathershaw and Thorne, 1985; Nelson et al., 1995; Papanicolaou et al. 2002; Diplas et al. 2008; Aberle et al., 2008; Celik et al. 2010, among others). The collection of near-bed flow velocity measurements allowed scientists to find a quantitative correspondence between the dislodgment of a particle and the bursting events. The decomposition of turbulence burst into their four flow events (ejection, sweeps, outward and inward interactions) indicated that the entrainment tends to be correlated to positive instantaneous value of streamwise velocity fluctuations, i.e. $u' > 0$ (Heathershaw and Thorne, 1985; Nelson et al., 1995; Dwivedi et al., 2011a). Instantaneous streamwise velocity defines the instantaneous drag force acting on the particle (Schmeeckle et al. 2007). The same cannot be asserted when it comes to the lift force, whose mechanism still lacks of a complete understanding (Schmeeckle et al., 2007; Cecchetto et al., 2016).

As shown by Diplas et al., (2008) entrainment is not simply related to the magnitude of the hydrodynamic forces (and therefore to the instantaneous local velocity $u$) but it also depends on their duration. They linked the variability of the entrainment to the drag form forces applied for a duration $T$, which corresponds to an impulse $I \propto \overline{u^2}T$, with $\overline{u^2}$ the squared average streamwise flow velocity in $T$. The physical interaction at the sediment-flow interface can potentially produce a wide range of impulses, but only particular combination of form drag forces and durations are responsible for the particles' dislodgment, suggesting that the impulse rather than the hydrodynamic forces better describes a threshold criterion for motion (Diplas et al. 2008; Celik et al. 2010; Valyrakis et al. 2010).

As previous studies showed that the entrainment process is also depending on the geometry of the bed (Kirchner et al., 1989), Papanicolaou et al. (2001) and Dey et al. (2011a) argued that the turbulence and the bed geometry (in particular the particle's arrangement and exposure) were statistically dependent variables that could not be simply related to the submerged weight of grains. The spatial study of the entrainment in natural gravel bed, linked to the instantaneous measurements of flow velocity, encouraged the study of the role of local surface irregularities and their response to the turbulent events (Bottacin-Busolin et al., 2008; Tregnaghi et al., 2012a,b). The Grass' study was reformulated in terms of instantaneous longitudinal velocity, $u$, showing that the velocity marking entrainment events is a random variable denoted by a probability distribution (Bottacin-Busolin et al., 2008; Tregnaghi et al., 2012a,b), (Figure 1.4b). This experimental evidence indicates the instantaneous local flow velocity $u$ as the most relevant hydraulic variable for the incipient motion of mobile sediment.

The concepts and language of probability not only helped scientists to better formulate the initiation of motion but they also provided an appropriate tool for the description of particles' trajectories. Attempts to estimate bed-load transport rate use two alternative, although equivalent, approaches to conceptually depict the collective motions of particles under steady, uniform conditions. Several authors described the bed load rate as the product of the mean velocity of moving particles and the particle concentration per unit streambed area (or particle activity), namely the "flux form" (Yalin, 1972; Van Rijn, 1984; Wiberg and Smith, 1989; Lajeunesse et al., 2010; Furbish et al., 2012a). Others defined the sediment flux as the product of the entrainment rate and the mean particle step length, which is the distance travelled by a particle from entrainment to deposition, namely the "entrainment form" first introduced by Einstein in 1950 (Wilcock, 1997; McEwan et al. 2004; Wong et al. 2007; Ganti et al., 2010; Furbish et al., 2012a). It is thought that the turbulent nature of the flow field along with the character of the

river bed, such as grain size distribution and bed surface arrangement, temporal variation in bed elevation and local channel morphology, could influence the transport behaviour of the bed particles. Given this level of intrinsic variability a probability distribution is considered a more appropriate way to describe particle motion from entrainment to deposition than a deterministic description.

Depending on the desired model complexity or on the specific context under investigation, stochasticity is often delegated to one individual term. A number of studies have introduced stochasticity in particle motion by considering the particle step length as a continuous random variable (Paintal, 1971; Wong et al. 2007; Lajeunesse et al. 2010; Ganti et al., 2010; Hassan et al. 2013; Roseberry et al. 2012). While a typical finding is that step lengths are approximately exponentially distributed for a given grain size (e.g., Nakagawa and Tsujimoto, 1980), with their mean increasing with grain size for a given shear stress (Wong et al., 2007), the true dependence of mean step length on grain size in sediment mixtures remains somewhat ambiguous. Ganti et al. (2010) demonstrated that a thin-tailed distribution of step lengths typically holds for uniformly-sized beds, whilst a heavy-tailed probability density function (PDF) can emerge for graded sediment. Lajeunesse et al. (2010) measured the lengths of individual trajectories of bed load particles with a high resolution image tracking system revealing a positively skewed distribution with the most probable travel length found to scale linearly with excess of the shear velocity (Figure 1.5a). Field experiments carried out by Hassan et al. (2013) focused on determining the tail characteristics of the step length distributions but their definition of travel distance included multiple step lengths as they surveyed the marked particles' locations along the river after one or several flood event.

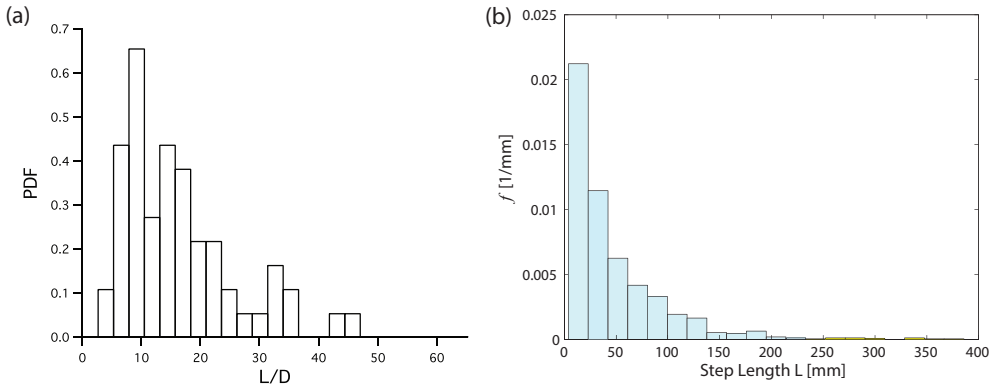


Figure 1.5: Example of frequency distribution for the measured step length (a) derived by Lajeunesse et al., (2010) and (b) calculated with the data collected in the experiments presented in this work in Chapter 4.

The limitations of these studies and the knowledge gaps in the description of bed-load grain motion are discussed in the next section. It is important to stress though that the stochastic analysis of the trajectory's variable, being it the grain's velocity or the step length, can only be attained by collecting sufficient information on the motion of a system of particles. The method of investigating single trajectories of the studied group of grains is known as the particle-based approach or Lagrangian analysis.

## 1.3 The particle-based approach

The interest in understanding sediment dynamics near the bed has led researchers to perform experiments in which the movement of few marked particles was closely followed. The behaviour of this group of particles is assumed to be representative of the entire grain population, so that minor efforts should be spent in tracking all moving grains. The use of marked grains, also known as *tracers*, is the basis of the particle-based approach necessary to stochastically describe the motion variables, such as grains' velocity, travelled distance, moving time and resting time.

This approach was made possible and advanced together with the development in filming technology, which allowed the motion of tracing grain to be captured with picture photography and video recording (e.g., Paintal, 1969; Grass, 1970; Abbot and Francis, 1977; Nino and Garcia 1996). Tracers had been employed in a number of field research studies each refining the technical capability of their imaging systems. For the first time, in 1987, Drake et al. applied this technique to a natural gravel river bed. By painting 125 bed grains of 4-8 mm size and following their motion over a constrained window, they obtained an analysis of the different transport modes of individual bed-load particles.

The authors described the motion of a gravel grain as composed of four different phases: entrainment, displacement, distrainment (the absence of horizontal net motion) and repose. The planar and vertical visualization of tracing grains allowed them to identify displacement by saltation, rolling and sliding. Saltation is characterized by a series of jumps with horizontal length between following bed contacts greater than two particle's diameter. Saltating particles tend to stop after abrupt impacts with the bed. If motion is denoted by significant rotation and the horizontal distance between consecutive collisions with the bed is smaller than two particle's diameter, grains are rolling over the channel bottom. Rolling trajectories are usually short (3-4 particle's diameter) and distrainment is anticipated by a gradual decelerating phase. Contrarily, a sliding particle remains in continuous contact with the bed. Sliding was typically observed for angular particles and as part of a rolling or salting trajectory (Drake et al., 1987).

The derivation of the travelled vector between two resting states and the grains' velocity associated to the motion phase revealed the variability in the frequency of their occurrences. Drake et al. (1987) also observed the temporary burial of some particles within the bed and the loss of tracers that travelled further downstream the investigated area. This research led the way to other applications of marked tracers.

The use of coloured tracers appeared to be inadequate in natural streams as long-term recovery rates proved to be too low to attain reliable results (Ferguson and Wathen, 1998). Coloured pebbles were then replaced by magnetically tagged bed grains that were employed in experiments along rivers to locate their position in time (Ferguson and Wathen, 1998) and to study the burial depth (Hassan et al, 1992; Hassan and Church, 1994). The two years of field experiments performed by Ferguson and Wathen (1998) was characterized by a recovery rate of 61%, with only the 26% of tracers recovered on the bed surface. The intermediate and final surveys of tracing grains location reveal the impossibility to recover and locate all the initially deployed tracers even with the use of a magnetometer, resulting in recovery rates ranging from 25 to 93% (Hassan et Church, 1994). This partial recovery was attributed to the vertical mixing of surface and subsurface material, a process that was observed to increase with time (Hassan and Church, 1994) and with the intensity of the competent flow (Wong et al, 2007). Higher recovery rates were achieved via passive integrated transponder (PIT) by Bradley and Tucker (2012). They yearly investigated the cumulative travel distance computed by PIT tagged particles along a river without digging out deep buried grains.

When the time separating subsequent sampling of particles' positions is so coarse, researchers can only infer the cumulative travel distance rather than attain data on the continuous travel of a particle's trajectory. This has compelled several studies to consider the trajectories as the sum of intermediate movements including both motion and resting, namely the overall distance of movement (Hassan et al., 1992), the global range trajectory (Nikora et al. 2002) or the travel distance over single or multiple flow events (Fergusson and Wathen 1998; Bradley and Tucker, 2012; Hassan et al. 2013).

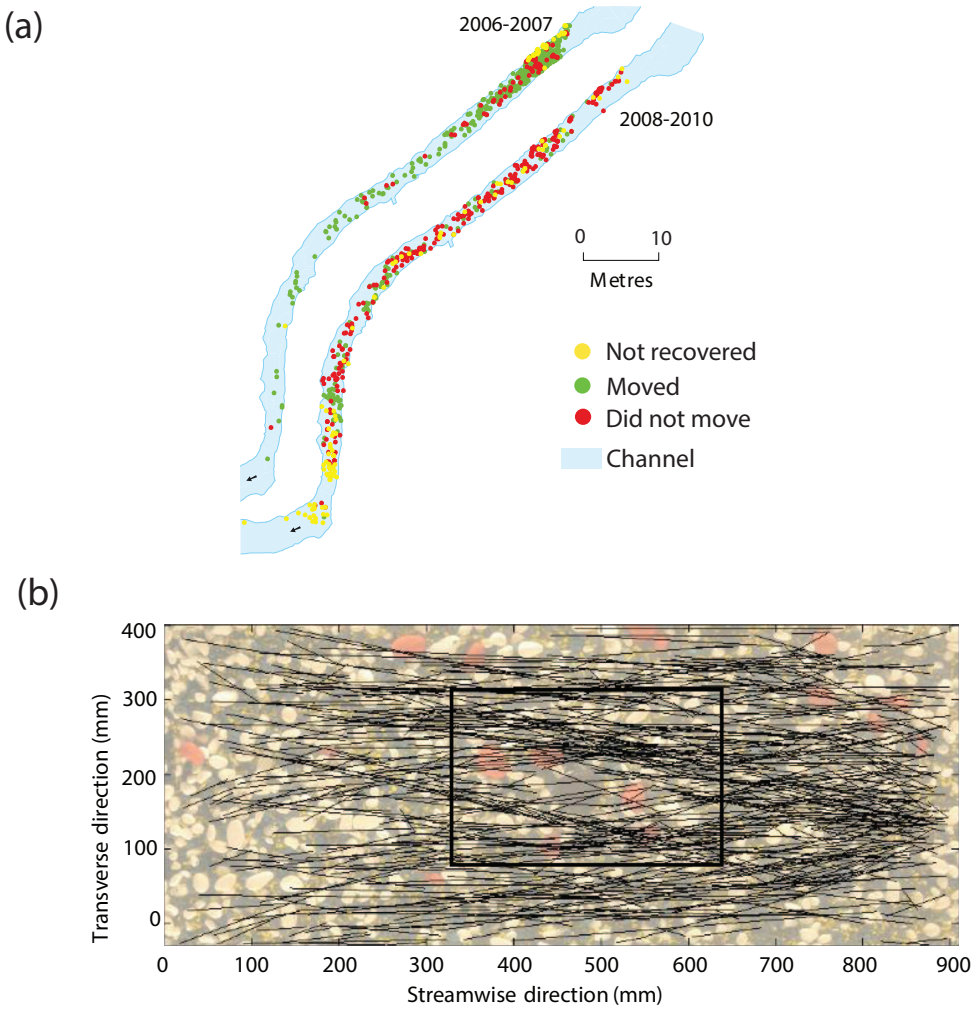


Figure 1.6: (a) Use of tracers in field experiments as reported by Hassan et al., 2013. The positions of the tracing grains in the same river reach are marked after two surveys of different temporal length. (b) Typical image of laboratory experiments with tracers. The image of the investigated bed area reports the trajectories of the moving particles and the smaller box delimitates the area of high-frequency data acquisition (after Heays et al., 2014).

Notwithstanding the advantages of studying the phenomenon in natural rivers, the use of an artificial channel in a controlled laboratory environment should improve the monitoring of grains motion over the bed. The investigation of bed-load sediment transport in indoor experiments benefited from the shorter temporal scale of the study, usually of the order of hours (Marion and Fraccarollo, 1997; Wong et al., 2007), as well as of a restrained area of focus over the erodible bed (Bottacin-Busolin et al., 2008, Lajeunesse et al., 2010; Chegini and Tait, 2011; Campagnol et al., 2013). Under such conditions, the recording of marked grains seemed a more reasonable activity that could be performed with the use of professional equipment for image acquisition. One high-resolution camera recording at the speed of typically tens of images per second proved

to be enough to gather information on the instant of particle's entrainment/deposition and on the series of positions occupied by a moving particle over a mobile channel bed. The following image analysis supported the derivation of automatic tracking algorithms that enabled a rapid processing of thousands of frames, even if they still require refinements and the users' check of the final results (Papanicolaou et al., 1999; Chegini and Tait, 2011; Campagnol et al., 2013, Heays et al., 2014).

On the other hand, the high-frequency acquisition of images in laboratory experiments is counterbalanced by the limited size of the field of view tracked by the recording system. As a consequence data collected in laboratory experiments typically lack full information on tracers travelling for much longer distances than the longitudinal size of the observed area (Bottacin et al., 2008; Lajeunesse et al., 2010; Furbish et al., 2012b; Tregnaghi et al., 2012b). For instance, Lajeunesse et al. (2010) measured the lengths of individual trajectories of bed load particles with a high resolution image tracking system over an area of 177.3 mm $\times$ 85.6 mm of the bed. They could only derive a partial distribution of the step length that lacked the grains with longer trajectories and for this reason they only inferred the most probable step lengths instead of the mean value of the overall step length distribution.

Within the currently available technology, investigating the bed-load motion with experiments using tracing particles faces two main challenges. In in-situ experiments one can study the transport process as it occurs in natural rivers and for long-term survey studies. However, the practical applicability of this method in the field is questionable due to the low-frequency data acquisition rates of tracer location and also the partial recovery of tracer particles trapped within the sediment bed. Conversely grain data sets collected via the high-frequency acquisition of images in laboratory experiments under controlled conditions suffers from the limited duration of the experiments and the size of the field of view tracked by the recording system. The data collected in laboratory flumes will thus cause a partial description of the probability distributions characterising the particles' trajectory.

A new technology has recently been employed in the study of sediment motion in water and its feasibility is currently under investigation. A sensor carrier has been produced sufficiently small to be inserted in pebbles (with longest axis greater than 60 mm), defined as *Smartstones* (Gronz et al., 2016). The cylindrical sensor carrier includes an active radio-frequency identification (RFID) chip, an accelerometer, a magnetometer, and a gyroscope. The transferred data and the RFID tag identification provide valuable information of the stone's motion as well as orientation, acceleration and rotation. Despite the errors associated to the results that were obtained in the first experimental applications (Gronz et al., 2016), these Smartstones could make significant progress towards the non-intrusive and accurate observation of grains' displacement and motion. Such measurements would help develop an understanding of the resulting forces acting on a grain at incipient motion conditions, transport and deposition. Future technological progress may also produce even smaller sensor carriers to be mounted in gravel-size grains.

Independently of limitations in the experimental studies on bed load transport, sediment tracers have been used in several studies to provide a Lagrangian description of particle motion that could be eventually incorporated into probabilistic models. The entrainment form of the sediment flux is particularly valued in treating tracer particles' data (Ganti et al., 2010). In this formulation stochasticity is introduced in particle motion by considering the particle step length as a continuous random variable that should be described with a probability distribution. Such a random behaviour in bed-load grains motion has been identified as a potential source of diffusion (Furbish et al. 2012a), and it was correlated to the evidence of different diffusive regimes (Ganti et al., 2010) that were originally associated to the spatial and temporal scales of

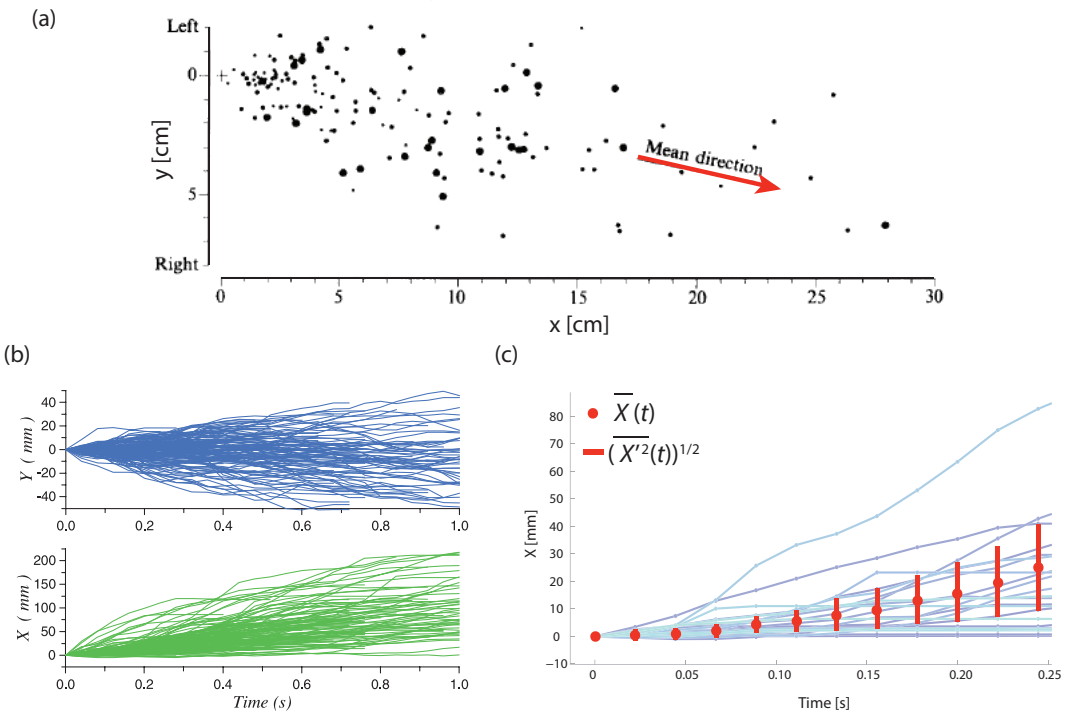


Figure 1.7: Example of particles trajectories. (a) Particles' displacement over the planar bed after 70 s with the size of the dots proportional to the diameter of the tracing grains (after Drake et al., 1988). (b) Streamwise and crosswise trajectories of particles in time (after Nikora et al., 2002). (c) Example from this work as presented in Chapter 2 where the streamwise trajectories are plotted in time with a focus on the variation of the first and second order moments of ensemble particles' locations.

grain motion (Nikora et al. 2002).

The indication of bed-load particles exhibiting an advective and diffusive pattern was obtained via experiments and theoretical formulations. The Lagrangian analysis of the trajectories of individual gravel grains as represented in Figure 1.7 demonstrated that the plume of traced grains spread longitudinally according to a Fickian diffusion (Drake et al, 1987) or to an anomalous type of diffusion as corrected with recent findings by Nikora et al. (2002) and Campagnol et al. (2013).

To physically model the experimental evidence of advection and diffusion, mass balance equations have been generally employed for cases of uniform flow conditions. In such formulations the evolution in time and space of the plume of tracers can be expressed as an exchange between mobile particles on the moving layer and immobile particles on the bed surface (Lajeunesse et al. 2013) or it can be reported in dependence on the entrainment and deposition rate of tracers in the surficial layer of the streambed expressed in function of the grains' travelling distance (Ganti et al., 2010; Furbish et al., 2012a; Pelosi and Parker, 2014). Examples of the simulations resulting from the two approaches are presented in Figure 1.8. These models account for the results provided by the Lagrangian analysis of particles motion, being it the grain velocity or the step length, in the attempt to include the observed stochasticity of random bed-load grains behaviour into the description of the diffusive rates.

However, the resolved nature of the diffusion process is not absolutely determined as it depends on the probability distribution assigned to the random variable that is considered in the formula. The use of the step length has implications in the mode of particle motion as for

thin-tailed PDFs the Ganti et al.'s model equation leads to a classical Fickian advection-diffusion process, while for a heavy-tailed PDF theoretical arguments suggest anomalous advection and diffusion of bed load transport. The experimentally derived distributions of step lengths, mostly right-skewed and fat-tailed, are generally assumed as a sign of super-diffusion (Bradley et al., 2010). Lajeunesse at al. (2010) in their first study observed that the PDFs of the stream-normal particle velocities are wider than Gaussian and concluded that the particles spread along the transverse direction following an anomalous diffusion process. In the next study (Lajeunesse at al., 2013) they argue that the concentration of the group of particles along the streamwise direction resembles a normal diffusion at longer times. The results are although based on the assumption of constant particles' velocity, and they are expected to change if the velocity is described by a continuous distribution (Lajeunesse et al., 2013).

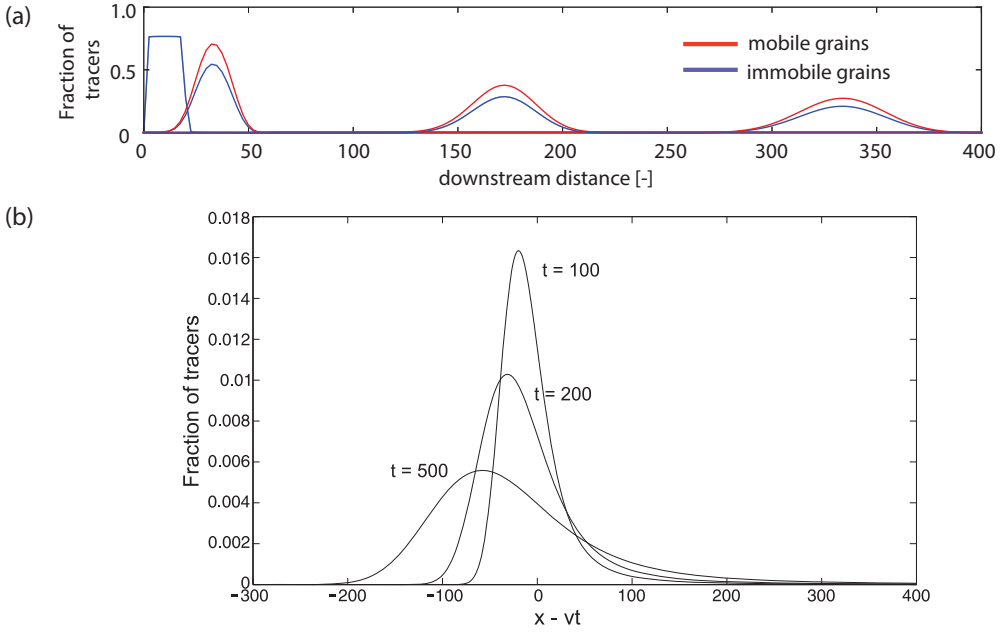


Figure 1.8: Model simulation of tracers concentration evolution in time and space presented by (a) Lajeunesse et al., 2013, and (b) Ganti et al., 2010. In plot (b) the time is expressed in days and the solution is reported for an anomalous diffusive behaviour.

The value in this research by the use of sediment tracers in field and in laboratory is counterbalanced by the intrinsic difficulties, which are still experienced nowadays, in performing experiments with tracers. A partial description of the grains' trajectories produces a negative cascading effect that can jeopardize the ability to predict bed-load sediment transport (Furbish et al., 2012b,c). The Lagrangian analysis proved the stochasticity of the grains' motion, but the physical limitation in the acquisition of information (recovery rate, temporal samplings, size of investigated area, among others) tends to limit the applicability of the results. An incomplete description of the probability distributions of the motion parameters could then generate discrepancies in the final modelled transport behaviour (Bradley et al., 2010; Bradley and Tucker, 2012). The description of the grains' motion, the type of diffusion associated to the motion of the bed material together with the concentration curves simulated by the mass balance based models (Figure 1.8) have been partially supported by few experimental studies (Sayre and Hubbell, 1965; Drake et al., 1988; Nikora et al., 2002; Bradley and Tucker, 2012). It is not clear then whether the stochastic model formulation is correct or which variables influence the transport the most (flow intensity or bed roughness).

The previously cited works highlight the need for implementing the use of tracers in innovative ways that overcome the former experimental limitations in order to identify appropriate models so as to explain the temporal evolution of sediment diffusion in rivers.

## 1.4 Description and objectives of this study

The questions this study is trying to answer stem from the gaps and limitations of the former scientific investigation of bed-load sediment transport. The initial deterministic approaches to this topic have proven to be inadequate in the attempt to explain the randomness of the sediment transport nature in streams. It had thus left space for the application of the language and tools of probability to the processes of grain's entrainment and motion. The stochasticity concepts came along with the necessity to collect experimental data that would support the new theoretical framework. The Eulerian method, which looks at the transport processes at a particular location in time, could not provide such information and it has been substituted by a more appropriate Lagrangian analysis of fewer analysed bed grains called *tracers*. A particle-based approach enabled researchers to gather single-trajectory's information of the moving tracer particles, so that the probability distribution associated to the motion variables could be computed. The experimental difficulties and technical limitations scientists faced in collecting field and laboratory data have led more often to partial descriptions of the particles' motion than to a complete assessment of the probabilistic distributions. This uncertainty is then reflected in the results of the transport models, which incorporate unreliable probabilistic information into their theoretical formulation. The predicted advection and diffusion of bed particles are entirely model simulations with no experimental data to validate their approaches. This means that a new method which allows a continuous tracking of tracing particles within the bed deposit in time is required.

In this study we aim to develop a sediment transport model that can predict the observed advection and diffusion of bed-load particles by considering the randomness of the single particle's trajectories. This study will then cover the following objectives:

- thoroughly and accurately study the bed-load grains' trajectories in order to stochastically describe the motion parameters, in particular the step length;
- investigate the bed-load transport processes in long-term conditions to collect experimental data representing the advective and diffusive nature of sediment transport;
- use experimental evidence and the results of the simulations to study the influence of the the bed-roughness, such as the relative particles' size and the grain size distribution, on the particles' trajectories and on the diffusion rates;
- develop a general model to simulate the advection and diffusion incorporating the complete experimental information on particles' trajectories following the probabilistic approach.

To fulfil the above objectives, a preliminary particle-based analysis of existing dataset of high-speed particle tracking collected during earlier independent experimental studies (Tregnaghi et al., 2012b) is firstly carried out with the aim of creating the conceptual framework for the study of the complex bedload particles' trajectories. The Lagrangian analysis allowed indications of bed-load particles diffusion to be collected following the model presented by Nikora et al. (2002) along with a preliminary description of the stochasticity denoting grains' motion in terms of step lengths. This initial study helped identifying two methods to solve the typical

problem of truncated probability distributions that originate from a partial description of grains' trajectories.

Here step length, $r$, is defined as one individual streamwise displacement between the position of entrainment and the subsequent deposition point. The one-dimensional Exner equation for tracer mass conservation is then reformulated to incorporate the probability density functions of step lengths $r$ and of the dependent travelling times $\tau_p$(or particles' velocity $v_p$ for $\tau_p = r/v_p$). The general formula is based on the idea that tracer particles arriving at position $x$ at time $t$ started their random hops $r$ at many different times $(t-\tau_p)$, with $\tau_p$ the time spent in motion. A simplified version of the formulation which derives the concentration of tracers in time along the main flow direction is used to model a series of experiments on advection and diffusion of bed load particles (Marion, 1995). From the comparison of the simulations with the experimental results from different tests it was possible to investigate the role of step length distribution in tracer motion over time and space, and the effect of the sediment bed composition on the fate of tracers.

The preliminary study of particles' motion from the two existent experimental databases has shown technical and conceptual limitations. The problems encountered have then helped defining a new series of experiments in the attempt to solve the following points:

1. reducing the influence of temporal duration of the tests and spatial dimension of the investigated area where tracing particles' information is collected;

2. investigation of the advective and diffusive behaviour for long-time equilibrium experiments by derivation of the tracers' concentration curves in time along the main flow direction;

3. monitoring in time the exchange processes that take place in the surficial layer of the bed by sampling the bed deposit with the minor disturbance as possible;

4. isolating the effect of bed roughness and relative particles' size as well as the influence of the flow conditions on the transport probability description.

To address the above points an annular flume was the most appropriate channel to work with. The closed system of annular flumes has proven to be appropriate for erosional studies as recirculation does not occur and the bed can so attain equilibrium conditions (Partheniades et al., 1966; Gharabaghi et al., 2007). The continuity of the system allows long-time experiments and the tracking of the particles without incurring interrupted trajectories. The visualization of the marked tracers is made possible by a bed composed of mixed-sized transparent beads, while the recording of tracers' motion on the surface and within the bed relies on high-speed cameras. The tracing particles consist of black-dyed beads of the same material as the particles composing the bed and they will provide information for both the Lagrangian analysis and the reconstruction of the concentration curves along the channel in time. With a transparent bed it is possible to locate also buried tracers, whose contribution to the diffusive rates would be otherwise lost. The influence of the bed roughness on the particles' motion and on the advective and diffusive rates is investigated by mixing different sizes of bed material and using tracers of different diameter under different hydraulic conditions applied. The investigation of the tracers' behaviour over the array of different roughness and hydraulic conditions would possibly help isolating the effect of these two contributions on the single and overall motion of particles.

The new experimental data would then be the basis for a complete analysis of the tracers' trajectories. Based on the new dataset of fully described displacements, it will be possible to assess which method performs better in case of truncated experimental data and to implement

the general model formulation which includes the stochasticity of step length and travelling time. The model performance is tested with the new collected concentration curves of tracers showing that an accurate assessment of the stochasticity of particles motion, once included into the general formulation, can provide a reliable estimation of the measured advective and diffusive rates.

# Chapter 2

# Particles' trajectory and diffusive regimes

The scientific and engineering interest in understanding sediment dynamics over a river bed has led to the performance of experiments in which the displacement of few moving particles was closely monitored. The behaviour of this group is assumed to be representative of the entire particle population. Monitoring the sample of the overall grain population is less than the effort that would be spent in tracking all moving grains. Bed-load particle motion has been monitored in experiments and either manually or automatically traced along the planar view of the bed in the longitudinal and transversal directions (e.g. Drake et al. 1987; Ferguson et al., 2002; Nikora et al. 2002, Tregnaghi et al. 2012, Radice et al. 2013). Images of the bed acquired at a high frequency, usually tens of frames per second, enabled researchers to record a single grain location and to compute a reasonable Lagrangian description of particles' trajectories. The results revealed that bed-load particles' displacement is a stochastic variable that should be described in probabilistic terms. The stochasticity of particles' motion stems from the heterogeneity of rivers' bed and, in turn, it is reckoned to be a source of diffusion (Drake et al., 1987; Nikora et al., 2002; Wong et al., 2007; Hassan et al., 2013). By recalling the diffusive regime model proposed by Nikora et al. in 2002, the diffusion of bed load grains is therefore linked to their displacement characteristics.

In this chapter research data from earlier experiments has allowed the preliminary study of particle travel distances for a range of flow conditions and for a model of the diffusion of granular material to be developed. The knowledge gained in this preliminary study has helped to reveal the limitation of the former tests and to led to the development of experiments to fully describe the grains trajectories and the associated diffusive process and so support the development of a stochastic based model of sediment movement, able to predict motion behaviour of a sediment population subject to a range of flow conditions.

## 2.1 Conceptual model

### 2.1.1 Diffusive regimes and particles' trajectories

Diffusion can be estimated from the variation in time of particles' coordinates. Unfortunately gathering information on particles' displacement over a bed is not an easy task. In riverine environments the study of particles displacement is usually limited by the recovery rate of

tracing grains. The tracers' trajectories also depend on the frequency of surveys. Particles' location is usually investigated in a timescale of days or after intense flow events (Ferguson and Wathen, 1998; Bradley and Tucker, 2012; Hassan et al., 2013), thus only information on the cumulative distance travelled by a particle between consecutive survey campaigns is available. In controlled laboratory experiments, assessing particle steps can be limited by several factors. The investigated areal extent is usually restrained to a scale of tens of centimetres due to equipment constraints (Nikora et al., 2002; Lajeunesse et al., 2010; Tregnaghi et al., 2012b), thus ignoring the particles whose steps are greater than the area dimensions. The accurate reconstruction of the trajectories is highly dependent on the frequency of the image acquisition. A higher frame rate would possibly help to determine the exact instant of entrainment and the duration of rest periods with less error. Eventually in order to obtain converged statistics of particles steps and rest times, the number of tracking grains should be adequate. As diffusion depends on particles' location with time, its accurate estimation can be greatly affected by the capability of the experimental set-up.

Nikora et al. (2002) presented a conceptual model for longitudinal and transverse diffusion which considered the temporal and spatial scales of bed load motion and associated them with a diffusion regime (Figure 2.1). Particles' motion can be divided into three categories: (a) local range, characterized by ballistic diffusion, which corresponds to a particle's trajectory between two consecutive collisions with the bed, (b) intermediate range, which refers to a particle's displacement between two subsequent periods of rest, denoted by normal or anomalous diffusion, and (c) global range, identified by subdiffusion, indicates particle's trajectory including many intermediate steps. The type of diffusion can be determined with the estimation of the growth of the second order moment of particles' location with time as explained in the next section.

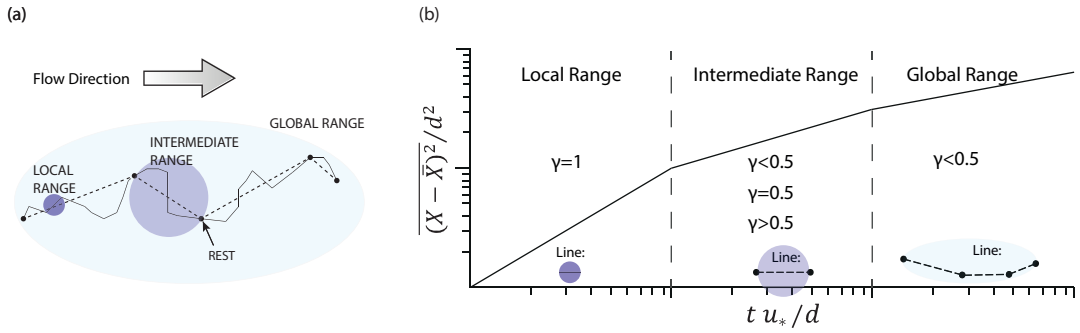


Figure 2.1: (a) Schematic illustration of the three ranges of particles' trajectories: local, intermediate and global and (b) diffusive scaling coefficient derivation (after Nikora et al., 2002).

The conceptual model presented by Nikora et al. (2002) still requires a strong numerical and experimental validation (Bialik et al., 2012; Campagnol et al., 2015). In existing numerical modelling studies the simplified description of particles' movement does not include the heterogeneity of the bed morphology and flow conditions. In field experiments the large temporal sampling to survey subsequent particles' locations cannot identify the local range and consequently confirm ballistic diffusion. On the other hand in laboratory experiments the limited extent of the investigated area can compromise the correct assessment of the global trajectories and therefore the assessment of the sub-diffusive regime.

### 2.1.2 Mathematical formulation

A trajectory is the sequence of a particle's position at every instant of time. Assuming that a particle $i$ is moving, and in every time interval $t_j$ performs a random step $\lambda_j$ along the three

coordinates $x$, $y$, and $z$, the position of particle $i$ after $n$ time intervals can be written as:

$$P_i(t) = \sum_{j=1}^{n} \lambda_j, \tag{2.1}$$

where $P_i = (x, y, z)$ is the position of a particle in the space, after a time $t = nt_j$. If the number of particles $N$ is large enough and all the particles have the same starting position it is possible to study the group behaviour of the moving particles. At any time $t$ it is possible to calculate the moments of the positions of the group of particles. The first moment of $N$ grains' locations in time can be calculated as follows:

$$\overline{P}(t) = \sum_{i=1}^{N} \frac{P_i(t)}{N}. \tag{2.2}$$

The first moment represents the centroid of the cloud whilst the second central moment denotes the *spread* of the cloud:

$$\overline{P'^2}(t) = \sum_{i=1}^{N} \frac{(P_i(t) - \overline{P}(t))^2}{N}. \tag{2.3}$$

Eq. 2.3 provides a measure of the magnitude of the diffusion in each direction. Assuming that all the displacements performed by each particle are independent from one another and all the steps are identically distributed according to the same probability distribution $f(\lambda)$. If the number of displacements (or time intervals) is large enough it can be demonstrated that the distribution of the particles' position along a fixed direction follows a normal distribution. This result can be obtained since in those conditions the Central Limit Theorem (CLT) holds. If the trajectory of each particle follows the hypothesis stated above the variance of the particles' position increases linearly with time, therefore $\overline{P'^2}(t) \propto t^{2\gamma}$ with $\gamma = 0.5$. When the variance of the particles' position scales linearly with time, diffusion is called *normal*. However, there are several reasons for which the movement of bed-load particles rolling on the rivers' bed does not respect the assumptions of the normal diffusion.

In case of normal diffusion the particles are constantly moving according to the probability distribution of the displacements, while in the case of bed-load transport particles alternate quick movements to longer resting phases (Einstein, 1950). This process can be better described as *diffusion among traps* (Bouchaud and Georges, 1990). In the normal diffusion an absence of 'long-range' correlations is supposed to occur. In the case of flume experiments these mechanisms cannot be excluded a priori. Some long-range correlations in the flow turbulence and broad distributions due to extremely long resting times may occur (Nikora et al. 2002). When the motion of bed-load grains is studied in rivers, many factors can affect the trajectories of grains, such as vegetation, bedforms, and near-bed turbulent events. For all these reasons bed-load grains that move along the river are more likely to show a process of *anomalous* diffusion.

The model used in this work to initially describe the diffusion was presented in two studies by Nikora et al. (2001, 2002) and it is based on the dimensional analysis of the evolution of particles' trajectories in time along the streamwise and the transverse direction. As shown above, the type of diffusive regimes can be determined by the scaling growth in time of the central moments of particle's coordinates:

$$\overline{X'^q} = \overline{(X(t) - \overline{X}(t))^q} \propto t^{q\gamma_x} \tag{2.4}$$

$$\overline{Y'^q} = \overline{(Y(t) - \overline{Y}(t))^q} \propto t^{q\gamma_y} \tag{2.5}$$

where $X(t)$, $Y(t)$ denote the longitudinal and transverse coordinate of particles, $q$ is the moment order and overbar denotes ensemble averaging. The $\gamma_x$ and $\gamma_y$ exponents indicate the type of diffusion regime in bedload particle motion: ballistic ($\gamma = 1$), superdiffusive ($\gamma > 0.5$), normal ($\gamma = 0.5$) or subdiffusive ($\gamma < 0.5$). Diffusion with $\gamma \neq 0.5$ is defined as anomalous diffusion (Fig. 2.1b).

The parameters that completely defines the problem are: $u^*$ shear velocity, $g$ gravity acceleration, $d$ particle diameter, $D$ characteristic dimension for roughness, $\nu$ fluid viscosity, $t$ particle travel time including rest period, $\rho$ the density of water and $\rho_s$ the density of the particle. With a dimensional analysis and mathematical manipulations, Nikora et al. (2002) expressed the second moment of particle coordinates as a function of the shear velocity, the particles diameter $d$ and the travelling time $t$ (including both time in motion and at rest):

$$\frac{\overline{X'^2}}{d^2}, \frac{\overline{Y'^2}}{d^2} \propto \left(\frac{tu^*}{d}\right)^2. \tag{2.6}$$

Experimental data or numerical simulation should support the derivation of the diffusion scaling coefficient $\gamma$. Nikora et al. (2002) attempted to describe the particles diffusion by means of experiments in an irrigation canal. The authors derived a super-diffusive regime linked to the intermediate stage of particles' trajectories but their conceptual models still requires a complete experimental validation.

## 2.2 Experiments

Experiments performed at the University of Bradford in 2009 (Tregnaghi et al., 2012b, Cecchetto et al., 2016) offered data that with suitable analysis can provide the information to potentially validate the above conceptual model. The experiment offered also a unique database for a detailed description of bed-load particles' displacements over a gravel bed under different flow conditions. This information is then used to extensively investigate the intermediate range of motion, from entrainment to rest, in order to describe the complete statistics of the distributions of particles' step length.

### 2.2.1 Experimental apparatus

The experimental apparatus consisted of a tilting flume with a length of 12 m and width of 0.50 m. The flume bed was filled with uniform natural gravel characterized by a lognormal grain size distribution. The mean bed diameter was $d_{50} = 5$ mm and the standard deviation $\sigma_g = 1.3$ mm with density of the gravel $\rho_s = 2650$ kg/m$^3$. The loose material was arranged to form a uniform and well mixed 60 mm layer of sediment and scrapped flat at the beginning at each of the tests. The bed material placed near the inlet (for a length of 1.5 m) was fixed to ensure the development of a stable turbulent boundary layer. In total 12 tests were carried out with increasing values of shear stress and constant water depth $h_u = 100$ mm. Results from 6 tests are presented. Because of time demanding analysis, out of 12 tests, only 6 have been so far processed to provide the necessary information on grains' movement. The main hydraulic parameters for each test are reported in Table 2.1.

The parameters include: $s_c$ the flume's slope in %, $Q$ the flow-rate, $U$ the depth averaged streamwise fluid velocity, $Re = 4R_H U/\nu$ the Reynolds number where $R_H$ indicates the hydraulic radius corrected to account for the smooth glass sided walls ($R_H = 0.0845$ m) and $\nu$ the fluid viscosity, $u^* = (gR_H s_c)^{1/2}$ the shear velocity and $\tau^* = \tau/g(\rho_s - \rho)d$ the Shields shear stress

Table 2.1: Main hydraulic parameters for the 6 tests presented.

| TEST | $s_c$ [%] | $Q$ [l/s] | $U$ [m/s] | $Re$ ($10^5$) | $u^*$ [m/s] | $\tau^*$ | $\tau^*/\tau^*_{cr}$ |
|---|---|---|---|---|---|---|---|
| T1 | 0.59 | 43.3 | 0.94 | 2.98 | 0.070 | 0.061 | 1.13 |
| T2 | 0.65 | 44.8 | 0.97 | 3.19 | 0.074 | 0.068 | 1.25 |
| T3 | 0.77 | 48.1 | 1.05 | 3.34 | 0.080 | 0.080 | 1.48 |
| T4 | 0.80 | 49.0 | 1.07 | 3.40 | 0.081 | 0.083 | 1.54 |
| T5 | 0.83 | 49.8 | 1.08 | 3.45 | 0.083 | 0.086 | 1.59 |
| T6 | 0.86 | 50.1 | 1.11 | 3.53 | 0.085 | 0.090 | 1.66 |

parameter. In the presented tests the ratio between Shields shear stress parameter and Shields critical shear stress parameter, $\tau^*/\tau^*_{cr}$, ranges from a minimum value of 1.13 (weak transport condition) up to the value of 1.66 (moderate transport condition). The choice of performing the experiments in low-transport conditions allowed for the very clear identification of the grains' entrainment and deposition events.

The experiment aimed to couple information of the near-bed 3D flow velocity to the motion of individual grains (Tregnaghi et al, 2012a, Cecchetto et al., 2016). The flume was equipped with three video cameras placed above the bed and acquiring images at a frequency of 45 Hz. Two cameras (2 and 3) were intended to reconstruct the velocity field at 8 mm from the bed crest with a stereoscopic PIV (Particle Image Velocimetry) system (more details in Cecchetto et al., 2016). A third camera (cam 1), vertically oriented, captured the motion of bed-load grains over the same area. The investigated area, 220 mm long and 80 mm wide, was located along the centreline of the flume's bed at approximately 6 m from the inlet (Figure 2.2). In this work only information from cam 1 regarding the sediment motion will be considered.

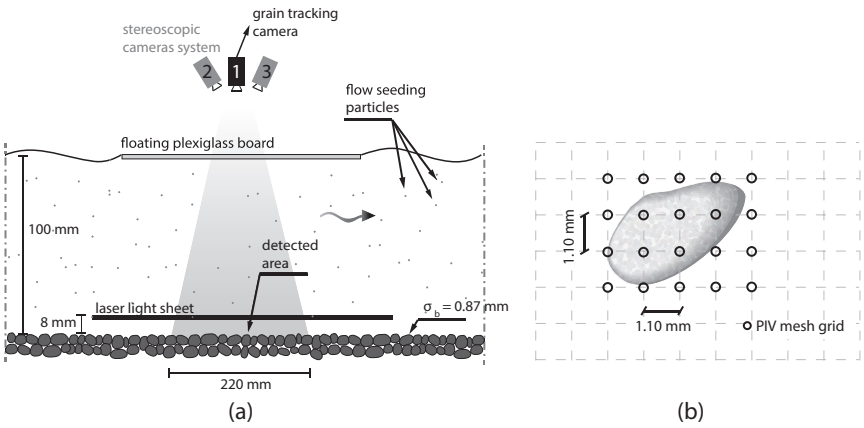


Figure 2.2: (a) Schematic representation of the longitudinal section of the flume in correspondence of the investigated area. (b) PIV mesh grid resolution. After Cecchetto et al., 2016.

### 2.2.2 Data analysis

For each flow condition 6000 images, out of the total 27000 recorded, were analysed. This corresponded to a time interval of approximately 2 minutes (133 s) from a total time series of 10 minutes-duration. The position of a moving particle was registered in each frame with a manual identification tracking procedure following the method developed by Bottacin-Busolin et al. (2008). The manual tracking enabled the user to differently code a grain based on its state being it starting to move (*start*), moving (*move*) or stopped (*stop*) thus identifying four

types of displacements according to the initial and final position of the grain with respect to the investigated area, as represented in Figure 2.3. This information along with the centroids location of the detected particles was saved in a database and resulted essential in the measurement of the grains' trajectories. The analysis of the images from all the tests provided a total number of 2460 tracked grains.

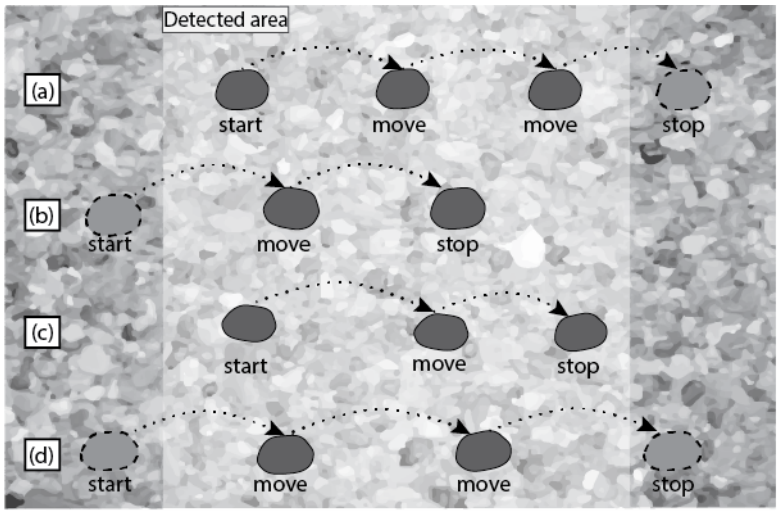


Figure 2.3: Sketch of the types of displacement: (a) *start-move*, (b) *move-stop*, (c) *start-stop*, and (d) *move-move*.

Correctly defining the trajectory computed by a grain can face several issues such as (i) definition of the duration of a competent resting time, (ii) very small displacements (compared with the particle's diameter) caused by shaking/vibrating grains rather than grains in transport, and (iii) spatial limitation of the investigated area.

Having examined hundreds of grain movements, it became apparent that the definition of particle's resting times is not obvious. A grain in its moving phase can sometimes rest for just a couple of frames (about 0.044 s) and then start moving again. To overcome this issue, a minimum threshold of 10 frames ($t_{min}$ = 0.22 s) was arbitrarily imposed as defining a grain having entered a resting state. If a grain stops for a time $t$ longer than the threshold $t_{min}$ it will be considered in rest; otherwise, if a grain stops for a time shorter than $t_{min}$ the grain position is registered as a part of its continuous original trajectory.

A second practical problem is related to the interpretation of extremely short travelling distances. If a grain had computed from its entrainment to its rest a distance smaller, in the longitudinal component, than its diameter, the displacement is neglected in the analysis, since it is considered an adjustment towards a stable position rather than an active motion. The criterion to neglect the very short displacements is based on the average diameter $d_{50}$ = 5 mm. This physical interpretation is considered reasonable as a grain re-adjusting its position on the bed is subject to different forces compared to a grain moving through the fluid. The first situation is heavily influenced by frictional forces whilst the second is greatly influenced by fluid drag forces.

A third practical problem is related to the physical boundaries of the investigated area. If a grain is entrained outside the examined window and then stops inside, the total travelled length cannot be calculated since the starting position is unknown (Figure 2.3). In this case the grain's displacement is called: *Move-Stop*. The same consideration applies to a grain that starts within the window and stops outside. In this case the resting location is missed and the displacement is called: *Start-Move*. A grain can also be entrained and stopped outside the window, resulting in

a displacement hereafter called *Move-Move* (Bottacin-Busolin et al., 2008). The latest definition can indicate total longitudinal travel lengths longer than the longitudinal areal extent $L_x$, i.e. 220 mm, or shorter in case the grain crossed the investigated area with a sidelong trajectory. The travelled distance can be readily measured only for those displacements that are completely recorded within the investigated area, so called *Start-Stop*, while nothing can be assessed in case of other displacement definitions. The fractions of different displacements categories for each test are presented in Figure 2.4 and summarized in Table 2.2. This experimental limitation and the influence it has on the results will be discussed in the following sections.

Table 2.2: Number of grains' displacements grouped in different types according to the initial and final position with regards to the investigated area extent. The minimum displacement is indicated by $d_{50} = 5$ mm, while $L_x$ denotes the longitudinal size of the investigated area. Results are presented for each test.

| DISPLACEMENT TYPE | T1 | T2 | T3 | T4 | T5 | T6 |
|---|---|---|---|---|---|---|
| Start-Stop $> d_{50}$ | 144 | 318 | 174 | 179 | 205 | 105 |
| Start-Stop $\leq d_{50}$ | 32 | 84 | 76 | 24 | 100 | 20 |
| Move-Stop | 80 | 235 | 133 | 106 | 236 | 154 |
| Start-Move | 88 | 177 | 122 | 96 | 202 | 126 |
| Move-Move $> L_x$ | 23 | 42 | 35 | 41 | 57 | 32 |
| Move-Move $\leq L_x$ | 13 | 59 | 61 | 31 | 165 | 71 |

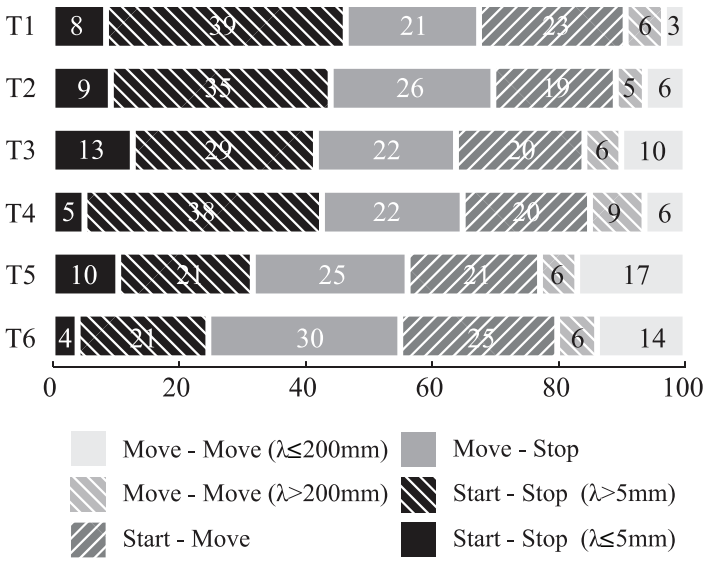


Figure 2.4: Percentages of travelled lengths divided into 6 types of displacements based on the grains' path with respect to the investigated area.

## 2.3 Results

The same procedure followed by Nikora et al. (2002) was applied to the longitudinal and transverse position of the particles that were detected in the six analysed tests. In order to have a consistent dataset of fully known trajectories, grains' path with starting positions outside the investigated area are neglected. Likewise for starting grains that exit the observed area. As their subsequent positions are unknown, the recorded path is discarded. The analysis includes then

only grains whose trajectories (from *starts* to *stops*) take place within the inspected area. In the first stages of the diffusion this effect is negligible, but it becomes relevant with the increasing of the observation time. The implications of this effect are discussed later.

### 2.3.1 Diffusion of bed-load particles

The analysis of the diffusion of bed-load particles requires the same reference system for all the moving grains. Detected particles should be entrained in the same location and at the same time. As the current experiment was focused on a relatively small area of the bed and recorded the particles' trajectories for two minutes, grain's locations have been scaled to the same origin point:

$$\begin{cases} X_i(t)^* = X_i(t) - X_i(t_0) \\ Y_i(t)^* = Y_i(t) - Y_i(t_0), \end{cases} \tag{2.7}$$

where $X_i(t_0)$ and $Y_i(t_0)$ are respectively the first recorded streamwise and crosswise positions of the $i^{\text{th}}$ grain in correspondence of the entrainment event that happened at $t_0$. Figure 2.5 shows the corrected trajectories resulting from the above scaling for test T1. By zooming on the initial stage of motion, it is possible to notice the downstream progression of the cloud's centroid, represented by the first order moment of particles' location, and the spatial evolution of the diffusion indicated by the second order moment. The temporal analysis of the second order moments should shed light on the type of diffusive processes taking place. The analysis of the streamwise and crosswise trajectories is performed for a time $T_{MAX} = 4$ s corresponding to 180 frames, for all the six tests. The 4-seconds analysis was enough to collect information on the trajectories of the grains moving within the investigated area.

In four seconds, the total number of intermediate trajectories ranges between 123 (test T6) and 342 (test T2). Some of these intermediate trajectories are computed by the same grain that was entrained and had stopped more than once within the investigated area. It was then possible to calculate the number of global trajectories, which consisted of 2 up to 5 subsequent intermediate displacements. No global trajectories consisting of more than 5 intermediate steps could be detected, and this is possibly ascribed to the longitudinal size of the investigated area.

Following Equation 2.6, the second moments of particles coordinates has been plotted versus $(tu^*/d)$ in log-log scale to determine the scaling coefficient $\gamma$. The group of plots in Figure 2.6 and 2.7 reports respectively the evolution of the dimensionless variance of longitudinal and transversal particles' position for all the tests. The results are also summarized in Table 2.3.

The analysis of particles' trajectories confirmed the presence of a *ballistic* diffusion for the initial part of the motion. The ballistic part is associated to the subsequent positions occupied by a grain during its collision with the bed before achieving a complete stop. It is then extremely important to capture these successive collisions. A relatively high image acquisition rate can make this possible. The 45 Hz of the cameras recording frequency resulted sufficient in the description of the local range of particles' displacement over the natural gravel bed. The diffusive coefficients for the streamwise trajectories, $\gamma_x$, are close to 1, indicating that diffusion grows with the squared of time. The lateral analysis of particles coordinates reveals the same diffusive pattern, even if the ballistic regime is replaced by a *super-diffusive* one, $\gamma_y = 0.7 - 0.8$. Diffusion on the local scale resulted in anisotropic behaviour as $\gamma_x \neq \gamma_y$.

The intermediate range, proposed by Nikora et al. (2002), is not represented as a diffusion process growing in time with constant diffusive coefficient $\gamma_x$ in this data. It is instead more likely to be identified as a transitional diffusive process (Figure 2.6). This trend is observed for

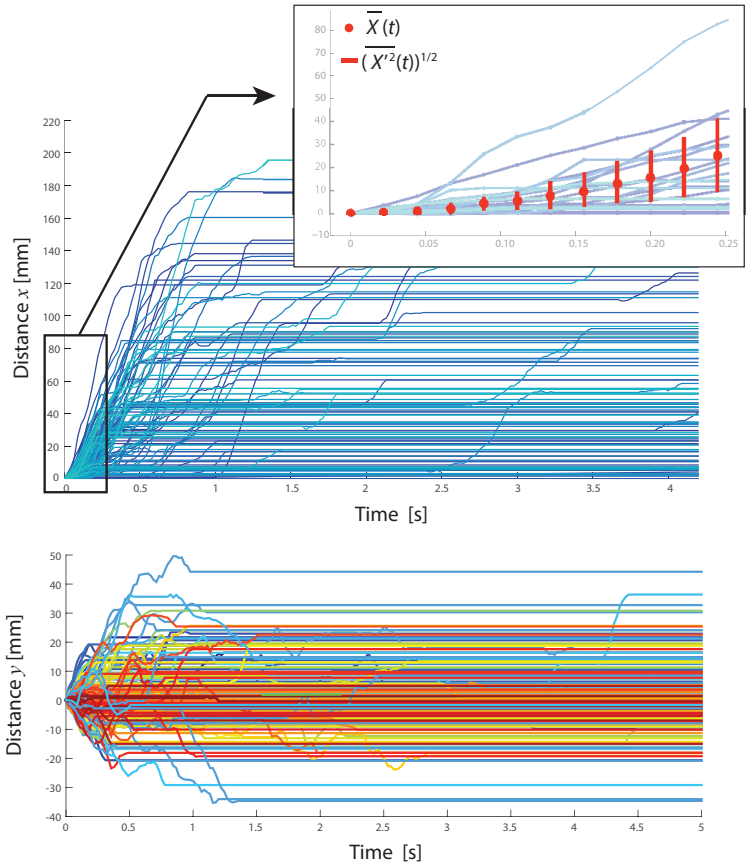


Figure 2.5: Particles longitudinal and transversal trajectories in 4 seconds for one of the six tests (T1). The top-right box focuses on the first 0.25 s to show the variation in time of the first order moment of particles locations and the square root of the second order moments.

all the experiments and the duration of the transitional zone appears invariant to the increase in average bed shear stress.

At the end of the intermediate transitional range, the global range takes place. A *subdiffusive* regime characterizes the motion of particles at this stage. Both the longitudinal and the transversal variances of particles' locations grow very slowly with time, $\gamma_x$, $\gamma_y$ = 0.1-0.2. If only the local and the global ranges are considered, their linear fittings meet at about $(tu^*/d) \approx 8$, $t \approx 0.6$s, reporting no dependences on the shear velocity.

Table 2.3: Longitudinal and lateral diffusive coefficients for each test.

| TEST | $\gamma_{x,LOCAL}$ | $\gamma_{x,GLOBAL}$ | $\gamma_{y,LOCAL}$ | $\gamma_{y,GLOBAL}$ |
|---|---|---|---|---|
| T1 | 1.18 | 0.11 | 0.88 | 0.13 |
| T2 | 0.97 | 0.10 | 0.80 | 0.09 |
| T3 | 1.10 | 0.11 | 0.79 | 0.11 |
| T4 | 1.07 | 0.11 | 0.92 | 0.06 |
| T5 | 1.14 | 0.11 | 0.73 | 0.09 |
| T6 | 1.02 | 0.11 | 0.78 | 0.07 |

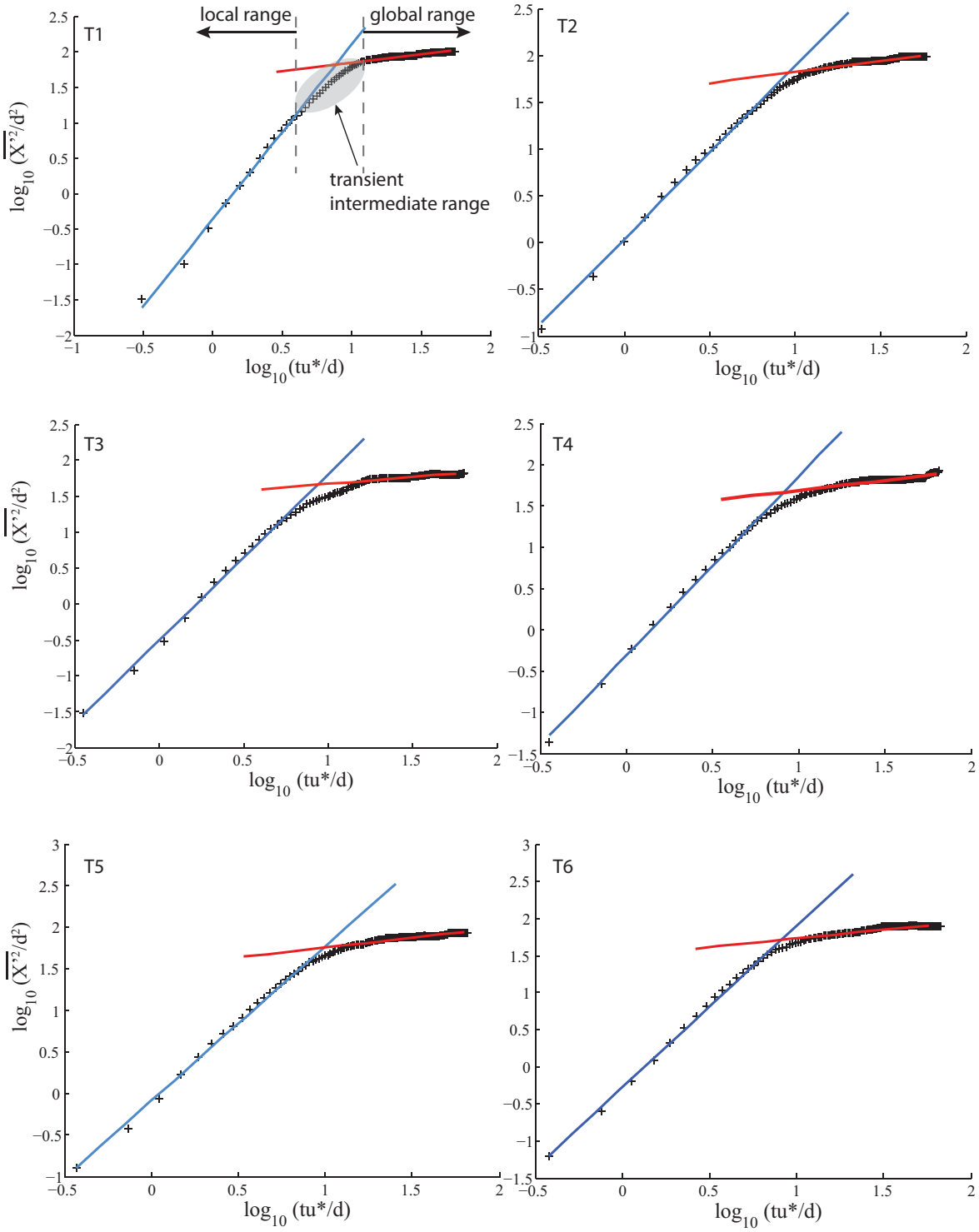


Figure 2.6: Change in time of the longitudinal dimensionless second order moment of particles coordinates. The three motion ranges are represented along with the best linear fit of diffusion rate coefficients $\gamma_x$. Results are reported for all the six tests.

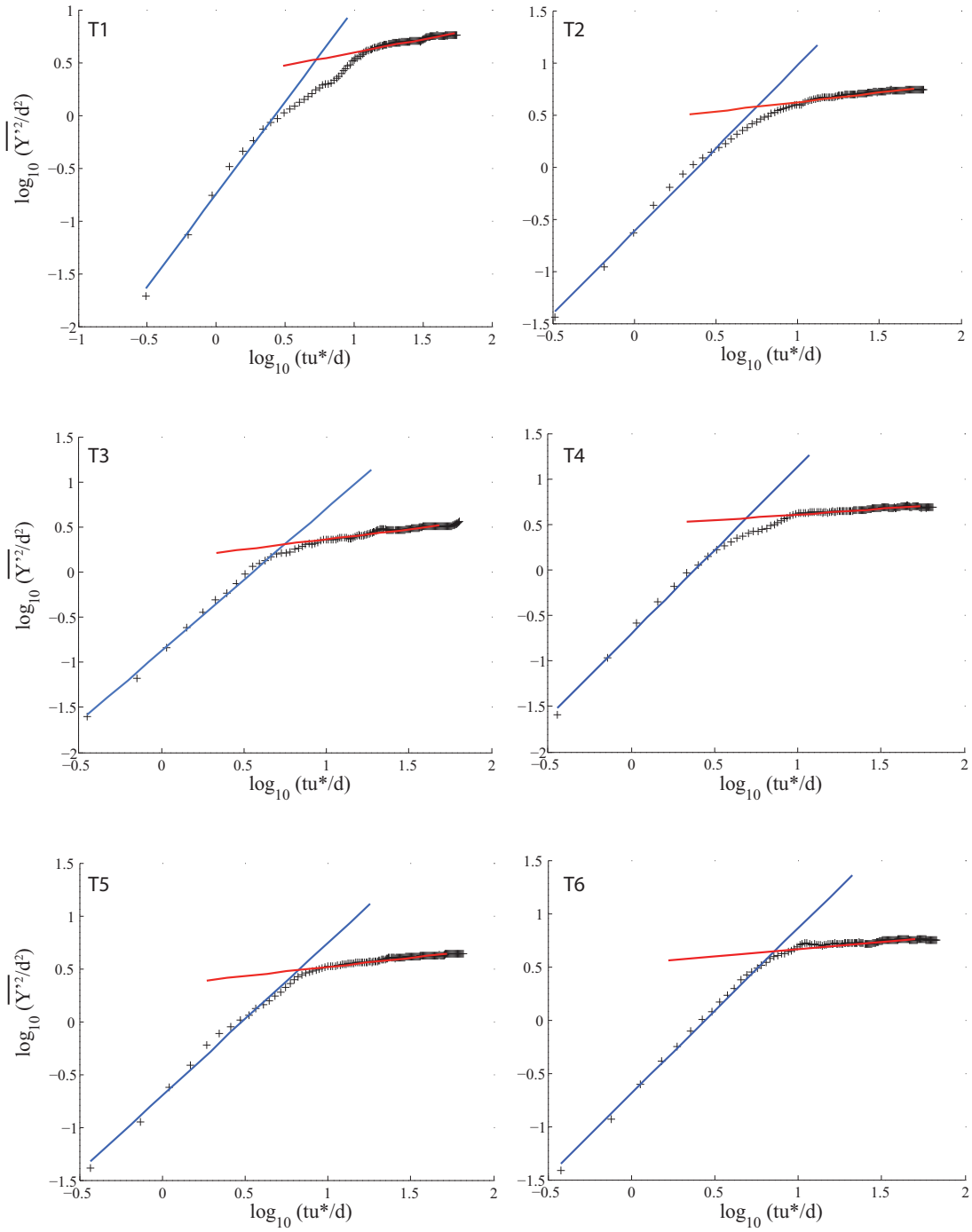


Figure 2.7: Change in time of the lateral dimensionless second order moment of particles coordinates. The best linear fit of the diffusion scaling coefficients $\gamma_y$ are presented. Results are reported for all the six tests.

The normalized third and fourth order moments of particles' location shows the great variability that influences particles' movement especially at the first stage of motion (Figure 2.8). A more stable behaviour of the streamwise Skewness and Kurtosis is observed after roughly $T_s = (tu^*/d) = 8 - 9$. Beyond this threshold the distribution of particles' position is no longer outlier-prone ($Ku = 0$, similar to Gaussian processes) but it keeps a limited asymmetry towards values greater than the mean ($Sk = 0.7 - 1.4$). The higher positive Skewness is also confirmed in the work of Campagnol et al. (2015), who obtained similar values of the third order mo-

ment. The stabilization of the third and fourth order moments, which takes place at $T_s$, finds correspondence with the beginning of the subdiffusive regime, suggesting the random nature of the entrainment process and of the early stage of particle's motion. The Skewness and Kurtosis for the lateral particles' location resulted more intermittent and scattered than the streamwise moments. The trends seem to approach stability for greater times, surely larger than 4 s, which is the upper limit of this analysis.

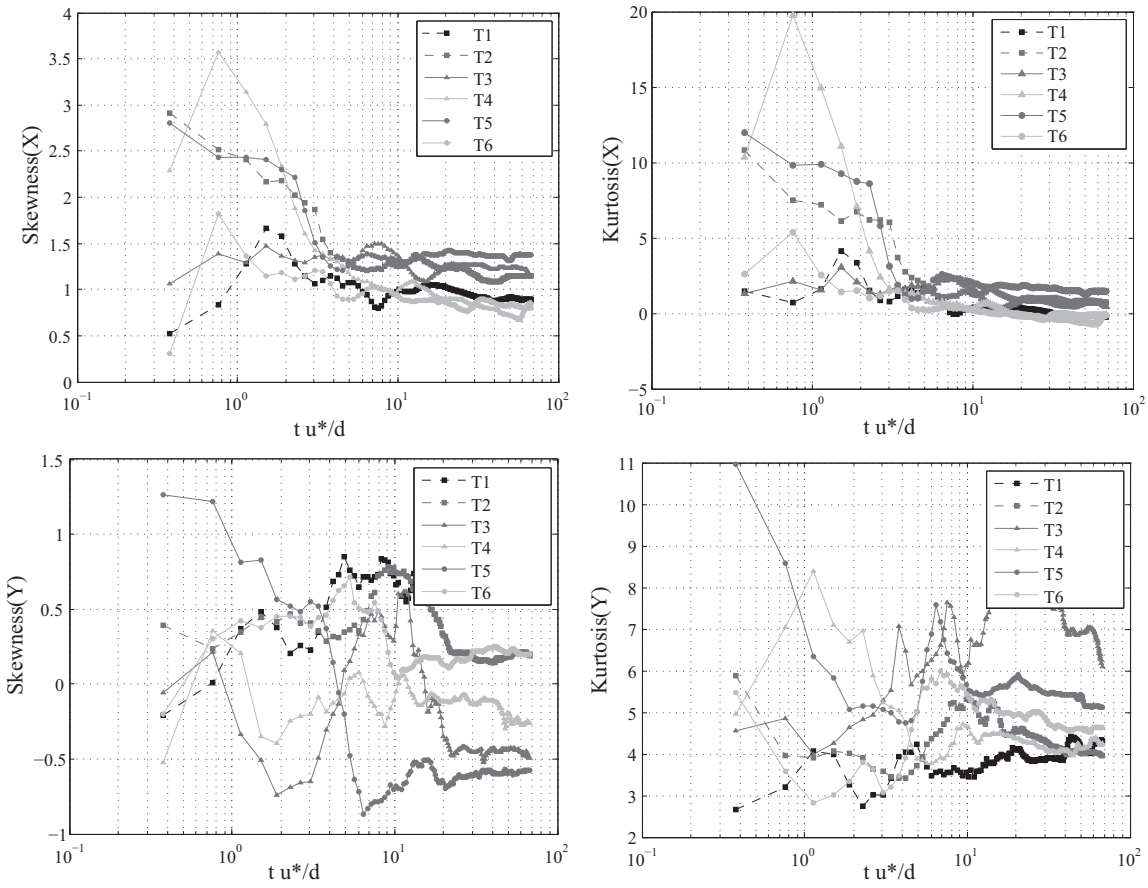


Figure 2.8: Normalized Skewness and Kurtosis for the longitudinal and transversal particles' position for all the tests.

### 2.3.2 Discussion

The frequency of image acquisition that characterized this series of tests was suitable to successfully confirm the ballistic regime of the conceptual model, which is denoted by diffusive longitudinal scaling component $\gamma_x = 1.0$. The end of the ballistic regime happens at approximately 0.30 s without observable trend with the increase of bed shear stress (Figure 2.6). In this stage particles are entrained and accelerated by the fluid to be fully brought into motion. Discussion has recently developed among researchers on the nature of the diffusion in the very early stage of bed-load particles' motion. Bialik et al. (2012), who performed numerical simulations, and Campagnol et al. (2015), with experimental data, reported a region of superballistic diffusion in correspondence of the first instants of movement. In this early stage of motion, the scaling coefficient of diffusion is greater than 1.0, approaching values of 2.0 in same cases. This behaviour would find justification in the acceleration experienced by the grains once entrained,

and the ballistic regime reported in Nikora et al.'s conceptual model ($\gamma_x, \gamma_y = 1.0$) would then take place afterwards. The transition dimensionless time between this superballistic and the subsequent ballistic diffusion is reported to be $tu^*/d = 3$ in Bialik et al. (2012) and $tu^*/d =$ 1.5-2.5 in Campagnol et al. (2015).

In this study, the scaling coefficient $\gamma_x$ has been derived by progressively adding successive points of the variance of the particles' position and fitting the group of realizations with a linear function, as long as the computed error stays lower than a threshold (Figure 2.6). To compare this work with other researchers' findings, the $\gamma_x$ is now calculated between consecutive points and plotted as a function of the dimensional time group as showed in Figure 2.9. It was found that $\gamma_x$ ranges between 1.0-1.4 in the first fractions of a second $t < 0.20$ s (exception made for T2 and T5, in which $\gamma_x$ is always 1.0), for then becoming equal to 1.0 at about $tu^*/d \approx 3.2$, very close to the threshold found by Bialik et al. (2012). Beyond this point the scaling behaviour is ballistic as suggested by Nikora et al. (2002). Large values of $\gamma_x$, similar to the ones of superballistic diffusion obtained by the other researchers, could not be found in this experiment. Surely the ballistic regime includes the initial acceleration particles are subject to and as a consequence $\gamma_x$ can be greater than 1.0 (Campagnol et al. 2015), but the diffusive scaling coefficients are also strongly dependent on the characteristics of the entrainment process (Bialik et al., 2012).

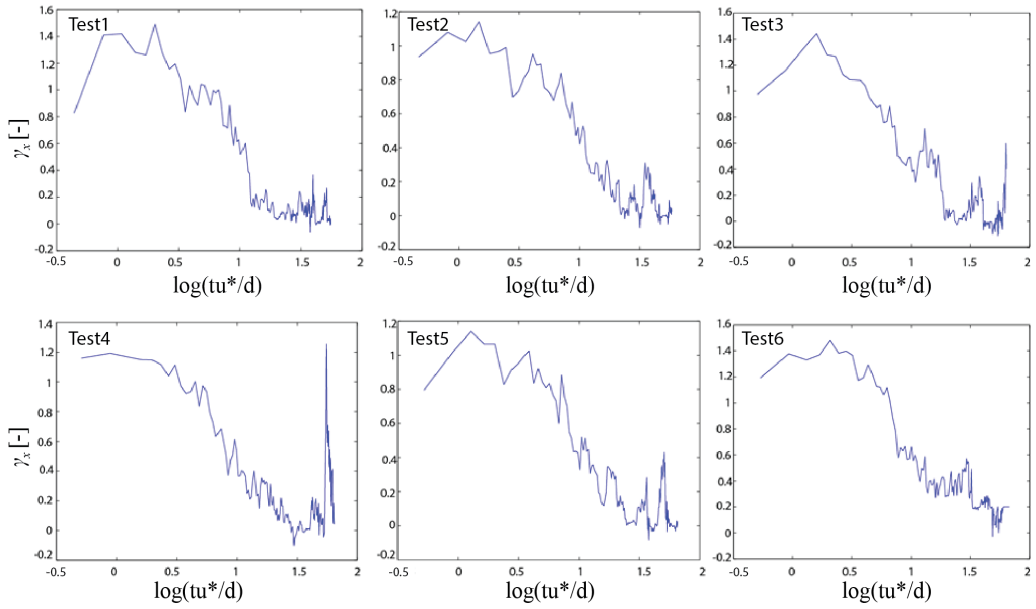


Figure 2.9: Semi-log plot of the variation of the longitudinal diffusive coefficient scaled to the dimensionless time, $tu^*/d$ for all tests.

Addressing the entrainment stage properly is then essential in the assessment of the correct diffusive regimes. Bialik et al. (2012) simulated the motion of spherical particles over a rough bed by numerically solving the trajectory for particles saltating in a fluid over an evenly-packed bed of spheres equal in size. Campagnol et al. (2015) studied the Lagrangian motion of light plastic grains in a high pressurized duct at frequency of 32 Hz. The results presented here have been obtained for bed-load gravel grains moving over a natural bed. Particles might not experience a great acceleration, because of their submerged weight (larger than plastic grains used in Campagnol et al.'s (2015) experiments) and because of the interaction with the roughness

created by the surrounding natural gravel material during the initial collisions with the bed. The frequency of image acquisition, 45 Hz, is also supporting this finding as it was good enough to reasonably identify the instant of particle's entrainment and to thus include the acceleration phase.

From the entrainment of grains the acceleration stage lasts up to $tu^*/d = 3.2$ presenting $\gamma_x$ = 1.0-1.4, and it is followed by the ballistic diffusive regime $\gamma_x = 1.0$, which stretches to values of $tu^*/d = 6.0 - 8.0$, depending on the test. The initial stage of particle's motion is characterized by a more erratic and intermittent behaviour when natural gravel material is considered, as one can also infer by the much scattered plots of the Skewness and Kurtosis (Figure 2.8). The bed arrangement and the type of bed material seems then to be a driving factor in the diffusion of bed-load grains, playing a fundamental role also at the very beginning of particles' motion.

Uncertainty is likely to occur in the interpretation of the global trajectories. Because of the limited dimension of the investigated area, that does not allow the data to account for longer displacements, after only 4 s all the moving particles are at rest and the variance of particles' coordinates is almost stable or slowly growing with time. The sub-diffusive regime is surely expected at this stage as $t$, i.e. particle's travelling time, accounts also for the resting times, but its value is probably underestimated in this work because of the impossibility to include long trajectories (due to limitation in the areal dimensions of the measurement area) and to observe the remobilization of particles (due to limitation in the duration of the analysis). The total number of global trajectories accounts for a minimum of 22 (test T5) and a maximum of 76 (test T2) trajectories, with the majority of them, i.e. about 80%, composed by only 2 intermediate trajectories. This would explain the greater values of diffusive scaling exponent ($\gamma_x = 0.33$) derived by Nikora et al. (2002) for the global regime when processing field data of Drake et al. (1987).

In the experiments carried out by Drake et al. (1987) images were taken with greater time interval (15 s) and over a larger area (approximately 800 cm$^2$). They could not identify the ballistic regime due to the coarser sampling time, but the larger investigated area and longer times enabled them to certainly include grains that computed more than 2 intermediate trajectories and so to cover the global range. It is interesting to note the correspondence of the boundary between global and intermediate range derived by Nikora et al. (2002) with the start of the global range in the present tests. In their work the transition between the two ranges was found for $tu^*/d = 15$, which happened to be the beginning of the subdiffusive regime here, as a reference $log_{10}(15) = 1.18$ in Figure 2.6. So according to their analysis where the global regime is derived from $tu^*/d = 15$ to $tu^*/d = 100$, the present experiment could only cover the first part of the subdiffusive regime.

From the analysis presented in Figure 2.6 the identification of the intermediate range is seemingly difficult. The variation of the second-order moment of particles' location between the local and the global ranges cannot be linearly fitted. As a consequence the diffusive scaling coefficient in this range of motion is not uniquely identified by a single value, but it rather decreases smoothly from the ballistic value to the subdiffusive one. For this reason it appeared more appropriate to indicate this range as a transitional one denoted by a non-constant diffusive scaling coefficient. The superdiffusive regime with constant $\gamma$ as described in the diffusive conceptual model by Nikora et al. (2002) could not be observed here. In their analysis the intermediate range took place from $tu^*/d = 0.2$ to $tu^*/d = 7 - 8$ (as a reference in Fig. 2.6 from $log_{10}(tu^*/d) = -0.7$ to $log_{10}(tu^*/d) = 0.84 - 0.90$). This temporal window might have incorporated also the local range. The ballistic regime did not appear as they identified the starting point of the trajectories with the point of grains' collision with the bed, instead of

the instant of entrainment (Bialik et al. 2012). The ballistic behaviour might have then been included into the intermediate one, originating a superdiffusive regime with constant scaling coefficient $\gamma$ lower than 1.0.

From comparison with experimental data of other researchers, in particular data from Drake et al. (1987) over a larger investigated area, one can perceive that the spatial scale of the analysis plays a role in the correct assessment of the diffusive scaling coefficient after the initial ballistic regime. Confirmation is found with the datasets here presented. The trajectories used in the derivation of the diffusive regimes are the ones entirely described within the investigated area, with initial state *Start* and with final state *Stop*, which means that the particles have stopped at least once within the investigated area (Figure 2.10).

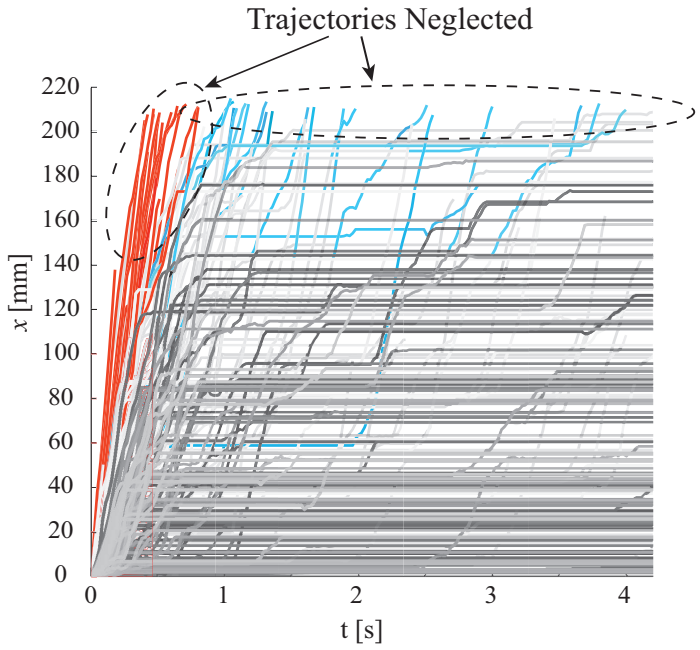


Figure 2.10: Streamwise component of the particles' location in time with the neglected trajectories highlighted (case *Move-Move* and *Start-Move* in red and light blue respectively).

In doing so, all the particles entering the investigated area in motion (*Move-Move*) are discarded as the starting point is missed and they cannot be scaled to the same origin point of the other starting grains. If included, this group of particles would probably increase the first order moment of grains' location as shown in Figure 2.11. Similar consideration can be applied to a grain that was entrained within the area but travelled out of the spatial boundaries (*Start-Move*). After having left, the grain is no longer considered as its positions are unknown as well as its contribution to the diffusive cloud. When a grain's trajectory stops contributing, the second order moment of particles' locations drops to a lower value thus creating fluctuations in its evolution with time. Figure 2.11 shows the importance of neglecting partially described trajectories in the assessment of the diffusive regime for test T1. Similar results were obtained for all the other tests.

To understand the extent of the second limitation (neglecting particles that leave the area still in motion), the first and second-order moments of particles' location have been derived for an area with shorter longitudinal dimension, $L_x = 100$ mm, and compared to the results reported in the previous section. When the investigated area is reduced, particles previously included in the analysis can no longer contribute to the moving cloud thus decreasing the mean and the variance of particles' location. The influence of the areal amplitude is more significant for the

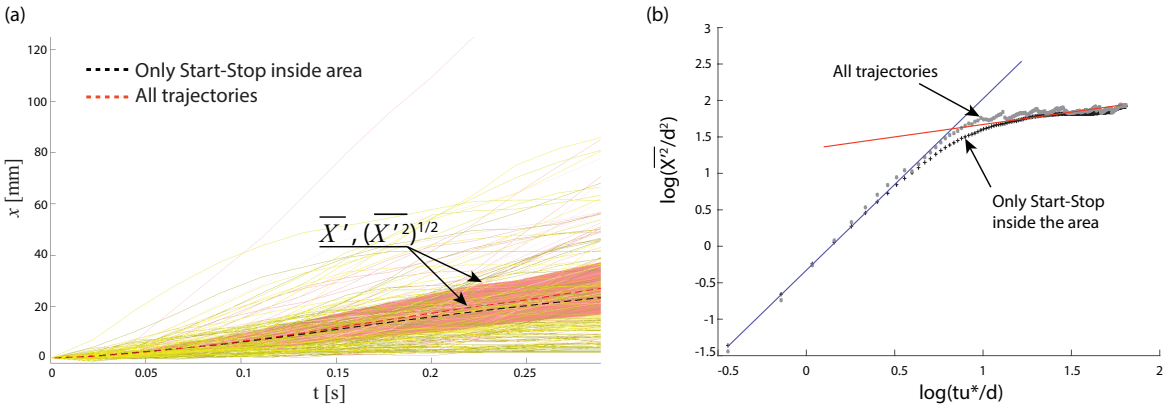


Figure 2.11: (a) Variation of the first and second order moment of longitudinal particles' location when all the trajectories are considered instead of only the *Start-Stop* inside the investigated area. (b) The temporal evolution of the second order moment for the two cases. Results are reported for test T1.

transitional-intermediate and global range since they are characterized by larger displacements (Figure 2.12a,b). The new streamwise component of the diffusive coefficient associated to the global regime, $\gamma_x = 0.03$ in Figure 2.12b, confirmed the initial concern. Limiting the length of the investigated area can lead to underestimating the actual scaling of the diffusion in the intermediate and global range (Nikora et al., 2002; Drake et al., 1987). The transitional-intermediate range almost disappears when the area is limited to $L_x = 100$ mm, whilst the scaling diffusive coefficient for the global one now tends to zero. The local trajectories however remain invariant, by presenting again the ballistic diffusive regime, $\gamma_x = 1.0$.

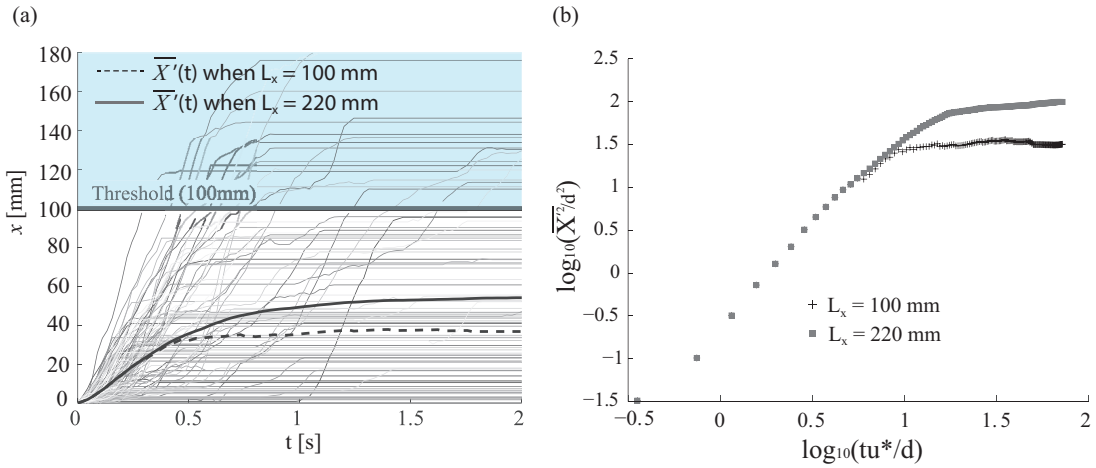


Figure 2.12: Influence of a limited observation area ($L_x = 100$ mm) on (a) the first and (b) second order moment of particles' location. Results are reported for test T1.

To summarize, while the transitional intermediate and global ranges seem to be affected by the size of the experimental area of investigation, the local range tends to be more sensitive to the definition of entrainment in natural beds and to the frequency of data acquisition in capturing the first stage of motion. Notwithstanding this limitation, the analysis has showed clear evidence of bed-load particles diffusion and in particular its growth with time, which apparently is independent on the hydraulic conditions. Experiments, characterized by longer spatial and time scales should provide a comprehensive dataset which will enable to comprehensively

describe the diffusive regimes and to link them to the correct particles' displacement.

## 2.4 The intermediate scale: the step length concept

Step length, hereafter denoted as $r$, has been defined as the streamwise distance travelled by a particle from the instant it is entrained to the moment it stops on the bed and rests, thus corresponding to the intermediate range. The concept of step length has widely been used in studies of sediment transport. It is included in the definition of the flux of sediment transport proposed by Einstein (1950), i.e. $q_x = E_b \cdot \overline{r}$, with $E_b$ indicating the average volumetric rate of particles entrainment per unit stream-bed area, and $\overline{r}$ the particles' average step length (Furbish et al., 2012a). Step length, described as a stochastic variable, is the source of different diffusive processes (Ganti et al., 2010). According to the conceptual model proposed by Nikora et al. (2002), the step length (= intermediate range) constitutes a type of displacement denoted by a particular diffusive regime.

As showed above, addressing properly the step length is critical mainly because of experimental limitations which result in the exclusion of steps with unknown localization of entrainment or disentrainment events. A slow temporal acquisition rate, especially in field experiments, will limit the analysis too, by grouping together several steps and by missing the instant of the initiation of motion. This will result in an incorrect or partial description of the whole population of possible steps. To tackle this issue, the six databases from the experiment of Tregnaghi et al. (2012b) have been considered as they provided high quality information to compute the steps for all the moving particles within the investigated area, i.e. *Start-Stop* displacement type. It is reckoned, and confirmed by the above analysis of ballistic regime, that the sampling frequency is appropriate to capture the first instant of particles' motion. Regardless to the steps longer than the longitudinal extent of the area (220 mm), the number of fully-known *Start-Stop* (more than 100 for each test) was enough to obtain converged statistics as showed in Figure 2.13.

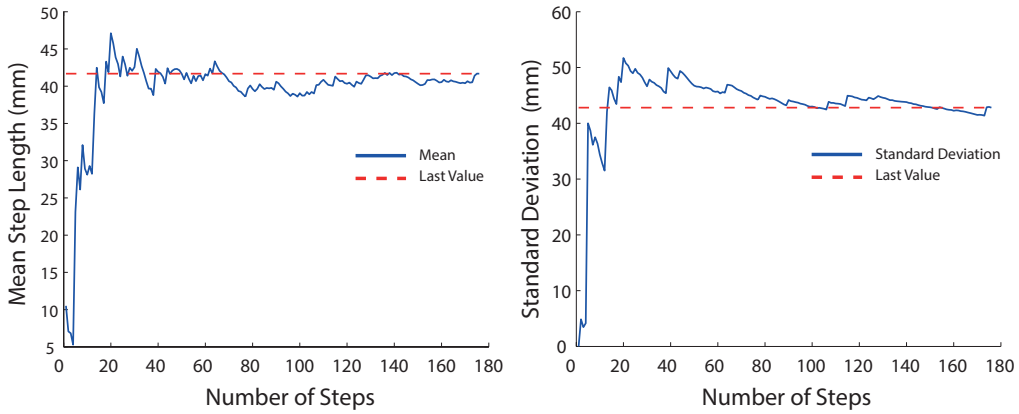


Figure 2.13: Convergence of mean and standard deviation of the step length by the number of observations. Results are presented for test T2.

Even if the number of sampled trajectories were sufficient to obtain converged statistics, the mean and standard deviation values are still underestimated as they do not include the longest steps, such as *Move-Move*, or the partially described paths *Start-Move* and *Move-Stop*. The

limitations in the dimension of the investigated area thus generate truncated distributions as qualitatively showed in Figure 2.14. The following sections present two methods to overcome the truncation of the step length data by considering (a) the fraction of missing steps, and (b) the joint probability of particles' velocity and step length.

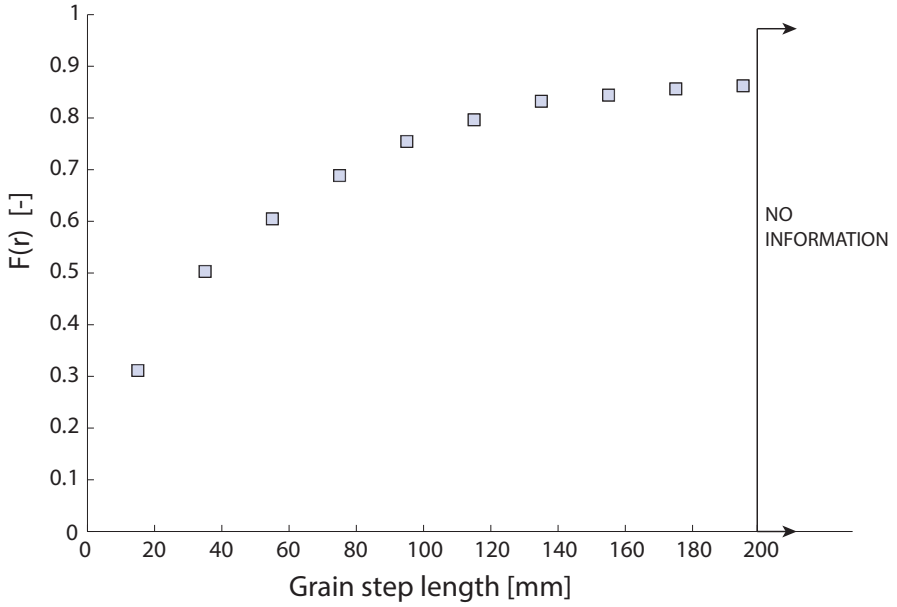


Figure 2.14: Truncated cumulative distribution of step lengths, test T1.

### 2.4.1 Method 1: Statistical models for truncated data

Recalling Table 2.2 that differentiated every sampled trajectory according to the location of the initial and final recorded state of the particles, the distribution of step length is derived for the category *Start-Stop* with exclusion made for the steps shorter than the mean bed diameter $d_{50} = 5$ mm. If $f(r)$ were calculated simply by considering the *Start-Stop* grains it would underestimate the actual population of the step lengths, because it would not consider step lengths longer than the investigated area. In order to include the effect of the *Move-Move* displacements in the PDF, $f(r)$ obtained for the observed *Start-Stop* step lengths is scaled by a multiplicative factor $R$. The value of $R$ represents the ratio between the area of the PDF which is known to the area which is unknown due to the limited extent of the measurement area under examination and it can be calculated as follow:

$$R = \frac{N(Start - Stop > r_{min})}{N(Start - Stop > r_{min}) + N(Move - Move > L_x)}; \tag{2.8}$$

where the numerator of this fraction indicates the number of steps that are completed inside the window and are longer than a particle's diameter $r_{min}$ but shorter than the area extent $L_x$, and $N(Move - Move > L_x)$ is the number of observed displacements that are greater than the investigated window. On average, the scaling factor is about 0.80, with a minimum of 0.77 for test T6 and a maximum 0.88 for test T2, as it can be seen in Figure 2.14 reporting the cumulative plots of $f(r)$. The number of *Start-Move*, *Move-Stop* and *Move-Move*($\leq L_x$) observations is assumed to be distributed evenly according to the ratio $R$.

Based on previous research (Einstein 1950; Ganti et al., 2010; Bradley and Tucker, 2012) four different statistical models have been applied to the original step length data, namely

Table 2.4: Probabilistic distribution models along with their cumulative function and statistics, i.e. mean $E(x)$ and variance $Var(x)$.

| Model | Cumulative function | Statistics |
|---|---|---|
| *Exponential* | $F(x) = 1 - e^{-\lambda x}$ | $E(x) = \lambda^{-1}$ |
| | | $Var(x) = \lambda^{-2}$ |
| *Gamma* | $F(x) = \frac{1}{\Gamma(\alpha)}\gamma(\alpha, \beta x)$ | $E(x) = \frac{\alpha}{\beta}$ |
| | | $Var(x) = \frac{\alpha}{\beta^2}$ |
| *Weibull* | $F(x) = 1 - e^{\left(-\frac{x}{\lambda}\right)^k}$ | $E(x) = \lambda\Gamma(1 + \frac{1}{k})$ |
| | | $Var(x) = \lambda^2\left[\Gamma\left(1 + \frac{2}{k}\right) - \left(\Gamma\left(1 + \frac{1}{k}\right)\right)^2\right]$ |
| *Lognormal* | $F(x) = \frac{1}{2} + \frac{1}{2}\text{erf}\left(\frac{ln(x)-\mu}{\sqrt{2}\sigma}\right)$ | $E(x) = e^{\mu + \frac{\sigma^2}{2}}$ |
| | | $Var(x) = \left(e^{\sigma^2} - 1\right)e^{2\mu+\sigma^2}$ |

Exponential, Gamma, Weibull and Lognormal. A mathematical description of the models and their statistics is reported in Table 2.4.

Each statistical distribution was applied to the scaled truncated cumulative distribution function (CDF) so that also the influence of the longest, and least frequent, steps could be accounted for. The numerical fitting procedure is performed by computing the mean squared error (MSE), denoted hereafter as $S$, of the measured, $F(r)$, and the modelled values, $F^*(r)$, of the cumulative density functions:

$$S = \frac{1}{n}\sum_{i=1}(F^*(r_i) - F(r_i))^2. \tag{2.9}$$

Each parameter of the proposed distribution functions has been varied within an interval of values $a_{min} - a_{max}$ upon which the modelled CDF was calculated. The parameter (in case of exponential distribution) or the combination of two parameters (for all the other distributions) providing the lowest error $S$ identifies the CDF statistics that better fit to the experimental curve. For every best fitting model it is then possible to derive the un-truncated distribution denoted by mean value $\mu_r$ and standard deviation $\sigma_r$, as reported in Table 2.5. Figure 2.15 summarizes the results for all the tests by plotting the best fit of each model to the original truncated CDF. The probability density functions, $f(r)$, are included in the Appendix (Figure A.1).

Table 2.5: Mean and standard deviation of the observed and modelled step length resulting from the minimization of the error $S$ in every test.

| | Observed [mm] | | Expon. [mm] | | Gamma [mm] | | Weibull [mm] | | Lognormal [mm] | |
|---|---|---|---|---|---|---|---|---|---|---|
| TEST | $\mu_r$ | $\sigma_r$ | $\mu_r^*$ | $\sigma_r^*$ | $\mu_r^*$ | $\sigma_r^*$ | $\mu_r^*$ | $\sigma_r^*$ | $\mu_r^*$ | $\sigma_r^*$ |
| T1 | 50 | 43 | 76 | 76 | 82 | 102 | 85 | 112 | 104 | 218 |
| T2 | 44 | 42 | 63 | 63 | 70 | 96 | 74 | 110 | 91 | 218 |
| T3 | 42 | 38 | 70 | 70 | 84 | 124 | 92 | 155 | 128 | 436 |
| T4 | 43 | 36 | 78 | 78 | 88 | 120 | 98 | 155 | 131 | 380 |
| T5 | 44 | 41 | 89 | 86 | 113 | 169 | 127 | 225 | 194 | 801 |
| T6 | 50 | 40 | 96 | 96 | 109 | 139 | 116 | 160 | 166 | 458 |

A two parameters statistical model is more appropriate than a single-parameter model to

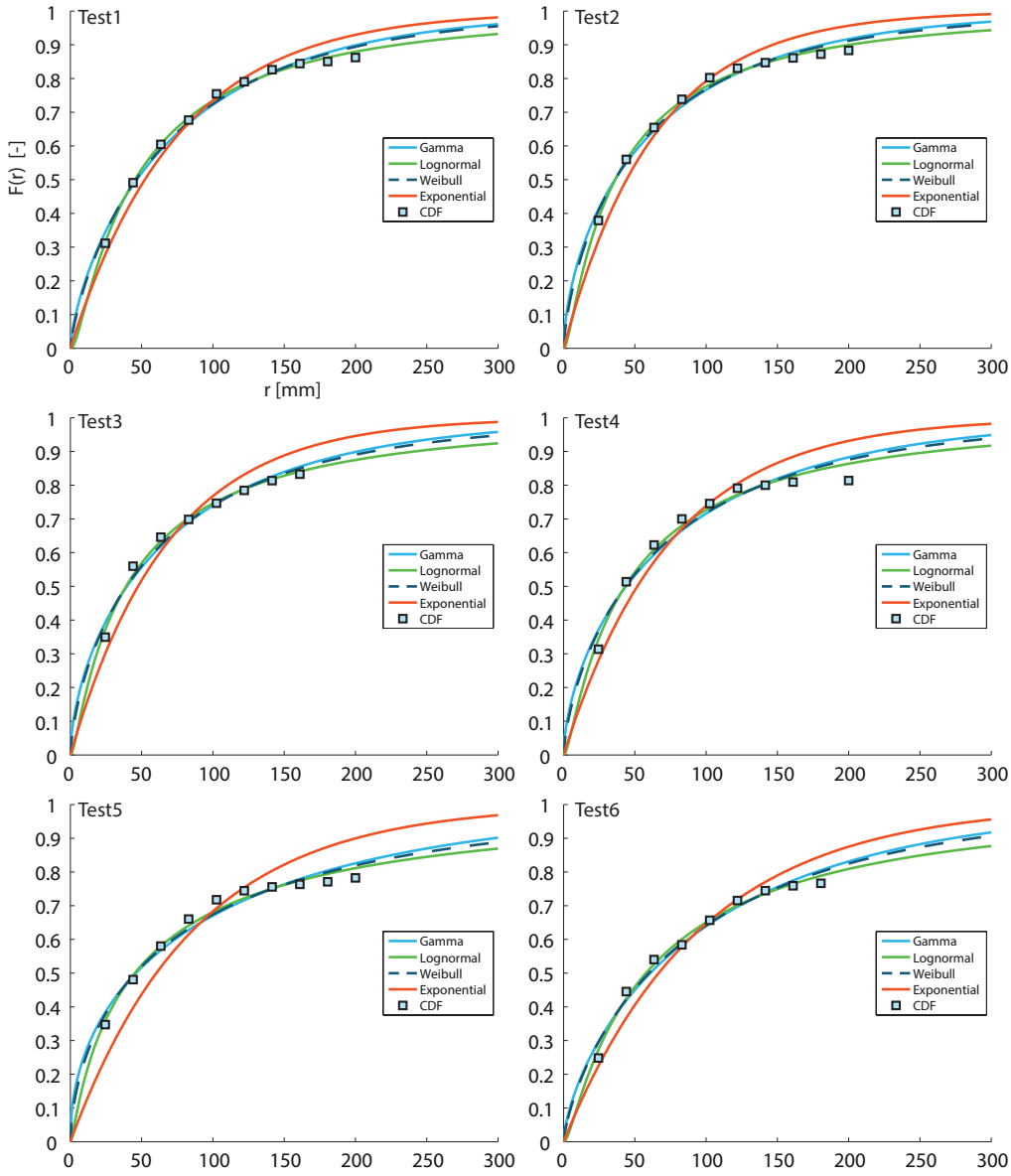


Figure 2.15: Cumulative distributive models fit to the experimental data (in squared markers) for all the six tests. The axis' labels reported only in the top-left plot apply to all the other plots.

handle the truncation of data (Figure 2.15). This is confirmed from the analysis of the error. In Figure 2.16 the MSE value, $S$, is reported as a function of the Shields parameter characterizing each test. The Lognormal presents the lowest error, followed by the Weibull and the Gamma whilst the results for the Exponential distribution are not plotted since the error is an order of magnitude bigger.

From the derivation of the error $S$ (Fig. 2.16) and the qualitative analysis of plots in Figure 2.15, the Lognormal function seems to be the most appropriate model to describe the truncated step length distribution although it produces the largest values of $\mu_r^*$ and $\sigma_r^*$ (Figure 2.17). This stems from the characteristics of the Lognormal function that tends to give greater importance to the extreme and least probable values of step lengths. The results of the Gamma and Weibull distributions are not far from the Lognormal ones; they are characterized by smaller statistical values but their fitting for longer steps is less accurate.

It is worthy to note that all the statistical models provided greater mean and standard deviation than the ones computed by simply considering the observed step lengths $r < L_x$.

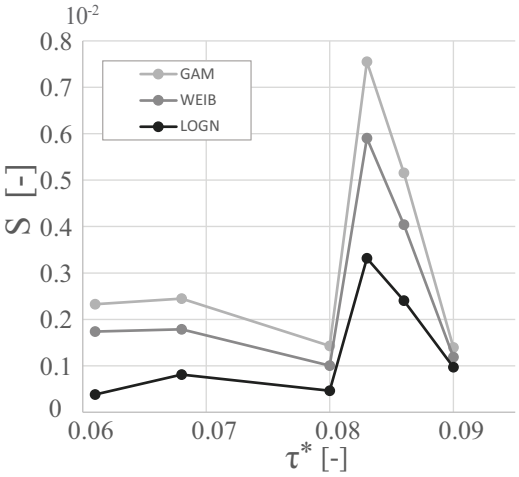


Figure 2.16: MSE values, $S$, as a function of the Shields' parameter for the Gamma, Weibull and Lognormal distributions.

As roughly 20% of the step length population is not considered due to areal limitation, the calculated statistics from a truncated distribution can result in underestimating the extent of bedload grains' displacement. The underestimation of the mean step length ranges between 50%, in case of exponential fitting, up to more than 100% for a Lognormal distribution.

Figure 2.17 reports the modelled $\mu_r^*$ and $\sigma_r^*$ as a function of the Shields' stress parameter associated to each test and compares these values with the observed ones. The mean step length seems to generally increase with $\tau^*$. A trend emerges for the standard deviation, even if its visualization can be difficult to appreciate in Figure 2.17 due the scale of the vertical axis. The high mean step length for the test with the lowest shear stress (T1) could find explanation in the different type of motion observed for the bed grains. In this test grains were sliding over the bed material rather than saltating or rolling as it was found in all the other tests. Over the uniform bed material, sliding grains were observed to travel undisturbed for long distances, in continuous contact with the bed, before achieving a stable repose condition. On the other hand, rolling and saltating particles often moved a few particle diameters between consecutive contacts with the bed and tended to abruptly stop in respond to a collision with the bed. Such collisions are responsible for a transfer of momentum from the moving phase to the reposing bed with, on some occasions, the generation of a new entrainment event, as reported in Cecchetto et al. (2016). As strong impacts with the bed are more likely to occur for rolling and jumping grains, these moving grains are more likely to experience a loss of momentum and, as a consequence, a higher likelihood of distrainment. Such trajectories can then be characterized by short longitudinal travel distances. The peak in correspondence of the second last test (T5) might derive from the nature of the observed PDF, which presented a higher frequency of long steps (close to 220 mm) thus moving the mean and standard deviation towards higher values.

### 2.4.2 Method 2: Joint probability of motion variables

The second method proposed here to tackle the truncation of the step length distribution is statistically based on the concept of joint probability. Let us assume that two variables are statistically dependent, in this case the particles' velocity, $v$, and the step length, $r$. Their joint probability $f_{v,r}(v,r)$ can then be expressed as the product of the conditional probability $f_v(v|r)$

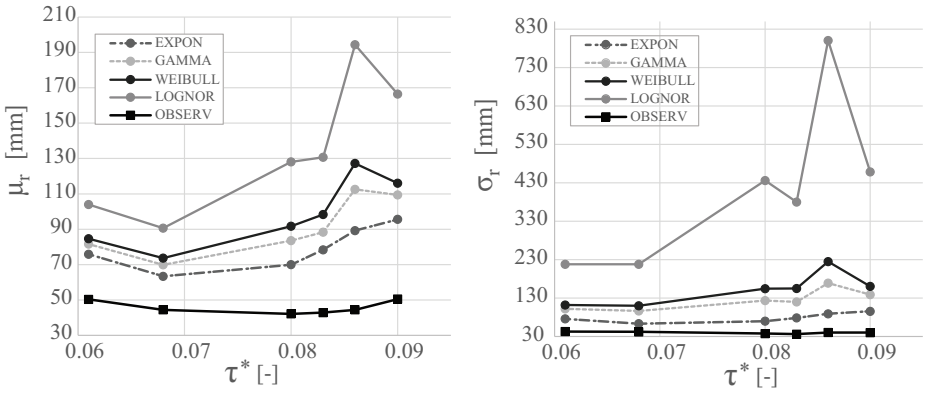


Figure 2.17: Mean and standard deviation values for the four statistical models and the observed data as a function of the Shields' parameter.

and the marginal probability of $r$, $f(r)$:

$$\underbrace{f_{v,r}(v,r)}_{\text{joint}} = \underbrace{f_v(v|r)}_{\text{conditional}} \cdot \underbrace{f(r)}_{\text{marginal}} . \tag{2.10}$$

The conditional probability $f_v(v|r)$ can be experimentally determined by assuming a distribution model whose statistics are formulated as a function of the variable $r$, i.e $\mu_v = g(r)$ and $\sigma_v = w(r)$. For every value of $r$ the possible realizations of $v$ are then distributed according to the $r$-dependent mean and standard deviation.

The determined joint probability $f_{v,r}(v,r) = f_v(v|r)f(r)$ if integrated over $r$ should provide the marginal probability density function (hereafter PDF) of the variable $v$, i.e. $f_v(v)$:

$$f_v(v) = \int_r (f_v(v|r) \cdot f(r))dr = \int_r f_{v,r}(v,r)dr. \tag{2.11}$$

The marginal PDF of $v$ calculated via Eq. 2.11 should be equivalent to the marginal PDF of $v$ obtained from the experimental observations, $f(v)$. The same analysis can be applied to the variables step length $r$ and travelling time $\tau_p$, but, since the investigated area is limited, also the travelling time distribution would be affected by truncation in the same extent of $r$. The sampling of particles' velocity instead should not be distorted by the areal limitation as its distribution can include velocities associated to partially recorded trajectories, such as *Start-Move*, *Move-Stop* and *Move-Move*. In the paragraphs below research of the equivalence between the calculated and the experimental marginal PDF of $v$ will help the derivation of the un-truncated step length distribution by determination of its statistics.

The first step of the analysis consists of the calculation of the experimental marginal PDF of particles' velocity, $f(v)$, by considering all the available trajectories. The frequency plot resulted well approximated by a gamma-like distribution as showed in Figure 2.18. Results for all the tests are presented in Figure A.2 in the Appendix.

The analysis of the particles' velocity enabled also the derivation of the conditional probability of $v$ as a function of $r$, $f_v(v|r)$. In this case only the complete steps within the investigated area (*Start-Stop*$> d_{50}$) have been considered in order to create a consistent database of step lengths and related velocities. For every class of step lengths centred in $r$, $r \pm dr/2$ with $dr = 10$ mm, the associated values of particles' velocity were obtained. Their frequency distributions were assumed to be gamma-like according to the marginal PDF of velocities, and their statistics were derived as a function of $r$ (Figure 2.19).

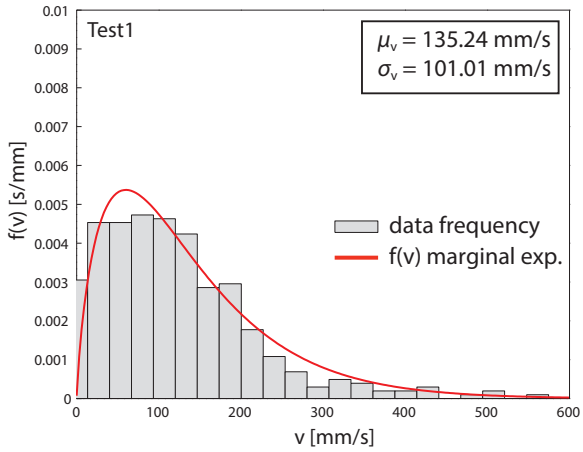


Figure 2.18: Frequency distribution of particles' velocities along with the gamma-like marginal PDF $f(v)$. Results are presented for test T1.

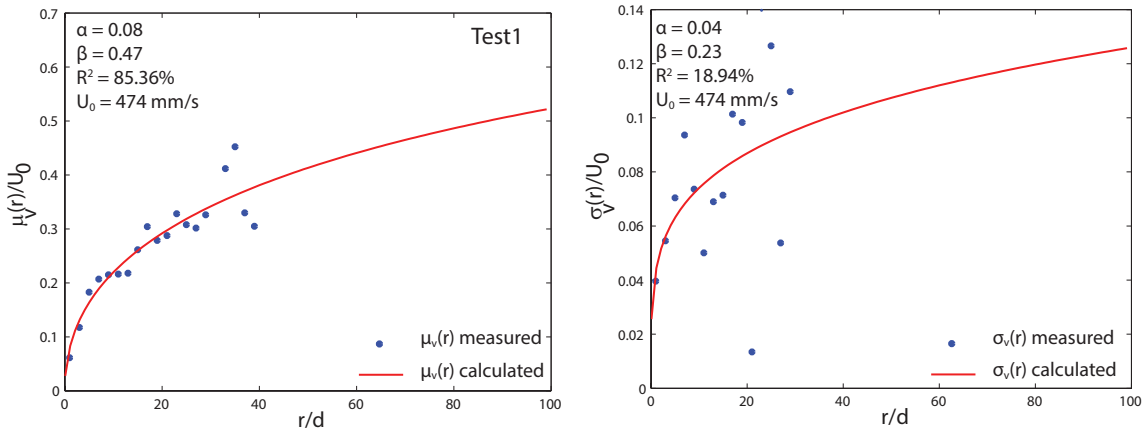


Figure 2.19: Mean and standard deviation of the particles' velocity scaled to the dimensionless step length $r/d$, with $d$ being the moving particles' size, for test T1. The asymptotic value $U_0$ reported in the plots is here calculated with the linear profile at $z_0 \simeq 1.0d_{50}$ as a result of the parameters calibration presented hereafter.

As the population is truncated for $r = 220$ mm, the mean values $\mu_v(r)$ were considered to follow an exponential growth to the asymptotic velocity $U_0$. Particles roll, slide or saltate over the bed exposing themselves to the flow field near the bed crests. For this reason their travelling velocity cannot grow indefinitely, it will reach a maximum asymptotic value, here denoted as $U_0$. $U_0$ is assumed to correspond to the averaged longitudinal flow velocity derived with the vertical velocity profile in correspondence of $z_0$, with $z_0$ being the vertical distance from the bed crest. The multi-layers formulation of double-averaged velocity profile over rough-beds presented by Nikora et al. (2001) can be used:

$$\begin{cases} \dfrac{\left\langle \overline{U}(z) \right\rangle}{u^*} = \dfrac{1}{\kappa} ln\left(\dfrac{z}{e}\right) + C, & \text{for } z > e \\ \dfrac{\left\langle \overline{U}(z) \right\rangle}{u^*} = C\left(\dfrac{z}{e}\right), & \text{for } z \leq e \end{cases} \tag{2.12}$$

where $\kappa$ indicates the von Kármán constant, $e$ the depth of the flow roughness layer and $C$ a constant coefficient determined by the type of bed material. In this application the roughness layer $e$, shown to vary from $1.0d_{50}$ to $1.5d_{50}$ (Nikora et al., 2001), was set equal to $1.0d_{50}$ whilst the

coefficient $C = 7.1$ is assumed, as reported by Tregnaghi et al. (2012b) for this experiment. The double-averaged velocity can be calculated with Eq. 2.12 and, depending on the bed elevation $z_0$, it will be described by a logarithmic or linear profile. The value of $U_0$ as represented in Figure 2.19 is obtained from the parameters calibration that is presented hereafter.

Similar analysis is performed for the standard deviation of the particles' velocity which is also scaled with the asymptotic velocity $U_0(z_0)$. Differently from the mean values, the standard deviations are more scattered and difficult to interpolate with any mathematical formulation. The erratic nature of the standard deviation values was indeed observed to be independent of the length of the travelled step (Figure 2.19). This is reflected in the best power law fit, which tends to return a constant value of particles' velocity standard deviation, e.g. Test 3, 5 and 6 reported in the Appendix (Figure A.3, A.4).

The analysis of the six databases proved the goodness of the two formulations of the mean and the standard deviation of particle's velocity, which can be expressed in function of $r$ as follow:

$$\frac{\mu_v(r)}{U_0} = 1 - \exp\left[ - \alpha_m \left( \frac{r}{d} \right)^{\beta_m} \right] \tag{2.13}$$

$$\frac{\sigma_v(r)}{U_0} = \alpha_s \left( \frac{r}{d} \right)^{\beta_s}. \tag{2.14}$$

The coefficients $\alpha_m$, $\beta_m$ and $\alpha_s$, $\beta_s$ for respectively the mean and the standard deviation in Eqs. 2.13 and 2.14 can be experimentally derived but they depend on the asymptotic velocity value $U_0$ that is chosen.

The integration of the conditional probability with the marginal PDF of the step length, $f(r)$, in $r$ would then result in the marginal PDF of the particles' velocity. Imposing the equivalence between the calculated and the experimental $f(v)$ should then provide the step length statistics, $\mu_r$ and $\sigma_r$. The probability distribution assigned to the step length is here assumed to be gamma, Weibull or lognormal-like according to the results presented in the Method 1 beforehand.

For each distribution model of $r$, the minimum error computed by solving the equivalence $f_v(v) \equiv f(v)$, is univocally associated to a couple of statistics $\mu_r$ and $\sigma_r$. These statistics would generate the un-truncated distribution of step lengths. The solution though is also depending on (i) the asymptotic value $U_0$ necessary to derive the conditional probability of velocities, and (ii) the error between the calculated and the experimental PDF of particles' velocities. The maximum particles' velocity $U_0$ was considered at a series of distances, i.e. from $z_0/d_{50} = 0.2$ to $z_0/d_{50} = 3.0$. At every distance $z_0/d_{50}$ the value of $U_0$ provided the best parameters $\alpha_m$, $\beta_m$ and $\alpha_s$, $\beta_s$ in Eqs. 2.13, 2.14 and related conditional probability $f_v(v|r)$.

With regards to the error computation, two methods have been applied to the data, namely relative RMSE and logarithmic RMSE. The relative RMSE calculates the linear error (Equation 2.15) for all the frequency values $f(v) \geq f_{MIN}$, with $f_{MIN}$ being a fraction of the maximum frequency $f_{MAX}$, i.e. $f_{MIN} = 0.00$, 0.05, 0.075 or $0.10 f_{MAX}$. The logarithmic RMSE instead applies the linear error to the frequency values greater than a threshold $f(v) \geq (f_{THRES} = 0.20 f_{MAX})$, and the logarithmic error to the least probable values where $f_{MIN} \leq f(v) < f_{THRES}$. In doing so, greater importance is attributed to the highest values of $v$, which are the ones influencing the correct assessment of the distribution statistics, by considering all of them when $f_{MIN} = 0.00 f_{MAX}$ or a fraction of values for the remaining $f_{MIN}$. This is schemat-

ically represented in Figure 2.20. The two errors have been calculated as follow:

$$\begin{cases} \text{Error}_{\text{lin}} = \sum_{i=1}^{n} \left( \frac{f_v(v_i) - f(v_i)}{f(v_i)} \right)^2 \\ \text{Error}_{\text{log}} = \sum_{i=1}^{n} \left( \frac{\log\Big(f_v(v_i)\Big) - \log\Big(f(v_i)\Big)}{\log\Big(f(v_i)\Big)} \right)^2 \end{cases} \tag{2.15}$$

where $f_v(v_i)$ indicates the computed marginal PDF and $f(v_i)$ the experimental marginal frequencies of particles' velocity. The two RMSE are then:

$$\begin{cases} \text{RMSE}_{\text{rel}} = \frac{100}{n} \sqrt{\text{Error}_{\text{lin}}} \\ \text{RMSE}_{\text{log}} = \frac{100}{n} \sqrt{\text{Error}_{\text{lin}} + \text{Error}_{\text{log}}}. \end{cases} \tag{2.16}$$

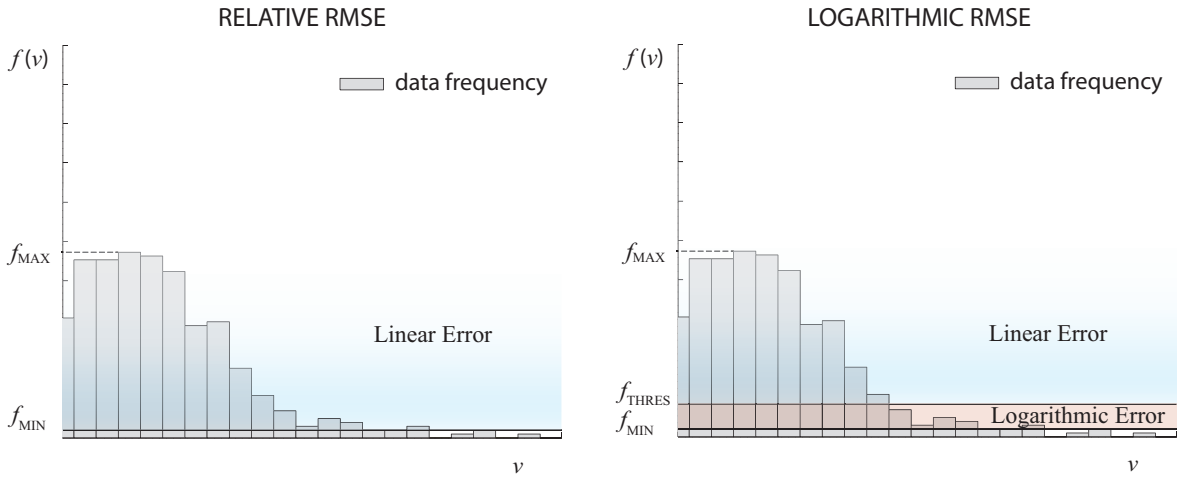


Figure 2.20: Schematic description of the application of the two errors' calculation, namely relative and logarithmic, to the frequency histograms of particles velocity.

Among all the possible combinations of (i) the type of marginal PDF of step lengths, (ii) the asymptotic value $U_0$ referred to different $z_0/d_{50}$, and (iii) the calculation of the RMSE, there will be a couple of parameters ($\mu_r$ and $\sigma_r$) which are denoted by the lowest calculated error between the computed and the experimental marginal PDFs of particles' velocity. Figure 2.21 helps in the visualization of the computational steps to derive the best fit parameters.

Results associated to the logarithmic method in the error calculation are denoted by the lowest values of RMSE, thus showing the importance of considering the logarithmic of the least frequent values of the distributions. Among the solutions with the logarithmic error, the smallest RMSE are derived when $f_{MIN}/f_{MAX} = 0.075$ and 0.100. On average the results are very similar (Table 2.6), so that it was decided to consider a minimum threshold of 0.075 to account for a bigger portion of the frequency data. The output values of mean and standard deviation of the step lengths attain stability for $z_0/d_{50} \approx 1.00$ (exact value $z_0/d_{50} = 0.95$). Beyond this dimensional distance the statistics do not appreciably change. Table 2.6 reports the RMSE, $\mu_r$ and $\sigma_r$, for the case of logarithmic error when $U_0(z_0/d_{50} \approx 1.00)$ for all the six tests. It results that assuming a Weibull PDF for the step length distribution returns a computed marginal $f_v(v)$ that more often fits the experimental one $f(v)$ with higher precision, as also shown in Figure 2.22.

The statistical parameters defining each step length distribution function (Gamma, Weibull

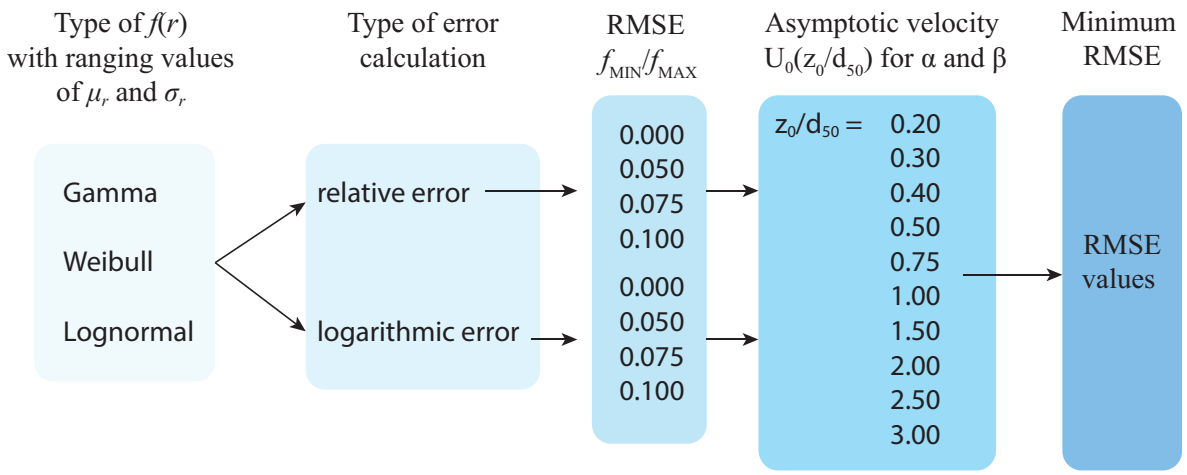


Figure 2.21: Summary of the possible computational combinations.

and Lognormal) that were generated by the minimization of the RMSE are plotted as a function of the Shields' parameter in Figure 2.23. While the Gamma and the Weibull are denoted by very similar and reasonable values of mean and standard deviations, the Lognormal function provides extremely large and unrealistic statistics, with standard deviations rarely lower than 1000 mm. The Lognormal results are also characterized by greater instability. In the following section the results derived with the two methods will be compared.

Table 2.6: RMSE ($RS$), mean and standard deviation step length (reported in mm) for the six tests. Results are presented for the case of logarithmic error considering different minimum threshold, when $U_0(z_0/d_{50} \approx 1.00)$. $G, W, L$ stands respectively for Gamma, Weibull and Lognormal PDF of step lengths. The lowest RMSE are highlighted in red for the $f_{MIN}/f_{MAX} = 0.075$ and 0.10.

| | | $f_{MIN}/f_{MAX} = 0.00$ | | | $f_{MIN}/f_{MAX} = 0.05$ | | | $f_{MIN}/f_{MAX} = 0.075$ | | | $f_{MIN}/f_{MAX} = 0.10$ | | |
|---|---|---|---|---|---|---|---|---|---|---|---|---|---|
| TEST | | G | W | L | G | W | L | G | W | L | G | W | L |
| | RS | 8.18 | 5.34 | 7.07 | 3.48 | 2.86 | 6.63 | 1.73 | 1.84 | 6.28 | 1.39 | 1.72 | 6.30 |
| 1 | $\mu_r$ | 135 | 140 | 240 | 110 | 135 | 240 | 110 | 130 | 240 | 105 | 120 | 240 |
| | $\sigma_r$ | 200 | 225 | 1400 | 160 | 215 | 1400 | 160 | 200 | 1400 | 150 | 185 | 1400 |
| | RS | 2.13 | 1.66 | 2.06 | 1.57 | 1.52 | 2.17 | 1.37 | 1.36 | 1.78 | 1.37 | 1.36 | 1.78 |
| 2 | $\mu_r$ | 105 | 115 | 195 | 95 | 110 | 195 | 95 | 110 | 215 | 95 | 110 | 215 |
| | $\sigma_r$ | 145 | 170 | 700 | 130 | 160 | 700 | 130 | 160 | 840 | 130 | 160 | 840 |
| | RS | 19.04 | 8.63 | 3.88 | 8.66 | 4.93 | 3.69 | 7.81 | 4.75 | 3.69 | 7.66 | 4.72 | 3.74 |
| 3 | $\mu_r$ | 150 | 135 | 275 | 140 | 140 | 275 | 140 | 140 | 275 | 140 | 140 | 275 |
| | $\sigma_r$ | 250 | 250 | 1400 | 235 | 250 | 1400 | 235 | 250 | 1400 | 235 | 250 | 1400 |
| | RS | 4.28 | 3.07 | 3.04 | 5.21 | 3.86 | 3.27 | 1.51 | 1.32 | 2.80 | 1.51 | 1.28 | 2.65 |
| 4 | $\mu_r$ | 165 | 160 | 295 | 165 | 160 | 300 | 125 | 140 | 295 | 130 | 145 | 295 |
| | $\sigma_r$ | 220 | 225 | 1200 | 220 | 225 | 1200 | 155 | 185 | 1200 | 165 | 195 | 1200 |
| | RS | 6.23 | 3.47 | 1.13 | 1.00 | 0.72 | 0.66 | 1.07 | 0.77 | 0.59 | 0.73 | 0.61 | 0.61 |
| 5 | $\mu_r$ | 135 | 145 | 180 | 105 | 110 | 160 | 105 | 110 | 165 | 100 | 105 | 165 |
| | $\sigma_r$ | 195 | 225 | 480 | 135 | 145 | 380 | 135 | 145 | 400 | 125 | 135 | 400 |
| | RS | 6.15 | 5.32 | 6.80 | 5.52 | 4.95 | 6.69 | 4.58 | 4.37 | 6.70 | 4.56 | 4.37 | 6.67 |
| 6 | $\mu_r$ | 170 | 185 | 300 | 165 | 180 | 300 | 155 | 165 | 300 | 155 | 165 | 300 |
| | $\sigma_r$ | 205 | 240 | 1000 | 195 | 230 | 1000 | 180 | 205 | 1000 | 180 | 205 | 1000 |

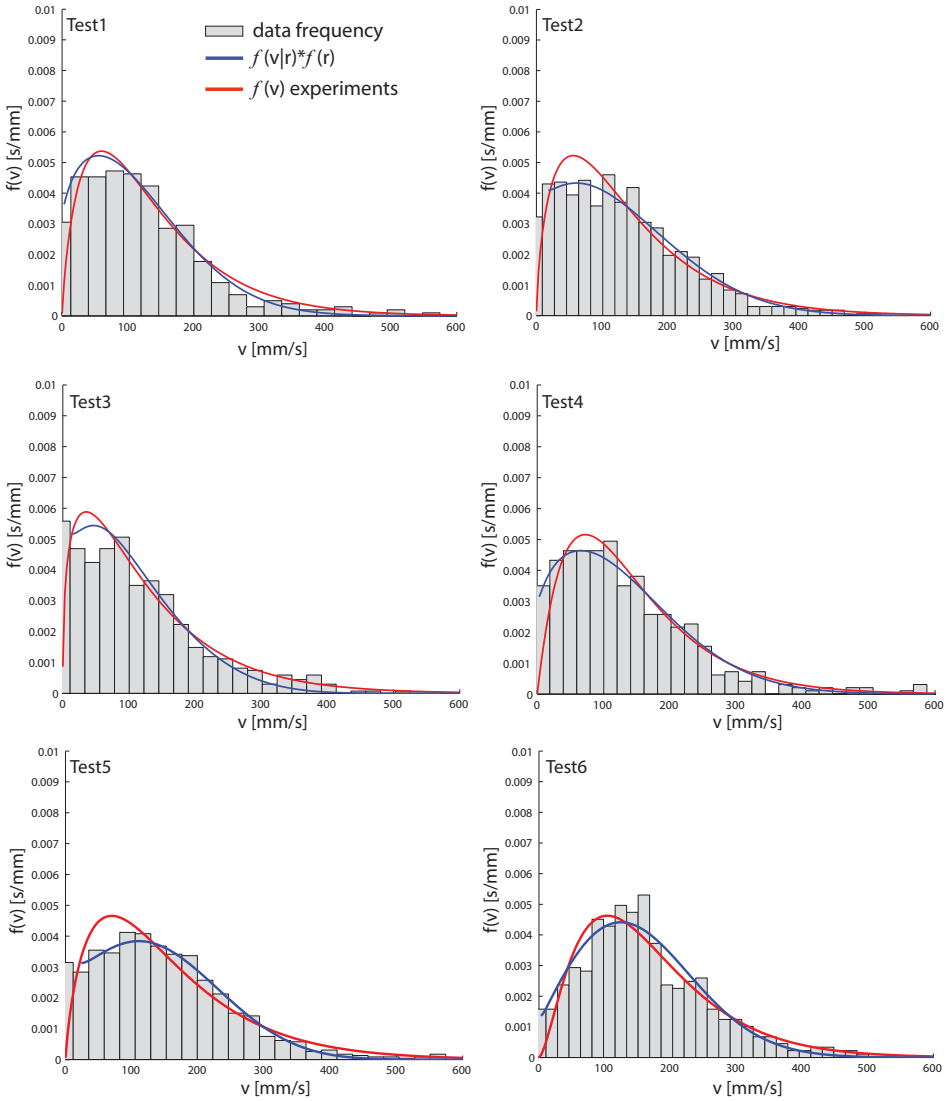


Figure 2.22: Results from the minimum error estimation between the data frequency of the measured particles' velocity and the computed marginal PDF (blue line). The gamma-like fit of the experimental data is reported too (red line). The presented case is for a logarithmic error derivation with $f_{MIN}/f_{MAX} = 0.075$, $U_0$ estimated at $z_0/d_{50} \approx 1.00$ and Weibull PDF of step length.

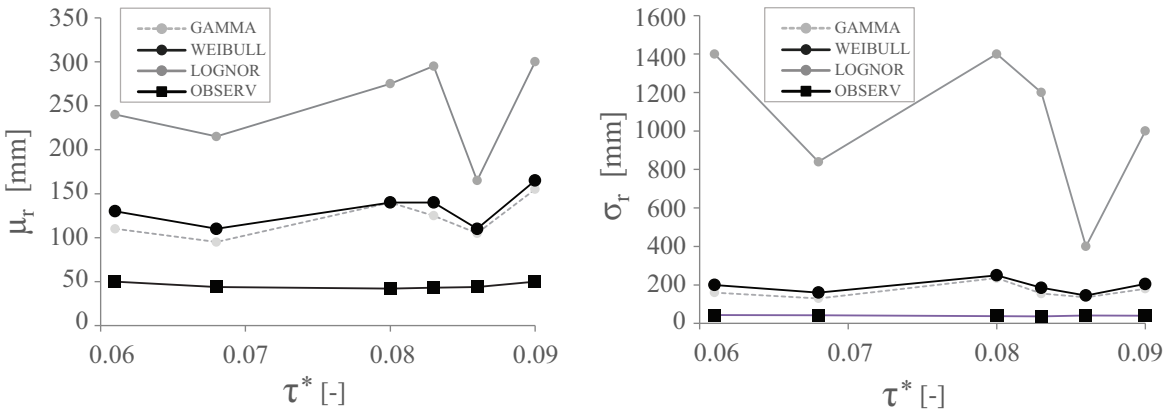


Figure 2.23: Mean and standard deviation of step length for the three statistical models and the observed data as a function of the Shields' parameter.

### 2.4.3 Discussion

Figure 2.24 presents the truncated experimental data and the cumulative distributions of step length associated to the lowest error resulting from the application of the two methods. For all tests a Lognormal distribution is assumed for Method 1 with statistics as reported in Table 2.4, whilst a Weibull distribution is considered from Method 2 for a threshold of 0.075 and $z_0/d_{50} \approx 1$ (Table 2.5). Likewise Figure A.5 in the Appendix reports the PDFs results for all tests.

The comparison of the results would suggest that the distribution's derivation based on the truncated data (Method 1) better interpolates the observed frequencies while it reconstructs the missing part of the distribution. Statistics of the Weibull distributions (Method 2) are not much dissimilar from the Method 1's values, but the overall fitting is not as accurate (Figure 2.24).

There is a good reason to believe that the longitudinal areal extent is playing a fundamental role also in this analysis though.

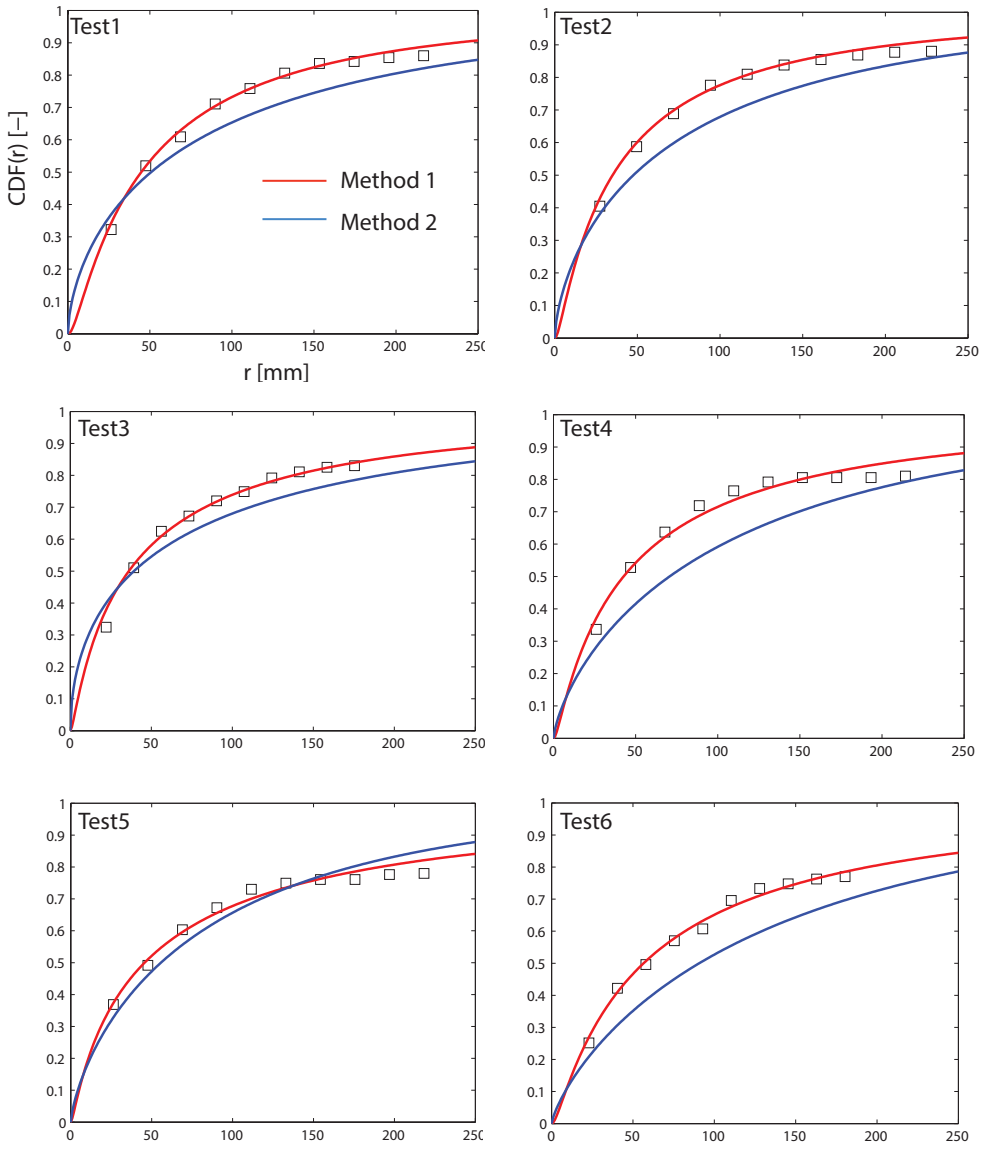


Figure 2.24: Cumulative distributions resulting from the two methods applied to the experimental truncated data. The red line refers to the Lognormal CDF of Method 1, whilst the blue line denotes the Weibull CDF of Method 2.

It was initially expected to find better results from Method 2 since the applied approach is

more statistically rigorous as it considers two dependent parameters, one of which not truncated. With this regard it is interesting to notice that if the investigated area is decreased to 100 mm long, the scaling $R$ of known trajectories on average goes down to 0.45, and the step length distributions from the second method are now more effective in interpolating the truncated data than the CDF of the Method 1 (Figure 2.25).

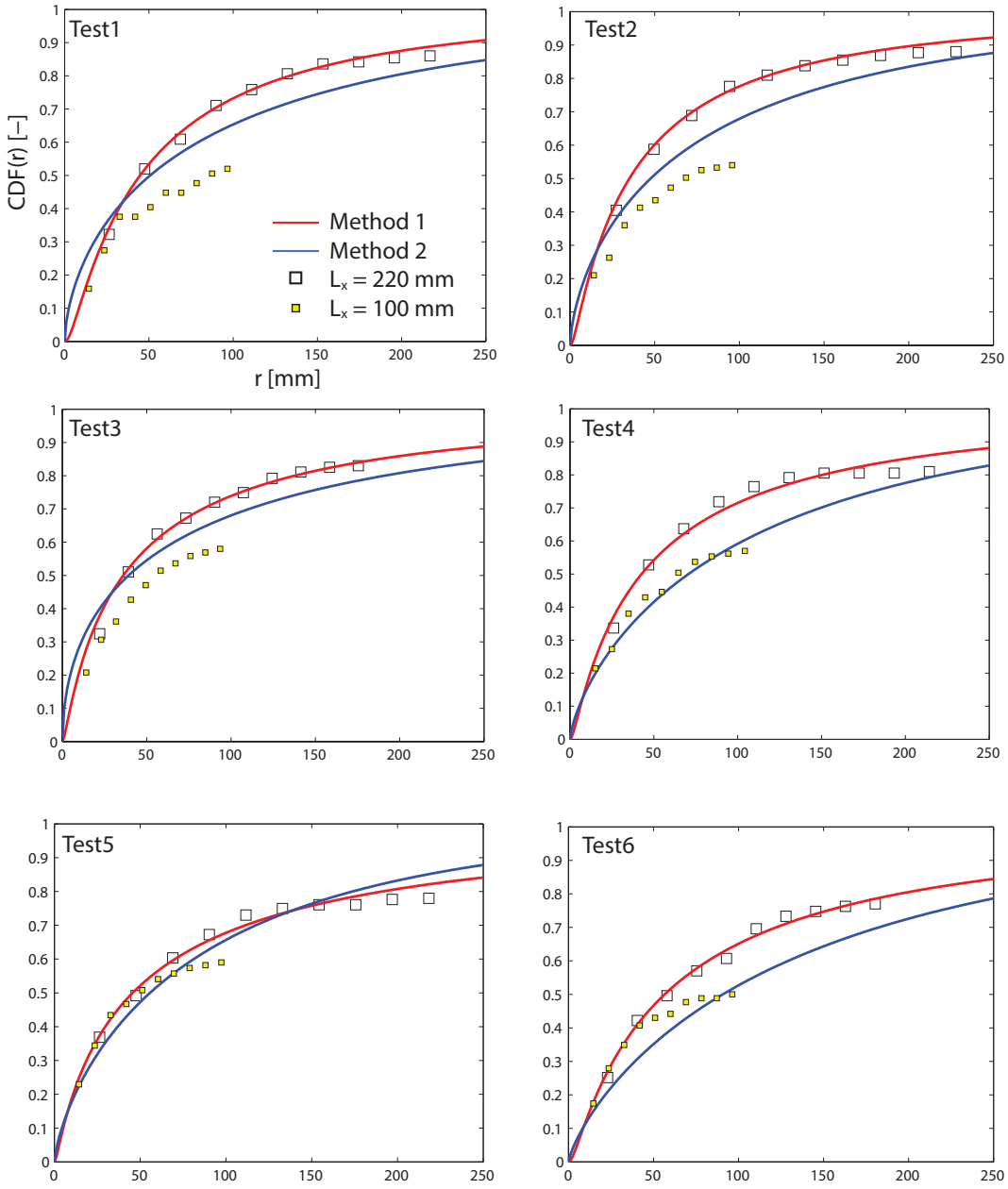


Figure 2.25: Cumulative distributions resulting from the two methods applied to the experimental truncated data with $L_x = 100$ mm (yellow squares) and 220 mm (blank squares).

The areal extent probably biases the fitting because of the frequency associated to the step lengths close to the longitudinal dimension of the investigated area. In other words, as the areal length, $L_x$, is decreased it will be less probable to observe steps as long as $L_x$ because of lower chances to observe grains that started at the upstream edge of the investigated area and stopped at the downstream boundary. The effect of this is noticeable in the cumulative plots, where in both cases, i.e. $L_x = 220$ and $L_x = 100$ mm, the last frequency values (for $r$ close to $L_x$) are

very similar to each other producing a plateau at the end of the observed distribution. This in turn would slow down the growth of the interpolating CDF to the asymptotic value of 1 thus generating greater values of the statistics for smaller areas.

To prove the last statement, Method 1 was applied to areas with progressively increasing longitudinal dimension, i.e. $L_x = 100$, 125, 150, 180 and 220 mm. The number of different types of displacement was derived for each case in order to calculate the related scaling parameter $R$, i.e. on average $R = 0.45$, 0.56, 0.66, 0.75 and 0.82. Results are shown for test T2 in Figure 2.26. The modelled values of mean and standard deviation scaled to their respective observed values (Table 2.26) decrease when a greater portion of the area, and therefore a more numerous and broader sample of steps, is considered. In particular the statistics tend to approach asymptotic values that could possibly be assumed as the real mean and standard deviation.

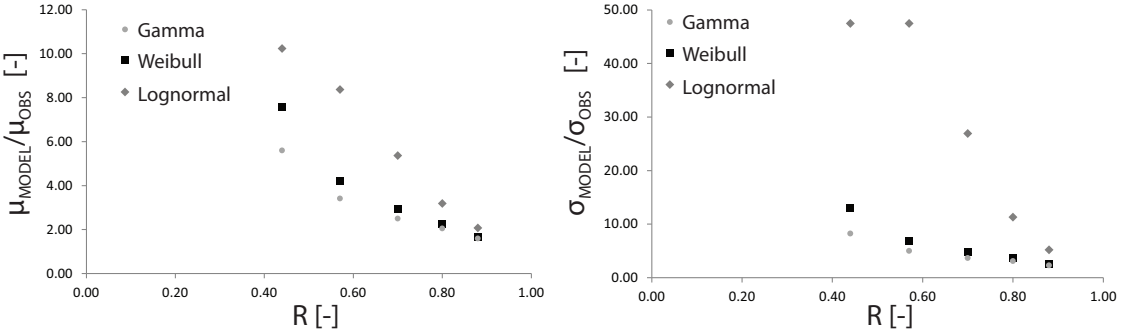


Figure 2.26: Scaled statistics resulting from the application of Method 1 to increasing portion of observed area, $L_x = 100$, 125, 150, 180, 220 mm, as a function of the scaling parameter $R$. Results are presented for test T2.

The last cumulative points would then jeopardize the derivation of the real step length statistics, especially in the first method. The longer the investigated area, the broader will be the range of observed trajectories and closer we can get to actual statistics of step lengths. At this stage of the analysis it is difficult to assess which method works best. Method 1 is easier to implement, it provides reasonable statistics and the results fit well the $L_x = 220$ mm cumulative data, but it is more likely to be biased by areal amplitude and thus by the plateau of least frequent observations. Method 2, statistically rigorous, is sensitive to a good number of parameters, such as the asymptotic velocity, but it is not influenced by the least frequent values of the longest steps. In both cases the statistics of the distributions $f(r)$ associated to the lowest errors are quite alike (Table 2.7) exception made for the standard deviations which resulted larger in the case of Lognormal distributions.

In the following chapter the results from the first method will be used to model the transport of sediment over rough beds. This decision is based on the evidence presented above. However, only new experiments with longer areal extent would enable the estimation of the real influence of the window dimensions on the particles' trajectories and, consequently, the most appropriate method to reconstruct truncated step length distributions.

Table 2.7: Mean and standard deviations associated to the lowest error-distributions resulting from the application of the two methods.

| | METHOD 1 | | METHOD 2 | |
|---|---|---|---|---|
| | Lognormal distribution | | Weibull distribution | |
| TEST | $\mu_r$ [mm] | $\sigma_r$ [mm] | $\mu_r$ [mm] | $\sigma_r$ [mm] |
| T1 | 104 | 218 | 130 | 200 |
| T2 | 91 | 218 | 110 | 1605 |
| T3 | 128 | 435 | 140 | 250 |
| T4 | 131 | 380 | 140 | 185 |
| T5 | 194 | 801 | 110 | 145 |
| T6 | 166 | 458 | 165 | 205 |

# Chapter 3

# Modelling advection and diffusion of sediment tracers

Sediment tracers have been used in several studies to provide a Lagrangian description of particle motion that could be incorporated into probabilistic models. Tracers are valuable in the modelling and estimation of the sediment flux (Ganti et al., 2010), notably involving exchanges between the active and inactive layers of the streambed (Wong et al., 2007). Previous studies have highlighted the need for implementing the use of tracers to identify appropriate models for temporal evolution of sediment advection and diffusion in rivers.

Hereafter a series of long-run flume experiments with graded bed deposits comprised of natural sand and crashed marble gravel are presented. The reconstruction of sediment tracer concentrations in time and space reveals an advective and diffusive pattern which is modelled with a modified Exner equation for natural tracers exhibiting randomly distributed paths. As shown in the above chapter, the random nature of particles' trajectories has been identified as a potential source of diffusion (Nikora et al., 2002; Furbish et al. 2012a), and for this reason it is included into the model formulation as a stochastic variable represented by a probability density function. The series of experiments on advection and diffusion of bed load particles helped investigating the role of step length distribution in tracer motion over time and space, and the effect of the sediment bed composition on the fate of tracers. The same definition reported in Section 2.4 is still valid, so that step length is henceforth defined as one individual streamwise displacement between the position of entrainment and the subsequent deposition point .

## 3.1 Modelling framework

Sediment particles are intermittently entrained and deposited during their transport over a water-worked river bed. Particle deposition and entrainment continuously modify the local bed geometry by removing from or dropping particles onto the bed surface. The starting point for this modelling framework is the entrainment-based one-dimensional Exner equation for sediment balance, which describes the temporal evolution of the local mean bed elevation $\eta$ as (e.g., Parker et al., 2000):

$$(1-\lambda_p)\frac{\partial \eta(x,t)}{\partial t} = D_b(x,t) - E_b(x,t) \tag{3.1}$$

where $\lambda_p$ is the bed porosity, $t$ the reference time and $x$ the streamwise coordinate. The variation of bed elevation ($\eta$) is defined as the difference between the volumetric rate per unit area of bed load deposition, $D_b$, and the volumetric rate per unit area of particles entrained into motion, $E_b$

at a single location ($x$).

The bed deposit can be divided in two layers: a surficial layer, known as the *active layer* (Hirano, 1971), which actively contributes to the bed-load transport and in which the grain size distribution is assumed to be well mixed, and a lower layer, i.e. the substrate, which can exchange sediment with the active layer but only in case of general aggradation or degradation of the bed. As the model is derived for application to experiments where tracer particles are used, Equation 3.1 can then be written in terms of the fraction of tracers $f_{tA}(x,t)$ and $f_{tI}(x,t)$ respectively in the active layer and in the substrate:

$$(1-\lambda_p)\left(f_{tI}(x,t)\frac{\partial\eta(x,t)}{\partial t}+L_a\frac{\partial f_{tA}(x,t)}{\partial t}\right)=D_{bt}(x,t)-E_{bt}(x,t) \tag{3.2}$$

with $L_a$ representing the thickness of the active layer, and $E_{bt}$ and $D_{bt}$ indicating the volumetric entrainment and deposition rates of tracers.

Assuming that over the timescales examined (i) the mean sediment bed elevation is in equilibrium with no net aggradation nor degradation; (ii) no tracer exchange occurs with the deeper layers of the sediment substrate; (iii) the volumetric entrainment rate is a time-averaged macroscopically determined quantity that applies uniformly at each location of the bed surface; and by letting $f_t(x,t)$ denote the concentration of tracers in the active layer $f_{tA}(x,t)$, Equation 3.2 can be reformulated as:

$$(1-\lambda_p)L_a\frac{\partial f_t(x,t)}{\partial t}=D_{bt}(x,t)-E_{bt}(x,t). \tag{3.3}$$

The fractional entrainment rate of sediment tracers $E_{bt}(x,t)$ can be linked to the total entrainment rate as $E_{bt}(x,t)=E_b(x,t)\cdot f_t(x,t)$, where $f_t(x,t)$ is the tracer concentration at time $t$. Likewise, the fractional depositional rate is related to the fraction of tracers, $D_{bt}(x,t)=D_b(x,t)\cdot f_t(x,t)$. Following Ganti et al. (2010), particles that become entrained by the fluid will travel a distance $r$ over the sediment bed before being deposited again. Because of variability in the local bed roughness, flow conditions, and grains size, $r$ is regarded as a random variable described by a probability density function $f_s(r)$. Deposition of tracers can then be reformulated as follow:

$$D_{bt}(x,t)=\int_0^\infty E_b f_t(x-r,t-\tau_p)f_s(r)dr. \tag{3.4}$$

The variable $\tau_p$ indicates the time required by a tracer to complete a longitudinal step $r$ and it is hereafter denoted as the travelling time. The step length and the travelling time are dependent on variables whose joint probability can be expressed as (Furbish et al., 2012a):

$$\begin{cases} f_{\tau_p,r}(\tau_p,r)=f_{\tau_p}(\tau_p|r)\cdot f_s(r) \\ f_{\tau_p}(\tau_p)=\int\Big[f_{\tau_p}(\tau_p|r)\cdot f_s(r)\Big]dr=\int f_{\tau_p,r}(\tau_p,r)dr. \end{cases} \tag{3.5}$$

Considering the volumetric entrainment rate constant for a given shear stress and grain size, the tracers' deposition rate is then reformulated in order to account for the joint probability of travelling time and step length:

$$D_{bt}(x,t)=E_b\iint f_t(x-r,t-\tau_p)f_{\tau_p,r}(\tau_p,r)d\tau dr. \tag{3.6}$$

By combining (3.3) and (3.6) it follows:

$$(1-\lambda_p)\frac{L_a}{E_b}\frac{\partial f_t(x,t)}{\partial t} = \iint f_t(x-r,t-\tau_p)f_{\tau_p,r}(\tau_p,r)d\tau_p dr - f_t(x,t). \tag{3.7}$$

By substituting the joint probability $f_{\tau_p,r}(\tau_p,r)$ with the expression in (3.7), the last equation results:

$$(1-\lambda_p)\frac{L_a}{E_b}\frac{\partial f_t(x,t)}{\partial t} = \iint f_t(x-r,t-\tau_p)f_{\tau_p}(\tau_p|r)f_s(r)d\tau_p dr - f_t(x,t). \tag{3.8}$$

Equation 3.8 includes a joint probability of step lengths and travelling times, thus incorporating the idea that tracer particles arriving at a position $x$ at a time $t$ started their hops, length $r$ at many different times $(t-\tau_p)$. Equation 3.7 can also be expressed in terms of particle velocity, $v_p$. Replacing the travelling time $\tau_p$ with the ratio $r/v_p$, the first derivative results $d\tau_p = -(r/v_p^2)dv_p$ and (3.7) becomes:

$$(1-\lambda_p)\frac{L_a}{E_b}\frac{\partial f_t(x,t)}{\partial t} = -\iint f_t(x-r,t-r/v_p)f_{v_p,r}(v_p,r)\frac{r}{v_p^2}dv_p dr - f_t(x,t). \tag{3.9}$$

Similarly to the travelling time formulation, the joint probability $f_{v_p,r}(v_p,r)$ can be obtained by determining the conditional probability $f_{v_p}(v_p|r)$ and the marginal probability $f_s(r)$, i.e. $f_{v_p,r}(v_p,r) = f_{v_p}(v_p|r)f_s(r)$. When inverting the order of integration over $dv_p$, Equation 3.9 becomes:

$$(1-\lambda_p)\frac{L_a}{E_b}\frac{\partial f_t(x,t)}{\partial t} = \iint f_t(x-r,t-r/v_p)f_{v_p}(v_p|r)f_s(r)\frac{r}{v_p^2}dv_p dr - f_t(x,t). \tag{3.10}$$

Both equations 3.8 and 3.10 represent general expressions of sediment transport where the parameters defining the particles' motion, $r$ and $\tau_p$ (or $v_p = r/\tau_p$), are stochastically described.

### 3.1.1 Descriptive statistics of step length

To solve either equation 3.8 or 3.10, it is essential to determine the probability distribution of the particles' step length, $f_s(r)$. The statistics defining this probability density function, such as mean and standard deviation, can be experimentally derived as shown in the previous chapter (2.4). To obtain a general expression for the parameters defining the distribution of longitudinal step lengths two experimental datasets have been used.

Lajeunesse et al. (2010) measured the frequency distribution of particle step lengths in three series of experiments where high resolution images were recorded over an area of potentially movable sediment bed approximately 175 × 85 mm in size to track black dyed grains under steady, uniform flow conditions. These series of experiments involved three uniformly-sized bed deposits with no appreciable bed forms and representative mean grain size, $d_{50}$, respectively equal to 1.15 mm, 2.24 mm, and 5.5 mm. Although the authors claimed they could not obtain a fully converged probability distribution of step length due to an insufficient number of tracked grains, they provided an empirical relationship for the most probable step length (namely, the mode of the distribution). This was found to scale linearly to the excess shear velocity, $u^* - u_c^*$ (with $u_c^*$ = threshold shear velocity), and inversely to the particle settling velocity $V_s$. Their data were re-analysed in this study to obtain a different relationship which does not include the time-averaged critical shear velocity $u_c^*$:

$$\Big\langle L \Big\rangle = d\Big[108.4\Big(\frac{u^*}{V_s}\Big)^2\Big], \tag{3.11}$$

where $d$ is the size of the moving grain. The quadratic relation between the mode of the step length $\langle L \rangle$ and the shear velocity $u^*$ reasonably agrees with the scaling suggested by Hu (1996) for travel distance of particles in bed load motion. The reason for favouring Equation 3.11 over the original formulation proposed by Lajeunesse et al. (2010) is that a critical value of shear velocity is no longer required, and that the step length is related to the actual flow conditions and not their variance from the incipient motion threshold. In the new formulation there is no need to provide a defined value for the threshold of motion as in this system it is now considered a stochastic variable rather than a deterministic parameter (Grass, 1970; Bottacin et al., 2008).

The validity of Equation 3.11 was tested independently with data on bed load motion collected during the experiments presented in Tregnaghi et al. (2012b). In their experimental setting the bed consisted of fairly uniformly-sized movable natural gravel with $d_{50} = 5.0$ mm. Six tests with different flow conditions were analysed and over 200 moving grains were tracked for each test, which provided a statistically significant population of step lengths for increasing values of the bed shear stress. Figure 3.1 shows that the mean step length exhibits a quadratic dependence on the ratio $u^*/V_s$ as observed for the modal data obtained by Lajeunesse et al. (2010). The frequency distribution of step lengths measured by Lajeunesse et al. (2010) is denoted by short tail presenting a quite symmetric shape around the most probable step length. The authors found that the average mode was about 11 times greater than the particles' diameter, a value that finds correspondence with the truncated measured mean steps of Tregnaghi et al., i.e. the mean step length is about $10d_{50}$ for all tests. The similarity of these values and the short-tailed distribution derived by Lajeunesse et al. (2010) allowed the application of the same relationship to the two datasets. It would also explain why the dimensionless mean values are distributed along the same fitting of the modes (Figure 3.1).

As pointed out in the previous chapter (Section 2.4) this dataset lacks measurements of the grain step lengths longer than the longitudinal size of the bed surface tracked by the recording cameras (approximately 200 mm). The experimental frequencies of occurrence of step length were then fitted with three distribution models (i.e., Gamma, Weibull, and Lognormal) in order to account for the fraction of grain motions that were not fully tracked by the recording system. The following analysis refers to the results provided by the fitting method based on the least error that is calculated on the cumulative distribution of step lengths (Method 1).

Results reported in Figure 3.1 show that the fitting models return different estimates of the mean step length as the weight of extreme values increases when moving from Gamma to Lognormal functions. However, for any given distribution model, all data exhibit a linear relationship between the mean step length and the squared ratio $u^*/V_s$ similar to Equation 3.11:

$$\overline{\mu_r} = d\left[g_1\left(\frac{u^*}{V_s}\right)^2\right], \tag{3.12}$$

with $g_1$ = constant depending on the selected fitting model (Figure 3.1). Discrepancies from this general behaviour occur for the test with the lowest value of the Shields parameter (roughly corresponding to the threshold of particle motion). This can be possibly explained in light of the observed proportions of different types of motion, as grains were seen to travel longer distances when in contact with the bed (sliding mode) with respect to rolling or saltating movements, which were mainly observed during tests with higher bed shear stress.

The fitting of data from Tregnaghi et al. (2012b) supported the complete derivation of the descriptive statistics of the step length distribution, leading us to assume the standard deviation of the step lengths to scale linearly with the mean value of the population, i.e. $\sigma_r = k\mu_r$, with $k =$

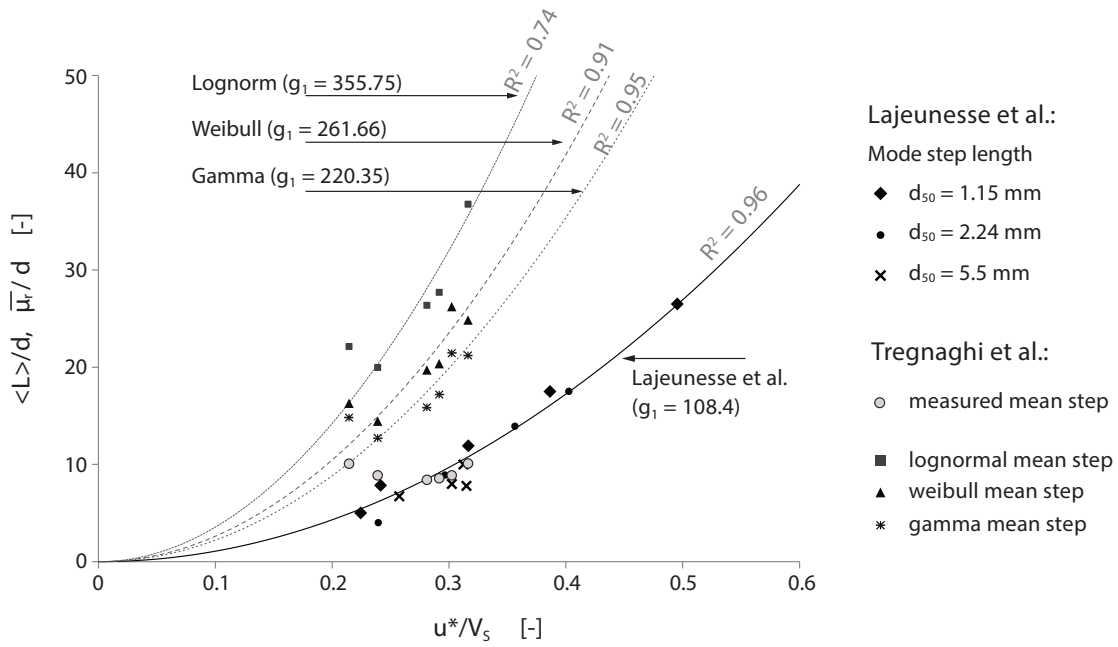


Figure 3.1: Mean step lengths versus ratios of shear and settling velocities, Eq. (3.12) (data after Lajeunesse et al., 2010 and Tregnaghi et al. 2012b). Calibration coefficients $g_1$ are reported for three distribution models (i.e., Gamma, Weibull, and Lognormal).

constant (Figure 3.2). The coefficient $k$ varies according to the fitting model, presenting greater values for long tail distributions. The lack of sufficiently detailed experimental measurements directed this analysis to assume a linear trend between the mean and the standard deviation of the step length distribution. This assumption however should be revised or confirmed with new experimental data of untruncated step length distributions, possibly derived for different hydraulic conditions and over different sizes of bed material.

The statistic parameters so far derived reflect the case of beds with fairly uniform sized grains. In both datasets, the bed consisted of uniform material, so that the role played by the bed roughness, in terms of relative size of moving grains to the mean bed diameter, in the extent of the travelled distance cannot be determined. It is reasonable to think that for sediment beds consisting of poorly sorted grains, coarse particles will travel longer distances than in uniformly-sized beds, while fine fractions will be more easily trapped within pockets in the sediment bed or shielded by upstream grains depending on the irregularities of the bed surface roughness (e.g., Wilcock et al., 2001). Bed elevation fluctuations are thus likely to affect the potential distance travelled by a particle of a given size.

As the size of moving particles exceeds the standard deviation of bed elevations, this will result in longer hop lengths by more easily overcoming bed surface obstacles that are encountered during particles' motion. Given the lack of data, it is here assumed that this roughness effect can be accounted for by a power law relationship between the particle size and the standard deviation of bed elevations, such as Equation 3.12 is modified as follows:

$$\mu_r = \overline{\mu_r}\left(\frac{d}{\sigma_b}\right)^{\epsilon} = d\left[g_1\left(\frac{u^*}{V_s}\right)^2\right]\left(\frac{d}{\sigma_b}\right)^{\epsilon}, \tag{3.13}$$

where $\overline{\mu_r}$ denotes the equivalent mean step length for a particle of size $d$ travelling over a uniformly-sized sediment bed, and $\sigma_b$ the standard deviation of bed elevations of a graded sediment deposit. The latter is estimated from earlier findings on bed surface variation in

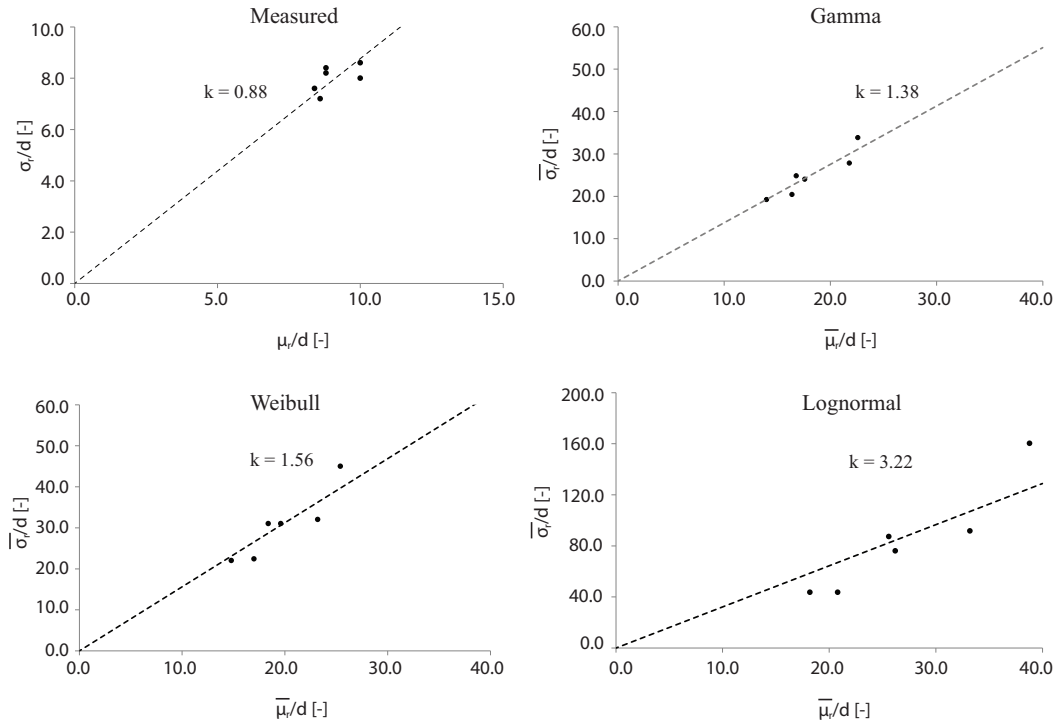


Figure 3.2: Standard deviation of step length as a function of the mean values along with the linear fit and corresponding coefficient $k$. Overbarred symbols denote the statistics parameters (mean and standard deviation) of the probabilistic distribution model, whilst the absence of overbar indicates the arithmetic statistics of the raw step length data.

natural gravel beds reporting that $4\sigma_b \approx 1.5d_{50}$, with $d_{50}$ = mean diameter of the particle size distribution of the surface material (Nikora et al., 2001). The standard deviation of bed elevations can be considered as a good indicator of the characteristic vertical scale for bed surface roughness. The proposed relationship ($4\sigma_b \approx 1.5d_{50}$) finds confirmation in the work by Coleman et al. (2011). Via statistical analysis of measured bed elevations in different channel beds, the researchers observed the ratio $d_{50}/\sigma_b$ to vary between 1.8 and 5.8, depending on the bed sediment size distribution and the water-working effect on the deposit material. The ratio used here ($d_{50}/\sigma_b \approx 2.67$) is in good agreement with Coleman et al.'s (2011) measurements for water-worked gravel and uniform sand beds, respectively $d_{50}/\sigma_b$ = 1.8-2.4 and $d_{50}/\sigma_b$ = 2.5-4.2. The calibration parameter $\epsilon$ will be obtained in Section 3.3 by minimizing the root mean square error between experimental and simulated tracer concentration data. This corrective factor will account for the selective distance travelled by fine and coarse particles in fractional bed load transport under given flow conditions but with different sediment bed compositions.

### 3.1.2 Conditional probability and model reformulation

The equations presented above, namely (3.8) and (3.10), were derived by considering the joint probability of the step length with respectively the travelling times and the particles' velocities. The two formulations require a definitive relation for the conditional probability of the two variables, $f_X(X|r)$ with $X$ being either the travelling time or the particle's velocity.

To do so, the variable $X$ should be described by a probability density function, whose statistics are determined as a function of the step length $r$. The appropriate model for the distribution of the variable $X$ can be obtained from experimental measurements of tracked bedload particles. Experimental data helps also with the derivation of the model statistics

as a function of the step lengths, i.e. $\mu_X(r)$ and $\sigma_X(r)$. The determined joint probability $f_{X,r}(X,r) = f_X(X|r)f_s(r)$ if integrated over $r$ should then provide the marginal probability density function (hereafter PDF) of the variable $X$, i.e. $f_X(X)$. The so-calculated PDF of $X$ should result equal to the PDF of $X$ obtained through the experimental observations:

$$f_X(X)|_{experiments} \equiv \int f_{X,r}(X,r)dr = \int f_X(X|r)f_s(r)dr, \tag{3.14}$$

where $f_X(X)|_{experiments}$ and $f_X(X|r)$ are represented by the same distribution model, e.g. exponential, gamma, or lognormal, with statistics of the conditional PDF expressed in function of the step length $r$, $\mu_X = g(r)$ and $\sigma_X = w(r)$. The realization of (3.14) is a required condition for the validity of the mathematical framework generating Equations 3.8 and 3.10.

With this regard, an available dataset is provided by the experiments performed by Tregnaghi et al. (2012), where information of particles' step, travelling time and velocity can be collected. The statistics of the conditional PDFs were expressed as a function of the step lengths $r$, by considering an exponential growth to the asymptote $U_0$ for the mean particles' velocity (Figure 3.3a). As most of the particles have been observed to roll or slide over the bed surface, the averaged maximum travelling velocity, which corresponds to the asymptotic value $U_0$, is imposed equal to the double-averaged fluid velocity in proximity of the bed at a vertical distance $z \approx 1.0d_{50}$(Chapter 2). The standard deviation of the particles' velocity was scaled to $r$ by a power law. The mean travelling time and the relative standard deviation were instead both described by a power law, as longer steps are reasonably associated to longer travelling times (Figure 3.3b).

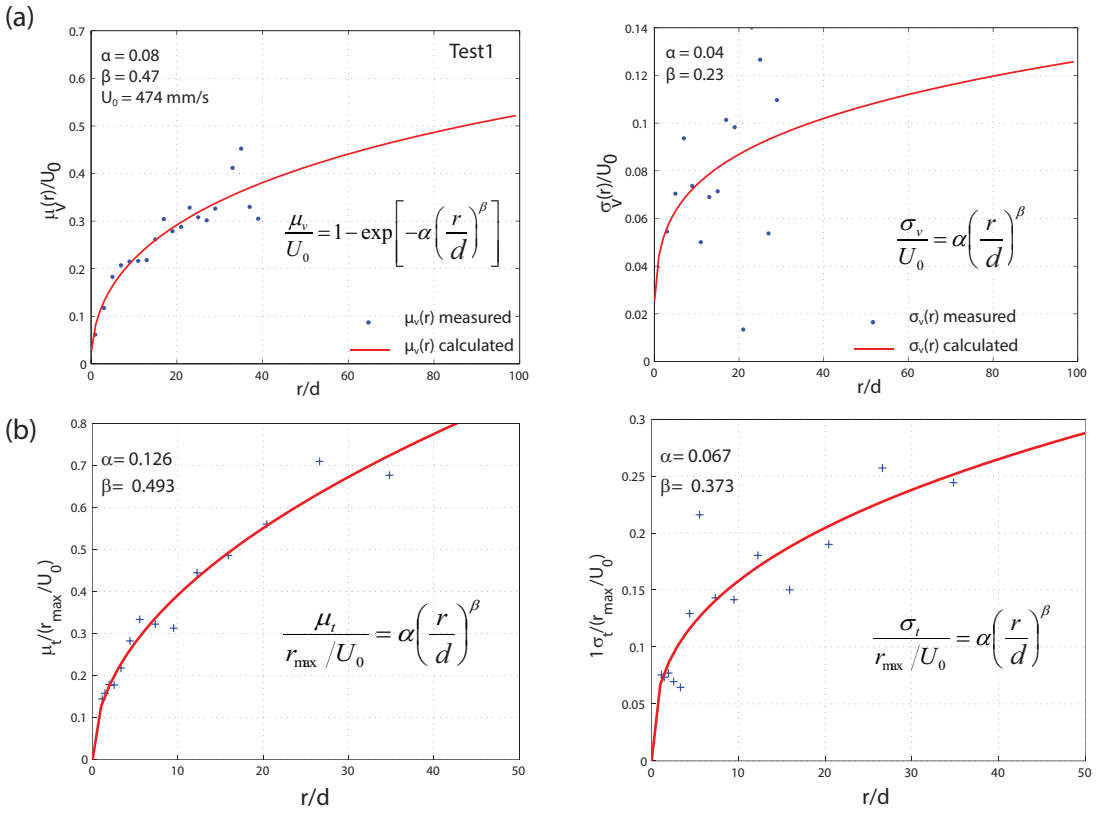


Figure 3.3: Mean and standard deviation of the particles' velocity (a) along with mean and standard deviation of travelling times (b) scaled to the dimensionless step length $r/d$. The fitting laws are reported for each parameter.

The integration of the conditional PDFs with the distribution of the step lengths over $r$, generates the marginal probability density functions of $\tau_p$ and $v_p$ that is then compared to the experimental PDFs, i.e. $f_{\tau_p}(\tau_p)|_{exp}$ and $f_{v_p}(v_p)|_{exp}$. The truncation of these variables as a consequence of the maximum observable step length $r = 220$ mm, requires a probabilistic model for the travelling time and the particles' velocity. In doing so, the two PDFs, calculated and experimental, can be obtained for multiple combinations of different fitting models as shown in Method 2 of Chapter 2. Such a great variability in the derivation of the PDFs creates an array of different possibilities and parameters that need to be calibrated in order to satisfy the condition 3.14.

Equation 3.8 and 3.10 were then simplified by assuming a constant velocity for all the particles which is not dependent on the step length $r$. In doing this, the equation is as follow:

$$(1-\lambda_p)\frac{L_a}{E_b}\frac{\partial f_t(x,t)}{\partial t} = \int f_t(x-r, t-r/v_p) f_s(r) dr - f_t(x,t), \tag{3.15}$$

where $v_p$ denotes the average particle velocity. This simplification is supported by the analysis of Chapter 2 on the particles' velocity distribution. Differently from the travelling time and the step length, the velocity variable is the least affected by truncation, since also partial trajectories can contribute to its derivation. The calculated average particle's velocity would then be closer to the actual value than the measured average time would do, thus favouring an ensemble averaged $v_p$ instead of a mean $\tau_p$ in the simplification of general model formulation. With the experimental data at hand, Equation 3.15 was preferred to the general integral equations (3.8 and 3.10) since a smaller number of assumptions should be made with regards to the conditional probability of travelling times and particles velocity. The new simplified equation differs from the others because it attributes the stochasticity of sediment motion only to the probability distribution of the step length.

A complete description of the motion of the bedload tracer particles would help addressing the dependence of the travelling time/particle velocity on the step lengths as well as gathering information of the total PDFs. With this information it would then be possible to solve the general equations 3.8 or 3.10.

### 3.1.3 Active layer, particles' velocity and entrainment rate

Equation 3.15 is solved with a finite different method to obtain the evolution of tracer concentration, $f_t(x,t)$, in time and along the streamwise direction, and the calibration parameters $\epsilon$ and $k = \sigma_r/\mu_r$ from the experimental data collected by Marion (1995) in the experiments described in Section 3.2. The particle step length, $f_s(r)$, is assumed to follow a Lognormal distribution according to the best fit obtained from data collected by Tregnaghi et al. (2012b), as the mean squared error associated to this distribution was found the lowest among different tested models (Exponential, Gamma, Weibull and Lognormal as presented in Section 2.4).

The exchange depth $L_a$, namely the active layer thickness, is here parametrized as a function of either the bed elevation fluctuations or of the mean grain size, resulting respectively $L_a = 1.62\sigma_b$ (Wong et al., 2007) or $L_a = 0.5 - 0.6d_{50}$ (Nikora et al., 2001, 2002). The two expressions yield similar active layer thickness when $\sigma_b$ is considered proportional to the mean bed diameter, $4\sigma_b = 1.5d_{50}$ (Nikora et al., 2001).

The ensemble velocity of bed load particles, $v_p$, is assumed to be reasonably approximated by the double-averaged fluid velocity at a distance from the mean bed elevation corresponding to 0.30 the mean particle diameter, $\langle \overline{U}(z) \rangle$ with $z = 0.30d_{50}$. The arbitrary choice of $z$ is

based upon the average velocity value derived for the measured particles' velocities of the six tests presented in Chapter 2. The corresponding velocity can be estimated from the multi-layers formulation of double-averaged velocity profile over rough-beds presented by Nikora et al. (2001). In this application the roughness layer $e$, shown to vary from $1.0d_{50}$ to $1.5d_{50}$ (Nikora et al., 2001), was set equal to $1.5d_{50}$ whilst the coefficient $C$ for non-uniform bed sediment is assumed, i.e. $C = 5.6$. The double-averaged velocity can be calculated with Eq. 2.12 and, depending on the bed elevation $z$, it will be described by a logarithmic or linear profile. Under the experimental conditions described in the following section, the vertical elevation $z$ always fell into the roughness layer ($z \leq e$) so that the particles' velocity was calculated with the linear expression.

The bed porosity, $\lambda_p$, can be assumed equal to 0.3 as reported by Marion (1995). The volumetric entrainment rate, $E_b$, can be estimated with the transport model derived by Wilcock (1997) for sand-gravel mixture. The fractional entrainment rate $E_{bi}$ is obtained as the product of the fractional mass, $M_{ai}$, entrained per unit area over a period of time $T$ (including only grains found within the area at the start of $T$) times the number of entrainment events, $N_i$, occurred during $T$:

$$E_{bi} = M_{ai}\frac{N_i}{T} = \left[\left(\frac{\pi}{6}\rho_s\right)F_i d_i \Delta_i Y_i\right]\frac{N_i}{T}, \tag{3.16}$$

where $i$ stands for either sand or gravel fractions identified by size $d_i$; $F_i$ denotes the sediment fraction of size $i$ on the bed surface and $Y_i$ the sediment fraction of size $i$ mobilized over the duration of the test; $\Delta_i$ discriminates between partial and full particle mobility depending on value of $Y_i$. When $Y_i \leq 0.5$, $\Delta_i$ results equal to 1 as entrainment affects only grains lying on the surface of the bed channel, whilst if $0.5 < Y_i \leq 1$ the parameter $\Delta_i$ accounts for also grains entrained from a volume $dx$ of the bed, i.e. $\Delta_i = dx/d_i$ with $dx$ the size of the fraction $d_{50}$ that is 50% mobile at $\tau_0$, $dx = 397(\tau^*_{50})^{1.5}$.

The frequency of entrainment events, $N_i/T$, for the sediment fraction of size $i$ is given by:

$$\frac{N_i}{T} = K\left(1 - 0.85\frac{\tau_{ri}}{\tau_0}\right)^{4.5}\left(\frac{d_{50}}{g}\right)^{(-1/2)}, \tag{3.17}$$

where $K$ is a calibration parameter equal to 0.01; $g$ the acceleration due to gravity; $\tau_0$ the time-averaged bed shear stress; and $\tau_{ri}$ the threshold shear stress that produces a reference value of the dimensionless transport rate equal to 0.02 (Wilcock and Kenworthy, 2002). The threshold shear stress is expressed as a function of the size $d_i$, $\tau_{ri} = 0.68d_i^{0.55}$.
The total volumetric entrainment rate $E_b$ is given as the sum of the individual fractional entrainment rates $E_{bi}$ calculated by combining equations 3.16 and 3.17 for each size fraction composing the bed mixture.

## 3.2 Experiments

The analysis of advection and diffusion of bed load tracing sediment presented in this study is supported by experiments carried out in the Waterloopkundig Laboratory Delft (Netherlands) (Marion, 1995). The experiments were originally designed to investigate the vertical structure of water worked mixed beds (Marion and Fraccarollo, 1997a) and to develop a new conversion model for areal sampling in fluvial sediment deposits (Marion and Fraccarollo, 1997b).

Experiments were also intended to studying the streamwise diffusion of bed particles during their motion over a rough bed, however no comprehensive analysis was presented to date. Sediment tracers, i.e. bed particles of known size marked with different colour than the underlying

sediment matrix, can be used to reveal significant features of bed load motion as these coloured particles are assumed to represent the behaviour of the entire grain population. Experiments reported in the next sections present the results of a computer-based image analysis which was performed to detect and quantify overall tracer motion and their advective and diffusive patterns for different size fractions.

### 3.2.1 Experimental equipment and method

The experimental apparatus consisted of two tilting flumes: the main flume was devoted to investigation of vertical mixing structures and tracer diffusion, while a secondary flume was used for preliminary bed preparation. The main 50-m-long, 1.5-m-wide flume (Figure 3.4) was divided into two adjacent, 0.5-m-wide channels, namely A and B, and tilted to attain a constant slope equal to 0.007, which reduced the maximum operating length to 30 m. This flume was configured in a close circuit where water and sediment were constantly recirculated. A collecting tank was placed at the downstream end of the flume and divided into two sections with different volumes to separate the coarse sediment from the fine material and collect samples of fractional transport rates. The larger grains were uplifted and separated through a cyclone pump, whilst the finest material together with water was directly pumped back to the upstream entrance. Throughout the experimental runs, particular care was taken to ensure uniform sediment re-injection at the upstream end of the flume by means of a transverse diffuser for both fine and coarse sediments. The 24-m-long secondary flume had the same width and inclination of the adjacent channels in the main flume. A simpler technology was implemented for the supporting flume but it maintained the same width, 0.5 m, and slope, 0.007, as the main one.

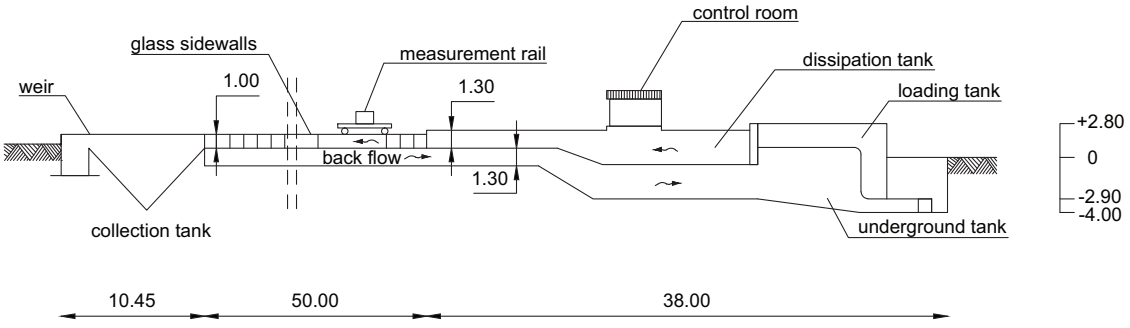


Figure 3.4: Sketch of the main flume (dimensions in meters).

Three tests were performed in total with different sediment mixtures: Tests 1 and 3 were carried out in the main flume, while the secondary flume was used for Test 2. All tests were run with steady, uniform flow conditions at approximately constant Reynolds Number ($1.3 \cdot 10^5$) by setting the flow rate to 20 l/s. Table 3.1 shows the duration, the main hydraulic parameters (shear velocity $u^*$, shear stress $\tau_0$, water depth $h$), and the characteristics of the sediment deposit mixture for the three tests.

A bimodal mixture consisting of well sorted crushed marble gravel and well sorted fine quartz sand formed the sediment bed mixtures for Test 1. The bed consisted of 66% in weight of black gravel, $d_{10} = 3.5$ mm, $d_{50} = 4.7$ mm, $d_{90} = 5.8$ mm, and 34% of grey fine sand, $d_{10} = 0.097$ mm, $d_{50} = 0.133$ mm, $d_{90} = 0.175$ mm (Table 3.2). In Test 1 the black gravel was replaced with

Table 3.1: Hydraulic parameters and bed sediment composition of the three tests. Sediment mixture is defined by the percentage in weight of each fraction.

| TEST | | FLUME | $u^*$ [m/s] | $\tau_0$ [N/m$^2$] | $h$ [mm] | GRAVEL | MEDIUM SAND | FINE SAND |
|---|---|---|---|---|---|---|---|---|
| 1 | | main | 0.055 | 3.03 | 51.6 | 66%,black | - | 34%,grey |
| 2 | | secondary | 0.051 | 2.65 | 49.0 | 35%,white | 30%,black | 35%,grey |
| 3 | A | main | 0.058 | 3.35 | 59.6 | 35%,white | 30%,white | 35%,grey |
| 3 | B | main | 0.060 | 3.54 | 59.3 | 35%,black | 30%,black | 35%,grey |

identical white gravel along a 3-m-long section in the upstream reach of the flume which was subsequently tracked via image acquisition (Figure 3.5a).

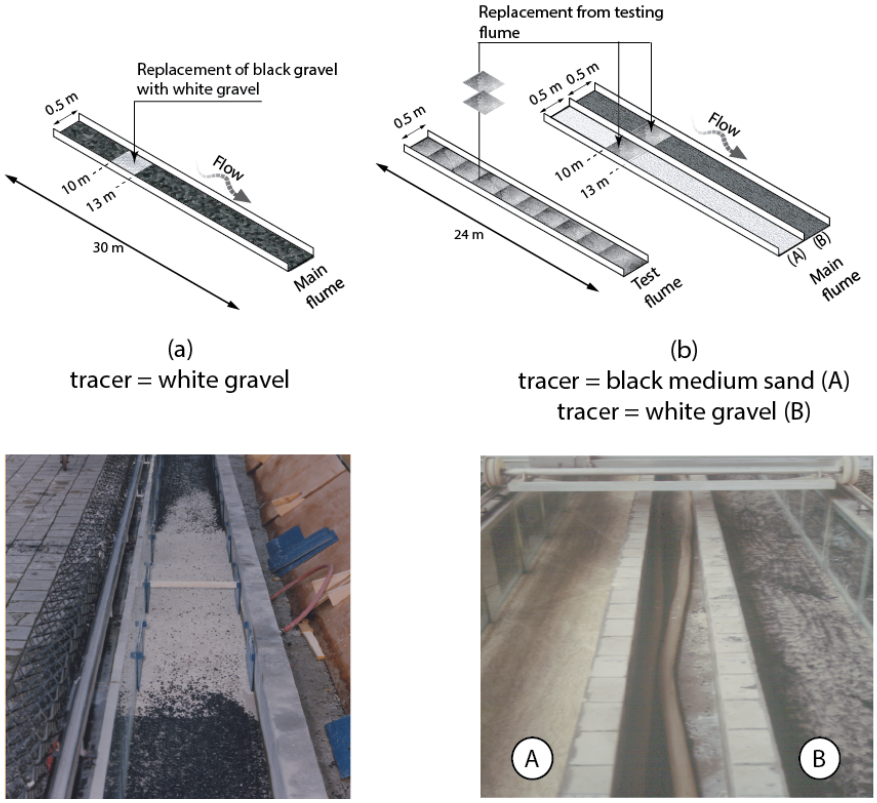


Figure 3.5: Representation of bed replacement with tracers for the bimodal Test 1 (a), and for the trimodal Tests 3A and 3B (b). Images of the flume are provided.

The experiment was run for several hours before the replacement took place to induce the development of a water-worked bed layer. For the next four hours, at 15, 30, 60, 120 and 240 minutes after replacement, five series of pictures were taken from a moveable platform located on top of the sidewalls of the flume, which recorded the positions of the tracing white gravel for a 22-m-long reach downstream of the replacement section. At the end of the recording session tracers were observed to be uniformly distributed along the channel length.

During Test 2 and 3 an intermediate size (medium sand) was added to the original sediment mixture to reproduce a trimodal grain size distribution (Figure 3.6). In Test 2, the bed was comprised of 35% white gravel, 30% black medium sand and 35% grey fine sand. After several hours from the beginning of Test 2, two 0.5-m-wide, 3-m-long blocks of sediment deposit, each consisting of six $0.5 \times 0.5$ m$^2$ smaller blocks, were extracted from the secondary flume, and afterwards used for replacement in the main flume during Tests 3A and 3B (Figure 3.5b).

Table 3.2: Grain classes by color and grain diameter.

| GRAIN CLASS | COLOUR | $d_{10}$ [mm] | $d_{50}$ [mm] | $d_{90}$ [mm] |
|---|---|---|---|---|
| Gravel | black | 3.50 | 4.70 | 5.80 |
| | white | 3.40 | 4.90 | 5.70 |
| Medium Sand | black | 0.67 | 0.84 | 0.98 |
| | white | 0.71 | 0.91 | 1.14 |
| Fine sand | grey | 0.097 | 0.133 | 0.175 |

To prevent alteration of the bed surface layer, the extraction technique consisted of freezing the blocks in place with liquid nitrogen, which were then stored in refrigerated containers at a temperature of -15 °C. After 15 hours the blocks were relocated back into the main flume and allowed to slowly defrost in place. The two sediment blocks obtained from Test 2 were placed 10 m downstream from the inlet of channel A and B, respectively. During Test 3A the black medium sand originating from the block was used as a sediment tracer, as the bed mixture in channel A was made of 35% white gravel, 30% white medium sand and 35% grey fine sand. During Test 3B the bed mixture in channel B consisted of 35% black gravel, 30% black medium sand and 35% grey fine sand. In this case the white gravel within the replacing block was used as a sediment tracer over the original dark deposit. To ensure similar surface grain packing arrangements of both the replacing material and the channel mixture, sediment beds in channels A and B were water worked by the flow for several hours before insertion of the replacement blocks.

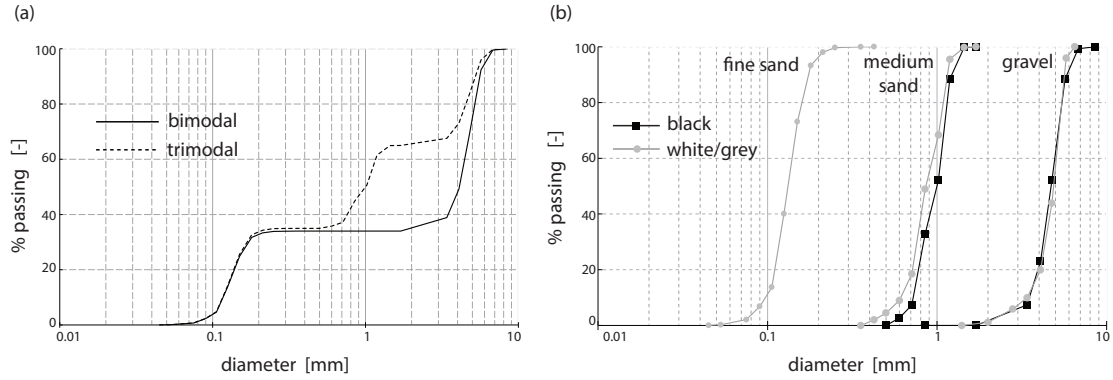


Figure 3.6: (a) Cumulative size distribution of bed material with bimodal (Test 1; solid line) and trimodal mixtures (Test 2, 3A, 3B; dashed line). (b) Distribution of grain sizes for the three components, fine sand, medium sand and gravel.

Tracer motion along channel A and B was recorded by acquiring images at 3, 6, 12 and 22 minutes after sediment replacement. Image acquisition ceased after only 22 minutes as sediment tracers were observed to be evenly distributed along the flume length. In both Test 2 and 3 images were taken over a drained bed. At selected times, the flume was slowly flooded to increase the water depth and suddenly stop sediment motion in order to prevent alteration of the bed structure; the channel was then gradually drained to record images of the sediment bed with no distortion caused by the water surface, afterwards the flow was slowly restored to keep the experiment running.

Measurements of sediment transport rates were recorded with regular sampling periods during each test. Before re-injection at the upstream end of the flumes, bed load material collected

from the tank was sampled over a short time interval, dried and weighted. Measures from a number of samples, ranging from 8 to 16 depending on the observed intensity of sediment transport, each with duration 10-30 seconds, were averaged to obtain a representative value of the sediment transport rate. Suspended transport was estimated by measuring the solid content of a volume of water either sampled with a probe (Bosman et al., 1987), or collected with buckets at the downstream end of the flume. The representative value of the suspended sediment transport rate was obtained by averaging individual measurements from 8 samples.

### 3.2.2 Image processing and volumetric conversion

Pictures acquired from Tests 1, 3A and 3B enables the tracking of respectively: (a) white gravel over a bimodal mixture, (b) black medium sand and (c) white gravel over a trimodal bed deposit. The image processing analysis was performed by Ranieri in 2005. This section presents the main steps of the procedure implemented to derive the area covered in tracers, whilst more details of the image processing work can be found in Ranieri (2005).

Images were converted into a digital format to obtain a continuous compound image of the bed surface by matching and scaling overlapping edges of individual frames. Each compound image was then processed to estimate the fraction of bed area covered by tracers and to assess their streamwise position along the flume at given times after their initial placement in the flume. Geometrical distortion due to lenses curvature and manual image acquisition was removed and pictures were then converted to grey-scale images with 256 spectrum frequency. This revealed different levels of brightness throughout a single image that stemmed from the camera integrated flash, which returned brighter images in the center than at the edges. Each picture was split into 27 lateral stripes and 4 streamwise rows to provide more homogeneous light conditions, thus identifying 108 sub-areas (Figure 3.7).

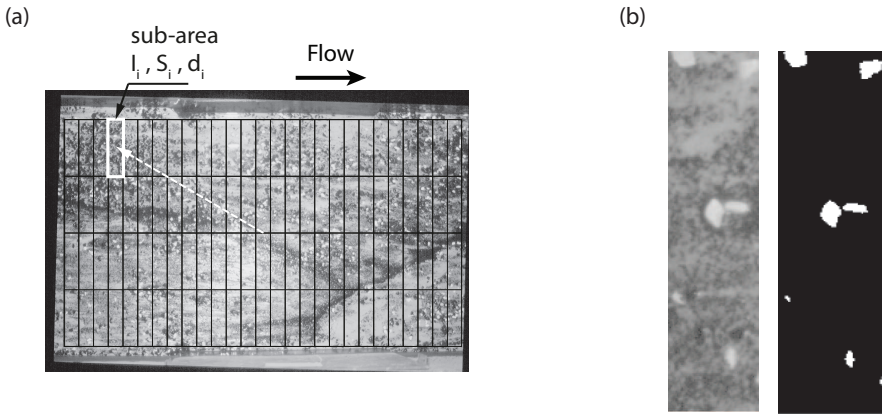


Figure 3.7: Example of picture recorded during Test 3B. (a) The image is divided into 27 × 4 sub-areas, each defined by an average light intensity $I_i$, a black-white separation threshold $S_i$ and distance from the centre of the image $d_i$. (b) The application of the algorithm to a sub-area in order to derive the fraction of white gravel. After Ranieri (2005).

Every sub-area was denoted by a frequency histogram, a graph that displays all the brightness levels contained in it, from the darkest to the brightest. Working on grey-scale images, this histogram provides separation between higher intensities, which defined bright-white areas of the image, and the lowest frequencies, corresponding to dark grey-black parts of the image. The separation threshold frequency, $S$, was then used to discriminate between white and black

image pixels, and thus to detect the area covered by either the white gravel or black medium sand tracers.

It was soon noticed that the threshold $S$ was dependent on the average brightness $I$, which in turn varies with the distance from the centre of the image. To optimize the image processing method the thresholds $S_i$ for each sub-area $i$ were correlated to the average subarea brightness, $I_i$, by introducing the parameter $\Delta_i = S_i - I_i$, and to the distance of the sub-area $i$ from the center of the image, $d_i$. A linear relationship was obtained between the variation of brightness intensity of the subarea $i$ compared to the central subarea, $\Delta'_i = \Delta_i - \Delta_{\text{centre}}$, and the squared distance $d_i$ of the sub-area as shown in Figure 3.8b. This allowed automatic calculation of $\Delta$ and $S$ for every subarea, given the distance of the $i^{th}$ sub-area from the center of the image was known. The method found confirmation when applied to other images of the bed. Based on the identified frequency threshold, pixels with higher brightness were classified as 1 (white), conversely pixels with lower brightness were denoted with 0 (black). An algorithm implemented this procedure for each subarea of every image and derived the percentage of area covered either in *black* or *white* sediment tracers. Validation of this method was performed by visual comparison of the original pictures and the black and white images resulting from the algorithm (Figure 3.7b). The application of this method to tests 1 and 3B enables the percentage of white tracing gravel for the entire flume length to be obtained.

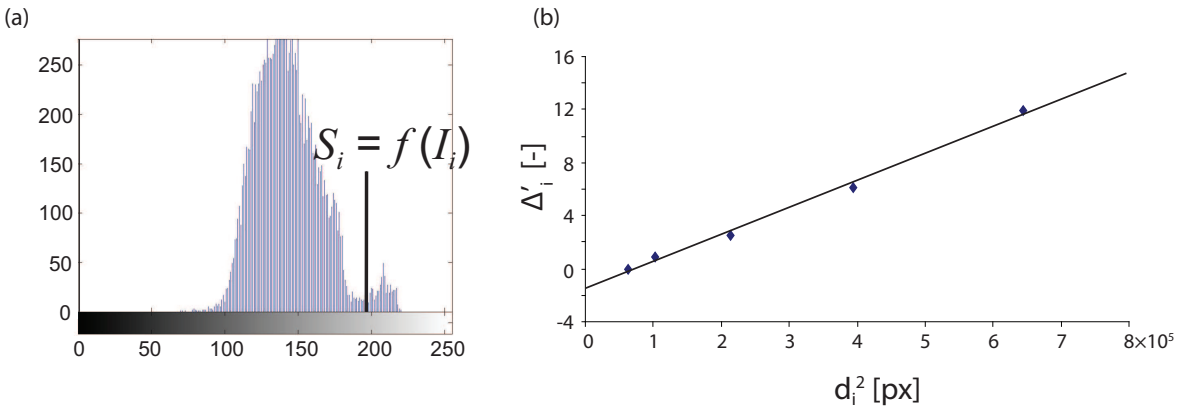


Figure 3.8: Example of the brightness histogram resulting from the analysis of a picture of Test 3B (a), and the variation of $\Delta = S - I$ as a function of the squared distance from the centre of the image (b). After Ranieri (2005).

For sediment bed images collected from Test 3A (where black medium sand was used as a tracer) histograms analysis did not allow the identification of a clear threshold frequency between higher and lower brightness levels due to the different response of black color to the artificial light and the presence of shadows producing low brightness levels for the grey fine sand. Brightness contrast was then enhanced with a filter reducing the lowest frequencies while maintaining the highest frequencies unaltered. Filtered images were subsequently converted into specular images where black and white pixels were inverted. For this test the *white* data actually denoted the fraction of bed area consisting of black medium sand (Figure 3.9).

Volumetric tracer concentrations were estimated from conversion of surface areal percentages obtained from image analysis as, among areal sampling techniques, photographic analysis is one of the least intrusive. The bed surface material composition was initially measured as

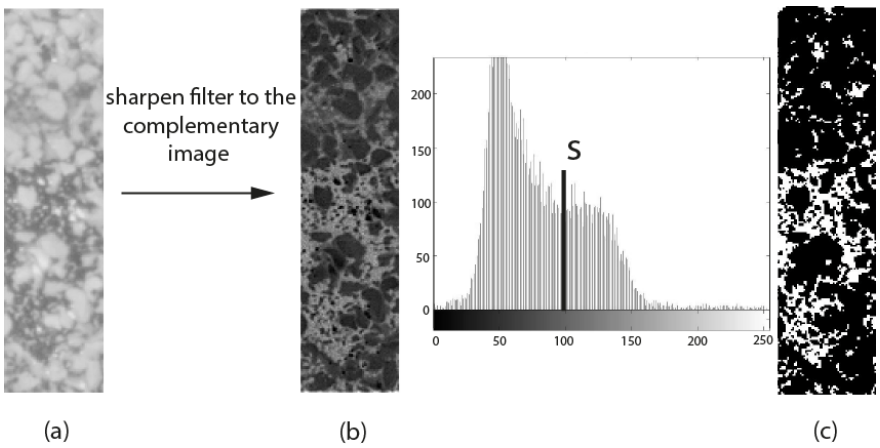


Figure 3.9: Sub-area of an image from Test 3A in grey-scale color (a), complementary image after filter application (b), black and white image after application of frequency threshold $S$ (c). The tracing black medium sand is eventually identified by white pixels. After Ranieri (2005).

the area covered by each fraction (i.e. surface by area $s$-$a$). This was then converted to percentages of area by weight ($a$-$w$) and finally to volume by weight ($v$-$w$) following the conversion model presented by Marion and Fraccarollo (1997b). This method overcomes the shortcoming of previous exponential conversion formulas (Kellerhals and Bray, 1971; Proffit, 1980; Diplas and Sutherland, 1988) as it is based on known statistical properties of sediment mixtures. For each grain size $i$ the volume-by-weight, $p_i^{v-w}$, is correlated to the area-by-weight, $p_i^{a-w}$, introducing a correction parameter for the sampling depth $D_s$:

$$p_i^{v-w} = \frac{p_i^{a-w}(1-p_{v,0})}{(D_s + d_i/2)\sum_{j=1}^{N} \frac{p_j^{a-w}}{(D_s+d_j/2)}}, \tag{3.18}$$

where $p_{v,0}$ denotes the void ratio, $d_i$ the diameter of grain size $i$. The ratio between volumetric and weight concentrations is then assumed proportional to $d_i^x$ with $x$ depending on the presence of voids, the type of wax in case of wax sampling and its penetration depth $D_s$, and the relative size of the sediment to $D_s$. In case of photographic sampling the sampling depth is $D_s = 0$ and the exponent $x = -1$ according to Kellerhals and Bray (1971). The application of this conversion model allowed the variation of the fraction by volume occupied by the white gravel in tests 1 and 3B, and black medium sand in test 3A along the flume with time to be obtained.

## 3.3 Comparison between tracer tests and numerical simulations

### 3.3.1 Experimental tracers' concentration

Figure 3.10 presents the experimental tracer concentrations obtained from the bimodal Test 1 with white tracing gravel, while Figure 3.11 and 3.12 report concentration curves for the trimodal tracer Tests 3A and 3B, respectively. The measurement data scatter originating from the intermittent transport dynamics affected the smoothness of the concentration curves, resulting in irregular shapes of tracer concentration curves particularly for the case of black medium sand. Despite these large local fluctuations, a clear pattern emerges showing that tracers are advected downstream and simultaneously spread over the flume length. The extent of diffusion is more pronounced and symmetrically distributed for the medium sand tracer used in the trimodal mixture (Test 3A).

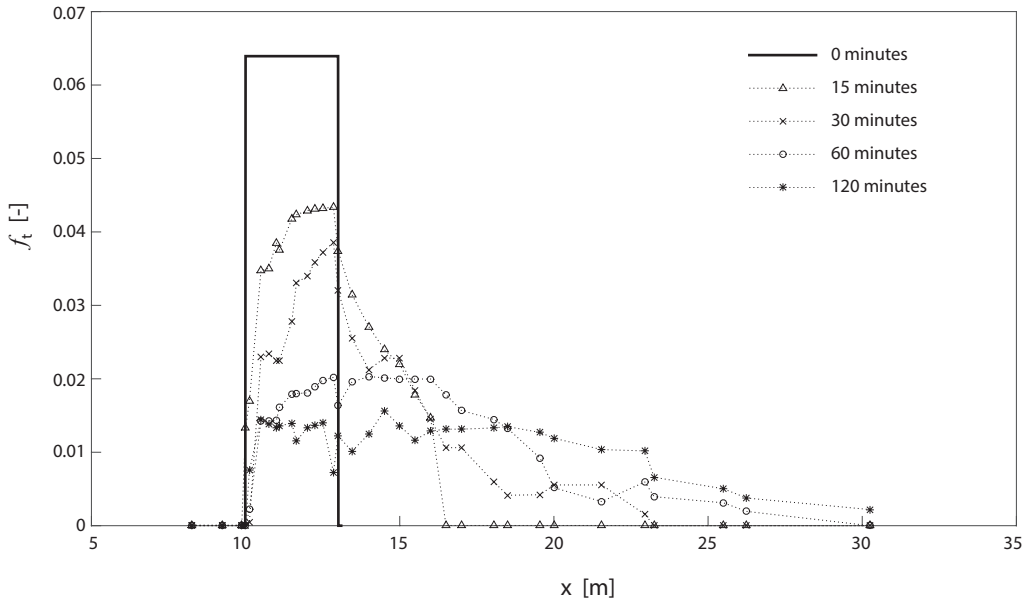


Figure 3.10: Volume-by-weight fractions of white gravel at different times along the streamwise direction (Test 1).

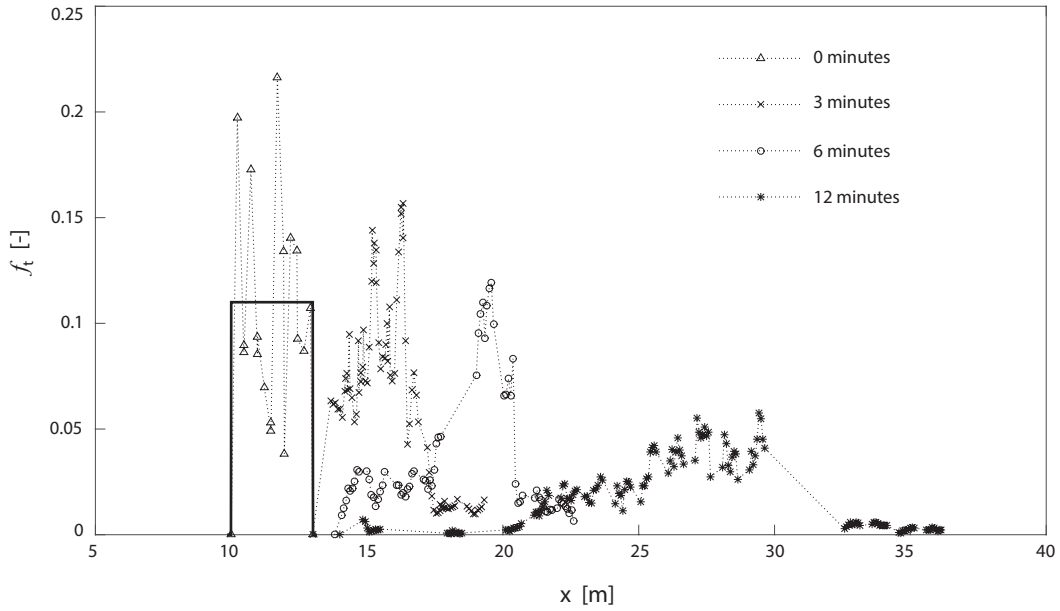


Figure 3.11: Volume-by-weight fractions of medium black sand at different times along the streamwise direction (Test 3A).

The motion of white gravel in the bimodal bed rather features two distinguished patterns: a moving forward front that diffuses faster, and a backward component that after 4-hour running test hardly leaves the area of the initial plateau injection. The effect of bed roughness elements is clearly apparent from comparison of the two tests with tracing gravel (Test 1 and 3B, respectively), which is found to move differently depending on sand content. In the bimodal experiment, characterized by a larger gravel fraction and representative grain size $d_{50} = 4.1$ mm, gravel tracers advected more slowly and only partially diffused, reaching downstream positions

after longer times than for the trimodal test, where the $d_{50} = 1.02$ mm. Direct observations from Test 3B also revealed that the damping of bed elevation fluctuations due to a higher sand content enhanced the mobility of coarse material.

The model, represented by Equation 3.15, proposes a description of these observed processes by formulating sediment transport in terms of tracing particles displacement characteristics, i.e. the longitudinal step length, and including an adjustment factor to simulate the influence of bed roughness.

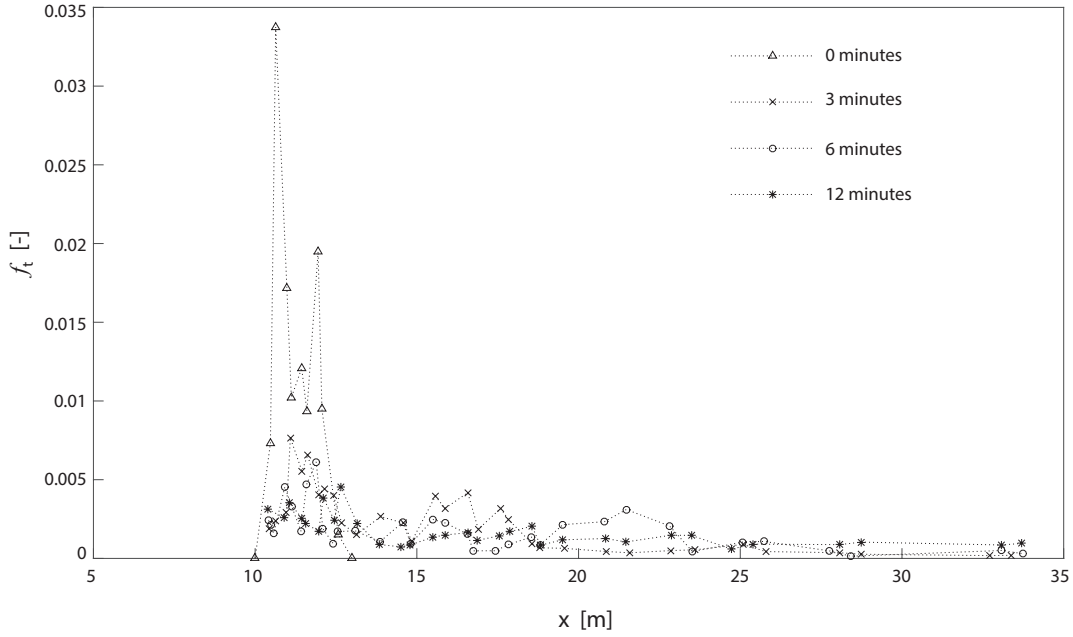


Figure 3.12: Volume-by-weight fractions of white gravel at different times along the streamwise direction (Test 3B).

### 3.3.2 Simulation of bimodal test: white gravel

For the bimodal mixture experiment (Test 1) Eq. 3.15 was solved using a grid with spatial resolution 0.008 m (i.e., twice the mean grain size of the sediment deposit) and temporal resolution 10 s, resulting in simulations of concentration curves over time for a total duration of two hours. The sediment matrix is identified by mean diameter $d_{50} = 4.1$mm whilst the mean size of the tracing gravel is $d_T = 4.9$ mm (Table 3.3). Eq. (3.15) is formally subject to the initial condition $f_t(a < x < b, t = 0) = 0.064$, with $a = 10.0$ m and $b = 13.0$ m, representing the initial volumetric fraction of white gravel, which is assumed to be uniformly distributed along the replacement section. In this experiment the shear velocity $u^* = 0.055$ m/s was selected to achieve values of the Shields parameter $\tau^*$ for the gravel material that were close to the threshold of incipient motion, such that conditions of fully mobility were never attained, and the proportion of mobilized gravel was approximately $Y_g = 0.13$. The total volumetric entrainment rate yielded by the sum of the fractional rates for the two sizes calculated with Eq. 3.16 is $E_b = 4 \cdot 10^{-6}$ m$^3$/m$^2$s. Under these experimental conditions the estimated fluid velocity at an elevation of $0.30d_{50} = 1.23$ mm from the mean bed surface approximates the ensemble gravel tracers velocity $v_p = 0.06$ m/s.

During Test 1 the replacement mixture embedding the white gravel tracers was inserted without being previously exposed to flowing water. For this reason the tracer concentration measured at $t = 15$ min was selected as the initial condition replacing the plateau-like approximation previously defined. From direct observations of sediment motion and subsequent image

analysis it was apparent that a significant fraction of tracers was hardly moved from their original position, possibly caused by the proximity to conditions of incipient motion for the coarse sediment. Due to the long duration of the bimodal experiment, the recirculated material was observed to appear at the upstream inlet of the flume. It was thus impossible to discriminate between the fraction of white material fed by the recirculation system and the initial replacement mixture still in place. These drawbacks resulted in modelled concentration curves for the bimodal mixture that are less accurate compared to those obtained for the medium sand in trimodal experiments (see next section). However, the key features of tracer concentrations are reasonably predicted by the model (see Figure 3.13). The relevant calibration parameters are mean step length $\mu_r = 0.58$ m and standard deviation $\sigma_r = 1.62$ m, which yield $\epsilon = 1.87$ and $k$= 2.8 as reported in Table 3.3.

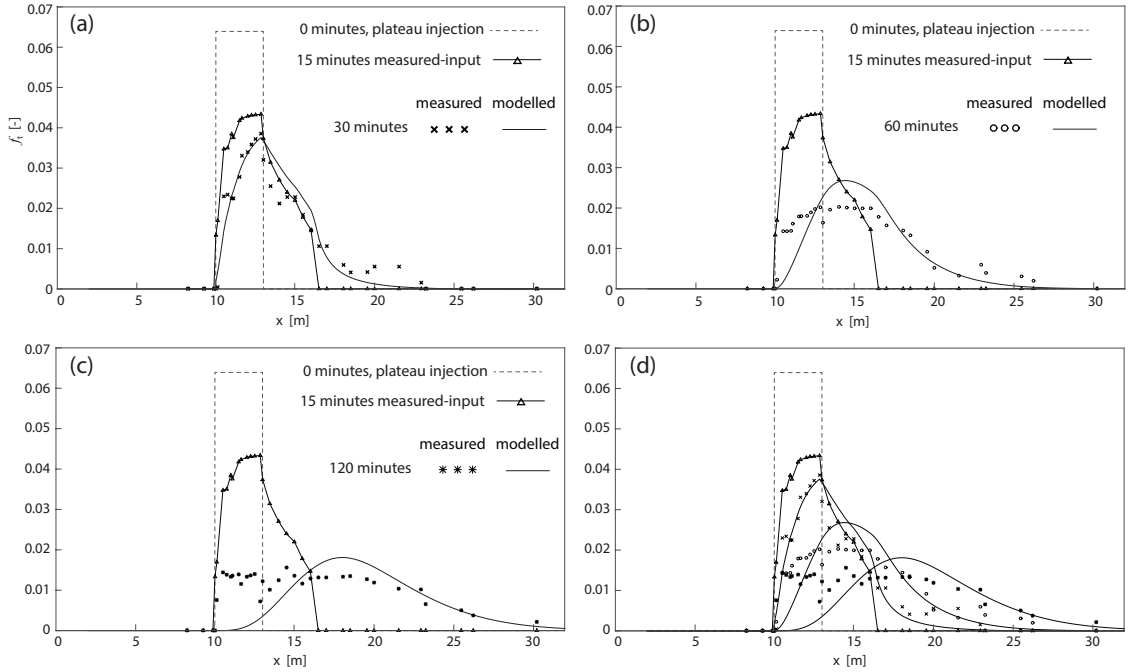


Figure 3.13: Concentration of white gravel with bimodal mixture (Test 1). Fitting curves are displayed at 30 (a), 60 (b) and 120 (c) minutes from the beginning of the experiment. Panel (d) summarizes all concentration curves.

### 3.3.3 Simulation of trimodal test: black medium sand

During Test 3A the sediment bed mixture had equivalent $d_{50} = 1.00$ mm, while the black medium sand tracer had mean size $d_T = 0.84$ mm. The concentration curves of tracers over time were obtained assuming an initial plateau concentration $f_t(a < x < b, t = 0) = 0.011$, corresponding to the black sand volumetric fraction embedded within the 3-m-long replacement material. In this experiment the time-averaged shear stress applied to the bed deposit was $\tau_0$ = 3.35 N/m$^2$, resulting in the shear velocity $u^* = 0.058$ m/s and values of Shields parameter above the threshold of motion for the tracing particles. Under these experimental conditions, the estimated ensemble tracer velocity is $v_p$= 0.07 m/s and the overall volumetric entrainment rate $E_b = 3.0 \cdot 10^{-5}$ m$^3$/m$^2$s, which results from the sum of the different grain size contributions as expressed in Eq. 3.16 with measured partial mobility of medium sand, $Y_s = 0.60$, estimated from image analysis.

Figure 3.14 shows the model outputs computed with Eq. 3.15 using a grid with spatial

resolution 0.01 m (i.e. 10 times the mean bed diameter $d_{50}$) and temporal resolution 1 s. The best fit is attained for values of mean step length $\mu_r = 0.32$ m and standard deviation $\sigma_r = 0.39$ m, which yields $k = 1.22$. Assuming a lognormal distribution (and the relevant multiplicative coefficient $g_1 = 355.75$) the roughness exponent $\epsilon$ is equal to 1.78, which is found to agree reasonably well with the value derived for the gravel tracers in the bimodal test. Comparison with experimental curves reveals large fluctuations of tracer concentration along the streamwise direction. Despite these highly scattered data measurements, advection and diffusion patterns of the black medium sand can be clearly identified and are reasonably predicted by the model.

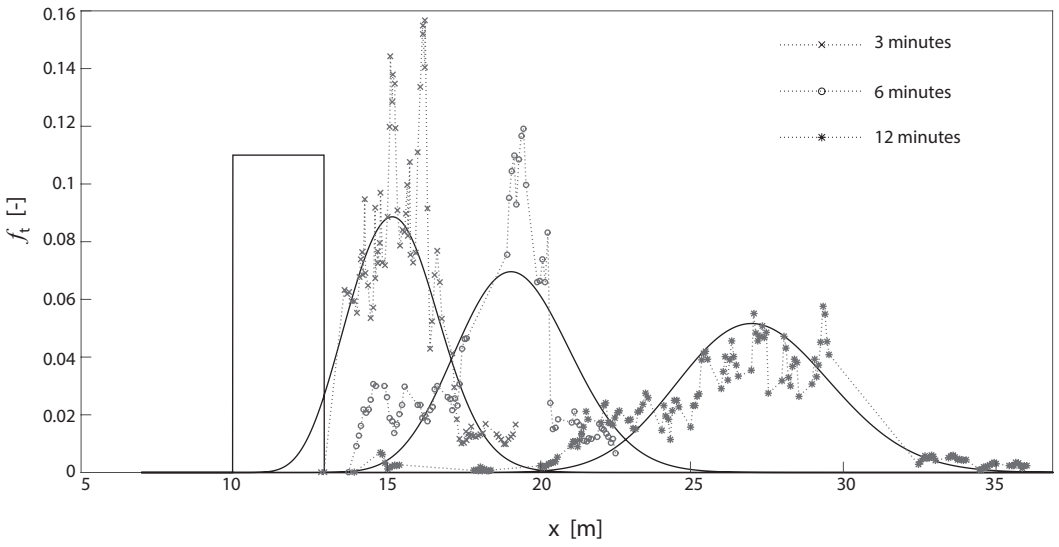


Figure 3.14: Concentration of black medium sand for the trimodal mixture (Test 3A). Measured concentration data (dotted line) and theoretical concentration curves (solid line) at 3, 6 and 12 minutes after sediment block replacement.

## 3.4 Discussion

The mass conservation model given by Equation 3.15 was calibrated using tracer concentration data from two of the three tracer tests, i.e. the bimodal Test 1 with gravel tracers and the trimodal Test 3A with medium sand tracers. Table 3.3 shows the calibration parameters used in the model for simulating Tests 1 and 3A. Values of $\epsilon$ are remarkably similar, while values of $k$ appear strongly influenced by the grain-size distribution. The data from the trimodal Test 3B was not used for calibration due to the observed patterns of the experimental tracer concentrations. Images during Test 3B were not collected fast enough to capture the evolution of the gravel transport, which happened to take place in the first few minutes. After only 3 minutes the gravel material had travelled the whole length of the flume resulting evenly spread in the last temporal sampling (12 minutes). Although the acquisition of images was insufficient in the first minutes of the experiment, the data from Test 3B is discussed here to provide an indirect validation of Eq. 3.13 that describes the statistics of the grains' step lengths. Equation 3.13 expresses the mean step length as a function of the squared shear velocity and the relative size of the moving particles to the standard deviation of the bed fluctuations.

Assuming an averaged $\epsilon = 1.83$ returns values of the mean step length for the case of gravel over a trimodal bed (Test 3B) up to approximately 8.5 m. This large value would account for the fast motion and rapid diffusion of gravel when the bed is rich in sand content and the

equivalent bed roughness is small compared to the size of coarse tracers. By comparison with the bimodal test, the size of gravel tracers in Test 3B was roughly five times larger than the $d_{50}$ ($d_T = 4.9$ mm and $d_{50} = 1.00$ mm), while the fraction in weight of gravel was halved. The gravel particles in the trimodal test are moving over an almost flat surface encountering a lesser number of obstacles along their path as the gravel content is reduced. The significant reduction of the relative bed elevation fluctuations is thus expected to dramatically enhance the mobility of the coarse material over a relatively flat sediment bed as accounted for by Eq. 3.13 which provided a large value of mean step length.

The composition of the sediment bed mixture is expected to affect the mode of transport by altering (i) the ensemble particle velocity as the presence of protruding bed elements reduce the velocity of the near-bed flow field (Nikora et al., 2001); (ii) the rate of particle entrainment depending on the fraction of fine material (Wilcock and Kenworthy, 2002); and (iii) the thickness of the active layer. This is confirmed by direct observations of the different transport patterns exhibited by the gravel material during the bimodal and trimodal experiments, respectively. In the bimodal experiment, where the sand content was 34%, gravel tracers took more than 2 hours to spread uniformly over the flume length, by advecting and diffusing at a slow rate compared with the grain motion tracked during the trimodal test. In this latter case the sand content was 65% and the same gravel material was observed to be uniformly distributed along the channel after a very short period of only 12 minutes even under similar hydraulic conditions (shear velocity $u^*$ is relatively close to the bimodal case, see Table 3.3).

Table 3.3: Model input parameters and calibration parameters.

| | Input parameters | | | | Calibration params. | |
|---|---|---|---|---|---|---|
| TEST | $d_{50}; d_T$ [mm] | $u^*$ [m/s] | $v_p$ [m/s] | $E_b$ [m$^3$/m$^2$s] | $\epsilon$ [-] | $k$ [-] |
| 1,white gravel | 4.10; 4.90 | 0.055 | 0.06 | $4.0{\cdot}10^{-6}$ | 1.87 | 2.80 |
| 3A,black medium sand | 1.00; 0.84 | 0.058 | 0.07 | $3.0{\cdot}10^{-5}$ | 1.78 | 1.22 |

Moreover the nature of the mixed size bed material influences the active layer, whose thickness depends on both the fluctuations of the local bed elevations and the mean diameter of the sediment deposit. The lower the fraction of fine material the deeper the surficial volume that constantly exchanges with the bed load and traps sediment within the bed substrate. In turn, particles that are stored in deeper regions of the active layer become less likely to be exposed to the flow and entrained into motion again.

In Section 3.1.3 the standard deviation of bed elevations, $\sigma_b$, and the depth of the active layer, $L_a$, are assumed to scale with the mean bed diameter as $\sigma_b = k_1 d_{50}$ and $L_a = k_2 d_{50}$ with $k_1 = 0.37$ and $k_2 = 0.60$. The sensitivity of the model to these parameters and the relevant effects on advection and diffusion patterns, are here investigated for different ratios of $d_T/d_{50}$ ranging from 0.4 to 2.0 (including $d_T/d_{50} = 0.8$ as in Test 3A). The experimental conditions of the trimodal Test 3A with black medium sand tracers are used as input parameters for simulating the transport of tracers with different relative sizes (with respect to the mean bed material), while varying the standard deviation of bed elevation and the thickness of the active layer. The dimensionless advection and diffusion coefficients, respectively $U_A$ and $E_D$, are estimated as:

$$U_A = \frac{\left(\frac{\overline{x}_{t+\Delta t} - \overline{x}_t}{\Delta t}\right)}{u^*} \tag{3.19}$$

$$E_D = \frac{\left(\frac{x^2{}_{t+\Delta t} - x^2{}_t}{\Delta t}\right)}{(u^* d_{50})}, \tag{3.20}$$

where over-barred $x$ and $x^2$ represent the first and the second order moments of tracer concentration curves at different times. Figure 3.15 shows that particles larger than the equivalent bed roughness steadily advect and diffuse more rapidly than fine particles as observed in these experiments. As the relative bed roughness increases (i.e., for larger $k_1$) the advection rate reduces and the extent of particle diffusion is restrained (Figure 3.15a, b) over the whole range of $d_T/d_{50}$, with a more pronounced effect in the case of coarse tracers (i.e., for larger $d_T/d_{50}$). Similarly, the depth of the active layer is found to be negatively correlated to particle advection and diffusion (i.e., both $U_A$ and $E_D$ reduce with increasing $k_2$) which agrees with the evidence that particles trapped within deeper regions of the bed take longer times to return to be exposed to the moving water (Figure 3.15c, d). This retention effect possibly explains the long-tailed concentration curves measured in the experiments with longer run times, Test 1. It is concluded that in these tests particles trapped within the bed were not able to readily reach the moving front, rather contributing to the bed load transport only after longer times when they were released from their rest positions.

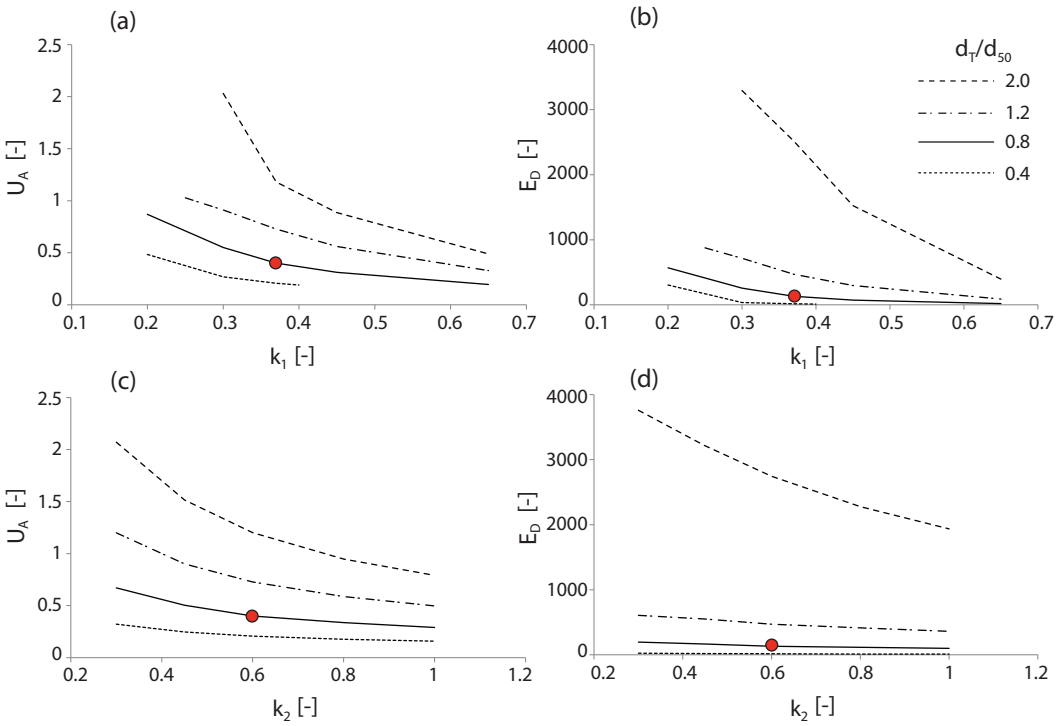


Figure 3.15: Effect of standard deviation of bed elevation (a, b) and active layer thickness (c, d) on dimensionless advection and diffusion coefficients. Simulations are reported for different ratios of $d_T/d_{50}$, i.e. 0.4, 0.8, 1.2 and 2. The red point indicates the data point of Test 3B.

## 3.5 Preliminary conclusions

A stochastic description of bedload particles step length was proposed. The descriptive statistics of particle step lengths were obtained from the analysis of existing dataset of high-speed particle tracking collected during two earlier independent experimental studies on bed load transport. It was then proposed that existing parameterizations of the mean step length of moving parti-

cles can be adjusted with a correction coefficient accounting for the effect of surface roughness elements in mixed sediment beds on grain step length distribution. The experimental PDF of grain step lengths was incorporated into the probabilistic Exner equation, which enabled the simulation of different advection and diffusion patterns of the naturally coloured tracers used in flume experiments with graded sediment deposits.

Data from three existing mobile bed experiments was used to calibrate and validate the probabilistic Exner equation. While for the medium sand tracers in the trimodal mixture numerical results fit well the observed transport features, in the case of gravel tracers in the bimodal deposit comparison between experimental and theoretical curves was less accurate. This was partially explained by the initial replacement of bed material with non-water worked tracer sediment which favours the formation of two distinguished advancing fronts with different transport patterns.

A major role is played by the presence of protruding bed roughness elements which affect the step length statistics and the depth of the exchanging surficial bed layer. The latter, known as the active layer, is supposed to be responsible for a main retention effect which delays the transport of trapped particles. Both experiments and model simulations suggest the existence of a significant retention process originating from the vertical diffusion of particles.

New experiments designed for tests over longer spatial and temporal scales with also the possibility to visualize the interaction of tracers with the different layers composing the bed are expected to provide quantitative evidence of this phenomenon. The use of sediment tracers in experiments where temporal and spatial sampling is no longer restricted would also offer the possibility of a complete statistical description of the particles' motion. The fully described parameters of motion, i.e. step length, travelling time and particles' velocity, generates the respective PDFs, which would then ensure that the statistical results were un-truncated. Such a comprehensive analysis can support the use of the integral equations 3.8 or 3.10 instead of the simplified version (3.15), leading to a general formulation of the mass conservation equation to bed-load sediment transport.

# Chapter 4

# Experimental work

The earlier chapters on the advection and diffusion of bed-load sediment indicated weaknesses in the previous analysis and highlighted the need for new experiments to investigate the interaction between the transported grains and the bed layers. While the application of the model based on the revised Exner's equation to the case of bed material requires the derivation of step lengths distributions, the conceptual model of diffusive regimes needs the continuous record of particles' displacements. Both step lengths and the three different motion ranges can be achieved via a continuous monitoring of grain positions. The tracking activity though should last long enough to obtain very stable statistics and to witness the vertical mixing of the sediment material. As the bed grains are free to move and interact with the deeper layers of the bed deposit, the tracing particles should be followed also within the bed volume and not only on the planar surface. Tracing grains buried underneath the bed surface should be accounted for as their contribution to the overall diffusive process may be substantial. A comprehensive view of the bed would help addressing the processes of grains interaction and retention.

The existing knowledge on sediment transport suggests that the motion is affected by the bed surface roughness. The roughness influence is also indicated by the different rates of diffusion that the tracers experienced in the bimodal and trimodal test presented before. To properly address the diffusive behaviour of bed load particles then the role played by the bed elevations and arrangement cannot be ignored.

The ability to study the effect of bed retention and surface influence on transport needs long time scale experiments. In the previously analysed data the timescale was of the order of minutes. The former analysis indicated that a timescale of hours was required. This cannot be achieved by the use of a conventional linear flume, however such timescales can be achieved via an annular flume, whose closed system allows long time scale experiments to be performed.

## 4.1 Experimental apparatus

The issues encountered in previous experiments, such as flume length, material/fluid recirculation and limited monitoring times, are here overcome by the use of an annular flume. The features of the annular flume are described in this section.

### 4.1.1 The annular flume

An annular flume consists of a circular lower channel which rotates independently of the top annular lid. In such flumes the flow is generated by the movement of the boundaries, i.e. the lower plate together with the walls, and the upper lid in contact with the water surface. The

annular flume can thus simulate a long length river, where the bed material and the fluid are not externally recirculated and a uniform shear stress is applied to the bed. This internal system enables sediment transport and bedforms to attain equilibrium and to perform experiments for much longer times than in linear flumes. Because of these characteristics, annular flumes have usually been intended to study cohesive sediment deposits (e.g. Graham et al., 1992; Krishnappan, 1993; Partheniades and Kennedy, 1996; James et al., 1996; Skafel and Krishanppan, 1999; Cantero et al., 2004), with few applications to bed-load transport (te Slaa, 2012).

Due to the curvature of the physical form of the apparatus, the formation of secondary currents is an inevitable consequence. The difference in the tangential flow velocities on the cross-section creates a complex 3D flow circulation. An extensive study carried out by Partheniades et al. (1966) and by Booij (1994) demonstrated that the generation of the secondary currents can be minimized by controlling the rotational speed of the top lid against the velocity of the lower plate. By imposing opposite velocities between the lid and the plate and adjusting them to the so called *optimal ratio* the secondary currents are counteracted and a quasi 2D flow can be assumed. When the flume is operated under this optimal condition, the circulating currents are minimized and the classical 2D erosion/deposition concepts can be applied. The derivation of the optimal ratio for the present flume is discussed in the following sections.

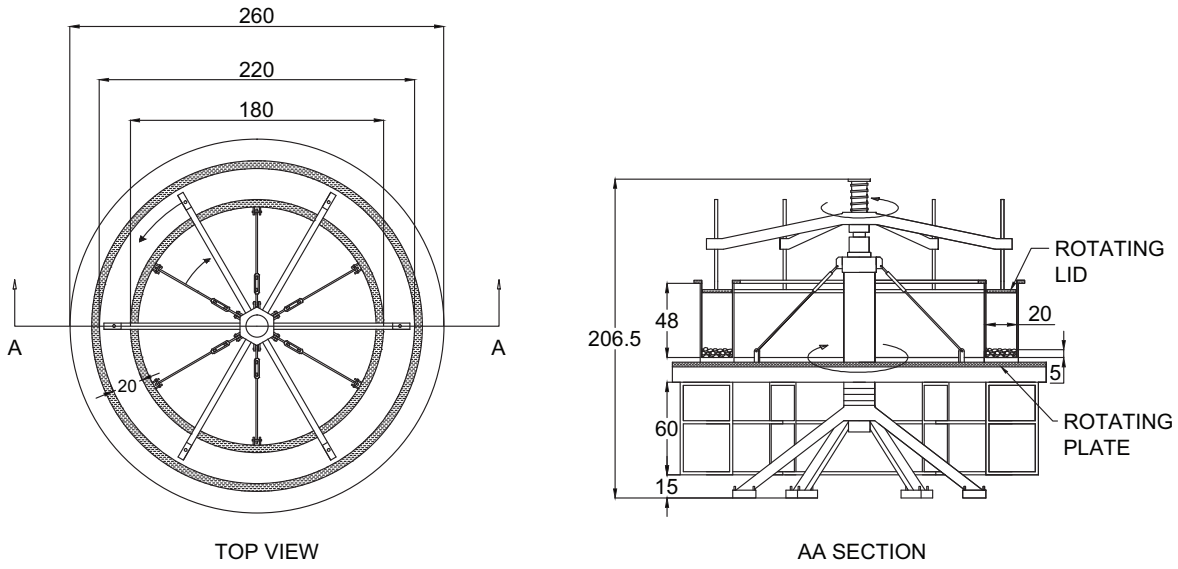


Figure 4.1: Top view of the annular flume together with the cross section along the line AA.

The experiments have been carried out in a rotating flume, whose construction started in 2013 and that was fully operative in September 2015. The external diameter is 2.20 m while the internal one measures 1.80 m, with mean diameter of 2.00 m. The flume presents a rectangular cross-section 0.20 m wide with a maximum available height of 0.48 m. A sketch of the flume is presented in Figure 4.1. The side walls and the bottom plate are made from cast poly-methyl methacrylate transparent sheet, also known as acrylic or acrylic glass, to allow for the flow and particle visualization. The lid, made of dark gray polyvinyl chloride (PVC), is divided into six sectors, one per each arm, which can be removed in order to access the channel (Figure 4.2). The lid can be manually lowered or lifted in order to set the desired water depth in the flume. A clearance of approximately 2 mm assures the absence of friction between the edge of the lid and the flume walls so that it can rotate smoothly.

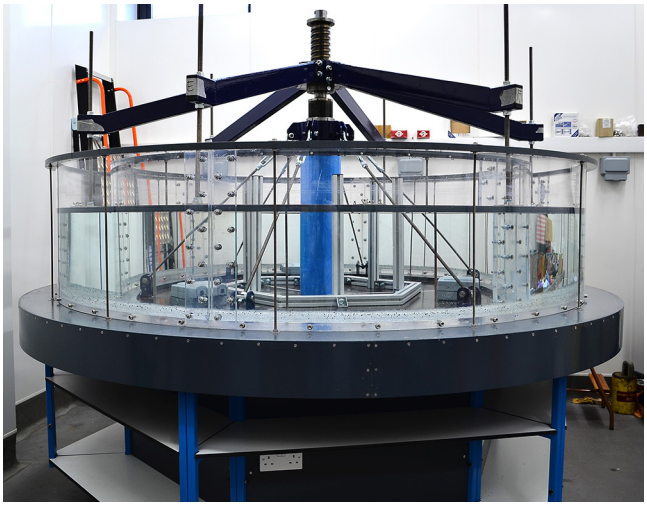

Figure 4.2: Picture of the annular flume with the lid lowered to the desired water depth.

The two units (lid and bottom plate) can be rotated independently as the carousel is operated by two motors. The first one runs the bottom plate together with the walls, whilst a central one spins the top arms connected to the lid. The motors speed is governed by a control setting panel, whose setting can vary between 0 and 10. A calibration test helped to convert the control panel setting into revolution per second for both motor units. The relationship obtained is presented in Figure 4.3 and it provided the following conversions:

$$\omega_{top} = 0.031 C_{top} - 0.0104 \tag{4.1}$$

$$\omega_{bottom} = 0.0125 C_{bottom} - 0.0038, \tag{4.2}$$

where $C$ denotes the control panel setting of the top and bottom motors respectively. The relationship derived between the controller settings, $C$, and the rotational speeds is linear, a handy conversion to use during the operational activity of the flume. The two parts of the flume are set into motion when knobs compute a quarter of rotation. With a minimum of 0 to a maximum of 10 switch rotations, the lid and bottom rotational speed range between, respectively, 0-0.31 rps and 0-0.12 rps. Although the use of switch rotation allows a great flexibility, the minimum increment of speed was set equal to 1/16 of switch rotation, which corresponds to an increase of 0.002 rps for the top unit and 0.0008 rps for the bottom plate. The motors resulted in very stable and reliable performance. The same relationship was found to stand throughout all the tests and the experiments carried out via repeated measurement.

The electrical power provided to the flume through a set of slip rings allowed the location of six main sockets on the internal horizontal plate. These sockets rotate together with the bottom plate and have been used to power the cameras of the image acquisition system.

### 4.1.2 Bed material

To observe particles' motion within the bed deposit, polished transparent glass spheres have been selected as granular bed material. Borosilicate glass was chosen among different glass types for its low index of refraction, i.e. 1.46. In fact, the refractive index of borosilicate glass is easily matched by a broad range of mineral oils and the first intentions were to replace water with oil. This would have ensured a clear vision of the bed deposit so that the coloured tracer particles could have been easily detected. Several tests demonstrated that a solution is provided by the off-the-shelf *Johnson's baby oil*. Baby oil is a clear mixture of mainly alkanes and cyclic

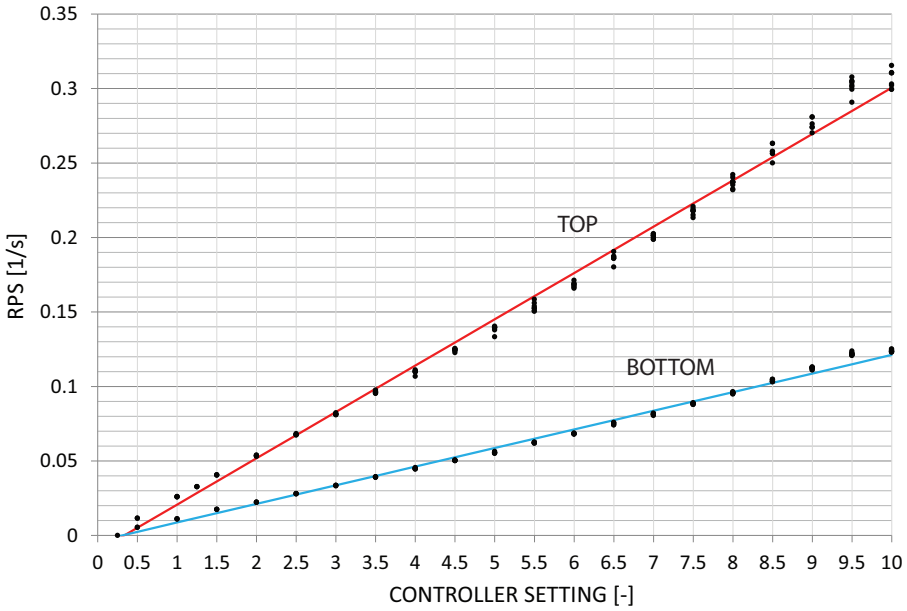


Figure 4.3: Relationship between the top and bottom rotational speeds and the controller settings, which is denoted by the numbers of motor-switch rotations.

paraffins whose index of refraction perfectly matches the one of borosilicate glass. One of the most important properties of the baby oil is its low viscosity together with its relative safety in laboratory environment, which makes it the most suitable solution for this kind of experiments. The baby oil behaves as a Newtonian fluid, whose viscosity is constant over a wide range of shear rates. A rheometer test showed that its dynamic viscosity at 20°C is about 30 times greater than water viscosity, i.e. $\mu_{oil} = 33$ mPas and $\mu_w = 1$ mPas. In the present case the large quantity of oil necessary to fill the annular flume (approximately 500 l) and the difficulty of cleaning and separating the spheres after each experiment made this solution impractical and forced to opt for water instead which still provided good optical properties.

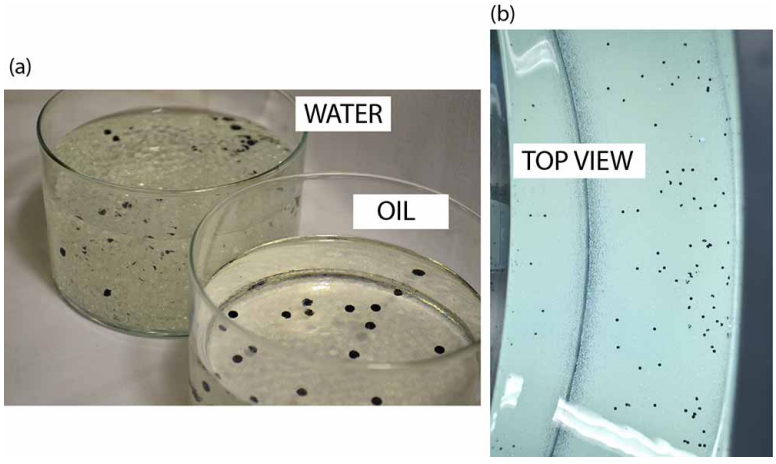


Figure 4.4: (a) Borosilicate spheres in water and baby oil. The black spheres appeared visible with the oil as the refractive indexes are matched. (b) Image of the flume bed taken at the end of an experiment from above. All the black tracers can be clearly detected.

The low index of refraction of the borosilicate glass could still represent an advantage as it is much closer to the water refractive index ($RI = 1.33$) than the one of normal glass ($RI = 1.52$).

The vision inside a deposit is not as clear as in the case of spheres immersed in oil but the results of feasibility tests showed to be quite promising (Figure 4.4). This was also confirmed during the preliminary annular flume tests. The shallow bed deposit (maximum 50 mm) and the maximum burial depth of tracers (10 mm) allowed to accurately spot all the tracer particles.

Another advantage of using the borosilicate spheres is that they came in a spherical shape with uncertainty. The production plant manufactured the beads with a diameter with a precision of $\pm 0.3$ mm, so that the material is more graded and not perfectly spherical. The density of glass spheres is 2230 kg/m$^3$, close to the typical density of natural gravel material, i.e. 2650 kg/m$^3$.

In order to recreate natural conditions, four sizes of particles were ordered: $d_1 = 2.5 \pm 0.3$ mm, $d_2 = 3 \pm 0.3$ mm, $d_3 = 4 \pm 0.3$ mm and $d_4 = 5 \pm 0.3$ mm. The poor precision of the manufactured spheres is a cost effective choice which, at the same time, enables us to have a more continuous granulometric curve as showed in Figure 4.5a. Every size of beads was used in the calibration process of the annular flume to assess the incipient motion conditions (see section 4.2.2). The different sizes were then mixed together in order to create two bed mixtures to test in the experiments: a coarse mix and a finer one.

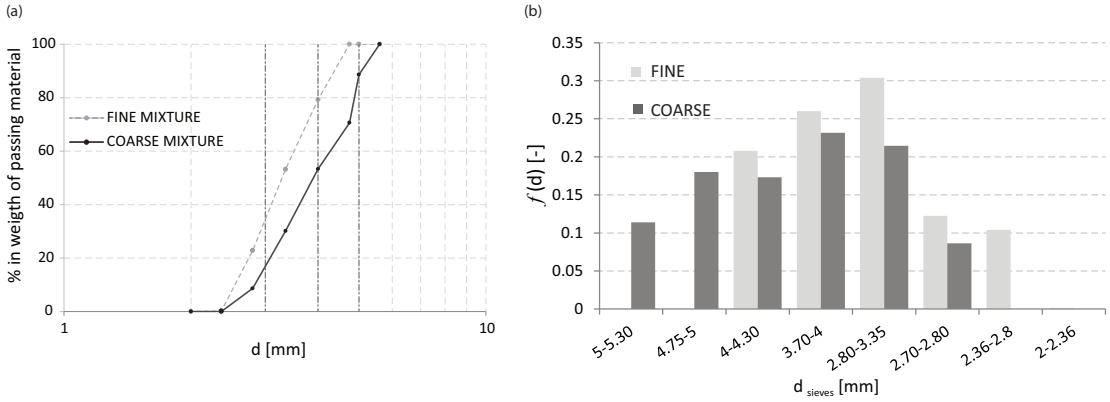


Figure 4.5: (a) Granulometric curve representing the percentage of the material passing a defined diameter for the fine and coarse mixture. Vertical lines indicate the sizes of the black tracers. (b) Distribution of grain sizes for the fine and the coarse mixture.

The coarse mixture consists of $d_2$, $d_3$ and $d_4$ spheres, with mean diameter $d_{50} = 4.1$ mm and standard deviation $\sigma_g = (d_{84}/d_{16})^{1/2} = 1.33$. The fine mixture is composed of $d_1$, $d_2$ and $d_3$ spheres, which is characterized by $d_{50} = 3.2$ mm and standard deviation $\sigma_g = 1.37$. The distribution of the grain sizes for the two mixtures shows a unimodal distribution peaked around $d_{50}$ (Figure 4.5b). The two mixture overall differ in size of 1 mm. Notwithstanding the limitations that stem from the use of spherical particles, the two varieties of mixture can contribute in assessing the influence of the bed roughness on grains movement.

In all the reported experiments, the bed deposit is created by manually mixing dry spheres together in the different component parts according to the required particle size distribution in order to ensure a random mix. The bed surface is then scrapped flat in order to make sure that no bedforms are present at the start of the test and the starting surface has a uniform surface roughness. Depending on the bed mixture, it is here considered appropriate to have a bed thickness of at least $10d_{50}$. In case of coarse mixtures the bed will be 45-50 mm thick, whilst for the fine mixture the maximum height is 35 mm.

Information on the grains motion is gathered by following the path of coloured tracers. Trac-

ers consist of black borosilicate glass spheres in the available size of 3.0, 4.0 and 4.7 mm. The spheres were directly manufactured in black so that the external surface resulted as being as polished as the one of transparent beads. The tracers' diameters have been considered representative of the main three sizes composing the bed deposit so that the tracers can be mixed up at the beginning of the experiments with the bed material.

Figure 4.6: Procedure of bed levelling by means of a spongy mop head 200 mm wide.

## 4.2 Calibration procedure

The particular configuration of a rotating flume makes it advantageous for long duration sediment transport studies. Due to the complexity of the generated flow field, however, a preliminary calibration phase proves to be necessary. In such flumes the flow is characterized by the geometry, such as the channel width, $b$, the water depth $H$, the average radius $R$, and by the rotational velocities of the lid $\omega_t$ and the bottom $\omega_b$. Based on these parameters different annular flumes can be compared together by a dimensional analysis. Similarity among flumes holds when these four dimensionless numbers are considered: (a) ratio of rotational velocities $\omega_t/\omega_b$, (b) aspect ratio $H/b$, (c) relative curvature $b/R$ and (d) the Reynolds number $\omega_b Rb/\nu$ with $\nu$ being the fluid kinematic viscosity.

Annular flumes are not as widely used as straight channels and this poses an additional difficulty when trying to make the flume operative. Two previous major studies can be considered for reference and guidance in obtaining the optimal flow conditions. The minimization of secondary currents was firstly tackled in the pioneering work from Partheniades (1966) who investigated the erosion and deposition of cohesive sediment with a rotating flume. In his work Partheniades demonstrated how the circulations could be reduced by running the lid and the bottom of the flume in opposite directions. The method when implemented to obtain the optimal flow conditions was improved with the subsequent works of Mehta and Partheniades (1973a,b). But it was only in 1994 when an extensive study of the tangential and radial velocity components was carried out. A carousel of 3.70 m diameter was used by Booij (1994) at the Delft University of Technology to measure the flow field over the cross-section of the channel. By varying the rotational velocity of the top and bottom plate for different aspect ratios he derived the optimal flow conditions that minimize the secondary currents and minimise the variation in the profile of the tangential velocity in proximity of the flume bed. These two studies constitute the basis upon which the calibration of the rotating flume at Sheffield is carried out.

Firstly the optimal flow conditions are attained for different water depths and bed roughness. Once the flume operates at the right settings, the use of different bed material allows the derivation of the critical bed shear stress as a function of the rotational velocities. With this

information it is eventually possible to reconstruct the vertical profile of the tangential velocity component along the centreline of the channel.

### 4.2.1 Optimal flow conditions

The difference in radius of the annular flume creates a velocity gradient on the cross-section. The velocity of the outer wall is greater than the one of the inner wall, so that the larger tangential velocities are near the outer part of the flume. This lack of uniformity in the tangential velocity profile is combined with the rotational velocity of the flume's moving parts. When the top lid spins in the opposite direction of the bottom plate we have the generation of secondary currents. The possibility of having two circulating flow cells (Sheng, 1989) found confirmation with the velocity measurements performed by Booij (1994). If only the top rotates, the upper cell would convect the tangential flow clockwise. On the contrary the flow is driven anti-clockwise by the lower cell when the bottom plate together with the sidewalls is the only moving part (Figure 4.7). As a result we have the formation of a complex 3D flow field which needs to be governed and minimized. The rotational velocities of the lid and the bottom play a fundamental role to attain the optimal conditions. They can be adjusted towards the so called optimal ratio, i.e. $\omega_{opt} = \omega_t/\omega_b$.

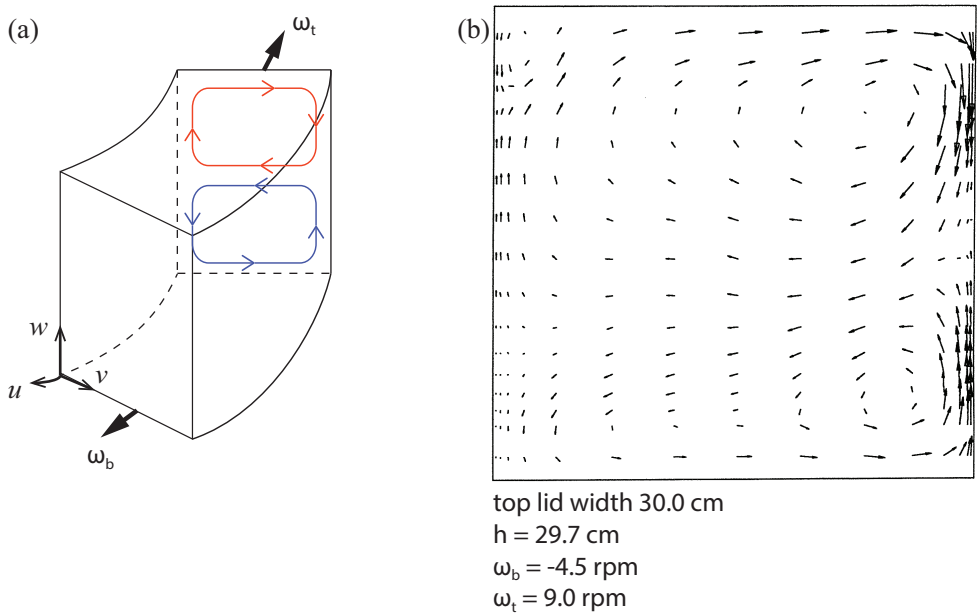


Figure 4.7: (a) Representation of the two flow cells. (b) Flow field measurements on the cross-section, after Booij (1994).

The accurate optimization of the rotational velocities can either aim to the minimal intensity of the secondary currents (first criterion) or to the uniformity in the tangential velocity component profile along the cross-section in proximity of the bed (second criterion). The two criteria applied by Booij (1994) to his annular flume showed no appreciable difference in the derived optimal ratios. In particular the second optimization resulted as the most difficult to obtain due to the broad variation of the optimum ratio. This allowed him to conclude that the attainment of the minimization of the secondary currents (first criterion) is good enough to also assume a uniform profile of the tangential velocity on the lower part of the channel. The uniformity of the velocity, and therefore also of the bed shear stress, is an important condition for sediment transport studies.

According to the first criterion, the formation of secondary currents is minimized by controlling the ratio of the rotating speed of the top lid, $\omega_t$, to that of the lower plate, $\omega_b$ (Partheniades, 1966; Booij, 1994; James et al., 1996; Gharabaghi et al., 2007). The determination of the optimal value of $\omega_t/\omega_b$ can be achieved by simply visualizing the displacements of plastic beads whose density is slightly larger than water (Partheniades, 1966). The size of the beads, in this study equal to 4 mm, is relative small compared to the boundary layer structure of the bottom. When the beads move along the centre line of the channel bottom the intensity of the secondary currents is minimal and a uniform distribution of tangential velocity and near-bed stress can also be assumed (Partheniades et al., 1966; Booij, 1994).

The application of this validated theory to the present flume provided a series of values of optimal ratio $\omega_t/\omega_b$ as a function of the water depth $H$ (Figure 4.8). $H$ was varied between 200 mm and 350 mm with incremental steps of about 25 mm for a total of 7 measurements. For every water depth the motion of the plastic beads was used to set the optimal conditions. In his work Booij presented a general formulation for the optimal ratio depending on the different relative magnitude of the two flow cells and the aspect ratio of the flume:

$$\frac{\omega_t}{\omega_b} = \frac{2(\lambda-1)\frac{H}{b} - \sqrt{\beta}}{2\lambda\frac{H}{b} + 1}, \tag{4.3}$$

with $H/b$ the aspect ratio of the flume, $\beta = 1 + 2(H/b)$ and $\lambda$ the constant in contact surface between the lower cell and the walls, i.e. $\lambda = c_\lambda(H/b)^{-1/2}$. The fitting of the optimal ratio to his experimental cases led him to consider $c_\lambda = 0.25$, which corresponds to the case of a lower cell that is in contact with approximately 1/4 of the sidewalls. The simplified linear relation resulted then:

$$\frac{\omega_t}{\omega_b} \simeq -f_{opt}\frac{H}{b}. \tag{4.4}$$

The above relation can be applied to the aspect ratios generally used with rotating flumes, i.e. $H/b = 0.5$-$2.0$ (Booij, 1994). $f_{opt}$ denotes a constant which was determined by Booij to be equal to 2.17 when trying to fit his experimental data and the optimal values derived by Karelse (1990). Good agreement is also found with the new measurements (Figure 4.8). The dependence of the optimal ratio on the dimensionless number $H/b$ is linear and the interpolation closely matches the simplified Booij's relation. The best fit is obtained when $\omega_t/\omega_b = -2.16(H/b)$. Even if the optimal conditions are derived by the visual inspection of the beads' motion, and therefore they are very dependent on the person's perception, the results correspondence with Booij's work supports this simple but effective method to determine the optimal ratio. The visual assessment was always carried out by more than one observer in order to have a set of values the optimal ratio could range in. For instance with a water depth of 325 mm, $\omega_{opt}$ ranged between -3.38 and -3.15, with averaged value of -3.24. The variability in the observed ratios is so small that the error bars associated to each measurement would be impossible to visualize in Figure 4.8.

Equation 4.4 was derived for the commonly used water depths in rotating flumes. When the aspect ratio is either small or large it is very difficult to indicate the optimal conditions as the pattern of the secondary currents shows more irregularities (Booij, 1994). Equation 4.3 still holds but the constant $c_\lambda$ can no longer be considered equal to 0.25. The influence of the aspect ratio is shown also with the present results. For shallower flows ($H/b = 1$, $H = 200$ mm) the optimal ratio is not aligned with the other measurements. Likewise when the water depth exceeds the 320 mm ($H/b = 1.63$). For these reasons it is convenient to range the water depth in this rotating flume between 230 and 300 mm, far from the two irregular flow conditions. A reasonable value of 300 mm has been designated as the operational water depth for all the

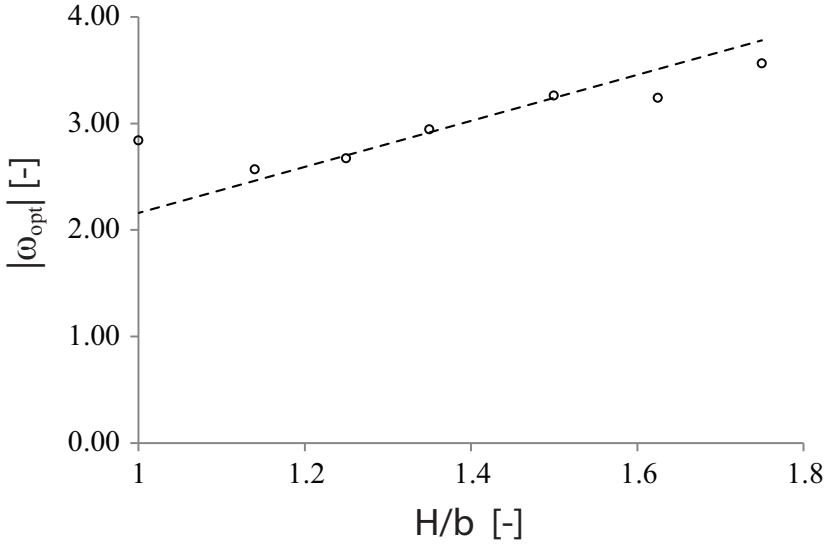


Figure 4.8: Derivation of optimal ratio as a function of the aspect ratio with observations for the present flume.

following tests and experiments.

### 4.2.2 Bed shear stress

Since annular flumes are usually intended to study the erosion and deposition of bed material, an accurate derivation of the applied bed shear stress is necessary. The purpose of this calibration is to determine the bed shear stress given the rotational velocity of the flume. Recalling the study of Booij (1994), the law of the wall can be used to estimate the frictional velocity $u^*$:

$$\frac{u_{av} - u_\omega}{u^*} \simeq \frac{1}{\kappa} ln\left(\frac{\delta t}{a_0}\right), \tag{4.5}$$

where $u_{av}$ is the tangential flow velocity component along the central region of the flume, $u_\omega$ is the base/wall velocity ($= \omega_b R$), $u^*$ is the shear velocity, $\kappa$ the Von Kármán constant, $\delta t$ the thickness of the turbulent boundary layer along the wall and $a_0$ the roughness length. The term on the right side of the above equation was indicated as a constant value, $c_t$, and assumed equal to 25 in Booij's work (1994).

For rotating flumes with small $b/R$, such as Booij's flume ($b/R = 0.16$) and the current channel ($b/R = 0.20$), it is possible to estimate the tangential flow velocity in the central region of the bed channel (Booij, 1994) as follow:

$$u_{av} = \omega_t R \frac{1}{1+\sqrt{\beta}} - \omega_b R \frac{\sqrt{\beta}}{1+\sqrt{\beta}}. \tag{4.6}$$

The constant $\beta$ denotes the ratio of the surface area of the flume over the surface area of the lid, $(b+2H)/b$. A comparison between the estimated velocity values (Eq. 4.6) and the velocity measurements with a laser-Doppler velocimeter suggested that the expression (4.6) provides a good estimation of the tangential velocity on the central region (Booij, 1994). The shear velocity calculated with equation (4.5) assuming the estimated values of $u_{av}$ (from Eq. 4.6) can then be used to derive the shear stress applied on the bottom of the channel, i.e. $\tau = \rho|u^*|u^*$ with $\rho$ the fluid density. Again this method to estimate the shear stress provided satisfactory results when

compared to the actual stress measurements in particular around the optimal conditions (Booij, 1994).

Combining equations 4.5 and 4.6, the shear stress acting on the bottom of the flume can thus be expressed as a function of the angular speed of the bottom, the optimal velocity ratio $\omega_{opt}$, the fluid density $\rho$, and the constant $c_t$ as follow:

$$\tau_{bed} = \rho \left[ \frac{\left( \frac{R\omega_b}{1+\sqrt{\beta}} \left( -1 + \omega_{opt} \right) \right)}{c_t} \right]^2 . \tag{4.7}$$

This expression is only theoretical and it requires validation from experimental measurements. The different geometry of the current flume and Booij's carousel makes it necessary to prove the goodness of this relation especially for the estimation of the constant $c_t$.

To confirm the quadratic increase of the bed shear stress with the rotating velocity of the flume, four sizes of bed material have been tested. All of them consisted of the existing transparent borosilicate glass spheres. Each class of material, corresponding to $d_1 = 2.5 \pm 0.3$ mm, $d_2 = 3.0 \pm 0.3$ mm, $d_3 = 4.0 \pm 0.3$ mm, $d_4 = 5.0 \pm 0.3$ mm as presented in the section 4.1.2, was sieved to reduce the variability so that a more uniform size distribution could be tested at each time. In doing so the material available to fill the entire flume length was reduced and a shallow bed of 15 mm was created with the remaining material of every class. This layer consisted of at least 3 particles' diameters assuring the presence of spheres also in eroded areas. The four available sizes are presented in Table 4.1 along with the theoretical critical stress for the incipient motion condition.

The threshold for each particle size distribution has been calculated with the van Rijn's expression for the Shields' diagram. To estimate the critical shear stress the dimensionless particle diameter $D^*$ is determined as follow:

$$D^* = \left[ \frac{(s-1)\, g}{\nu^2} \right]^{1/3} d_{50}, \tag{4.8}$$

where $s$ denotes the relative density $\rho_s/\rho$ being $\rho_s$ the density of the spheres, $g$ the gravity acceleration, $\nu$ the fluid kinematic viscosity, and $d_{50}$ the spheres mean diameter. The dimensional diameter allows the derivation of the Shields' parameter, $\tau^*$ (van Rjin, 1984). It is then possible to calculate the bed shear stress $\tau_{cr}$ as:

$$\tau_{cr} = \tau^* \left( \rho_s - \rho \right) g d_{50}. \tag{4.9}$$

The tests were carried out for each particle size, first minimizing the secondary currents by the adjustment of the ratio of top and bottom speed, and, secondly, attaining to the threshold of motion for that particular size of material. Plastic beads slightly denser than water were located on the top of a 15 mm erodible bed of glass spheres. The water depth was set to 300 mm on top of the glass material. The velocity of the lid and the bottom of the flume were slowly increased in order to move the plastic beads and the ratio of the velocities was adjusted to allow the beads moving along the centre line of the static bed. An increase in the lid angular velocity drives the beads towards the inner wall, whilst an increase of the bottom velocity convects the plastic beads outside. Once the optimal ratio of the rotating speeds had been achieved, the velocities were further increased to yield the incipient motion of the glass spheres always keeping constant the optimal ratio. The threshold conditions were determined by visual inspection of the spheres motion. It is here considered that the threshold is reached when there is net motion of the

bed material, even if single particles travel intermittently, according to the definition of *weak* transport given by Kramer (1932, 1935). As its assessment depends on the personal perception of motion, the evaluation was always undertaken by more than a single person. The error bars in the Figure 4.9 represent the spectrum of variability in the assessment obtained by several observers.

Table 4.1: Size range, mean diameter, Reynolds particle number, dimensionless particles' diameter, Shields' parameter and critical bed stress for each bed material used in the calibration tests.

| Size range [mm] | $d_{50}$ [m] | $Re_p$ [-] | $D^*$ [-] | $\tau^*$ [-] | $\tau_{cr}$ [Pa] |
|---|---|---|---|---|---|
| 2.20-2.80 | 0.0025 | 89.1 | 57.34 | 0.042 | 1.27 |
| 2.80-3.25 | 0.0030 | 120.2 | 68.81 | 0.044 | 1.60 |
| 4.00-4.30 | 0.0041 | 200.9 | 94.04 | 0.049 | 2.40 |
| 5.00-5.30 | 0.0051 | 287.7 | 116.98 | 0.052 | 3.18 |

Table 4.2: Angular speed of the top and bottom at incipient motion conditions. The optimal ratio is also reported.

| $d_{50}$ [m] | $\omega_t$ [rad/s] | $\omega_b$ [rad/s] | $\lvert\omega_{opt}\rvert$ [-] |
|---|---|---|---|
| 0.0025 | 1.19 | 0.33 | 3.64 |
| 0.0030 | 1.33 | 0.36 | 3.72 |
| 0.0041 | 1.54 | 0.42 | 3.70 |
| 0.0051 | 1.72 | 0.45 | 3.86 |

Table 4.2 reports the values of the lid and bottom rotational velocities for the four sizes at the incipient motion conditions. The optimal ratios derived for each test show a linear growth with the mean bed diameter $d_{50}$ (Figure 4.9). The linear relationship was obtained by including also the optimal ratio derived for water only ($H = 300$ mm). In the latter case the mean diameter is equal to zero as the bed consisted of smooth acrylic glass. The results report also the estimation of the incipient conditions from the tests with mixed material (coarse, $d_{50} = 4.1$ mm, and fine, $d_{50} = 3.2$ mm) which were carried out in a successive phase. These values well agree with the linear fit, thus confirming the goodness of the method. The linear interpolation provided the following relation between the optimal ratio and the mean grain diameter:

$$\omega_{opt} = 0.114 d_{50} + 3.31. \tag{4.10}$$

The increase in the bed roughness is counterbalanced by a larger difference between top and bottom rotational speeds and, consequently, by greater optimal ratios. As the flow is not accelerated, the shear velocity applied on the top and bottom surfaces should be the same. Beds consisting of larger grains are mobilized by larger values of fluid shear velocity, hence larger values of $u^*$ applied on the sediment surface. To obtain the corresponding value of shear velocity also on the top surface in contact with water, the rotational velocity of the lid has to be increased. If the experimental data referring to the smooth acrylic surface is removed from the linear fitting of Figure 4.9, it can be noticed that the optimal ratio associated to the different rough beds is approximately constant. This consideration stems from the restrained variability of the available spheres' sizes used in the calibration tests (Table 4.2), which can be mobilized over a relatively small range of bed shear velocities.

For every class of material, the test was running for approximately 30 minutes after the

realization of incipient motion, in order to study the evolution of the bed. If the optimal ratio of the top and bottom speed were not correct, there should be an accumulation of glass spheres towards the inner or the outer part of the flume. Nor preferential accumulation or degradation close to the inner and outer wall was observed, confirming the accuracy of the calibration technique. After 30 minutes under these rotational velocities the bed was maintained fairly flat suggesting that the radial distribution of bed shear stress was correctly determined.

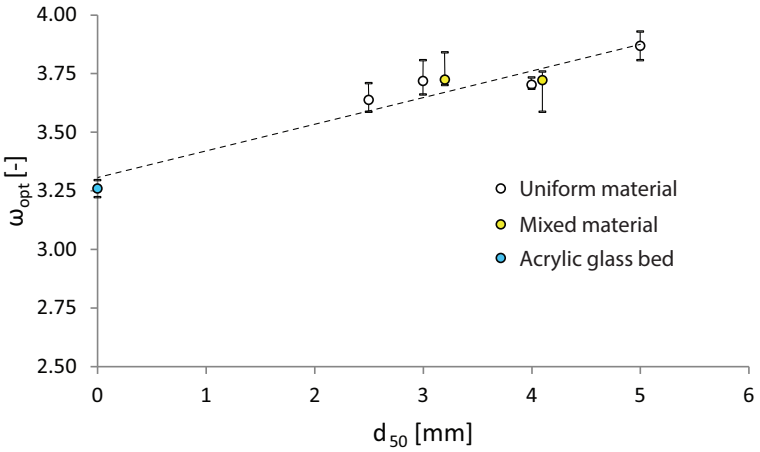


Figure 4.9: Optimal ratio as a function of the mean diameter for the four classes of single size material, the smooth Perspex bed and the two mixtures.

The critical bed shear stress obtained with the application of the Shields-van Rijn diagram has been compared to the theoretical bed shear stress formulation presented by Booij (1994) in Equation 4.7. For each particle size the incipient motion conditions correspond to defined values of top and bottom velocities. The procedure of minimizing secondary currents provided the optimal ratio of the rotational speeds of the lid and the base. These values, i.e. $\omega_b$, $\omega_t$ and $\omega_{opt}$, allow the determination of the tangential velocity in the central region of the flume, $u_{av}$, and then the critical bed shear stress using Equation 4.7.

As the optimal ratio does not broadly vary among the different classes of bed material, an initial average value of -3.73 was assumed. At first attempt $c_t$ was imposed equal to 25 as suggested by Booij (1994). In this case the observed values of bed shear stress calculated with the Shields' diagram are not matched by the quadratic relationship with the angular bottom speed. The trend however seems to be similar (dashed line in Figure 4.10).

The best fit was obtained varying the constant $c_t$, with a procedure of minimization of errors. The constant $c_t$ resulted equal to 13.3 (black line in Figure 4.10). This fit is an averaged result as a constant optimal ratio is assumed for all the four uniform sizes. If the curves are derived by imposing the correct $\omega_{opt}$ derived for each class of particles, $c_t$ is observed to vary between 12.7 and 14.1 (grey lines in Figure 4.10). The solution was then confirmed by the data collected from the tests with the fine and coarse mixture as can be seen in Figure 4.10. The quadratic increase of the shear stress as a function of the bottom speed can be appreciated for the tests with similar optimal ratio, namely $d_{50} = 3.2$ mm, 4.1 mm and 4.1 mm mixed material. In this case the optimal ratios are close to -3.71 and to an increase in bed roughness corresponds a greater shear stress which grows along the curve with $c_t = 13.3$.

The scatter between the best fit and the point measurements can stem from several factors. Firstly, one can argue the calculation of the critical shear stress via the Shields-van Rijn method

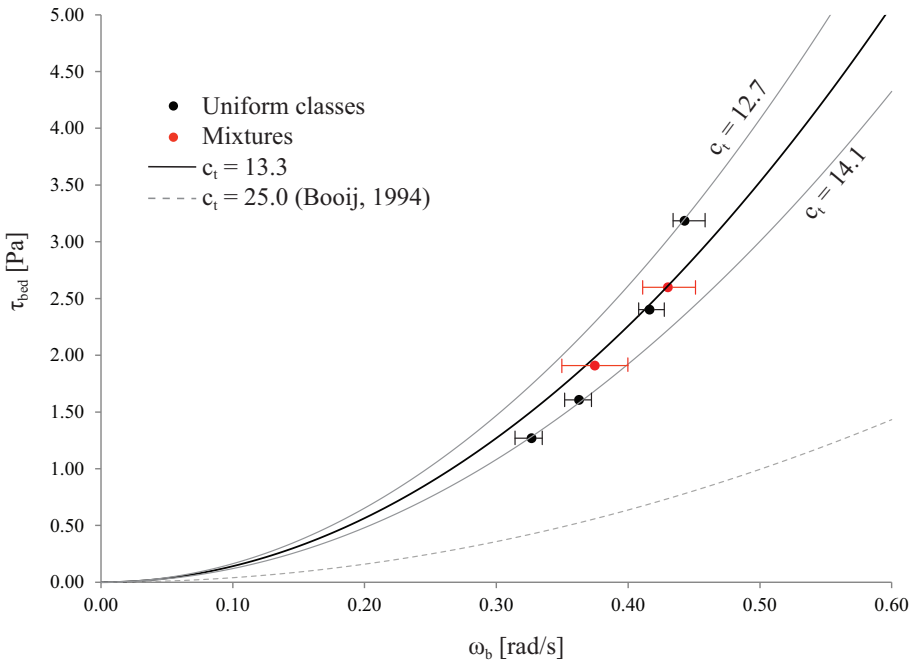


Figure 4.10: Calibration of the bed shear stress as expressed in the form of Equation 4.7. The figure shows the averaged fit for the four granulometric classes, continuous black line, and the lower and upper boundary of its variation (continuous grey lines). The original trend with $c_t = 25$ from Booij (1994) is denoted by the dashed grey line. The circles represent the calculated values of the critical shear stress via the Shields-van Rijn diagram for the four uniform classes in black and for the two mixtures in red.

has uncertainty. The incipient motion condition can vary over a range of values, being it a stochastic variable rather than a deterministic threshold (Grass, 1970; Buffington, 1999). Secondly, the system is affected by errors due to the estimation of the optimal flow conditions with plastic beads as this criterion provides a range of optimal ratios. These ratios depend also on the type of bed roughness as shown in Figure 4.9, instead an averaged value was here considered (black line, Figure 4.10). The empirical evaluation of the incipient motion conditions as well is affected by uncertainties related to the operators' sensitivity. For this reason in Figure 4.10 the error bars report the minimum and maximum value of bottom rotational velocities associated to the evaluation of incipient conditions by different persons. The errors do not include all the listed factors but they help giving an idea of the range of possible values. By acknowledging this, it is reasonable to expect a scatter between the estimated shear stress and the averaged fitted curve.

The relationship used here was obtained by Booij from actual measurements of the flow field with a Laser Doppler Velocimetry (LDV) in his flume. The expected growth of the shear stress with the bottom velocity found confirmation so that the theoretical formulation of the bottom stresses (Eq. 4.5) is assumed valid. The resulting smaller constant $c_t$ can be a direct consequence of the slightly different configuration of this rotating flume and Booij's flume. As the complete similarity no longer holds, especially for the rotational velocities and the aspect ratio, $c_t$ is expected to change too. A decrease in the constant $c_t$ is related to an increase in the roughness length $a_0$, which in turn corresponds to larger wall shear stresses. According to Booij (1994), this has to be compensated with greater rotational velocity of the top part yielding to larger values of the optimal ratios. The optimal ratios obtained with the present flume are indeed slightly larger than the ones observed by Booij, which range between 1.6 and

3.0 for different aspect ratios and rotational velocities. However the optimal values found fair agreement with the results presented by other researchers (Mehta and Partheniades, 1973a,b; Karelse, 1990).

### 4.2.3 Vertical velocity profile and operational optimization

The study of the incipient motion for different sizes of bed material allows also the estimation of the vertical profile of the tangential velocity component, $u$, along the centreline of the flume. The two boundaries, top lid and bottom walls, rotate with different velocities and are characterized by two distinct types of roughness. While the bottom roughness coefficient can be evaluated by knowing the distribution of the bed material, the PVC lid's roughness requires estimation. The vertical velocity profile, from the bottom and from the lid, has been assumed to follow the classic logarithmic profile with the same shear velocity, $u^*$, but different roughness length, $k_s$. For continuity, these two profiles will meet at a certain height of the flume, $z_1$, where they are denoted by also equal first derivatives. Figure 4.11 describes the conceptual model, which can be summarized as follow:

$$\begin{cases} u = -\omega_b R, & 0 \leq z < h_s \\ u = u_b = -\omega_b R + \frac{u^*}{\kappa} ln\left(\frac{z-h_s}{k_{sb}}\right), & h_s \leq z < z_1 \\ u = u_t = \omega_t R - \frac{u^*}{\kappa} ln\left(\frac{H+h_s-z}{k_{st}}\right), & z_1 \leq z < H + h_s \\ u = \omega_t R, & z = H + h_s \end{cases} \tag{4.11}$$

with $z$ being the vertical coordinate, $k_{sb}$ and $k_{st}$ the roughness length of respectively the bottom and the top of the carousel, $h_s$ the sediment deposit thickness and $H$ the water depth.

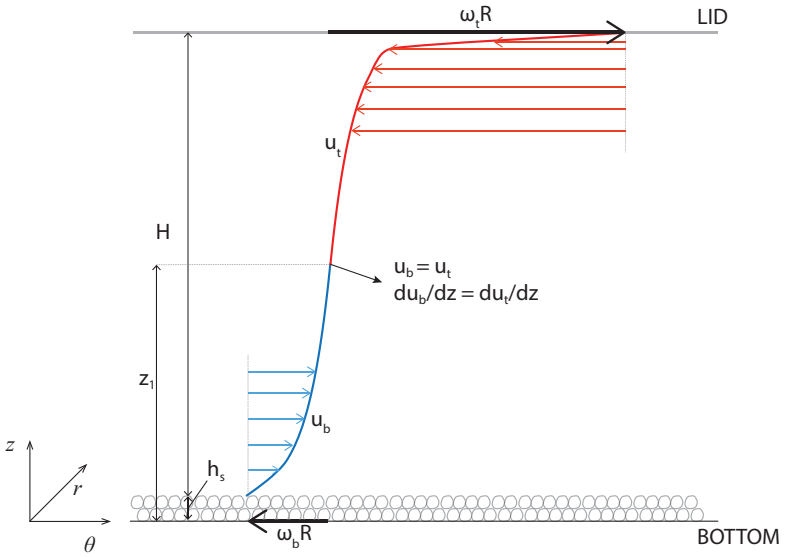


Figure 4.11: Schematic representation of the vertical profile of the tangential velocity along the centreline of the flume.

The two profiles, $u_b$ and $u_t$, match each other when the condition $du_b/dz = du_t/dz$ is met. This is realized for $z$:

$$z = \frac{H}{2} + h_s \rightarrow \begin{cases} u_t = u_b \\ \frac{du_t}{dz} = \frac{du_b}{dz}. \end{cases} \tag{4.12}$$

The only unknown variable in the above set of equations (4.11) is then the roughness length

of the lid, which will be derived in order to have a continuous vertical profile of the tangential velocity. To do so, the calibration tests carried out for the incipient motion condition turned out to be useful. For instance, in the case of a bed consisting of glass spheres with $d_{50} = 4.1$ mm, the shear velocity $u^*$ is calculated from the Shields-van Rijn shear stress and it results equal to 0.049 m/s. As the flow is not accelerated and the base and top areas are equal, $u^*$ is considered alike on the top and bottom boundaries of the flume. The values of angular speed for top and bottom are assumed equal to the experimental ones at incipient motion conditions when the water depth $H$ is set to 300 mm and the bed consists of a sediment layer 15 mm thick. The roughness length for the flume bottom is considered equal to the $d_{50}$ of the bed material. Under these conditions and the constraints presented in equations 4.12, the roughness of the top lid can be estimated as follow:

$$k_{st} = \frac{H}{2}\exp\left[\ln\left(\frac{H/2}{k_{sb}}\right) - \frac{\kappa R(\omega_t + \omega_b)}{u^*}\right]. \tag{4.13}$$

The two profiles match when $k_{st} = 0.43$ $\mu$m. This value is quite close to the one reported in literature for PVC pipes, which is generally of the order of magnitude of 1 $\mu$m. The continuous vertical velocity profile of the tangential velocity is presented in Figure 4.12.

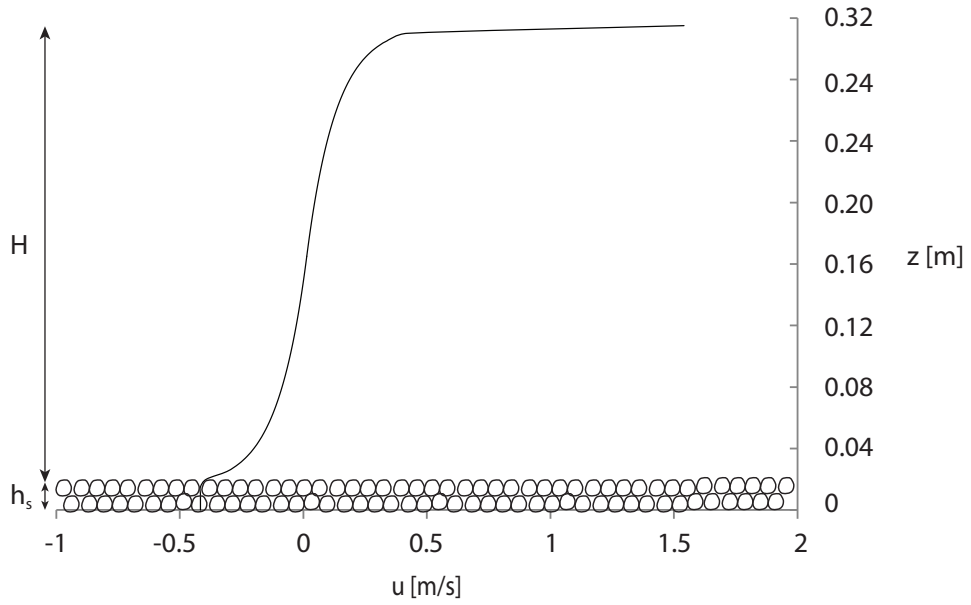


Figure 4.12: Vertical profile of the tangential velocity component, $u$, along the centreline of the channel over 15 mm thick bed of spheres with $d_{50} = 4.1$ mm and water depth of 300 mm.

The same procedure was then applied to the bed material consisting of the uniform mixture with $d_{50} = 3$ mm. The results are well aligned to the previous one. In this case the two profiles met for values of $k_{st} = 0.19$ $\mu$m, when the shear velocity from Shields-van Rijn model is assumed, i.e. $u^* = 0.04$ m/s. A slight increase in the shear velocity, e.g. $u^* = 0.042$ m/s, provides the exact same value of top material's roughness for the case of 4.1 mm bed. Similar values of PVC roughness are derived from the remaining tests and are summarized in Table 4.3. Notwithstanding the variability of the four derived roughness lengths, the order of magnitude of $k_{st}$ is in good agreement with the standard values for PVC material. An average top roughness of 0.39 $\mu$m is hereafter considered representative for surface material of the top lid in contact with the water surface. Knowing the vertical profile of the tangential velocity components is intended to better optimize the performance of the annular flume. It is in fact possible to apply

Table 4.3: Top surface roughness for the four uniform bed materials.

| TEST ($d_{50}$ [mm]) | $k_{st}$ [$\mu$m] |
|---|---|
| 2.5 | 0.24 |
| 3.0 | 0.19 |
| 4.1 | 0.43 |
| 5.1 | 0.69 |

a greater bed shear stress by increasing the roughness of the lid. This could be accomplished by sticking sandpaper on the top surface in contact with water. For instance, coarse sandpaper (grit 36) is denoted by an average diameter of 530 $\mu$m, which can be considered the indicator of its roughness length. Keeping constant all the other operational characteristics, i.e. $\omega_t, \omega_b, H$, and $k_{sb}$ the new shear velocity can be obtained as:

$$u^* = \frac{R(\omega_t + \omega_b)\kappa}{\ln\left(\frac{H}{2k_{sb}}\right) + \ln\left(\frac{H}{2k_{st}}\right)}. \tag{4.14}$$

A new lid roughness of 530 $\mu$m would produce an increase in shear velocity of approximately 80%. For instance, in the case of bed material with $d_{50} = 4.1$ mm the new shear velocity would be equal to 0.087 m/s, corresponding to an applied bed shear stress $\tau_{bed} = 7.53$ Pa, threefold larger than with the smooth PVC lid, i.e. $\tau_{bed} = 2.40$ Pa. Figure 4.13 shows the variation in the vertical profile of the tangential velocity over the bed deposit characterized by $d_{50} = 4.1$ mm when the top roughness length changes. Likewise for the 3 mm spheres bed deposit, the shear velocity would now result 0.073 m/s instead of 0.040 m/s of a smooth top. Such a small adjustment in the flume configuration would allow the realization of the same shear conditions, and therefore the mobilization of the same bed material, for lower values of angular velocities. Moreover, the opportunity to apply a higher shear stress on the flume bed will give the possibility to test coarser mixtures of material as now larger spheres can be triggered into motion.

Another way to modify the friction velocity consists of changing the water depth. Rearranging Equation 4.14 and combining it with equation 4.4, the shear velocity can be expressed as a function of the water depth $H$:

$$u^* = \frac{R\omega_t\kappa\left(1 + \frac{1}{f_{opt}(H/b)}\right)}{\ln\left(\frac{H^2}{4k_{st}k_{sb}}\right)}. \tag{4.15}$$

The evolution of the shear velocity, divided by the top rotational speed, is presented in Figure 4.14. As it can be seen, the water depth plays a minor effect on the shear forces, compared to the roughness of the top surface in contact with water. The greatest impact on the shear velocity is obtained for shallower flows, where $H \leq 200$ mm. For small water depth, however, the minimization of secondary currents is more troublesome as the circulation flow pattern presents great irregularity. When the water depth starts increasing though the influence is reduced, leaving the shear velocity almost invariable. This constitutes and additional support to the decision of performing all the tests and the series of experiments with a fixed water depth of 300 mm.

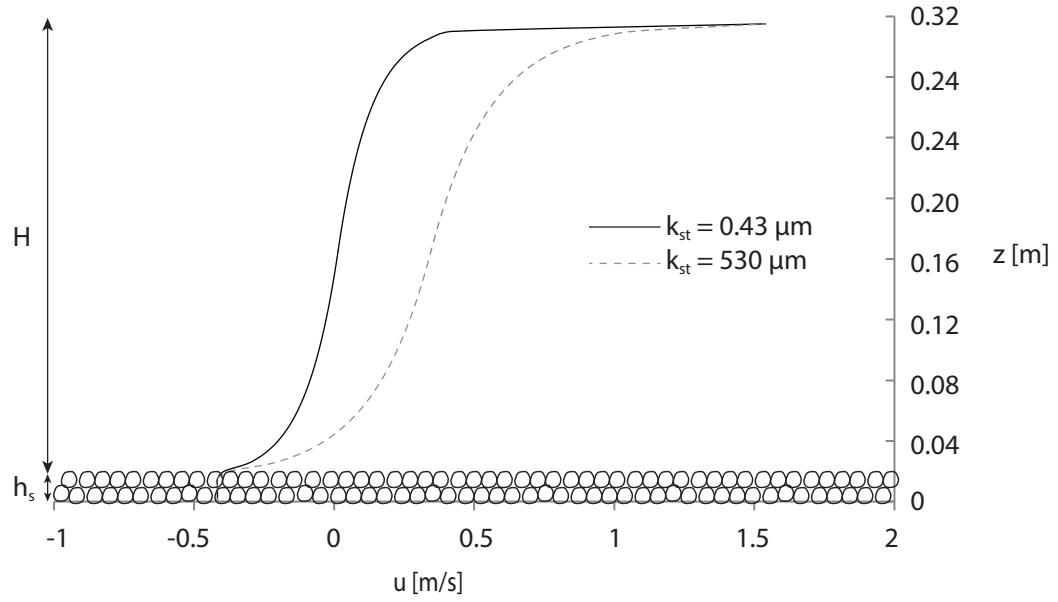


Figure 4.13: Tangential velocity profiles, $u$, over 15 mm bed deposit consisting of glass spheres $d_{50} = 4.1$ mm. The profiles are characterized by different roughness lengths of the top lid in contact with water, simulating the case of PVC (continuous line) and coarse sandpaper (dashed line).

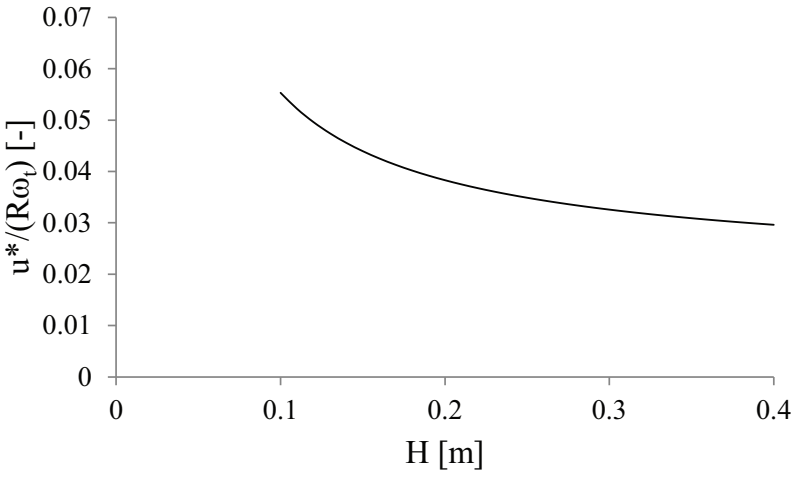


Figure 4.14: Modified shear velocity as a function of the water depth. The vertical axis reports $u^*$ divided by the top rotational velocity.

## 4.3 Image acquisition system

A system of 12 cameras was intended to capture the motion of the tracer spheres. The opaque material of the lid and the electrical power supplied only to the bottom plate with waterproof sockets led to the final cameras outline. It consisted of six cameras, located on the lower plate to monitor the side of the flume, together with other six elevated cameras acquiring images of the channel bed above the base of the bottom plate. The cameras system was then operating throughout the entire duration of each experiment in order to acquire a continuous recording of the flume bed.

### 4.3.1 System description

The image acquisition system has been rearranged as shown in Figure 4.15. Cameras are allocated between the centre of the flume and the channel's walls so that they move together with the bottom plate. A hexagonal aluminium frame was fixed to the flume bottom plate and it created a stable support for the devices. Six vertical bars held the top-view cameras whereas the side-view cameras were secured to the hexagonal horizontal frame (Figure 4.16). The set-up is good enough to visualize the flume from the side and from above providing an adequate overlap of images from adjacent cameras. The top cameras are tilted at 50 degrees with respect to the vertical at a height of 500 mm whilst the side-cameras are placed 180 mm above the bottom plate and parallel to the flume walls. The higher location of the side-cameras was decided in order to avoid the presence in the image of the cameras sockets (located between the camera rail and the flume wall). Every camera is denoted by a number. Even numbered cameras (2, 4, 6, 8, 10 and 12) compose the top-view system, whilst odd-numbered cameras (1, 3, 5, 7, 9 and 11) are placed on the horizontal frame and constitute the side-view system.

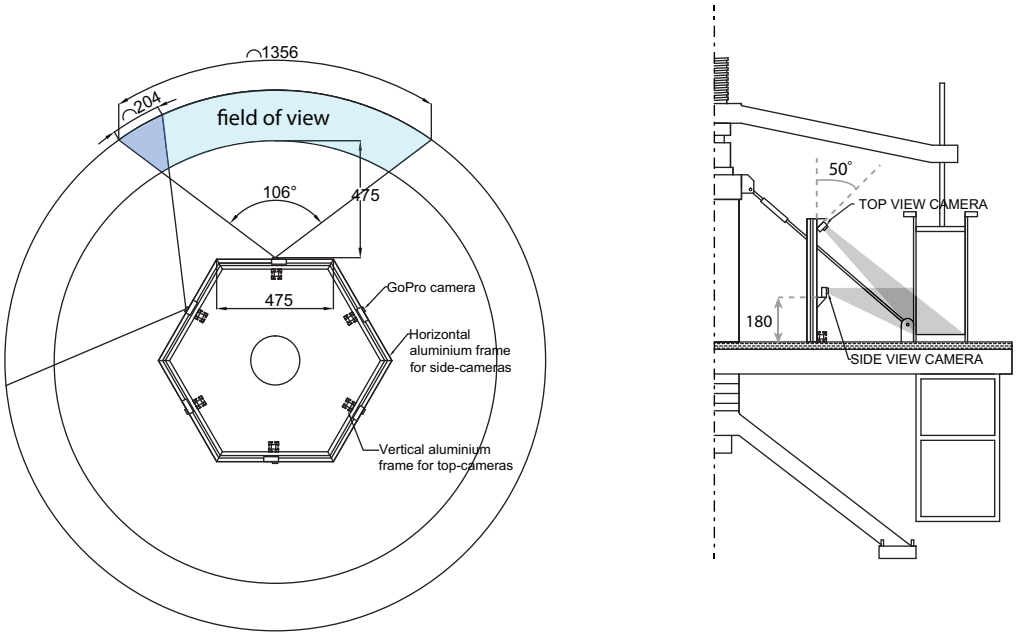


Figure 4.15: Image acquisition system. Both top and side views of the flume are presented. All length measurements are in millimetres.

The required specifications for the cameras system are a high frequency acquisition rate, a long recording duration, and a sufficient resolution. GoPro cameras proved to satisfy all the requirements. They can continuously record at 30 Hz for about 7 hours with $1080 \times 1920$ px high resolution frames. This resolution means that the smallest tracers (3 mm diameter) can be identified by at least 10 pixels. GoPros have also been chosen because of their wide-angle lens. This feature helps limiting the number of cameras that are necessary to monitor the entire flume. The 6.28 m circumference was covered with only six cameras assuring an overlap of about 0.20 m between adjacent cameras.

Cameras are continuously powered by two USB hubs connected to the waterproof sockets (Figure 4.16). The hubs maintained a constant charging level and never caused overheating problems that would result in powering off the cameras. An additional advantage of using GoPros is that they can be remotely controlled. All the cameras in fact respond to one single remote control that can be used to power cameras on/off, adjust the operational settings and

start/stop recording or shooting photos. The external control greatly helped in reducing the manual operation of the cameras which were only touched during the extraction/insertion of the SD cards. Extra care was always taken in the extraction/insertion procedure so that any variation in the cameras' original position was minimised.

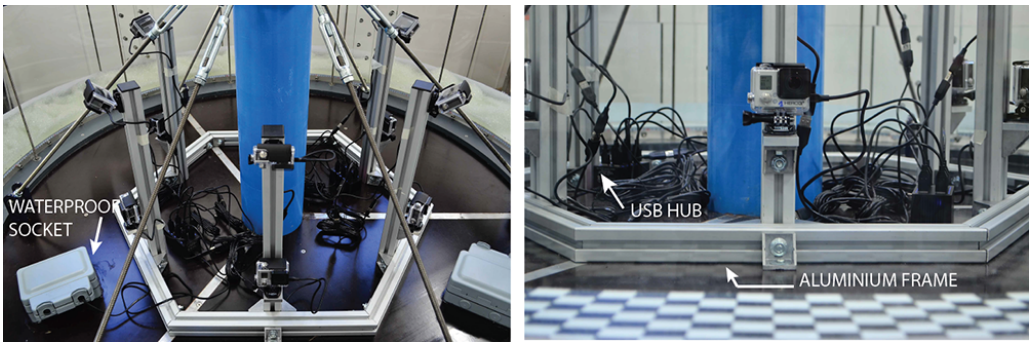


Figure 4.16: Picture of the image acquisition system with a focus on the side-view cameras.

Even if all the cameras respond to the same remote control, they experience a delay in the signal reception. The signal delay causes a temporal lag, usually lower than 10 frames (0.33 s), among the recorded videos. For this reason a synchronization procedure was carried out at the beginning of each experiment. As cameras record at 30 Hz, a light impulse is reckoned to be sufficiently accurate to work out the lag among the cameras. In addition to this, a stop watch, built ad-hoc for a similar experiment and with a precision of 1/1000 of second, is passed in front of each camera before the experiment starts. According to the size of the lag, in the post-processing phase the videos are shifted backwards or forwards in order to have temporal correspondence among the cameras. The small temporal lag is assumed to stay constant throughout the duration of the recording.

GoPros can continuously record a time series of images acquired at 30 Hz with a resolution of $1080 \times 1920$ px for 6 hours and 44 minutes, filling a 64 Gb SD card. The entire recording duration is internally split into smaller sub-videos of 26.04 minutes length, for a total of 46890 frames each. A preliminary check guaranteed that no information is lost between subsequent sub-videos. It was observed that the images that resulted were bright enough and evenly illuminated without the use of extra light sources. To enhance the contrast between the transparent spheres and the black tracers, white self-adhesive laminated paper was stuck on the bottom of the channel. The transparent channel bed in fact lies over the grey bottom plate, which creates a dark background below the sediment deposit. The white bottom together with a white paper stripe around the outer wall of the flume provides a uniform background in all the images (Figure 4.17).

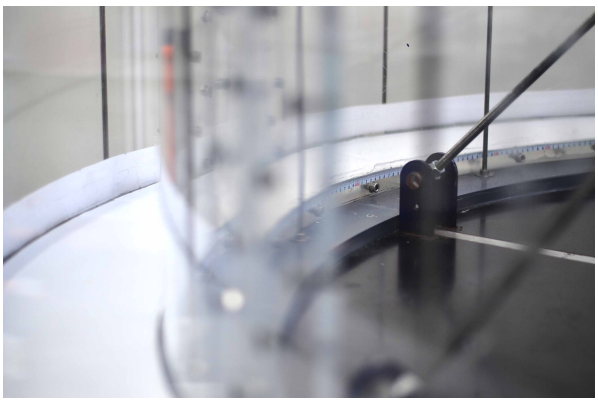

Figure 4.17: Channel bed covered in the white paper.

### 4.3.2 Images calibration and reconstruction

The advantages, described above, obtained when using the GoPro cameras come with a side effect. The wide angle of the lenses creates highly distorted images. The use of a calibration board, composed of black and white checkers, helps to eliminate the barrel-lens distortion along with the additional distortion due to the curved shape of the flume. This calibration board was used to transform the distorted image of the circular channel into a continuous straight bed, to reflect the flow patterns within the flume. The radial component $r$ would then become the transverse coordinate $y$, whereas the angular component $\theta$ would be substituted by the longitudinal coordinate $x$ (Figure 4.18a). In doing so, a Cartesian system can be implemented in the subsequent data analysis.

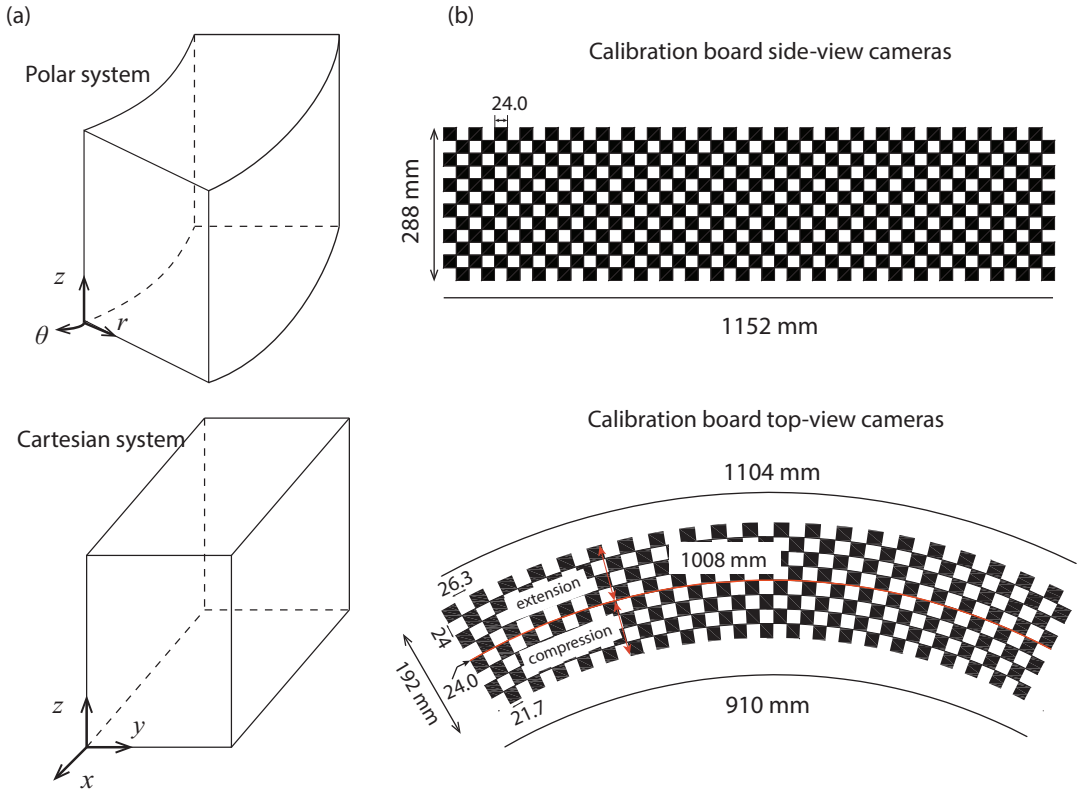


Figure 4.18: (a) Coordinates transformation from a polar to a Cartesian system. (b) Drawings of the calibration boards with relative measurements in millimetres.

Two checkerboards were used in order to correct the side and the top view cameras respectively (Figure 4.18b). The first calibration board consists of a rectangular laminated sheet with black and white checkers of 24 mm size. The flexibility of the material allowed the calibration checker board to be attached either to the inner or to the outer wall of the flume whilst the lamination made the board water resistant. This board is intended to correct the distortion of the side-cameras, which is due to the lens' wide angle and the curvature of the walls.

The calibration of the top view cameras turned out to be more challenging. The barrel distortion of the lenses is complicated by the curved shape of the channel bed and the inclination of the camera plane to the surface of the sediment deposit. To account for all these factors a radial shaped checkerboard was created (Figure 4.18b). The size of the checkers increases with the distance from the centre of the flume by maintaining their radial length always equal to 24 mm. The board is drawn so that only the checkers along the centreline are characterized

by the same length of the radial dimension, i.e. 24 mm. Below the centreline the checkers are compressed, above the centreline they are stretched. The board was printed in high resolution on a 1 mm thick PVC sheet which is flexible and waterproof. The sheet was then mounted on top of an aluminium frame that is 40 mm high to make sure that the calibrated area corresponds to the bed surface (Figure 4.19a). The board was then placed on the bed and moved along the channel in order to collect pictures from the top cameras as described in Figure 4.19b. From every camera a central image of the board was taken along with two more images with the board on the right and on the left side of the lens. The lateral images of the board were used to extend the calibration to the border of the images and to create a reference pattern in the overlap area of adjacent cameras. The images of the checkerboards (straight and curved ones) were all taken with the flume filled with water.

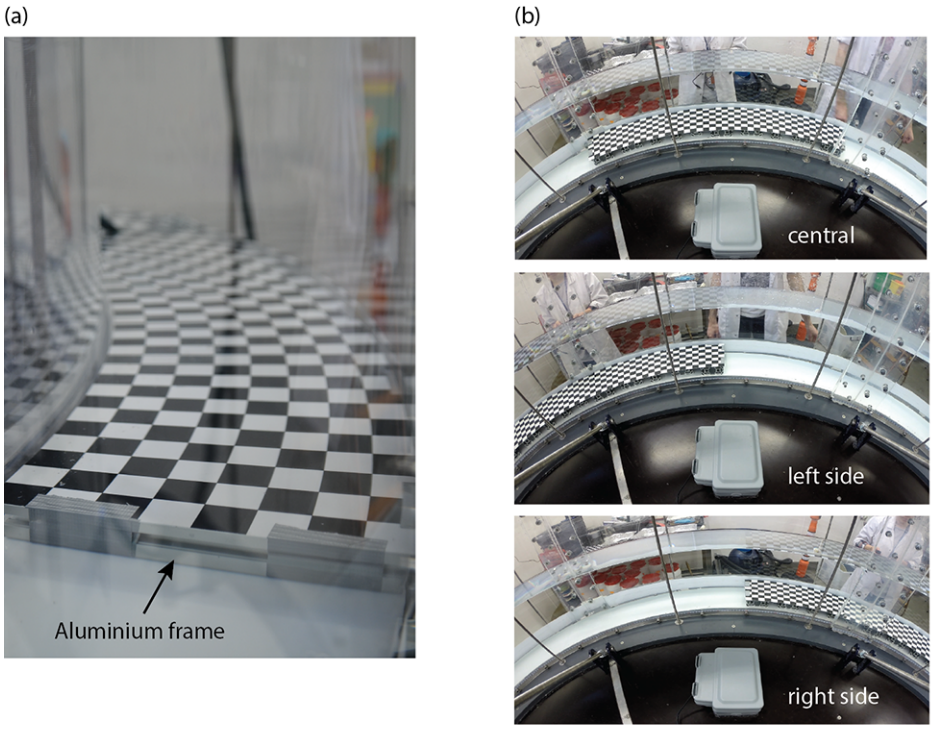


Figure 4.19: Focus on the aluminium frame sustaining the curved checkerboard (a). Series of images taken from camera 4 as part of the calibration procedure (b).

An algorithm was implemented in Matlab to derive the calibration parameters necessary to correct the distorted images. The code detects the black and white pattern in the image by the identification of the corner points of each checker. By knowing the exact size of the checkers, the detected pattern is then corrected so that the mapped checker lines result perpendicular to each other. To do so a third degree polynomial function is used to correlate the identified location of the corner points to their position on the corrected perpendicular grid. The application of the algorithm to the rectangular boards captured by the side cameras was more straightforward and the results are showed in Figure 4.20b. The reconstructed pattern is now made of a perpendicular grid of checkers and the output image looks well calibrated.

In the case of the top-view cameras a smaller area of the image is covered by the curved board. This, along with the interference caused by the vertical rods of the flume walls and the junctions of the consecutive vertical Perspex flume wall sections, forced the images to be spilt into three parts and to operate the calibration routine individually on each image section. To correct the image borders the lateral pictures of the board (refer to image 4.20b) were used.

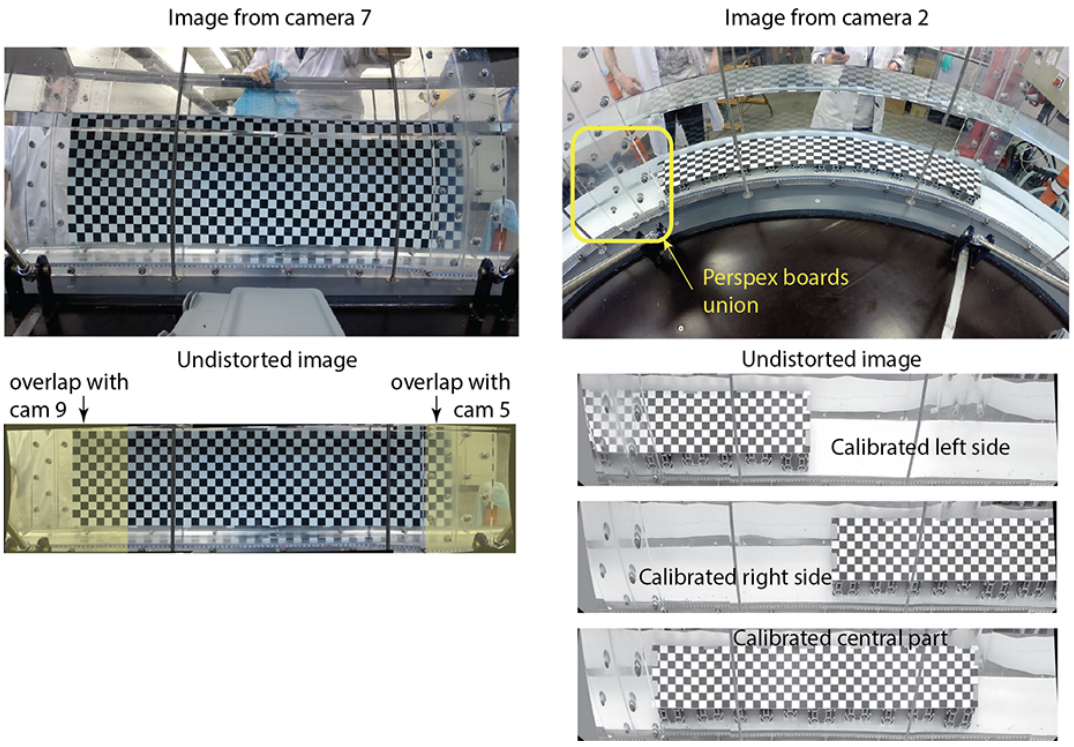


Figure 4.20: Distorted and undistorted images of the checker boards following the calibration procedure. The comparison is shown for both the side cameras (camera 7) and the top cameras (camera 2).

The union of the vertical Perspex flume walls (three in total in the inner wall of the flume) falls into the field of view of every top camera and it creates a downward shift of the pattern which is firstly removed. The corrected lateral parts are then re-united to the calibrated central part by using mutual reference points. The image now shows a flat perpendicular pattern of checkers in correspondence of the channel bed (Figure 4.20b). In the final result it is like observing the channel from a camera placed directly on top of the bed, as it appeared in the first ideal set-up. The radial configuration of the checkers has also helped with the transformation of the curved flume bed into a straight channel.

The corrected images have a resolution of 2 pixels per millimetre. The coarser scale was chosen to reduce the volume of data that is subsequently used by the tracking code. The resolution was still accurate enough to detect the centroid of the black tracer spheres (Figure 4.21).

The algorithm provided the calibration parameters which are then used to remove the distortion from the frames extracted from the videos of each experiment, as shown in Figure 4.21. The application of the transformation code to the side images does not produce good results as the difference in the refractive index between the borosilicate glass and water impedes the visualization of the black particles within all the 200 mm radial width of the bed deposit. Images from the side cameras, which were intended to provide the location $(x, z)$ of the tracers, turned out to be useless. It was although noticed that the buried black tracer particles can be detected in the top images because of the shallower layer of transparent particles covering them. On average, black particles can be spotted up to 20 mm deep in the bed with greater accuracy when the covering transparent layer is less than 10 mm. The videos recorded from the top cameras are sufficient to gather information on the location $(x, y)$ of all the moving black tracers even when they are stored in the bed. All tracers can then be identified on the planar bed $(x, y)$ but the

difficulty to visualize black spheres in the side images makes impossible to estimate the vertical component $z$. From now on results will be based only on the inspection of the top images.

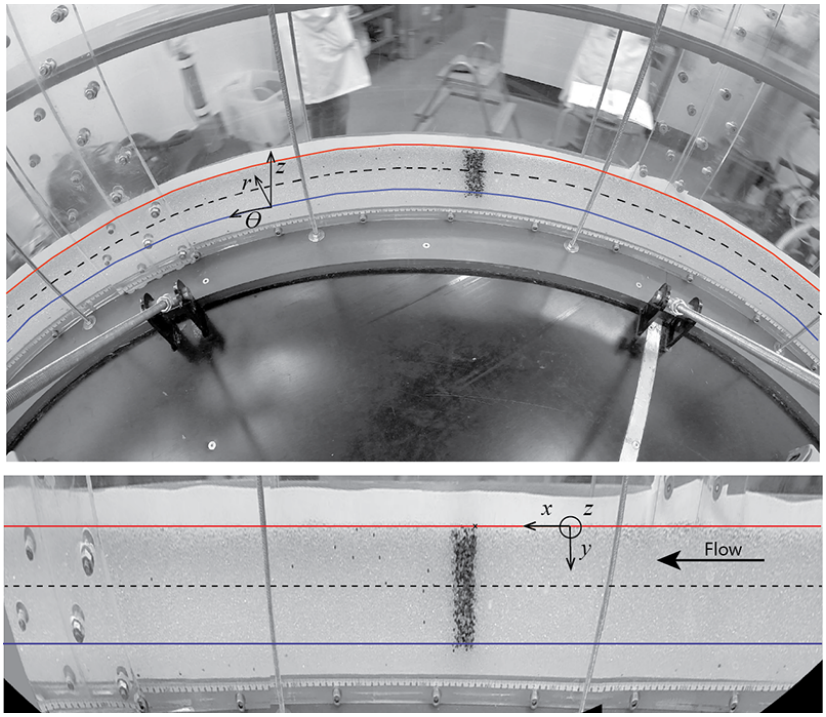


Figure 4.21: Comparison between the same image of the bed before and after the application of the corrective algorithm for top cameras.

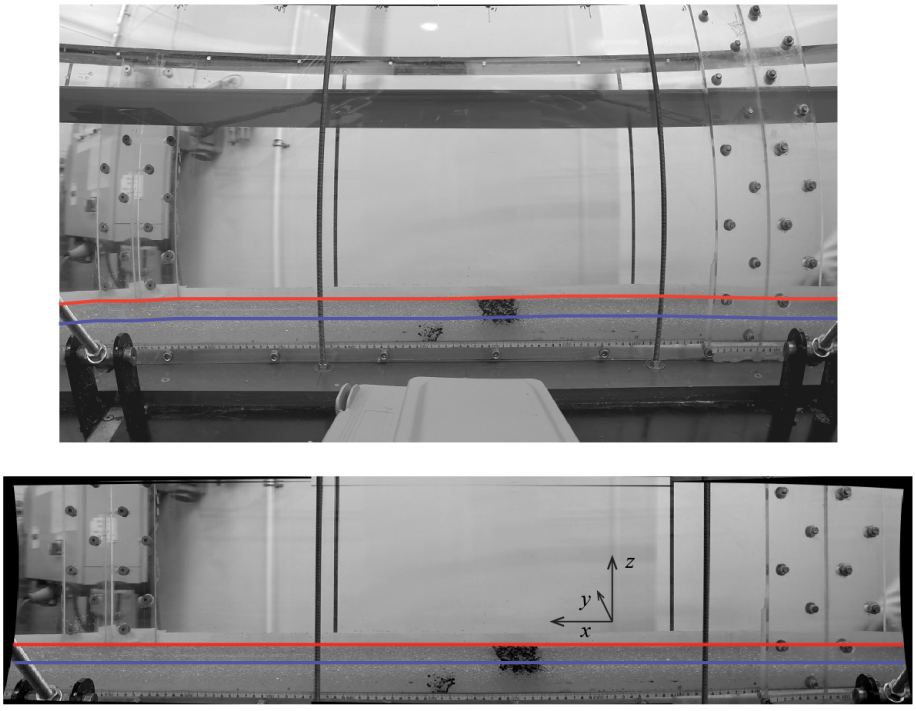


Figure 4.22: Comparison between the same image of the bed before and after the application of the corrective algorithm for the side cameras. Blue and red lines corresponds to the delimiting lines of Figure 4.21

Once all the cameras are calibrated, it is possible to concatenate adjacent images to recon-

struct the entire flume bed. The frames capturing the lateral checkerboards provide a common pattern that can be used to detect reference points from contiguous cameras. For instance, the right-side checkerboard in camera 2 was also captured by camera 12 but in this case it will be on the left-side of the frame as shown in Figure 4.23. The wide overlap area and the pattern of the checkerboard support the identification of common reference points. The two images can then be joined together in a single image of the bed. The extraction of the reference points for all adjacent cameras enables these images to be combined into a series of images so that a continuous rectangular picture of the channel bed is achieved. Knowing the union points between the cameras is essential in the reconstruction of particles' trajectories and tracers' concentration. When a tracing particle exits the field of view of one camera it will appear in the next camera's view so that its path can be continuously monitored without interruptions.

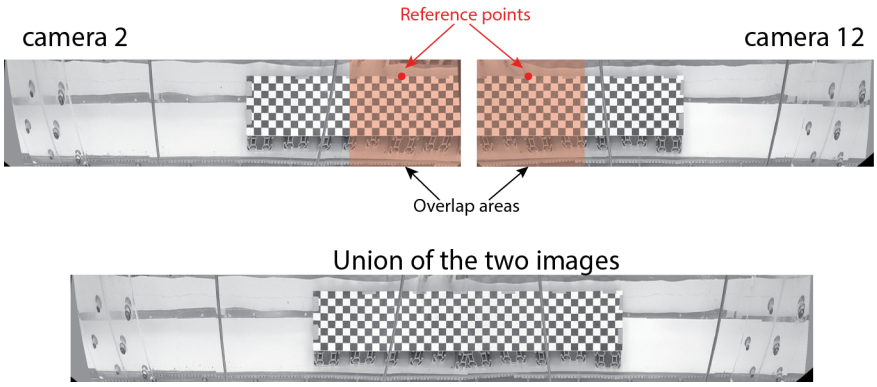


Figure 4.23: Concatenation of images taken from adjacent cameras. In this case the union of camera 2 and camera 12 is presented.

### 4.3.3 Error estimation

Once images have been corrected to eliminate the lens distortion and the flume curvature, the reference system for the tracking activity is now Cartesian, with $x$ being the streamwise coordinate and the $y$ indicating the transverse direction. The correction algorithm provides images of the same dimensions for subsequent cameras as can been seen in Figure 4.24a. Checkerboards are perfectly aligned and with equal checkers size, i.e. 24 mm. The curved checkerboard was designed to follow the radially oriented deformation of the channel bed so that the first checkers, closer to the inner wall, were compressed whilst the outer checkers were stretched (Figure 4.24b). The tangential length of the squares is progressively increasing with the distance from the centre of the flume by maintaining the radial dimension always 24 mm long. Along the centreline of the calibration board no distortion takes place as the checkers' size is exactly 24 mm.

Because the flume curvature is fairly small, i.e. $b/R = 0.20$, the arc lengths are not affected by the distortion as can be seen in Figure 4.24b, where the length of the checkers ranges between 21.7 to 26.3 mm. In order to obtain a perpendicular grid of 24 by 24 mm squares, the algorithm preserved the correct crosswise dimension but conversely stretched the checkers below the centreline and compressed the squares above it (Figure 4.24b). As the tracking is carried out with the calibrated images the hops computed by the black tracers on the upper part result are then compressed. Alternatively the hops measured in the lower part are extended. This has an implication on the actual distance travelled by the bedload particles. The measured hops should then be corrected depending on the particle's transverse position on the bed (Figure 4.24c).

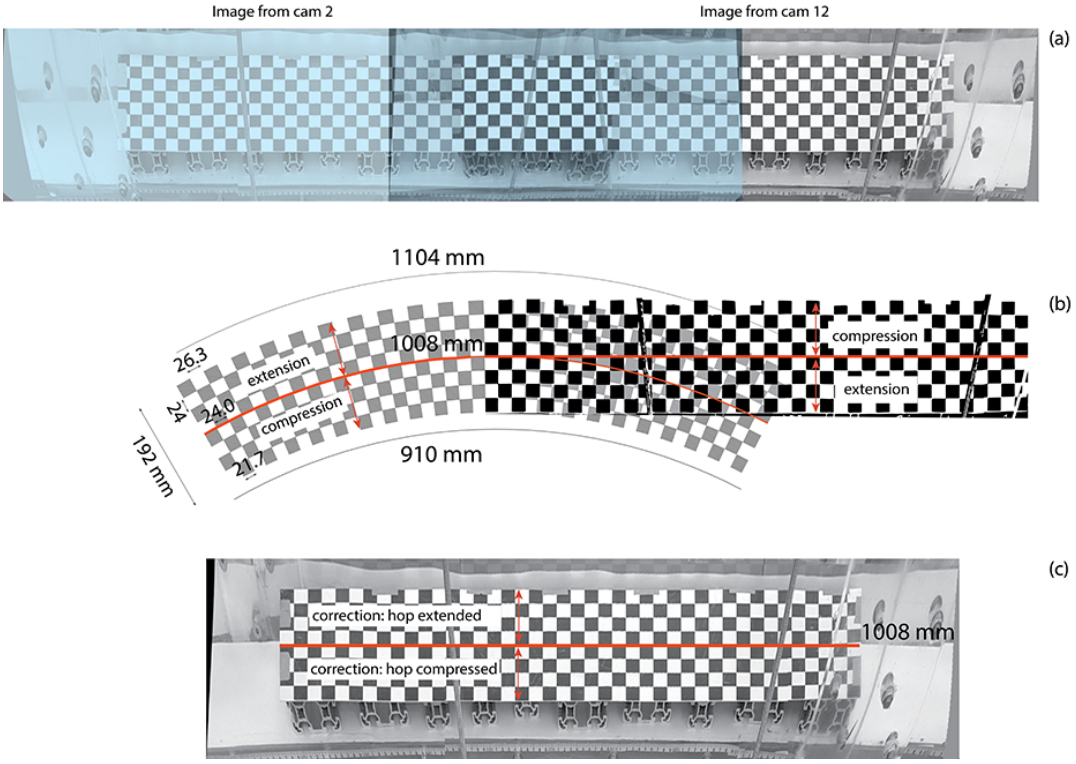


Figure 4.24: (a) Concatenation of undistorted images from two consecutive cameras. (b) Sketch of the real calibration board overlapped by the corrected checkerboard. (c) Application of the correcting algorithm to the board and its implication to the actual hops computed by bed tracers. The red line indicates the centreline not affected by the radially orientated distortion.

Figure 4.25a illustrates the case of a particle $p_1$ which has moved to position $p_2'$ in the following frame, that is after $\Delta t = 0.033$ s. On the calibrated image the upper right corner of the tracers stripe is chosen as the origin of the Cartesian axis system, $O(0,0)$. With this reference system the tracing bead occupies position $p_1(x_1, y_1)$ in $t_1$ and $p_2(x_2, y_2)$ in $t_2 = t_1 + \Delta t$. To counteract the compression-extension of the calibration algorithm, the transverse position of the particle should be considered. In this example the particle lies above the centreline, so according to the checkerboard transformation the streamwise travelled distance, $\Delta x_{\text{meas}} = x_2 - x_1$, should be extended. The new position $x_2'$, would then result:

$$x_2' = x_1 + f_C \Delta x_{\text{meas}}, \tag{4.16}$$

where $f_C$ denotes the conversion factor that takes into account the abovementioned compression-extension. $f_C$ grows linearly with the radius, assuming minimum value of 0.9 on the inner wall (blue line in Figure 4.25a) and maximum value 1.1 in proximity of the outer wall (red line in Figure 4.25a). Reporting $f_C$ in the Cartesian system where $y$ is equal to 0 on the top red line, the conversion factor becomes $f_C = 1.1 - 0.001y$, with $y$ being the transverse coordinate of the particles in millimetres. In doing so, the conversion factor is equal to 1 when $y = 100$ mm, that is the centreline location not affected by the radially oriented distortion. Along this line distances are maintained.

Once the particle is entrained, the correction is applied to every subsequent collision of the particle with the bed, frame by frame. This is intended to minimize the error associated to the derivation of the conversion factor. Since each particles' position is denoted by two components $(x, y)$ the conversion factor could be derived at the previous transverse location $(y_1)$ or at the

following one ($y_2$) as shown in Figure 4.25b. The difference in calculating the new position $x_2'$ with $f_C$ attributed to either $y_1$ or $y_2$ is:

$$e = x_2'(y_2) - x_2'(y_1) = (f_C(y_2) - f_C(y_1))\,\Delta x_{\text{meas}} = 0.001(y_1 - y_2)\Delta x_{\text{meas}}. \tag{4.17}$$

The analysis of the first dataset extracted from the experiment E6 showed that the average particle's streamwise hop between consecutive collision with the bed is 1.72 mm with standard deviation of 0.22 mm, whilst the transverse average hop is 1.09 mm with standard deviation 0.11 mm. Assuming $\Delta x_{\text{meas}}$ and $(y_1 - y_2)$ respectively equal to the average streamwise and transverse hop lengths, the average uncertainty in determining the actual position of a particle is 0.0019 mm, i.e. 0.11% of the mean longitudinal hop. By selecting the transverse position upon which the conversion factor is calculated, the introduced error is still negligible. This is a direct consequence of the geometry of the flume, whose small curvature helps in minimizing the radially oriented distortion of distances. The maximum shift of position takes place in correspondence of the outer and inner wall. For instance, in $y = 0$ mm the new longitudinal position is $x_2' = x_1 + 1.1\Delta x$, and by considering $\Delta x$ equal to the average streamwise hop the new longitudinal coordinate is moved downstream of 0.17 mm. Likewise when $y = 200$ mm, $x_2'$ is displaced upstream by 0.17 mm.

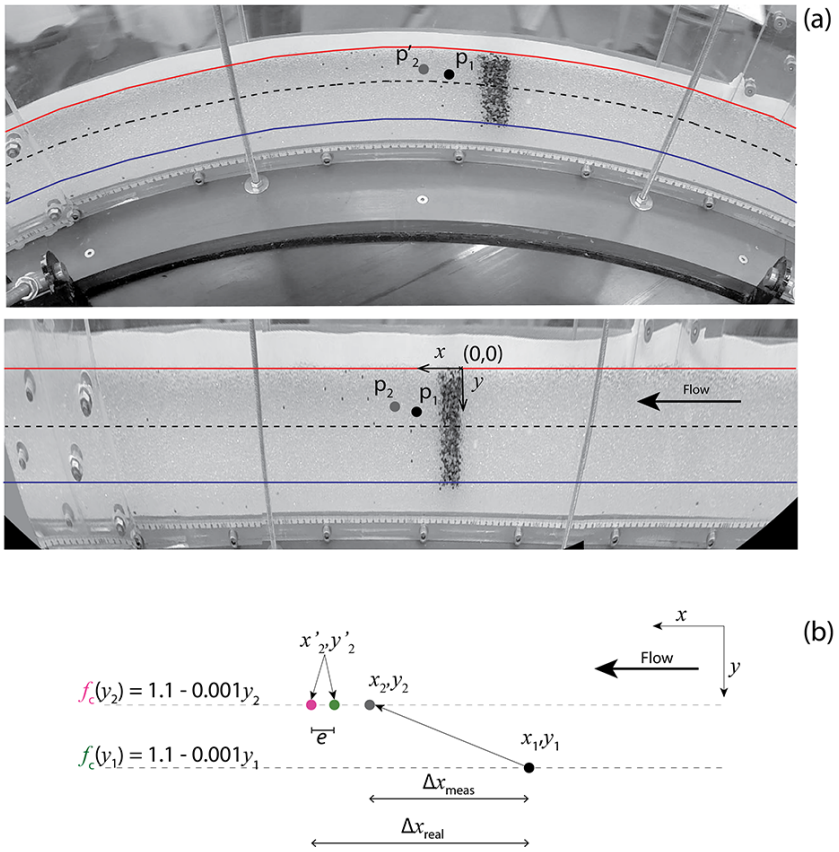


Figure 4.25: Particle's location after a hop in real and undistorted image (a), and graphical representation of the error computed in the conversion factor choice (b). The error is identified as the distance between the two calculated positions (pink and green dots).

For the following analysis it was decided to use the conversion factor calculated in correspondence of the last position $y_2$. As the correction is applied to every single hop computed by a tracer in 0.033 s, the values of the step length, i.e. distance travelled from entrainment

to rest, can be considered accurately derived. A step length is by definition composed by a series of subsequent collisions of the particle with the bed, here called hops, from the time it is entrained to the moment it rests on the bed. Applying the compression-extension conversion factor to the final position of the step would mean that the calculated new position is affected by a greater error. If the correction is applied to every recorded position of the particle's trajectory (every 0.033 s) instead, the location is continuously adjusted along the path. The subsequent new positions are determined with greater accuracy as the conversion factor is derived at every particle's transverse location occupied in each frame. Figure 4.26 well illustrates the concept. The final position results then more precisely identified.

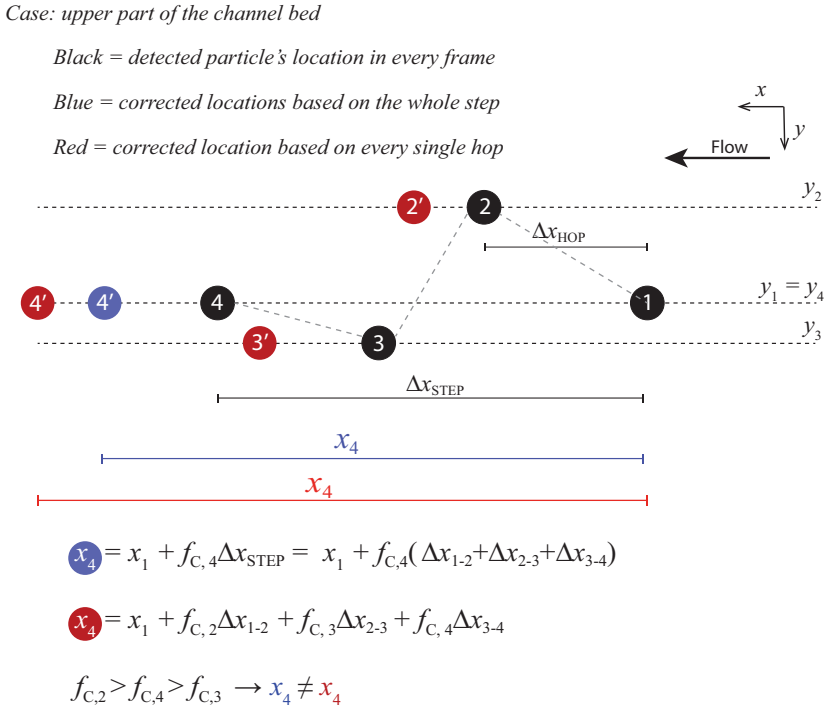


Figure 4.26: Illustration of the different results obtained in the determination of the longitudinal particle's location based on the entire step (blue spheres) and on the single hops (red spheres). The example is referred to a particle moving on the upper half of the channel bed.

## 4.4 Series of experiments

Once the calibration of the annular flume had been accomplished a series of experiments were completed. The experiments aimed at studying the mechanics of bed-load sediment transport by measuring the movement of a small group of tracer particles. Experiments were generally performed for 6 hours during which the movement of tracer grains was constantly filmed. The two sediment mixtures, fine and coarse, were tested in these experiments.

To obtain a sediment deposit at least $10d_{50}$ thick, 100 kg of borosilicate glass spheres were used for the coarse mixture and 60 kg for the fine mixture. All the different sizes composing the mixture were first mixed in batches of 3 kg capacity according to the percentages in weight of the particle size distributions of the fine and coarse mixtures. The spheres were then gently placed on the bottom of the flume to form the deposit and the bed was scrapped flat. The tracer particles used in this study consist of black borosilicate glass of size 3.00 and 4.00 mm. To place the tracers in the bed, the part of the channel allocated for the tracers was first filled with the

sediment mixture and then the required volume was carefully scooped out. The removed part was then sieved to separate the transparent spheres of the same size of the tracers. The black spheres replaced the same amount of removed beads and were added back to the mixture after being randomly mixed. The new material was afterwards stirred and located in its original position into the flume (Figure 4.27). This assured that the original composition of the mixture was maintained so that no discontinuity in the bed sediment particle size distribution could be observed in all the bed deposit.

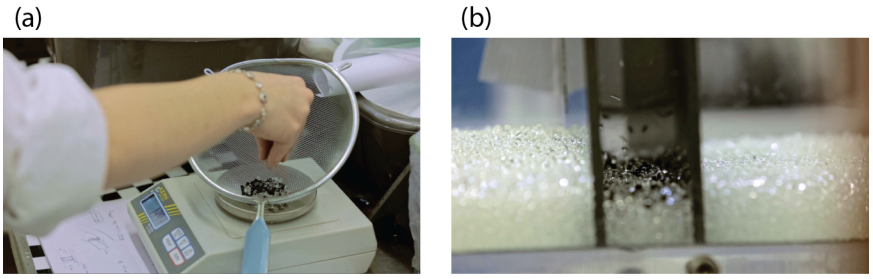


Figure 4.27: Tracers' insertion procedure: (a) replacement of the same amount of transparent spheres with black tracers of equal diameter, (b) mixture re-allocation in the original position of the channel. The vertical plates were used to isolate the required volume of bed material.

Table 4.4: Experimental parameters namely type of mixture, mean bed diameter, tracer diameter, rotational velocities, friction velocity, bed shear stress, Shields' parameter, excess of shear stress and bed mobility index. The averaged tangential velocity component along the centreline is derived with Equation 4.6 and the law of the wall (Equation 4.5). The duration of the experiments are reported in hours. Information on the bed arrangement at the end of the experiments is also presented.

| Date | TEST | Mixture | $d_{50}$ [m] | $d_T$ [m] | $\omega_t$ [rps] | $\omega_b$ [rps] | $\omega_t$ [rad/s] | $\omega_b$ [rad/s] |
|---|---|---|---|---|---|---|---|---|
| 01/02/2016 | E1 | coarse | 0.0041 | 0.003 | 0.280 | 0.075 | 1.759 | 0.473 |
| 05/04/2016 | E2 | fine | 0.0032 | 0.003 | 0.284 | 0.073 | 1.785 | 0.457 |
| 11/04/2016 | E3 | fine | 0.0032 | 0.003 | 0.248 | 0.067 | 1.559 | 0.421 |
| 22/04/2016 | E4 | fine | 0.0032 | 0.003 | 0.261 | 0.070 | 1.639 | 0.437 |
| 29/04/2016 | E5 | fine | 0.0032 | 0.003 | 0.237 | 0.063 | 1.487 | 0.399 |
| 06/05/2016 | E6 | fine | 0.0032 | 0.004 | 0.237 | 0.063 | 1.487 | 0.399 |
| 03/08/2016 | E7 | fine | 0.0032 | 0.004$^\star$ | 0.237 | 0.063 | 1.487 | 0.399 |
| 10/08/2016 | E8 | fine | 0.0032 | 0.004 | 0.237 | 0.063 | 1.487 | 0.399 |

$\star$ = coloured tracers

| TEST | $u^*$ [m/s] | $\tau$ [Pa] | $\tau^*$ [-] | $(\tau - \tau_{cr})^{1.5}$ [Pa] | $I_m$ [-] | $u_{av}$ [m/s] | $u_{av}$ [m/s] | Duration [hours] | Notes |
|---|---|---|---|---|---|---|---|---|---|
| E1 | 0.056 | 3.091 | 0.062 | 0.357 | 1.194 | 0.271 | 0.267 | 6.0 | fairly flat bed |
| E2 | 0.055 | 3.028 | 0.078 | 1.198 | 1.594 | 0.290 | 0.275 | 5.0 | bedforms |
| E3 | 0.049 | 2.360 | 0.061 | 0.313 | 1.243 | 0.239 | 0.225 | 6.0 | shallow bedforms |
| E4 | 0.051 | 2.596 | 0.067 | 0.581 | 1.366 | 0.255 | 0.240 | 6.0 | bedforms |
| E5 | 0.046 | 2.141 | 0.055 | 0.119 | 1.127 | 0.230 | 0.217 | 6.0 | fairly flat bed |
| E6 | 0.046 | 2.141 | 0.055 | 0.119 | 1.127 | 0.230 | 0.217 | 6.0 | fairly flat bed |
| E7 | 0.046 | 2.141 | 0.055 | 0.119 | 1.127 | 0.230 | 0.217 | 18.0 | fairly flat bed |
| E8 | 0.046 | 2.141 | 0.055 | 0.119 | 1.127 | 0.230 | 0.217 | 12.0 | fairly flat bed |

The experimental conditions for the series of experiments are detailed in Table 4.4. The table reports the bed material characteristics, i.e. mean bed diameter $d_{50}$ and the tracers' size $d_T$, the hydraulic conditions such as the rotational velocity of the top lid and bottom plate in rps and rad/s, the friction velocity $u^*$, the shear stress applied to the sediment deposit $\tau$, the dimensionless bed shear stress $\tau^*$ and the excess of shear stress $(\tau - \tau_{cr})^{1.5}$. The index of mobility presented in the table is calculated as $I_m = \rho u^{*2}/(\tau^*_{cr}(\rho_s - \rho)gd$, (Bialik et al., 2012). The tangential velocity component along the centreline, $u_{av}$, was derived by means of Equation 4.6 and by the law of the wall (Equation 4.5). A fairly good agreement is evident for the two calculated values, thus proving the validity of the formulation proposed by Booji (1994). The water depth in all experiments was 300 mm. In Table 4.4 the total duration of each experiment together with a brief consideration about the bed arrangement at the end of it are included.

The selection of the hydraulic parameters and the bed characteristics for each test is intended to investigate the effect of these two factors on the tracers' transport behaviour. For instance, the same shear conditions are applied to different bed mixtures (tests E1 and E2, as well as E1 and E3), whilst the same bed material composition is tested under three different excess of shear stress (E3, E4 and E5). To study the effect of the relative size, different sizes of tracers have been used in two identically performed tests (E5 and E6). The duration of the tests has then been extended to 12 and 18 hours (tests E8 and E7 respectively) to observe the evolution of the tracers' transport in long-time experiments.

### 4.4.1 Test E1: coarse mixture, 3 mm black tracers

The first experiment was run with a bed deposit consisting of the coarse mixture. The 3 mm black beads replaced the transparent 3 mm spheres in a volume 20 mm deep and 50 mm long so that the fraction in weight of tracers is 0.18 as shown in Figure 4.28a. The incipient motion conditions were first obtained at a critical Shields' parameter $\tau^*_c = 0.052$. The flume top and bottom velocities were then increased in order to attain a stable value of dimensionless shear parameter $\tau^* = 0.062$, which corresponds to a shear velocity of 0.056 m/s (Table 4.4). The lid and bottom velocities were set at $\omega_t = 1.76$ rad/s and $\omega_b = 0.47$ rad/s and the experiment was run for 6 hours under this condition. At the end of the test the bed was fairly flat.

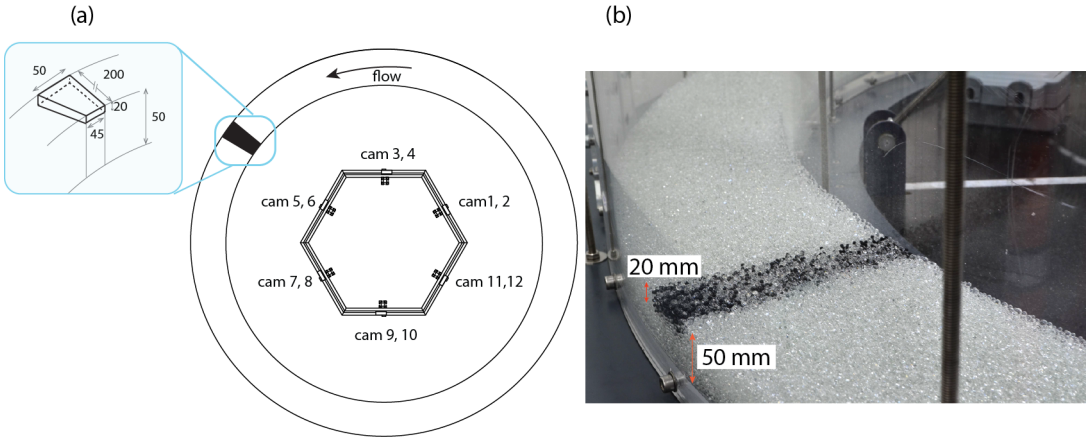


Figure 4.28: (a) Schematic top view of the channel bed with the localization of the tracers stripe. (b) Image of the bed with black tracers before the channel was filled with water.

### 4.4.2 Tests E2, E3, E4, E5: fine mixture, 3 mm black tracers

To increase the mobility of the 3 mm diameter spheres the coarse bed material mixture was replaced by the fine mixture. In doing so, the influence of the bed roughness on the motion of the same class of particles can be studied. In all the experiments with fine mixtures (E2-E8), the bed thickness was 35 mm, still guaranteeing at least 10 particles diameters. To compare the transport of the 3 mm black spheres over different beds, the same shear velocity, and therefore same shear stress, as that applied in Test E1 characterizes the experiment E2, i.e. $u^* = 0.056$ m/s. The result was the formation of bedforms in the form of very pronounced alternated bars. This was due to the very high mobility of the bed material indicated by the excess in shear stress, $(\tau - \tau_{cr})^{1.5} = 1.20$ (Table 4.4). A new experiment was then performed, namely E3. In this case the Shields parameter, instead of the friction velocity, is set equal to the experiment E1. The application of a dimensionless shear stress of 0.061 allowed an experiment with analogue bed shear stress conditions but different bed roughness. After 6 hours the bed was fairly flat and the surface developed shallow alternate bars, very similar to the ones obtained in the experiment E1. The satisfactory results led to carry out two more experiments, E4 and E5, where the excess in shear stress, $(\tau - \tau_{cr})^{1.5}$, was respectively doubled and halved compared to the value characterizing experiment E3. While in the first case, E4, the bed developed clear alternate bars, in the second case E5 no bedforms emerged and the bed could be considered essentially flat.

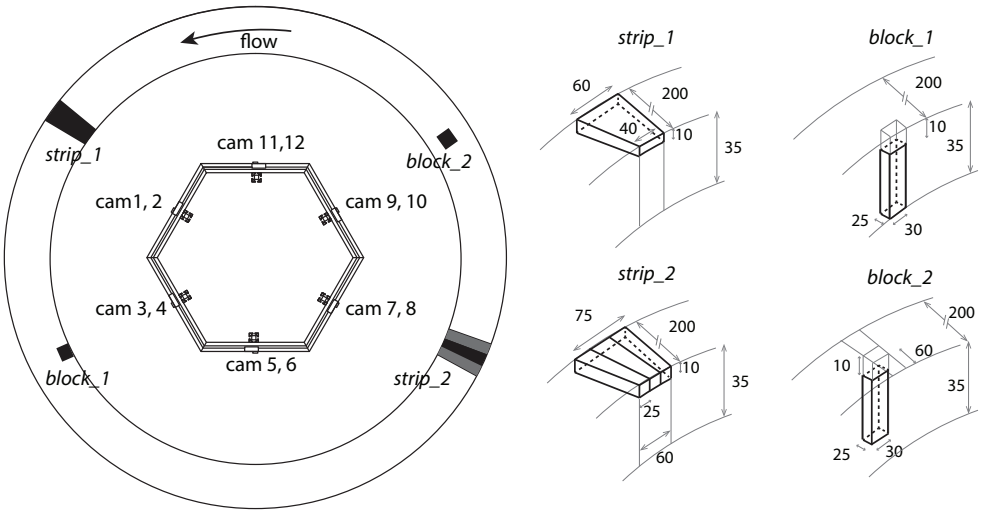


Figure 4.29: Schematic representation of the tracers' locations, strip 1, strip 2, block 1, and block 2 at the beginning of the experiments. Dimensions are reported in mm and here referred to the experiment E2.

For these experiments it was decided to create two surficial strips of tracers and to insert two submerged blocks as shown in Figure 4.29. The surficial strips (10 mm deep) were intended to study the motion of the particles over the bed, while the two blocks (buried underneath 10 mm of spheres) should have provided information on the extent of the erosion and vertical mixing of the bed material. For the two blocks and the strip 1 the tracers of 3 mm size replaced the same transparent bed material for the 30.4% in weight, according to the fine mixture composition. The strip 2 contained the same amount of tracers as strip 1 but it mimicked a Gaussian distribution

by spreading the tracers over a wider area made of 3 stripes (Figure 4.30). The size of the blocks of tracers remained invariant at the start of each test. However the sizes of the tracers' stripes slightly changed in every experiment due to the manual insertion of the tracers.

The optimal top and bottom rotational ratio was confirmed in each test to vary between 3.72 and 3.84, and the incipient motion conditions, found by observation, were reached at approximately a velocity $\omega_t = 1.40$ rad/s and $\omega_b = 0.38$ rad/s. The calculated critical Shields parameter for this mixture is then $\tau_c^* = 0.049$.

Once an experiment was completed the water was entirely removed, the black spheres were picked up by hand, and the bed material was manually worked inside the flume to recreate a well-mixed deposit. Afterwards the bed was scrapped flat again and tracers were re-located in their original position so that a new experiment could be performed again with a deposit with similar particle size distribution and surface roughness characteristics.

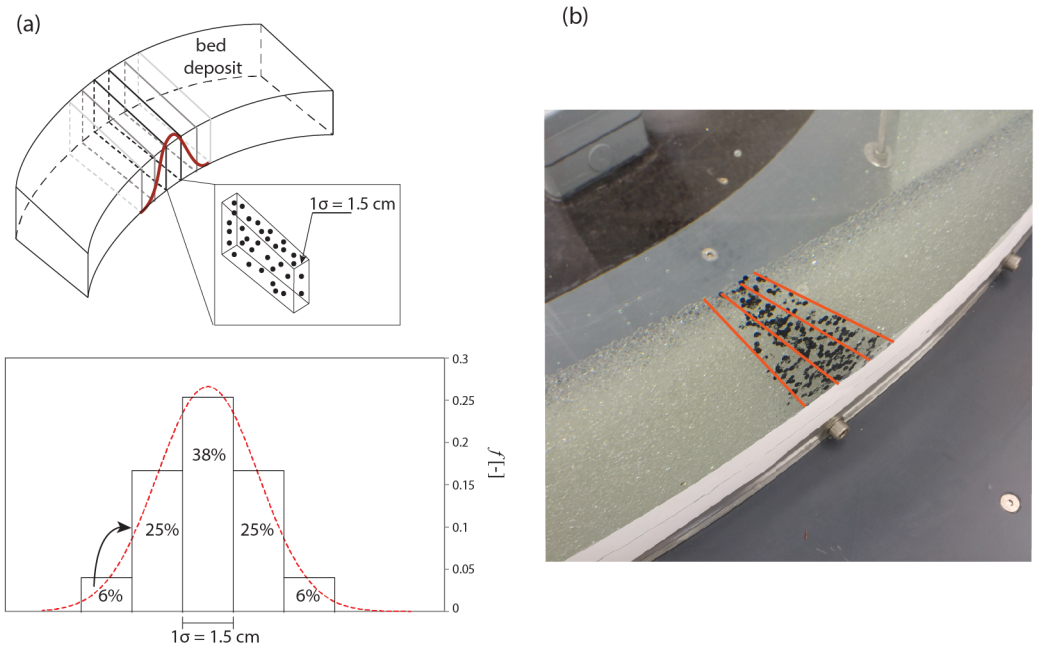


Figure 4.30: Gaussian distribution of black tracers in strip 2. Schematic representation of the ideal concentration distribution (a) and its realization in the bed deposit (b). The five bins, each measuring 15 mm in the radial direction, were then reduced to three strips in order to avoid very low concentration on the two furthest strips. The bin length is equal to the standard deviation of the Gaussian distribution.

### 4.4.3 Test E6: fine mixture, 4 mm black tracers

To isolate the effect of the relative size of the moving material over the same bed, different tracers were mixed with the bed material. The size of the black spheres, $d_T = 4$ mm, is now comparable to the biggest particles composing the fine mixture. The black spheres replaced the same size material according to the mixture proportions, i.e. 25% in weight. The hydraulic conditions of experiment E6 were similar to E5. The applied shear velocity resulted in a Shields parameter $\tau^* = 0.055$ and in an overall excess of shear stress $(\tau - \tau_{cr})^{1.5} = 0.12$. Even if the shear stress acting on the bed is low, the relative size of the tracers over the average bed material assured a good mobility of the black spheres.

Advection and diffusion was observed for tracers originally placed in correspondence of strip 3. In this test it was in fact decided to add a larger surficial stripe of tracers in case the mobility

of tracers from the other two stripes had not been sufficient. Although this was not the case, the third strip turned out to be the most worked by the water (Figure 4.31). Strip 3 was 70 mm long on the outer wall and 55 mm long on the inner wall. It was also possible to notice that strip 1 was entirely covered by upstream moving material. The buried blocks instead have never been exposed. The experiment was run for 6 consecutive hours and the bed did not evolve into bedforms. This experiment provided very good results in terms of particles' transport, although a first screening of the acquired data revealed a temporal issue. As all tracers are coated black it is impossible to distinguish the original stripe the black spheres belong to when they cross a downstream strip. For instance, when a particle originally located in stripe 1 reaches and crosses stripe 3, it mixes with the mobile particles from stripe 3. This is potentially troublesome in the analysis of the concentration of particles along the flume length in time. With time, tracers of different stripes could have travelled further downstream and could be wrongly attributed to the tracers' cloud originating from another stripe.

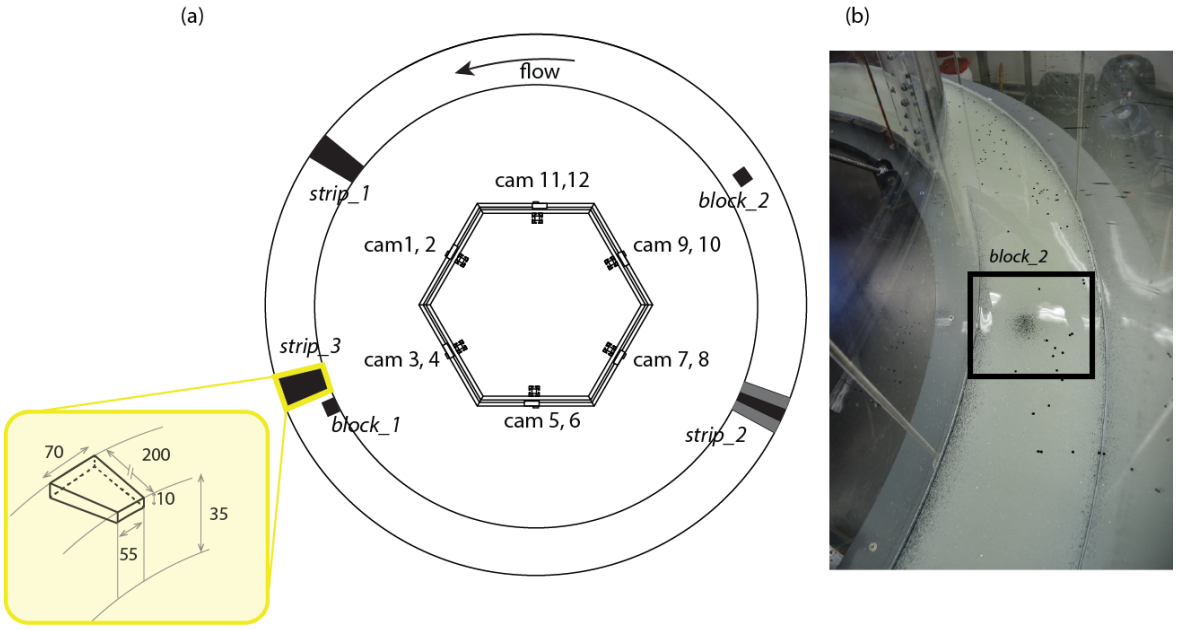


Figure 4.31: (a) Schematic representation of the initial set up with highlighted the new surficial stripe strip 3. (b) It is also reported an image of the bed after 6 hours of run for experiment E6 with details of the block 2 from above. All measurements are reported in mm.

### 4.4.4 Test E7: fine mixture, 4 mm coloured tracers, 18 hours

The results emerging from a preliminary analysis of the experiment E6 showed the necessity of performing longer-time experiments. In six hours the advection and diffusion of the tracers are outlined but limited. To avoid the temporal issue mentioned above, that is the impossibility to distinguish which strip the tracers originally belong to, three different colours of tracing particles have been used in E7. Around 1000 transparent spheres of size 4.00 mm were manually painted with two permanent markers, a green and a blue one. The grain surface were then as polished as for the black spheres and the permanent markers proved to be water resistant for few days. With this new set of sediment tracers experiment E7 was performed. The three stripes are arranged as in Figure 4.32 and they all are about 70 mm long in the tangential direction. The submerged blocks were moved close to each other with the introduction of a third one placed in proximity of the outer wall. This configuration is intended to study the uniformity of the transport and the vertical mixing along the radial direction.

The experiment was run under the same hydraulic conditions of the last two experiments E5 and E6, but for longer times. The three days run enabled the recording of the bed evolution for 6 hours a day for a total of 18 hours.

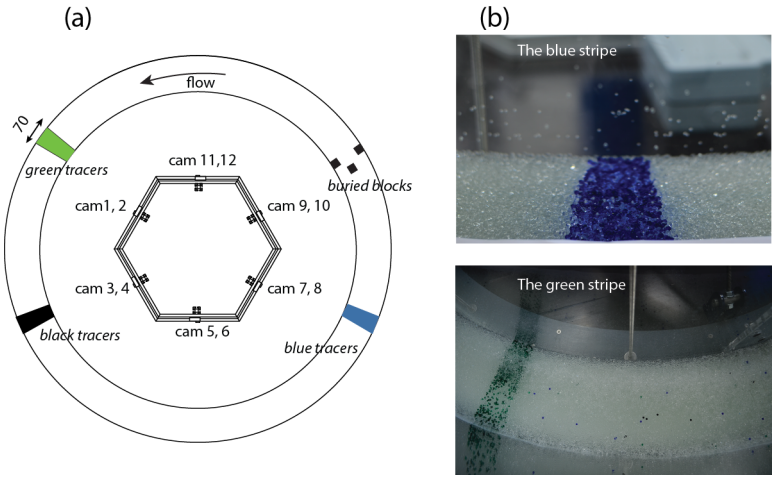


Figure 4.32: (a) Schematic representation of the initial set up with the new surficial stripes of different coloured tracers. (b) Image of the blue stripe at the beginning of the experiment and picture of the green stripe at the end of the 18 hours run.

### 4.4.5 Test E8: fine mixture, 4 mm black tracers, 12 hours

The 18 hours run of experiment E7 showed the temporal evolution of the advection and diffusion of the coloured particles. For this reason it was decided to run one last experiment, namely E8, to confirm the results. E8 was performed by the application of the same hydraulic conditions of E7. In this case, however, a single wider stripe made of black tracers of 4.00 mm diameter was used. The longer strip would provide a greater number of tracing particles contributing to the advective-diffusive flux so that the resulting concentration curves should contain more grain observations. To do so, a strip measuring 150 mm along the tangential direction was placed in the surficial layer of the bed as showed in Figure 4.33. The experiment was run for two consecutive days for a total of 12 hours. E8 was terminated after the observed advection and diffusion were well developed along the flume.

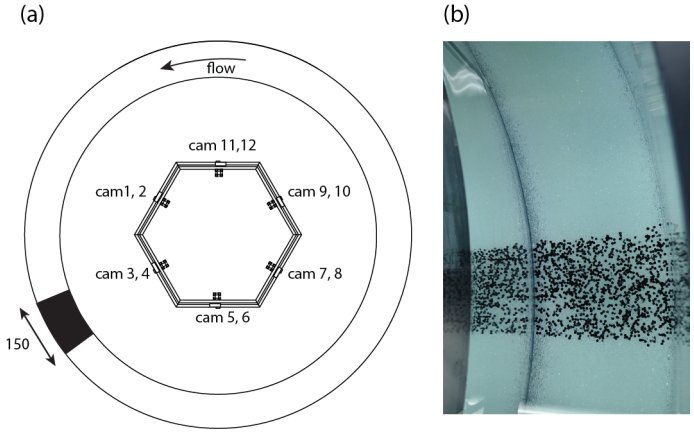


Figure 4.33: (a) Schematic representation of the initial set up with the single stripe of black tracers. (b) Image of the strip at the beginning of the experiment E8 taken from above.

## 4.5 Data analysis: GSLab software

The acquired images once corrected are now ready for the next phase of data analysis. First of all the trajectories of the black moving tracers have to be determined. With this information it will then be possible to derive statistically stable distributions of the step lengths and resting times. To obtain the location of each black sphere in every single frame the software GSLab is used. The software was originally developed by Bottacin-Busolin (see Bottacin-Busolin et al., 2008) to manually track the movement of gravel grains for videos recorded at 45 Hz. With the same software it was also possible to reconstruct gravel grains' trajectories in a similar work by Tregnaghi et al. (2012b). The software is denoted by a user-friendly interface which allows the visualization of the sequence of frames composing the video (Figure 4.34). The user can then detect the moving particles and attribute them information about their state, such as start at the entrainment location, move for the motion phase and stop for the resting position. By means of a recognition algorithm the software automatically identifies the same particle with a number. The final output is a database containing for each frame the number of detected particles along with their location $(x, y)$ in real-world coordinate system, their state (start, move or stop) and their identifying number.

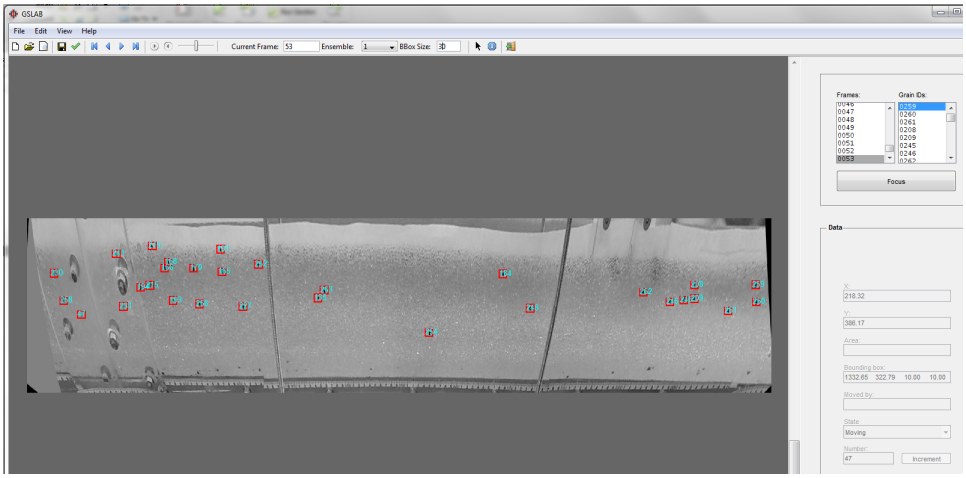


Figure 4.34: GSLab interface with black tracers identified with a number (light blue) and a red bounding box.

The software was adjusted to the size of the current images and to the frequency of frames acquisition, in this case equal to 30 Hz. The calibrated images extracted from every sub-video recorded by the GoPro cameras created the basis of the manual tracking. The possibility to develop a faster automatic tracking procedure was prevented by the shortage of time at the end of the experiments. Some efforts have been invested in the coding of a self-recognition algorithm, which in a preliminary stage revealed promising results. Other available software of automatic tracking, such as Streams203 (Nokes, 2012), were tested but they all showed some limitations. Firstly they miss the first particle's location at the entrainment instant as they detect moving particles by subtracting consecutive frames and identifying only the beads that changed their position. The sphere would then be identified when already in motion after the first hop. Secondly the quality of these images is reduced due to the different brightness noticeable in a series of frames taken by the same camera. This stems from the rotational system which is always in a different position with respect to the source of light. For this reason, structural elements, such as rods, bolts and parts of the union between Perspex boards, can be detected as moving objects in consecutive frames. All this additional noise would affect the tracking

results especially when it comes to recognise the same moving particle in following frames. The consequence is then the necessity of extra time to double-check the collected information. It was then reckoned that the use of GSLab was a reasonable choice to obtain reliable results.

The large amount of data collected for each test, together with the time-consuming nature of the tracking activity, has compelled the current research to devote all the efforts towards the analysis of one test. The results presented in the following chapters are then referring to the analysed experimental data of a single test. To give an example of the data resulting from the tracking activity, in Figure 4.35 a group of trajectories is shown. Connecting the consecutive positions $(x, y)$ occupied by a tracer, as they were recorded manually in GSLab and afterwards corrected to account for the compression-extension error, provides the path of the sphere over the bed. The detailed plot in Figure 4.35 zooms in to focus only on fewer trajectories so that the locations of distrainment, labelled as *Stop* in the tracking procedure (coloured dots), could be highlighted along the path of a tracer. It is interesting to notice the variety of different trajectories, some of them denoted by several reposing phases (e.g. light blue trajectory in detailed plot) and others of continuous motion for more than 100 mm in longitudinal direction (e.g. orange trajectory in detailed plot). The distance between two consecutive resting positions occupied by a grain along its path supports the derivation of the longitudinal and transversal step length, respectively $r_x$ and $r_y$, as described in the detailed plot. The longitudinal distance covered by a tracer is greater than the transversal displacement, confirming that the movement occurs mainly along the longitudinal direction with a crosswise deviation probably due to the different bed arrangements encountered along the trajectory.

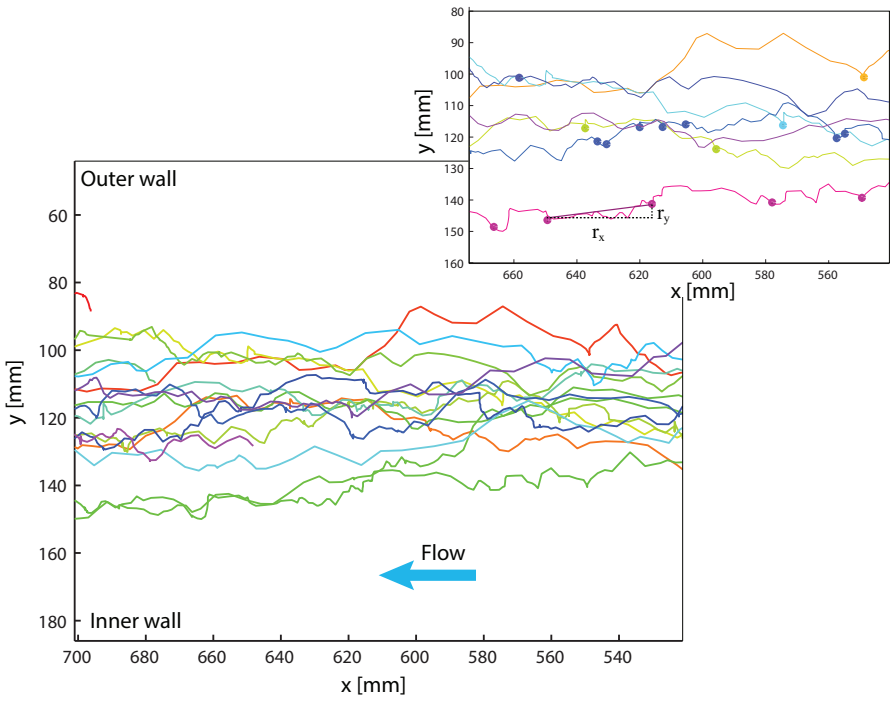


Figure 4.35: Example of tracing particles' trajectories resulting from the tracking activity. The detailed plot focuses on a fewer grains' paths to show the distrainment location (dots) and the extension of the step length

The collected information of the series of position occupied by the tracing particles in time over the erodible bed will create the basis for the Lagrangian analysis that is presented in the next chapter.

# Chapter 5

# Experimental results: Lagrangian analysis

The information gathered on grain movement with the support of the GSLab software has been processed in order to describe the trajectories of the black tracer particles that have moved. The work to process the data required significant manual tracking so analysis focussed on images collected in Experiment E6. This experiment was selected as initial visual screening indicated that the collected images were characterized by a large number of moving particles and they clearly showed the advective and diffusive pattern of tracers. The bed did not evolve into bed-forms maintaining a fairly flat surface as the former experiment E5, which is denoted by the same hydraulic conditions but different tracers size. On a future perspective, comparison between the results provided by experiment E6 and E5 would help addressing the influence of the relative size of the moving grains, $d_T/d_{50}$, in the transport process. In the meantime the analysis of experiment E6 is intended to prove the conceptual framework proposed in this study.

Images from camera 4 located above the stripe 3 (see Fig. 4.31 in the previous chapter) were extracted, corrected to remove distortion, and analysed in GSLab. The 1-meter-long area covered by the camera's lens resulted in a long enough area to fully describe the trajectories of all particles, so that all the motion states were identified within the image boundaries. In this case there were no *Move-Move* displacements recorded as all tracers completed their trajectories from entrainment (*Start*) to deposition (*Stop*) inside the measurement area.

Table 5.1: Experimental parameters namely friction velocity $u^*$, bed shear stress $\tau$, Shields' parameter $\tau^*$, excess of shear stress $(\tau - \tau_{cr})^{1.5}$. The duration of the experiments is reported in hours. Information on the mean bed diameter, $d_{50}$, and size of tracers $d_T$ is also presented.

| TEST | $u^*$ | $\tau$ | $\tau^*$ | $(\tau - \tau_{cr})^{1.5}$ | Duration | $d_{50}$ | $d_T$ |
|---|---|---|---|---|---|---|---|
| | [m/s] | [Pa] | [-] | [Pa] | [hours] | [m] | [m] |
| E6 | 0.046 | 2.141 | 0.055 | 0.119 | 6.0 | 0.0032 | 0.004 |

The recorded session lasted for about 6 hours which corresponds to 648000 frames. It appeared immediately impracticable to manually track particles frame by frame for the entire duration of the experiment. For this reason 14 sub-sessions of variable length were extracted to be subsequently analysed with the tracking software. The majority of them consisted of 12000 frames, i.e. 400 s, with the longest one extending to 22800 frames (= 760 s), in order to obtain stable statistics of step lengths and resting times as it is shown later on. In doing so, it was also possible to compare the statistical results at different stages of the experiment and to observe a possible evolution with time of the motion parameters characterizing the trajectories. Table 5.2

presents the summary of the number and duration of the extracted sessions. When the number of black tracers originating from the stripe started reducing, so did the number of mobile traceable spheres, and the extraction was stopped at about 275 minutes from the beginning of the steady flow conditions. The processed frames produced a well-populated database made of 242 traced particles, each of them moving along trajectories consisting on average of 9 *Start-Stop* displacements as the cameras were operating at a sampling frequency at 30 Hz.

Table 5.2: Extraction summary of the 14 sub-sessions with respective time of start and stop of analysis, number of extracted frames and duration of analysis in minutes.

| SUB-SESSION | Start [s] | Stop [s] | Start [min] | Stop [min] | Number of extracted frames | Extracted duration [min] |
|---|---|---|---|---|---|---|
| 1 | 80.00 | 483.00 | 1.33 | 8.05 | 12090 | 6.72 |
| 2 | 633.00 | 723.00 | 10.55 | 12.05 | 2700 | 1.50 |
| 3 | 1203.00 | 1443.00 | 20.05 | 24.05 | 7200 | 4.00 |
| 4 | 4169.00 | 4479.00 | 69.48 | 74.65 | 9300 | 5.17 |
| 5 | 4889.00 | 5172.00 | 81.48 | 86.20 | 8490 | 4.72 |
| 6 | 5232.00 | 5652.00 | 87.20 | 94.20 | 12600 | 7.00 |
| 7 | 5807.00 | 6567.00 | 96.78 | 109.45 | 22800 | 12.67 |
| 8 | 7350.00 | 7750.00 | 122.50 | 129.17 | 12000 | 6.67 |
| 9 | 8298.00 | 8698.00 | 138.30 | 144.97 | 12000 | 6.67 |
| 10 | 10351.00 | 10751.00 | 172.52 | 179.18 | 12000 | 6.67 |
| 11 | 11424.00 | 11824.00 | 190.40 | 197.07 | 12000 | 6.67 |
| 12 | 13347.00 | 13747.00 | 222.45 | 229.12 | 12000 | 6.67 |
| 13 | 14550.00 | 14950.00 | 242.50 | 249.17 | 12000 | 6.67 |
| 14 | 16113.00 | 16513.00 | 268.55 | 275.22 | 12000 | 6.67 |

## 5.1 Diffusive regimes associated to particles' trajectories

With the available information on particles' location in time and space it is now possible to perform the analysis proposed in Chapter 2 about the diffusive regimes associated to the different stages of the trajectories. The conceptual model proposed by Nikora et al. (2002) distinguished three different ranges of particles motion, namely local range, intermediate range and global range. Each of these ranges was associated to a different type of diffusive regime, respectively ballistic diffusion, anomalous diffusion (being it superdiffusive, subdiffusive or normal) and subdiffusion. The type of diffusive regime is indicated by the growth of the second order moment of the particles' location in time, which can be expressed by the scaling coefficient $\gamma_{x,y}$ as follow:

$$\frac{\overline{X'^2}}{d^2}, \frac{\overline{Y'^2}}{d^2} \propto \left(\frac{tu^*}{d}\right)^{2\gamma_x,\gamma_y} . \tag{5.1}$$

Differently from the previous experiments (Tregnaghi et al., 2012), the longer investigated area did not produce incomplete trajectories in the form of *Move-Move* grain actions. In this experiment any tracer's path, from entrainment to distrainment to the following entrainment and distrainment event and so on, could be entirely followed in time and space. To perform a consistent analysis only the sub-sessions of duration greater or equal to 400 s have been considered, i.e. in Table 5.2 sub-sessions 1 and from 6 to 14. In doing so, the sub-databases could be joined together to obtain a uniform analysis of 400 s duration. This together with the

greater areal extent enables the same particles to be followed for a longer part of its trajectory as it can be seen in Figure 5.1.

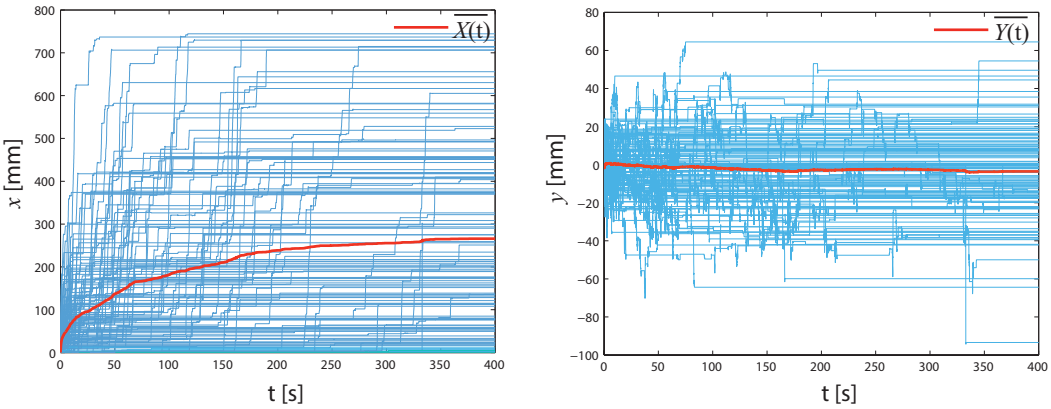


Figure 5.1: Particles' longitudinal and transversal trajectories in 400 seconds analysis. The red line indicates the location of the first order moment of particles' location in time.

The transversal trajectories plotted in Figure 5.1 demonstrate the adequate calibration performed with the annular flume in the attempt to minimize the near bed secondary currents. The ensemble first order moment along the crosswise direction is nearly zero (with time averaged value equal to -0.32 mm) and the trajectories are symmetrically spaced, which means that particles do not follow any preferential path towards either the outer or the inner wall of the channel during the 400 seconds of analysis.

Following Equation 5.1, the single trajectories have been referred to the same starting point in time and space so that the second moments of particles coordinates could be derived and plotted versus $(tu^*/d)$ in log-log scale to determine the scaling coefficient $\gamma_{x,y}$. The diameter $d$ indicates the size of the moving particles, that is $d_T$ in the present case. Figure 5.2 shows the growth in time of particles' diffusion along the streamwise and transversal directions.

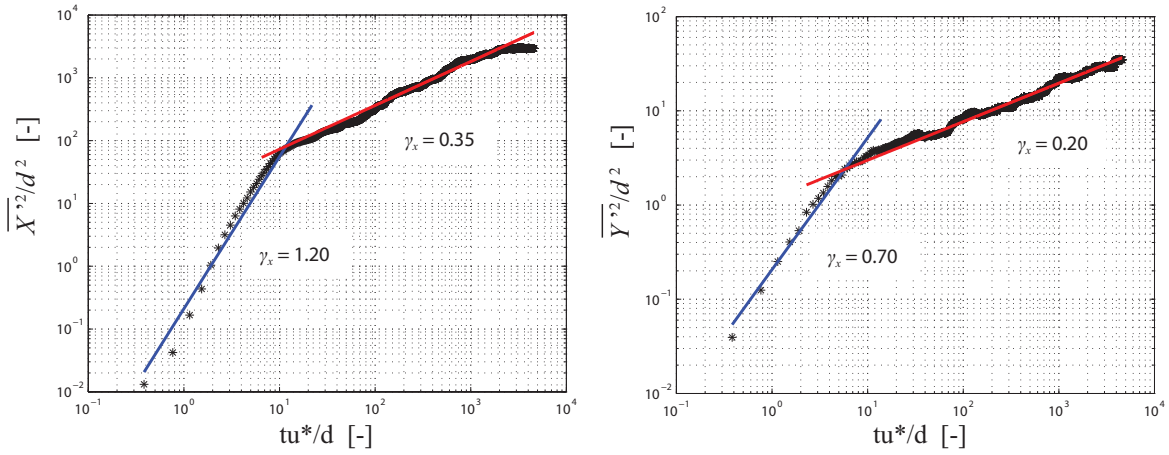


Figure 5.2: Change in time of the longitudinal and transversal dimensionless second order moment of particles coordinates. The two motion ranges are represented along with the best linear fit of diffusion scaling coefficients.

Similarly to the results presented in Chapter 2, two types of diffusion are evident in Fig. 5.2. The first stage of motion is denoted by a ballistic diffusive regime along the streamwise direction with the scaling coefficient slightly larger than 1, i.e. $\gamma_x = 1.20$. At this stage lateral diffusion

shows an anisotropic behaviour with $\gamma_y$ smaller than 1, that is $\gamma_y = 0.70$, in good agreement with the previous analysis of Tregnaghi et al.'s data. The greater value of the longitudinal scaling coefficient obtained here could stem from the initial acceleration phase of motion characterized by superballistic diffusion. As can be noticed in Figure 5.3, the derivation of $\gamma_x$ for adjacent values of the second order moments reveals peaks in the value of $\gamma_x$ up to 2, as reported also by Bialik et al. (2012) and Campagnol et al. (2015). The transition between the superballistic diffusive regime and the ballistic one happens at approximately $tu^*/d = 3.16$, very close to the one observed with the experimental data of Tregnaghi et al. (2012), i.e. $tu^*/d = 3.20$.

The ballistic diffusion is then followed by a regime of subdiffusion. The anomalous diffusive part associated to the intermediate range, that was proposed in the conceptual model and identified as a transient region in Chapter 2, has now been completely replaced by a subdiffusive regime denoted by $\gamma_x = 0.35$ and $\gamma_y = 0.20$. These values, especially the longitudinal one, closely follow the scaling coefficient $\gamma_x = 0.33$ that was obtained from the reformulation of Drake et al.'s experimental data carried out by Nikora et al. (2002). More noteworthy is the change in diffusion type between the first ballistic regime and the subsequent subdiffusive regime. In the present analysis the two linear fits meet for $tu^*/d = 11.74$, which falls between the (i) $tu^*/d = 9$ and the (ii) $tu^*/d = 15$ corresponding respectively to (i) the intersection between the ballistic and the subdiffusive fitting presented in Chapter 2 from Tregnaghi et al.'s data, and (ii) the transition from the intermediate to the global range denoted by subdiffusion in Nikora et al.'s (2012) work. The three datasets examined present similar values of dimensionless time parameter $tu^*/d$ associated to the beginning of the longitudinal subdiffusive regime. The same correspondence is found with the current data and the analysis in Chapter 2 for the crosswise diffusion. The end of the lateral superdiffusion and beginning of subdiffusive regime takes place for $tu^*/d = 5.75$ in the annular flume data and for $tu^*/d = 5.62$ in Tregnaghi et al.'s experiment. No correspondence was found with the transverse diffusive analysis presented by Nikora et al. (2012).

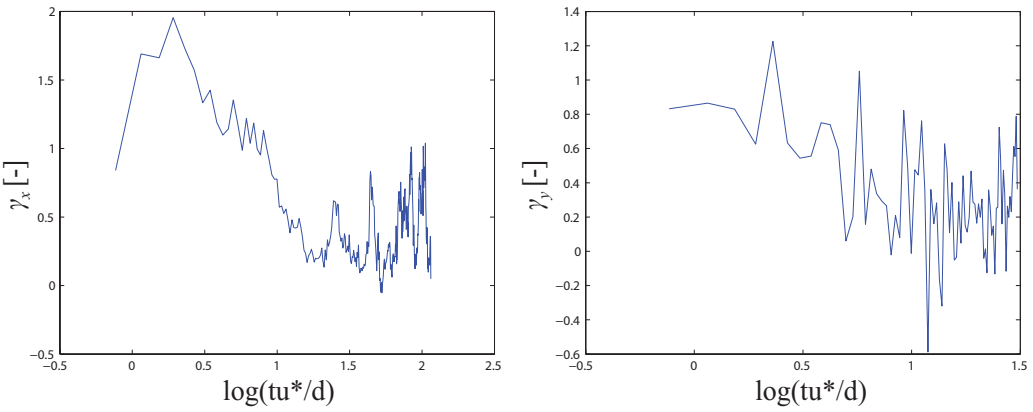


Figure 5.3: Semi-log plot of the variation of the longitudinal and transversal diffusive coefficients scaled to the dimensionless time, $tu^*/d$.

The erratic nature characterizing the first instants of particles' motion is confirmed here by the scattered values of the normalized Skewness and Kurtosis (Figure 5.4). The third order moment of particles' locations is found greater than zero along the streamwise direction as also reported in Chapter 2 and in Campagnol et al. (2015), whilst it varies around zero for the crosswise component of the trajectories. Differently from the previous studies, the longitudinal and transversal normalized third and fourth moments tend to fluctuate in time without approaching

an asymptotic stable value. This is particularly evident in the case of the Kurtosis, whose great variability indicates the presence of infrequent extreme observations in the particles trajectories. The bed arrangement in the current experiment can be responsible for such irregular trend that could only emerge in experiments where the sampling time interval and the size of the observation area are no longer limited. The experiments reported in Chapter 2 as well as the work presented by Campagnol et al. was performed over a bed consisting of uniform material whilst the sediment mixture in the annular flume included particles of different sizes, ranging from 2.20 to 4.30 mm diameter. The small, but significant, heterogeneity of the bed material could be responsible for a minor group of particles' trajectories that deviates from the average causing the observed variability in the Kurtosis values. In graded beds where different classes of material are mixed together, two particles starting from the same point can encounter different roughness elements along their path, leading them to follow divergent paths. The initial erratic phase of the transport would then extend to a longer portion of the particle's history.

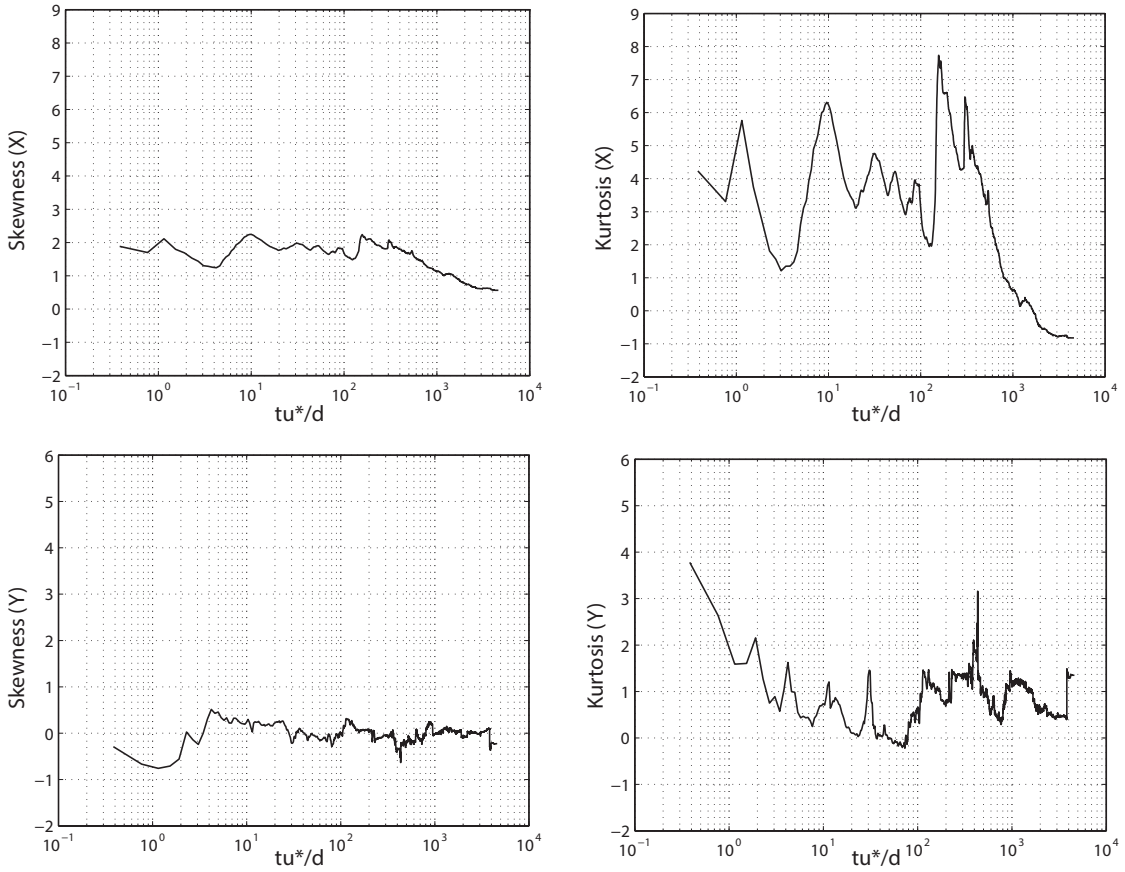


Figure 5.4: Normalized Skewness and Kurtosis for the longitudinal and transversal particles' position.

The data collected in the annular flume has enabled a more complete analysis of particle motion to that started in Chapter 2 by overcoming the previous issues, such as the incomplete trajectories, the limited temporal sampling, and the influence of bed roughness. To summarize, diffusion has been confirmed to be anisotropic with a ballistic diffusive regime associated to the first stage of particles motion along the streamwise direction, $\gamma_x = 1.21$, and a superdiffusive regime on the lateral particles' positions, $\gamma_y = 0.70$. The ballistic regime is preceded by a short acceleration phase ($tu^*/d < 3.16$), where the diffusion is superballistic ($\gamma_{x,y} > 1$). At the end

of the ballistic regime a subdiffusion takes place along both coordinates, $\gamma_x = 0.35$ and $\gamma_y = 0.20$. The initiation of the longitudinal subdiffusive regime is associated to a characteristic non-dimensional time, $tu^*/d \approx 12$, which is in close agreement with previous findings, $tu^*/d = 15$. Along the $y$-coordinate the transition between the superdiffusive and subdiffusive regime occurs earlier, for $tu^*/d = 5.75$, as in the case of Tregnaghi et al.'s data. The complete description of the entire trajectories thanks to the longer dimension of the investigated area and the greater time window has allowed the subdiffusion associated to the later stage of particles motion to be fully observed and derived. The frequency of image acquisition, 30 Hz, has been showed to be good enough to also capture the ballistic and superballistic regime. A sign of the bed roughness influence on the particles' path is visible in the evolution of the Skewness and Kurtosis with time. It is the fourth order moment in particular to reflect the erratic nature of the bed-load transport as it accounts for those infrequent particles whose trajectories significantly deviate from the *average* behaviour.

## 5.2 Statistics of particles' trajectories

The new database of the test E6 consisting of the individual trajectories of the group of black spheres is of great importance in the derivation of the statistics of particles' motion, such as the travelling distance, the time spent in motion and the time resting on the bed, and the particle velocity. Particles' states have been labelled according to the previous analysis, so that entrainment corresponds to *Start*, motion to *Move* and distrainment to *Stop*. All the recorded displacements occurred within the field of view of the 1-meter-long investigated area. Particles left the measurement area with time, but the long sampling window (on average 400 s) ensured several sequences of motion states covered for each tracked sphere. This has created a unique database with complete trajectories where parts of tracer particles' paths are no longer missing.

To facilitate the manual tracking, it was decided a priori to set a minimum resting time. As a particle in motion is often observed to stop without achieving a complete state of rest, it will be labelled as *Stop* when it maintains the same position for at least 3 frames, i.e. 0.1 s. This is a choice that can be revised during the analysis as shown hereafter, but it helped in the manual process as rule of thumb to distinguishing between continuous motion and rest. In the detection of an entrainment event the tracking software can automatically recognise the new particle as an already tracked one that had previously stopped in the same location. To make sure that the sphere is correctly attributed to the former labelling number the user went backwards of at least 1000 frames ($\approx$ 35 s). If the new tracer is indeed the old stopped one, it will be identified with the same number, otherwise it will be considered as a new entrained grain. Due to the considerable number of frames analysed in each sub-session, it was impractical to rewind the entire session every time a new entrainment was associated to a previous detected sphere. The time interval of at least 1000 frames was reckoned to be appropriate in this analysis to both saving time and creating a consistent database.

### 5.2.1 The step length

In this work the step length has been defined as the longitudinal distance travelled by a grain from the entrainment to the instant it stops on the bed and rests. In order to present results on both the streamwise and lateral step length, in this section the definition comprehends also the lateral component of the travelled distance, so that $r$ is denoted by a longitudinal step $r_x$ and a transverse one $r_y$. According to the analysis presented in Chapter 2 and the literature in this

field (e.g. Campagnol et al., 2013), the definition of step length discarded the so called shakes, i.e. an adjustment of position denoted by a longitudinal step lower or equal to the particle's diameter. From the analysis of the extracted sub-sessions it was possible to derive the statistics, mean and standard deviation, of the longitudinal and transversal component of the step length with time as showed in Figure 5.5. The temporal trend is then compared to the overall statistics that account for all the sub-sessions together (dashed red line in Figure 5.5). It is interesting to note that the mean values slightly fluctuate around the ensemble mean step length showing no visible trend for all these parameters throughout the 6 hours run.

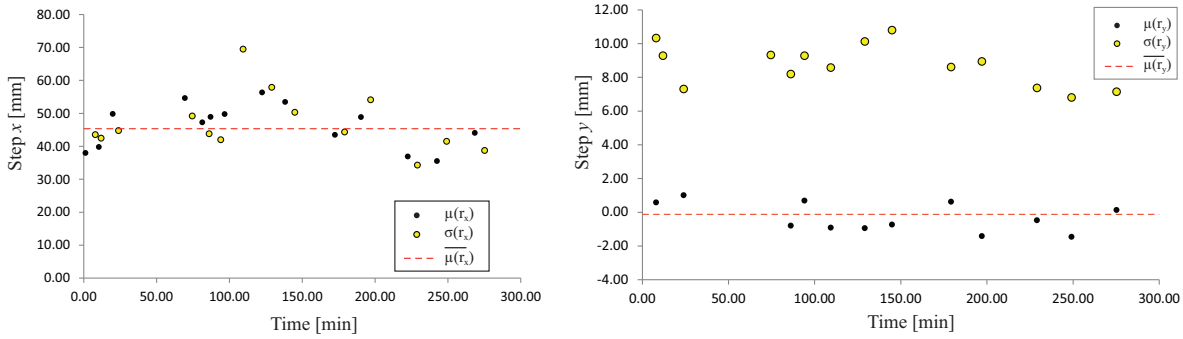


Figure 5.5: Mean and standard deviation of longitudinal and crosswise step lengths derived in each sub-session. The average values are compared to the ensemble mean step length (dashed red lines).

The confirmed stability of the step length in time has allowed the merging of the individual sub-sessions into a unique database of more than 1400 steps, which will constitute as a basis for the following analysis. The longitudinal steps are distributed as shown in Figure 5.6 with mean value $\mu(r_x) = 46.16$ mm and standard deviation $\sigma(r_x) = 48.26$ mm. The database is so well populated to clearly obtain stable grain statistics (Fig. 5.6).

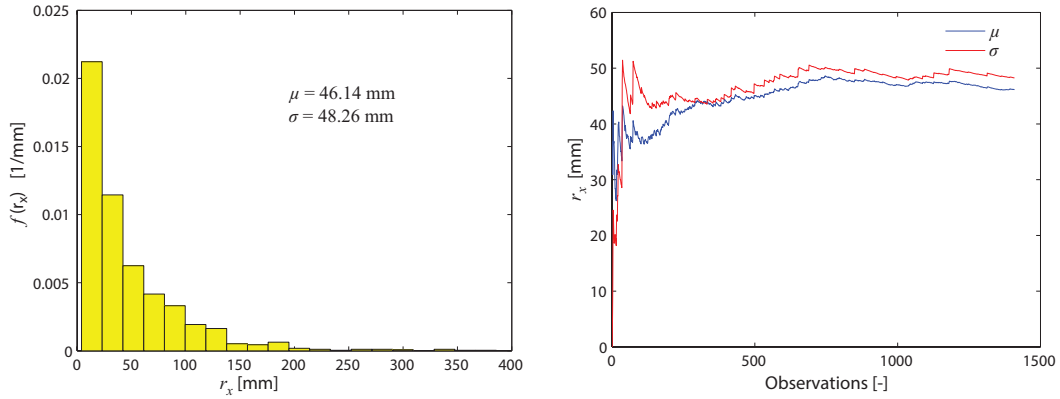


Figure 5.6: Frequency distribution of the longitudinal step lengths and the variation of the statistics as a function of the number of observations.

The frequency distribution has then been fitted with three probability functions, i.e. Gamma, Weibull and Lognormal distributions, following the analysis presented in Chapter 2. Contrarily to the previous analysis, the distribution is not truncated as all steps occurred within the investigated area. The three models well describe the experimental data both in terms of the cumulative and the probability density functions (Fig. 5.7). To better appreciate the fitting accuracy of each distribution the MSE (mean squared error) has been derived for each function (Table 5.3 reports the same analysis also for the other variables defining the grains' motion),

proving that on the CDF plot the Lognormal is the most accurate, while in the case of the PDF the Weibull is characterized by the lowest error. The errors attributed to each function are although very similar, so that both Weibull and Lognormal can be considered as a good approximation of the experimental data.

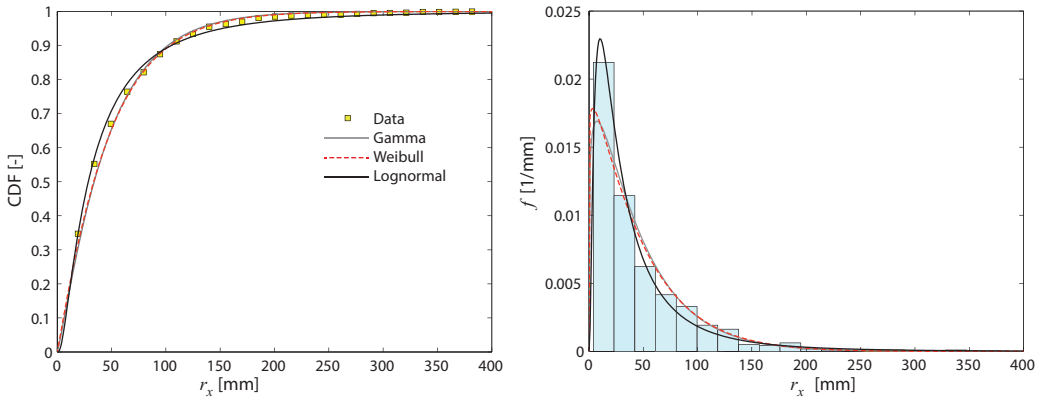


Figure 5.7: Cumulative and probability frequency of longitudinal step lengths with the three fitting functions, namely Gamma (grey line), Weibull (dashed red line) and Lognormal (black line).

The analysis of the crosswise step lengths proved once again the goodness of the preliminary calibration phase of the annular flume. The influence of the secondary currents should be visible in the transverse component of particles' steps with any resulting preferential trajectory towards the inner or the outer boundary of the channel. Figure 5.8 shows that the crosswise steps symmetrically distribute around zero, with an average value of -0.22 mm, i.e. the 5% of the sphere's diameter. This is a further confirmation of the attainment of a laterally uniform flow condition in proximity of the flume bed.

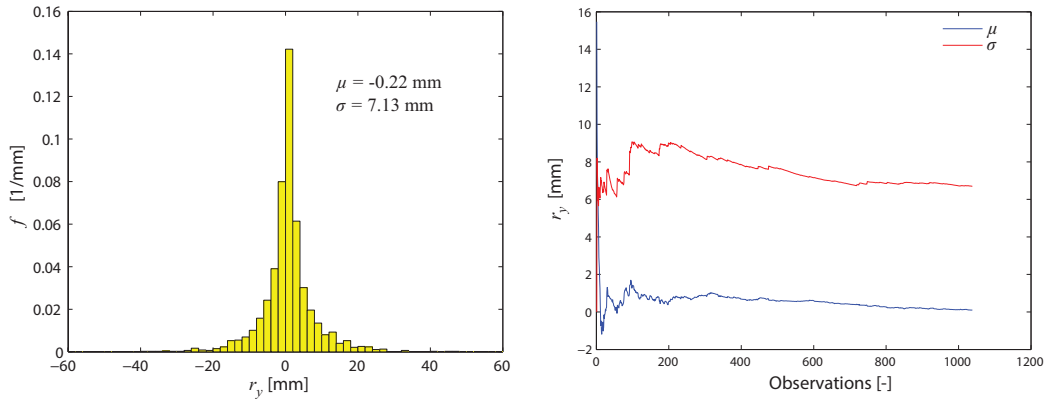


Figure 5.8: Frequency distribution of the crosswise step lengths and the variation of the statistics as a function of the number of observations.

Table 5.3: Fitting parameters, mean and standard deviation, of the three functions applied to the frequency data of the trajectory's parameter, i.e. longitudinal steps length, travelling time and particles' velocity. The MSE values are reported for the PDF and the CDF fitting for each model.

| | Longitudinal Step [mm] | | | | Travelling time [s] | | | | Particle velocity [m/s] | | | |
|---|---|---|---|---|---|---|---|---|---|---|---|---|
| | $\mu_{fit}$ | $\sigma_{fit}$ | MSE PDF $(\cdot 10^{-5})$ | MSE CDF $(\cdot 10^{-3})$ | $\mu_{fit}$ | $\sigma_{fit}$ | MSE PDF $(\cdot 10^{-1})$ | MSE CDF $(\cdot 10^{-3})$ | $\mu_{fit}$ | $\sigma_{fit}$ | MSE PDF $(\cdot 10^{-5})$ | MSE CDF $(\cdot 10^{-3})$ |
| Gam | 46.1 | 42.3 | 4.6 | 5.7 | 0.88 | 0.52 | 2.2 | 4.7 | 45.7 | 24.7 | 4.7 | 0.4 |
| Weib | 6.2 | 43.7 | 3.0 | 4.1 | 0.88 | 0.59 | 2.3 | 10.1 | 45.9 | 24.4 | 5.3 | 2.5 |
| Logn | 47.9 | 64.2 | 7.3 | 3.9 | 0.88 | 0.55 | 2.0 | 0.3 | - | - | - | - |

### 5.2.2 The travelling time and velocity

The travelling time associated to the above step lengths is shown in Figure 5.9. Differently from the previous analysis carried out for the experimental database collected by Tregnaghi et al. (2012b), here the available information of the fully-described trajectories has allowed the derivation of the correct statistical description of the particles' travelling time. Particles move for an average time of $\mu(\tau_p) = 0.88$ s with standard deviation $\sigma(\tau_p) = 0.58$ s.

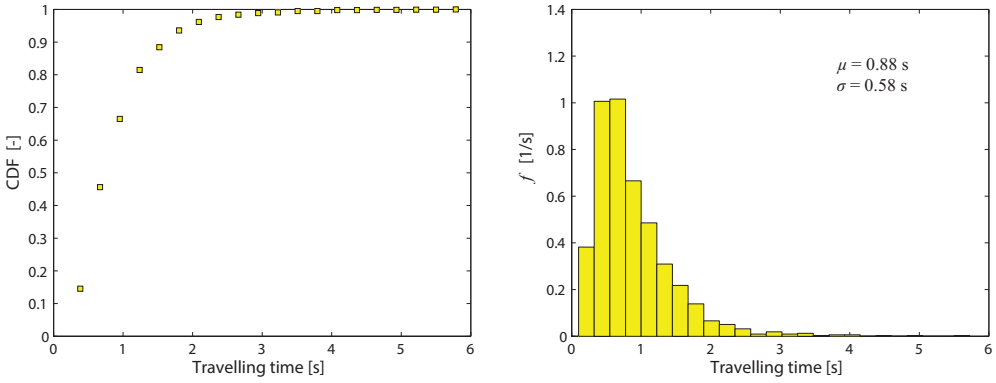


Figure 5.9: Cumulative and probability frequency distribution of particles' travelling times.

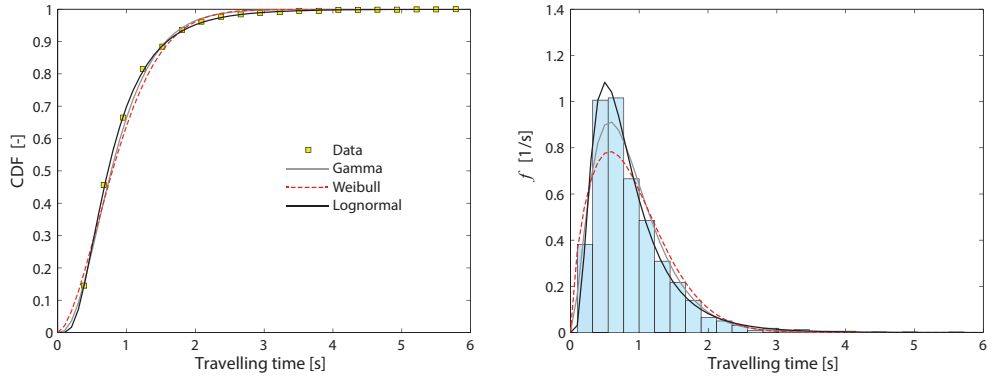


Figure 5.10: Fitting results of the three distributive functions, i.e. Gamma (grey line), Weibull (dashed red line) and Lognormal (black line), to the travelling time frequency data.

The cumulative and probability frequency data has then been described with three functions, Gamma, Weibull and Lognormal (Figure 5.10). The fitting of the lognormal distribution results as the most accurate in both CDF and PDF calculations as can be seen in the values of MSE presented in Table 5.3. A lognormal distribution is able to match the measured peak observed in the frequency density plot, as well as the right-tailed shape of the least frequent values as can been observed in the cumulative density graph.

Knowing the step lengths and the travelling time, it is possible to calculate the particles' velocities. The distribution of the frequency data is presented in Figure 5.11.

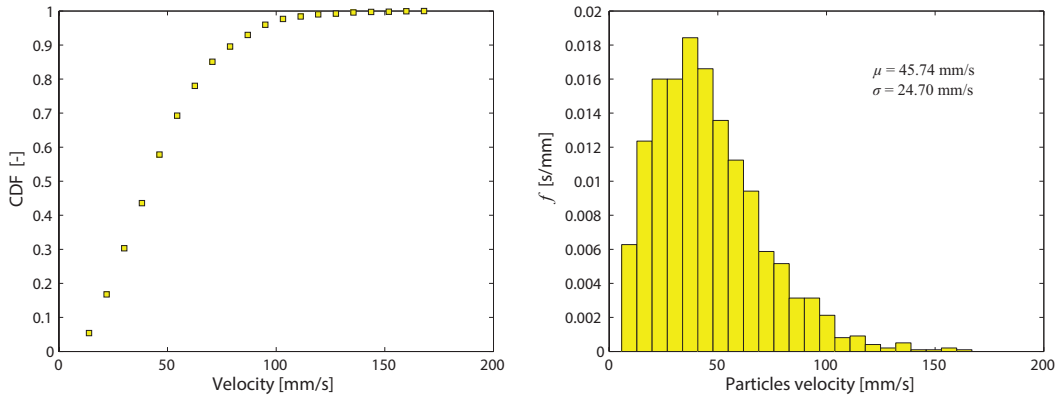


Figure 5.11: Cumulative and probability frequency distribution of particles' velocity.

When a Gamma-like and a Weibull distributions are used to fit the experimental frequency data, the gamma model shows to be the most appropriate as it is characterized by the lowest values of MSE both on the CDF and PDF calculations (Table 5.3). This is particularly true for the cumulative plot, where the error associated to the Gamma function is one order of magnitude smaller than the Weibull's one. The lognormal is not presented here as it poorly fitted the distribution of the particles' velocity. The ensemble averaged streamwise velocities of bed-load tracers resulted equal to 45.74 mm/s with standard deviation $\sigma_{v_p} = 24.70$ mm/s. In Chapter 2 Section 2.4.2 it was assumed that the ensemble particles' velocities as well as the velocities referring to a specific value of step length distribute accordingly to a Gamma distribution. This is now confirmed with the new dataset of un-truncated trajectories. The variables named travelling time and particles' velocity will be further investigated in the sections to come.

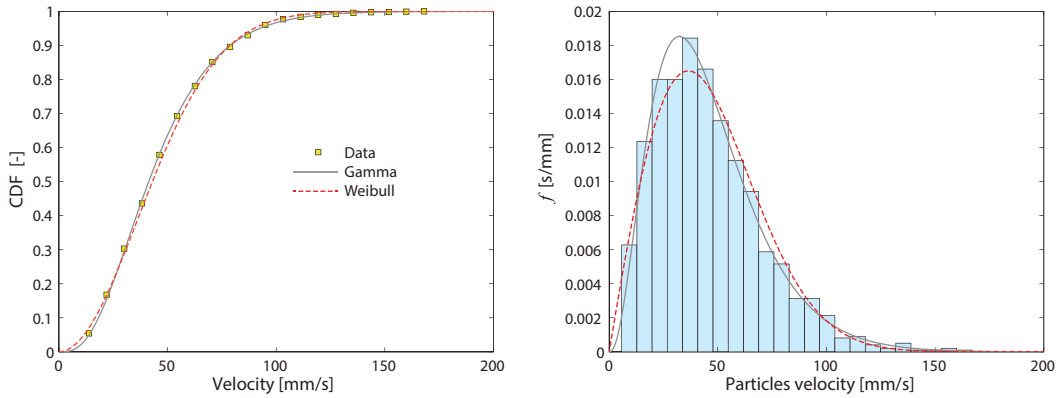


Figure 5.12: Fitting results of the two distributive functions, i.e. Gamma (grey line), Weibull (dashed red line), to the particles' velocity frequency data.

### 5.2.3 The resting time

The particle resting time is defined as the time interval from the distrainment of a particle to its next entrainment event. The description of the resting time results then intrinsically difficult due to the definition itself. It is surely limited to the temporal interval considered. A particle still at rest at the end of the analysis can be actually characterized by a much longer waiting time than the calculated one because we do not track its future movements. The value of the resting time is also depending on the duration of the experiment. This is particularly true in the case of the annular flume, where particles could hypothetically experience entrainment and distrainment for as long as the flume is kept in motion. Some of those particles, if buried in time within the bed domain, could occupy the same resting position even for hours. There is also the case of particles that moved at the very beginning of the experiment and, after having stopped, never experienced a second entrainment event. To obtain a significant description of the resting time population and to get closer to stable statistical values, one should extend the analysis in time but an indefinite extension of the sampling interval is impractical from a tracking point of view.

With the annular flume it is possible to track the same group of particles for the entire duration of the experiment, i.e. 6 hours, by following their path in consecutive cameras, and this would help to account for also the infrequent extreme values of resting times. For the time being, it was reckoned more reasonable to analyse the sub-session of the video, instead of focusing on the entire 6 hours recording. From an initial plan of short sub-sessions, it was noticed that stability of the resting time was achieved for sampling interval of about 6 minutes (400 s). An extra extended session (7 in Table 5.2) of 12 minutes was added to compare the statistics of resting time and to attain a more comprehensive description of the phenomenon.

Figure 5.13a presents the evolution in time of the mean and standard deviation when all the resting times occurring within the temporal window of the analysis are considered, that is the time between a *Stop* and the next *Start* of a tracked particle. The same analysis is performed also when a minimum resting time, in this case $t_{\mathrm{THR}} = 1$s, is imposed between distrainment and the following entrainment (Figure 5.13b). In both plots, the temporal values fluctuate around the ensemble average resting time, without showing any particular trend with time.

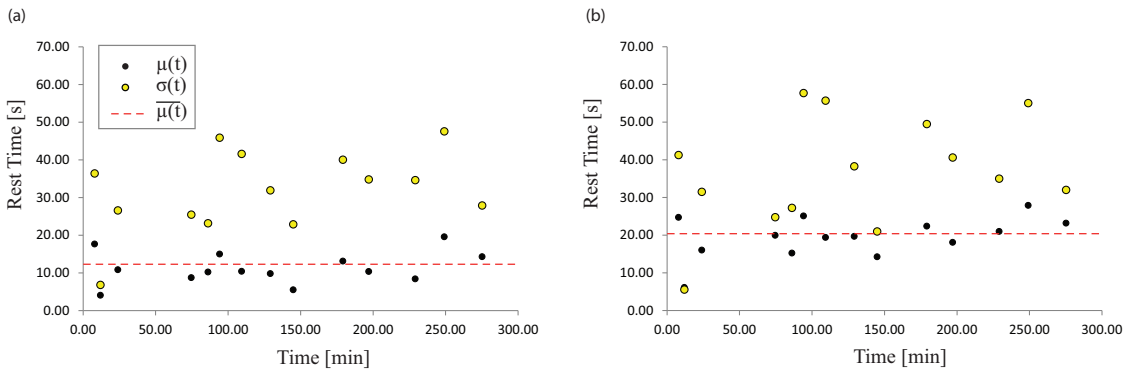


Figure 5.13: Mean and standard deviation of (a) all resting times and (b) resting times greater than 1 s, derived in each sub-session. The average values are compared to the ensemble mean step length (dashed red lines).

By imposing a threshold on the resting time, the statistics increase in value. This is evident in the derivation of the distribution frequency plot (Figure 5.14 and 5.15). When all the resting times are included in the analysis the mean value is $\mu(t) = 11.39$ s, and standard deviation $\sigma(t) = 36.51$ s, whilst in the case of minimum resting time of 1 s, the mean and standard

deviation become respectively $\mu(t) = 20.26$ s and $\sigma(t) = 44.21$ s. The choice of 1 s-threshold is based on two considerations. First, the resting time is defined as the time spent by a particle at rest after a collision with the bed significant enough to trap the grain for a time larger than the time scale of motion (Bradley et al., 2010). In this experiment the relative travelling time is denoted by a mean value of 0.88 s, so that a minimum resting time of 1 s is larger than the average time scale of motion. Secondly, recalling the results presented on the diffusive regimes (Section 5.1) the transition between the ballistic and the global range takes place for $tu^*/d \approx 12$, which corresponds roughly to $t = 1$ s. Imposing a threshold of 1 s as minimum resting time would assure that the grain motion is no longer in the local range, discarding so the motion time scale associated to the continuous movement of grains (Nikora et al., 2002; Bradley et al., 2010). It is interesting to notice that the statistical values obtained for the longest sub-session 7 ($\approx$ 12 minutes analysis) are well aligned with the statistics of the other sub-sessions and of the whole dataset, i.e. $\mu(t) = 10.41$ s and $\sigma(t) = 41.57$ s for the case of no threshold, and $\mu(t) = 19.37$ s and $\sigma(t) = 55.66$ s for the case of 1 s threshold. Doubling the duration of the analysed interval did not correspond to longer average resting times. Sub-session 7 is although characterized by the longest resting time, i.e. 544 s, which is probably reflected in the values of standard deviation observed for this sub-session, among the largest measured (increase of respectively 14% and 26%).

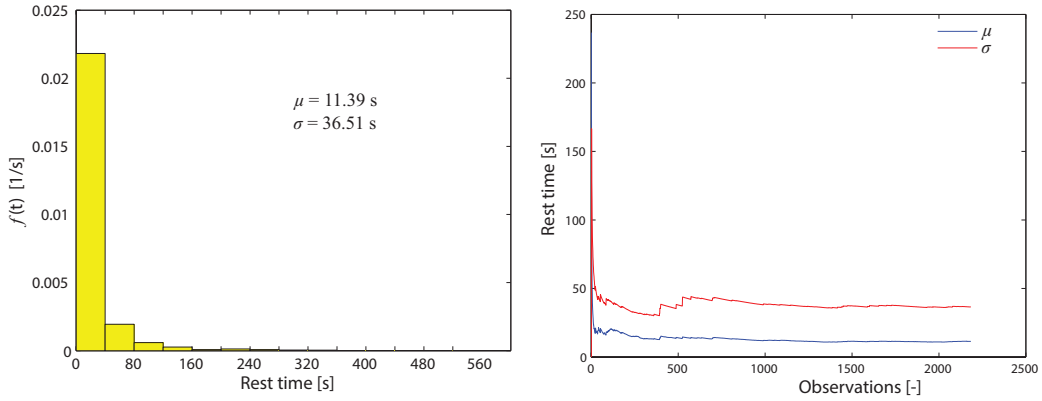


Figure 5.14: Frequency distribution of all the resting times with the variability of the statistical values as a function of the number of observations.

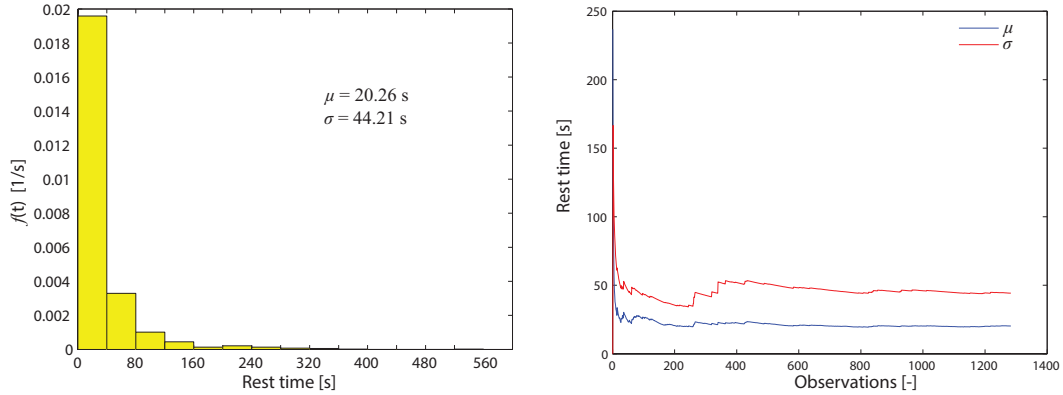


Figure 5.15: Frequency distribution of the resting time greater or equal to 1 s with the stability of the statistical values as a function of the number of observations.

The analysis of the database indicated a group of particles that, once stopped on the bed,

never observed an entrainment event again. For this group of particles the resting time cannot be univocally calculated as one can only say that they rest for at least a time equal to $t_{\text{end}} - t_{\text{stop}}$, with $t_{\text{end}}$ being the end of the analysis and $t_{\text{stop}}$ the instant of the last distrainment. For this reason these incomplete resting times were not included in the results showed above. They constituted a small fraction of the all resting times, 183 compared to 2184 complete rests (from distrainment to entrainment), but if included they cause an increase of the statistical values. As showed in Figure 5.16, the new average resting time is 23.21 s and the standard deviation 61.08 s, almost doubled compared to the previous results. Similar results are obtained when a minimum resting time of 1 s is imposed too.

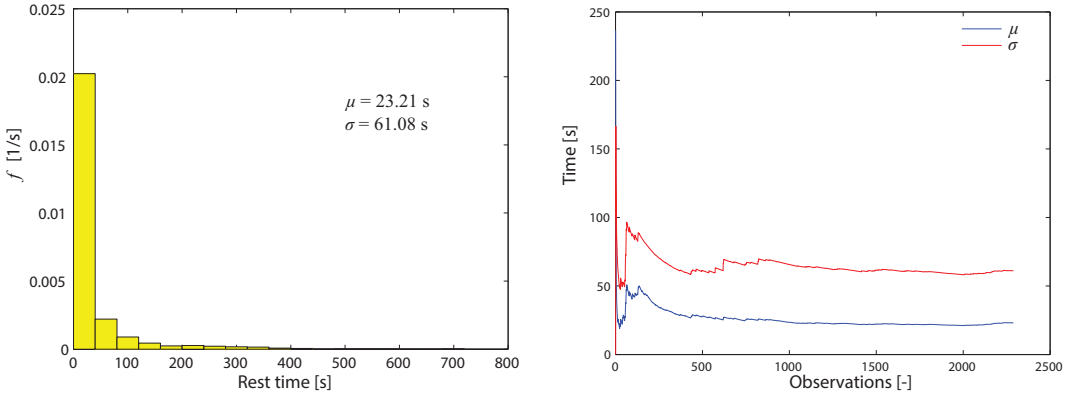


Figure 5.16: Frequency distribution of the resting time when also the incomplete rests are included, that is $t_{\text{rest}} = t_{\text{end}} - t_{\text{stop}}$ with $t_{\text{end}}$ being the end of the analysis and $t_{\text{stop}}$ the instant of the last distrainment. The stability of the statistical values as a function of the number of observations is reported too.

A closer examination of the dataset 7, of approximately 12 minutes analysis, has helped in understanding the results. The resting time population for this sub-session is composed by 472 complete rests ($t_{\text{rest}} = t_{\text{next-start}} - t_{\text{stop}}$) and by only 20 incomplete resting times which have been calculated as $t_{\text{rest}} = t_{\text{end}} - t_{\text{stop}}$ with $t_{\text{end}}$ being in this case equal to 760 s ($\approx$ 12.7 minutes). The first group's statistics are respectively $\mu(t) = 10.41$ s and $\sigma(t) = 41.57$ s. When merged together with the partially described resting times, the mean value increases up to 18.70 s and the standard deviation to 69.92 s. This large increase stems from the small population of incomplete rests, which is denoted by $\mu(t) = 214.36$ s and $\sigma(t) = 203.69$ s.

In order to obtain an estimation of the actual resting times of these 20 spheres, their last position have been monitored in a sequence of following frames extracted every 10 s. When the particle disappeared from the original marked location, the extraction of frames was refined to search for the closest instant to the entrainment event. Out of 20 spheres only one was never brought into motion till the end of the experiment, meaning that its resting time is $t_{\text{rest}} \geq 16208$ s (= 4.5 hours), the maximum measured resting time. For all the other particles it was now possible to assess their waiting times, which resulted on average equal to 3037.21 s with standard deviation of 4841.58 s as shown in Figure 5.17. The population of resting times is too small to obtain a continuous distribution, however this constitutes a first attempt in the derivation of a more extensive description of the variable.

The complete rests characterized by smaller statistics of the order of tenth of seconds ($\mu(t) \approx$ 10 s or 20 s if a 1 s-threshold minimum rest is imposed) and these extreme waiting times ($\mu(t) \approx 3000$ s) could be the sign of two different types of rest, i.e. one associated to the continuous motion of particles and the other one attributed to a more sporadic type of motion.

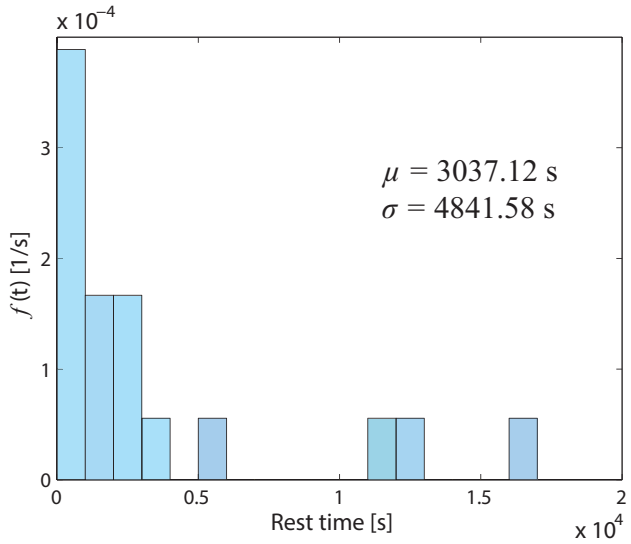


Figure 5.17: Frequency distribution of the 20 resting time of sub-session 7.

While the first one can be derived with a shorter time interval analysis, the second type could require hours of monitoring in order to observe a new entrainment event. The extreme values are though limited in number constituting on average the 8% of the entire population of rests. Yet this part can substantially influence the derivation of the statistical values as its mean and standard deviation are in the order of magnitude of 1 hour. A broader analysis of the database, where particles are continuously followed for hours along the entire length of the flume should shed light into these two processes by helping identifying the two time scales and probability distributions characterizing the different rest types.

## 5.3 Derivation of step length distribution: comparison of two methods

Chapter 2 ended with an open question about the approach to be used in dealing with truncated step length distributions. Two methods were proposed, one deriving the un-truncated statistics by application of different distribution functions to the truncated CDF (Method 1), whilst the other one calculated the complete marginal distribution by using the concept of joint and conditional probability of two variables (Method 2).

With the recently acquired data it has been possible to compare the results of the two methods with the actual statistics of the complete dataset when they are applied to differently truncated distributions of step length. To do so, the total area of observation was progressively reduced so as to derive the number of *Start-Stop*, *Move-Move*, *Start-Move* and *Move-Stop* displacements as a function of the longitudinal areal dimension, $L_x$. Knowing the different types of displacements has allowed the calculation of the truncated statistics and the reduction factor $R$, i.e. $R$ = (#Start-Stop)/(#Start-Stop + #Move-Move). Table 5.4 reports these values for longitudinal lengths $L_x$ of 50, 75, 100, 125, 150, 200, 300 and 1000 mm. The area-based analysis was stop for $L_x = 300$ mm, that is when $R$ became equal to 1. The 1000 mm-length results are reported for reference as they include the whole database of step lengths. According to Method 1, the mean and the standard deviation associated to the best fit were obtained with the three distributive functions, namely Gamma, Weibull and Lognormal. The statistical values reported in Table 5.4 present the same trend for the three functions.

Table 5.4: Reduction factor, $R$, for different values of longitudinal dimension of the investigated area, $L_x$. The table reports the statistics of the truncated data and of the fitting functions denoted by the lowest error according to Method 1. All the statistics are expressed in mm. For the case of $L_x = 1000$ mm, the statistics are calculated on the entire database of step lengths.

| | | Truncated data | | Gamma | | Weibull | | Lognormal | |
|---|---|---|---|---|---|---|---|---|---|
| $L_x$ | R [-] | $\mu_{calc}$ | $\sigma_{calc}$ | $\mu_{fit}$ | $\sigma_{fit}$ | $\mu_{fit}$ | $\sigma_{fit}$ | $\mu_{fit}$ | $\sigma_{fit}$ |
| 50 mm | 0.51 | 15.44 | 8.91 | 54.00 | 58.00 | 58.00 | 66.00 | 106.00 | 296.00 |
| 75 mm | 0.76 | 20.16 | 14.16 | 42.00 | 50.00 | 44.00 | 54.00 | 60.00 | 138.00 |
| 100 mm | 0.92 | 24.96 | 19.39 | 32.00 | 32.00 | 32.00 | 32.00 | 36.00 | 50.00 |
| 125 mm | 0.97 | 28.60 | 23.60 | 30.00 | 30.00 | 30.00 | 30.00 | 34.00 | 42.00 |
| 150 mm | 0.98 | 29.85 | 24.90 | 32.00 | 32.00 | 32.00 | 32.00 | 34.00 | 40.00 |
| 200 mm | 0.99 | 33.61 | 29.98 | 34.00 | 34.00 | 34.00 | 34.00 | 38.00 | 44.00 |
| 300 mm | 1.00 | 39.77 | 37.86 | 40.00 | 40.00 | 40.00 | 40.00 | 42.00 | 48.00 |
| 1000 mm | 1.00 | 46.14 | 48.26 | 46.10 | 42.30 | 46.20 | 43.70 | 47.90 | 64.30 |

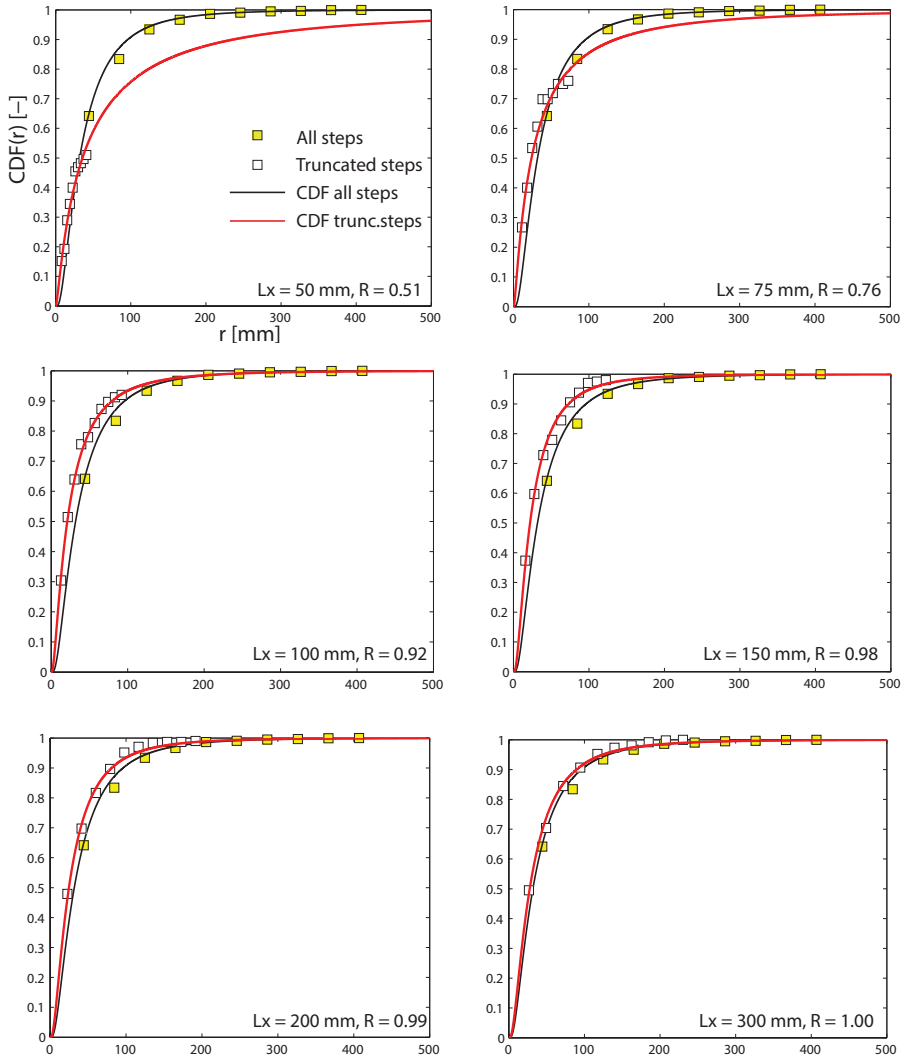


Figure 5.18: Series of truncated cumulative frequency distributions (white squares, red line) compared with the actual CDF of the observed data (yellow squares, black line). The two fitting functions are lognormally distributed.

To an initial increase of mean and standard deviation a reduction in the values follows,

causing an underestimation of the real statistics. This underestimation is progressively reduced with the increase of the areal dimension, approaching the real stable measured statistics for $L_x > 300$ mm (Figure 5.18). The series of truncated cumulative frequency distributions (white squares) are plotted in Figure 5.18 and compared with the actual CDF of the observed data (yellow squares and black line). The correspondence between the two curves is reached for values of $R \geq 0.98$, below which the truncated data poorly matches the real data distribution. This difference could be a consequence of the assumptions which Method 1 is based upon.

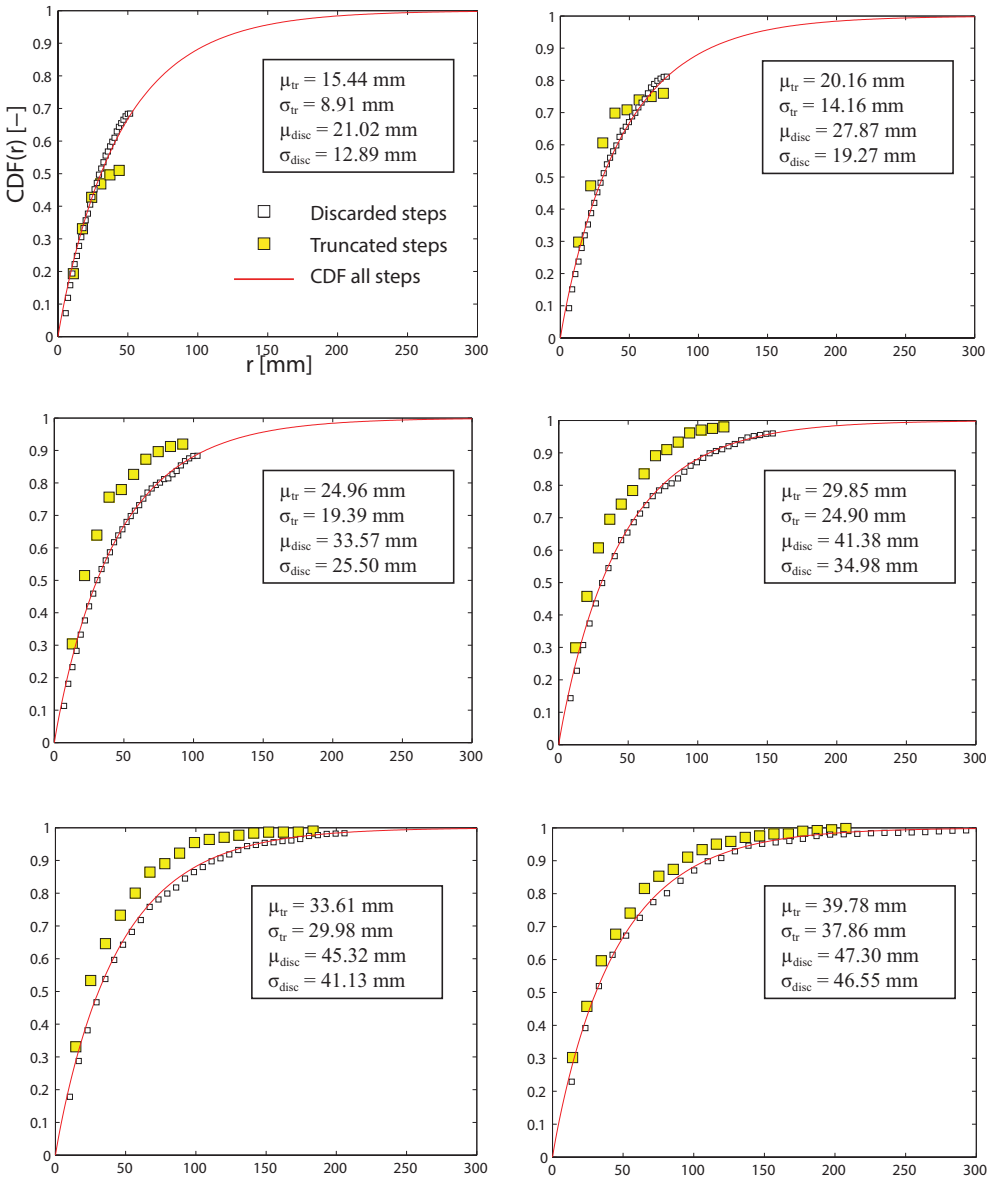


Figure 5.19: Series of truncated cumulative frequency distributions (yellow squares) compared with the frequency distribution of discarded steps, *Move-Stop* and *Start-Move*, in white squares, together with the respective statistics. The actual Lognormal CDF of the observed data (red line) is also plotted.

One of the assumptions Method 1 is based on is that the population consisting of *Move-Stop* and *Start-Move* equally distributes according to $R$. With the new database it was possible to derive for each value of $L_x$ the $R$ coefficient of the discarded step lengths (*Move-Stop* and *Start-Move*) by distinguishing among them the ones greater or smaller than the longitudinal areal

extent. As can be seen in Figure 5.19 and in Table 5.5, the scaling coefficients $R$ are different as well as the statistics and the distribution of the cumulative frequency data. The difference in the two distributions, in return, is related to the procedure followed in the data extraction. When the analysis of *Start-Stop* displacements is limited to the longitudinal dimension $L_x$, it is less likely to detect steps close or equal in longitudinal length to $L_x$. The generated distributions that result are distorted by presenting a flatter part for frequency values near to the potential maximum step. The discarded population instead is not limited by the investigated area and it correctly follows the real distribution. As it was also found in Chapter 2, for $R \geq 0.80$ the application of Method 1 produces statistics that are greater than the ones calculated by means of only the truncated data, but at the same time it underestimates the original mean and standard deviation (Table 5.5).

Table 5.5: Values of $R$ for the truncated steps (*Start-Stop* $< L_x$) and the discarded steps (*Start-Move* and *Move-Stop*) as a function of $L_x$.

| R | 50 mm | 75 mm | 100 mm | 125 mm | 150 mm | 200 mm | 300 mm |
|---|---|---|---|---|---|---|---|
| Truncated | 0.51 | 0.76 | 0.92 | 0.97 | 0.98 | 0.99 | 1.00 |
| Discarded | 0.68 | 0.81 | 0.88 | 0.93 | 0.96 | 0.98 | 0.99 |

The statistical formulation of Method 2 found instead confirmation with the new data. Hereafter the recently collected data of particles' step length and velocity are used to validate the formulation presented in Chapter 2:

$$f(v)|_{exp} \equiv f_v(v) = \int \left[ f_v\left(v|r\right) f_s(r) \right] dr = \int f_{v,r}(v,r) dr. \tag{5.2}$$

According to equation 5.2, the marginal PDF of particle's velocity $v$, $f_v(v)$, calculated in dependence of the step length $r$, should be equivalent to the marginal PDF of $v$ obtained from the experimental observations, $f(v)$.

The experimental PDF of particles' velocity presented in Section 5.2.3 has shown to be well approximated by a gamma-like distribution. The analysis of the particles' velocity enabled also the derivation of the conditional probability of $v$ as a function of $r$, $f_v(v|r)$. Their frequency distributions were assumed to be gamma-like, according to the marginal PDF of velocities, and their statistics were derived as a function of $r$ (Figure 5.20). The dimensionless mean velocity is described by an exponential function whilst the standard deviations are approximated by a power law.

In this case the marginal distribution of the step lengths, $f_s(r)$, can be determined with the experimental data as shown in Section 5.2.1. Recalling the results about the longitudinal step lengths, the complete set of steps distributes lognormally with known mean and standard deviation. It is now possible to derive the marginal PDF of particles' velocity, $f_v(v)$, as expressed in Eq. 5.2 and to compare it with the gamma-distributed one from the experimental data. The best match between the two curves is attained for an asymptotic value of velocity $U_0$ equal to 110 mm/s, which corresponds to the fluid velocity in correspondence of $z_0 = 1$ mm $\approx 0.30 d_{50}$ (Figure 5.21). The asymptotic value is also confirmed by the fitting of the mean and standard deviation of particles' velocity as a function of $r$ as shown in Figure 5.20.

Since the error (MSE) associated to a Lognormal fit of the step length distribution frequency is relatively close to the Weibull's one, the same analysis was also performed in the case of a Weibull-like distribution of step lengths. In this case the best match between the marginal

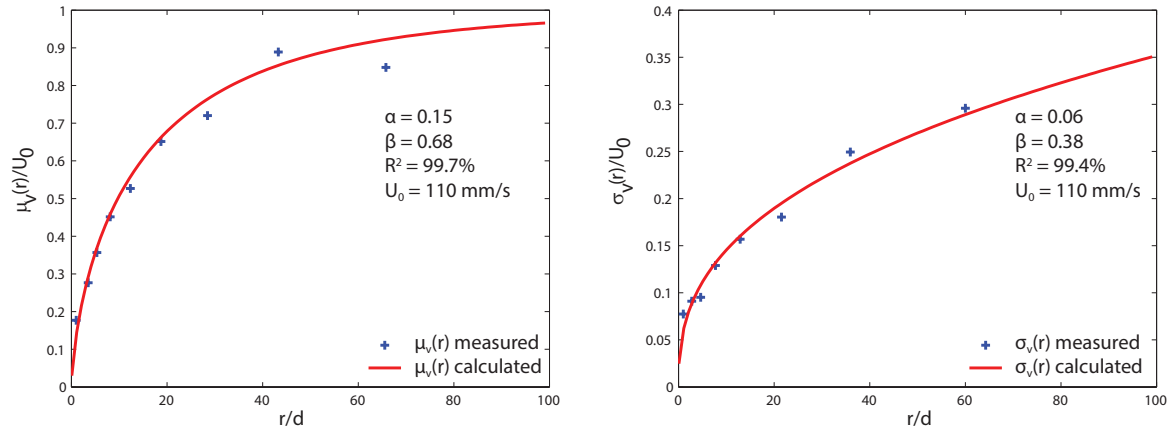


Figure 5.20: Mean and standard deviation of the particles' velocity scaled to the dimensionless step length $r/d$, where d indicates the tracers' size. The asymptotic value $U_0$ reported in the plots is here calculated with the linear profile at $z_0 \approx 0.3d_{50}$.

PDFs of particles' velocity is reached for $U_0 = 170$ mm/s, that is for $z_0/d_{50} \approx 0.50$ (Figure 5.21b). Both functions well perform in the reconstruction of $f(v)$ presenting also similar values of asymptotic particles' velocity $U_0$.

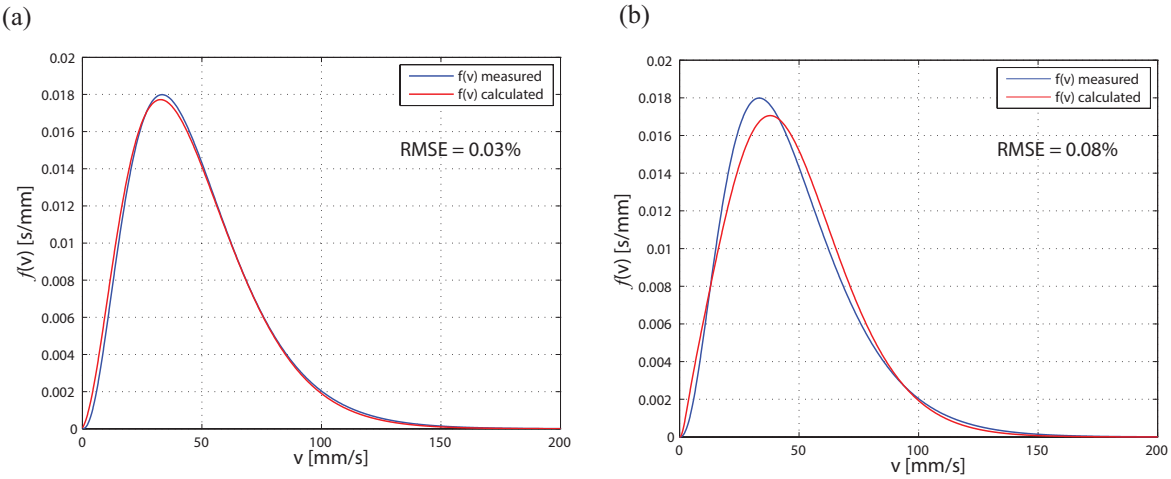


Figure 5.21: Correspondence between the calculated marginal PDF of particles' velocity (red line) and the experimentally observed PDF (blue line) when step lengths are (a) lognormally distributed or (b) Weibull-distributed. The linear RMSE value is reported too.

The derived marginal PDF well approximates the experimental one as demonstrated by the low value of RMSE for both cases of step lengths lognormally or Weibull-distributed, respectively RMSE = 0.03% and RMSE = 0.08%. This suggests the robustness of the statistical method as it is based on two dependent variables, i.e. the step length and the particles' velocity, with the latest less affected by truncation. When the investigated area is limited, the velocity population can include also the truncated trajectories, namely *Move-Move*, *Start-Move* and *Move-Stop* displacements. In doing so, the set of velocities is more representative of the entire range of possible realizations that could only be derived with a well extended area. This is confirmed with the annular flume data. When the longitudinal dimension of the area is restricted to 75 mm (R = 76%) the average and standard deviation obtained by means of all trajectories, including the incomplete ones, are respectively $\mu(v) = 46.81$ mm/s and $\sigma(v) = 24.73$ mm/s, very close

to the values derived from the complete set of steps (for reference $\mu(v) = 45.74$ mm/s and $\sigma(v) = 24.70$ mm/s). It is now possible to explain the output of Method 2 when applied to the truncated data of Tregnaghi et al. (2012b). In that case the calculated step length CDF never matched the truncated cumulative frequency data, which in turn was always located above the CDF curve (Figure 5.22). Initially this was attributed to an uncertainty in the statistical formulation, but when compared to the new data, the error should be attributed to the truncated steps and their trend when plotted on a cumulative graph. The results of Method 2 cannot then be compared to the experimental data.

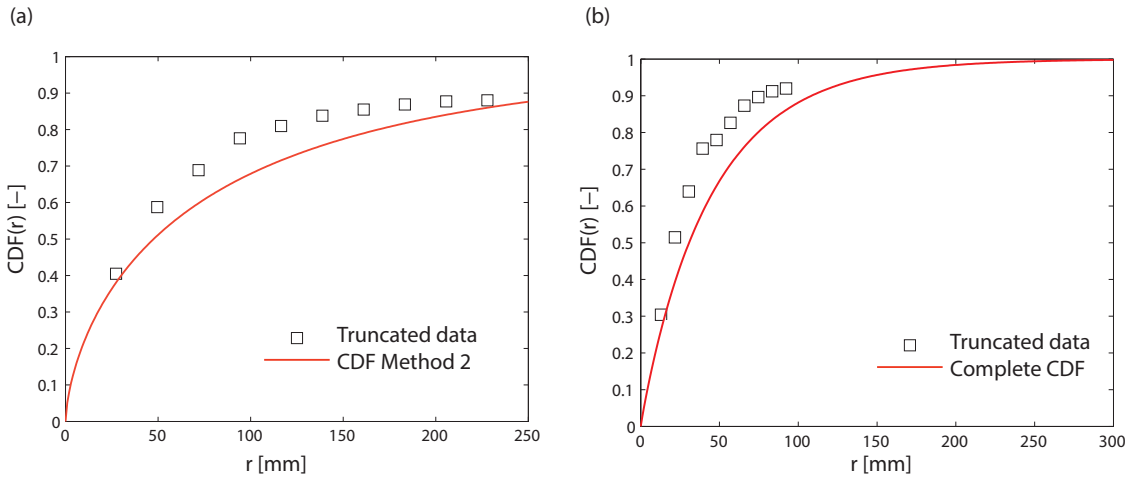


Figure 5.22: Comparison between the (a) the results of Method 2 to the truncated steps data of Tregnaghi et al. (2012b) and (b) the artificially truncated data from the annular flume experiment along with the complete cumulative distribution of step lengths. The reported case refers to (a) Test 2 and (b) $L_x$= 100 mm.

Overall the new data contributed in showing the limitations of the first method, which are intrinsically depending on the procedure of data extraction, and also in confirming the correctness of the statistical formulation at the basis of Method 2. This should help in formulating a practical tool that can be used in future for similarly truncated experimental data.

# Chapter 6

# Model application to the new experimental data

In this final chapter of the thesis the model proposed and developed in Chapter 2 is applied to simulate the concentrations of tracers that have been measured in the new experiments in the annular flume. The annular flume data enabled the use of the more general formulation expressed by Eq. 3.7:

$$(1-\lambda_p)\frac{L_a}{E_b}\frac{\partial f_t(x,t)}{\partial t} = \iint f_t(x-r,t-\tau_p) f_{\tau_p,r}(\tau_p,r) d\tau_p dr - f_t(x,t). \tag{6.1}$$

By recalling the definition of the joint probability $f_{\tau_p,r}(\tau_p,r)$, the above equation results:

$$(1-\lambda_p)\frac{L_a}{E_b}\frac{\partial f_t(x,t)}{\partial t} = \iint f_t(x-r,t-\tau_p) f_{\tau_p}(\tau_p|r) f_s(r) d\tau_p dr - f_t(x,t). \tag{6.2}$$

Equation 6.2 constitutes the basis of the modelling simulations, whose input parameters are derived from the Lagrangian analysis of the experimental particle tracer data. The evolution of the tracers concentration $f_t(x,t)$ will then be compared to the concentration curves obtained from the Eulerian study of the black spheres transport in the annular flume.

## 6.1 Lagrangian analysis: model inputs

The recording of particles' location in time and space has proven to be fundamental in the description of the distributions of particles' motion parameters. With reference to Eq. 6.1, the model requires the derivation of the joint probability of step lengths and travelling times. The joint probability can be expressed in terms of the marginal probability of step lengths and the conditional probability of the step length and travelling time:

$$\begin{cases} f_{\tau_p,r}(\tau_p,r) = f_{\tau_p}(\tau_p|r) \cdot f_s(r) \\ f_{\tau_p}(\tau_p) = \int \Big[ f_{\tau_p}(\tau_p|r) \cdot f_s(r) \Big] dr = \int f_{\tau_p,r}(\tau_p,r) dr. \end{cases} \tag{6.3}$$

The first expression in the group of equations 6.3 provides the joint probability $f_{\tau_p,r}(\tau_p,r)$ that is essential in the model formulation. The integral of the joint probability in $r$, as reported in the second equation of 6.3, i.e. $f_{\tau_p}(\tau_p)$, should be equivalent to the marginal PDF of travelling times derived from experimental measurements. From experimental evidence in Chapter 5 the marginal PDF of the step lengths has been assumed to be lognormally distributed, as well as the

marginal distribution of the travelling times. The conditional probability $f_{\tau_p}(\tau_p|r)$ is calculated by considering that the travelling times associated to every single $r_i$ distribute according to a lognormal distribution, whose mean and the standard deviation are linked to the step length by a simple power law:

$$\begin{cases} \frac{\mu_t}{r_{max}U_0} = \alpha_1 \left(\frac{r}{d}\right)^{\beta_1} \\ \frac{\sigma_t}{r_{max}U_0} = \alpha_2 \left(\frac{r}{d}\right)^{\beta_2} \end{cases}, \tag{6.4}$$

with $r_{max}$ being the maximum measured step, $d$ the tracers' diameter and $U_0$ the asymptotic value of fluid velocity that was derived in Chapter 5 for the same analysis performed in the case of joint probability of step lengths and particles' velocities. Letting the statistics of $\tau_p$ being expressed by a power function is a good approximation of the experimental measurements as shown in Figure 6.1.

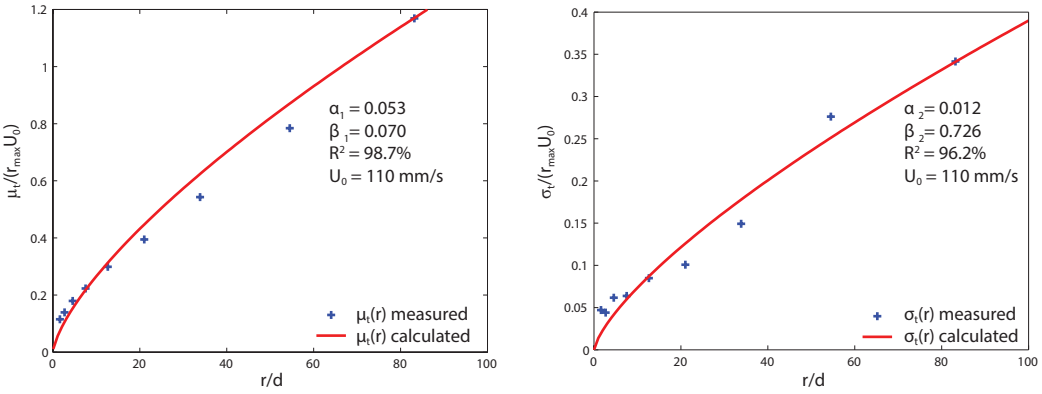


Figure 6.1: Dimensionless mean and standard deviation of travelling times scaled to the step length $r/d$. The red line indicates the power law fitting with calibration parameters $\alpha$ and $\beta$. The correlation $R^2$ between the data and the relationship expressed by Eq. 6.4 is shown in each graph.

The parameters $\alpha$ and $\beta$ defining the statistical distribution of the travelling times are respectively $\alpha_1 = 0.053$ and $\beta_1 = 0.070$ for the mean values, $\alpha_2 = 0.012$ and $\beta_2 = 0.726$ for the standard deviations. With this information it is now possible to calculate the joint probability $f_{\tau_p,r}(\tau_p, r)$, that, once integrated over $r$, provides the marginal PDF of the tracer travelling times. Figure 6.2 demonstrates the equivalence between the calculated $f_{\tau_p}(\tau_p)$ and the experimental curve, which was presented in Section 5.2.2 from the fitting of the measured travelling times. The correspondence between the two curves is high as stated by the low value of the root mean squared error (RMSE). The RMSE, expressed as a percentage, was calculated by adding the linear error associated to the observed and calculated distribution values greater than $0.20Y_{max}$ (where $Y_{max}$ denotes the maximum observed frequency), to the logarithmic RMSE derived for the frequency values lower than the threshold $0.20Y_{max}$:

$$\text{RMSE} = \frac{100}{n_{lin} + n_{log}} \left[ \sum_{i=1}^{n_{lin}} \left( \frac{Y_{m,i} - Y_{c,i}}{Y_{m,i}} \right)^2 + \sum_{j=1}^{n_{log}} \left( \frac{\log(Y_{m,i}) - \log(Y_{c,i})}{\log(Y_{m,i})} \right)^2 \right]^{0.5}. \tag{6.5}$$

The variable $Y$ indicates the measured (with $m$ subscription) and the calculated (with $c$ subscription) frequency of travelling time, while $n_{lin}$ and $n_{log}$ denotes respectively the number of frequency values above and below the threshold $0.20Y_{max}$. The resulting RMSE $= 0.30\%$ demonstrates the validity of the conceptual approach in the statistical description of the dependent

variables step length $r$ and travelling time $\tau_p$.

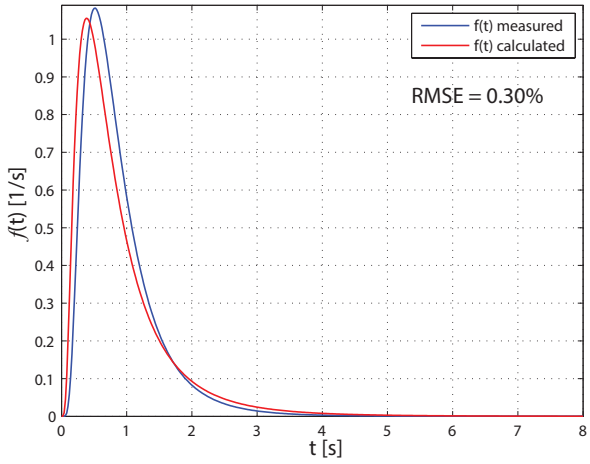


Figure 6.2: Experimental and calculated marginal PDF of the tracer travelling times. The accuracy between the two curves is reported by the linear RMSE = 0.30%.

The benefits of the Lagrangian analysis of particles motion are evident also in the calculation of the tracers' entrainment rate, $E_{bt}$. The volumetric rate is derived by counting the number of particles entrained $n_e$ over the investigated area in a particular time interval:

$$E_{bt} = \frac{n_e\left(4/3\pi\left(\frac{d}{2}\right)^3\right)}{L_x L_y \Delta_t}, \tag{6.6}$$

where $d$ is the tracer' diameter, $L_x$ and $L_y$ the longitudinal and transversal dimension of the investigated area and $\Delta t$ the time interval. Letting $n_e$ be replaced by the number of deposited particles, $n_d$, one can obtain the corresponding volumetric deposition rate $D_{bt}$. The volumetric rates per unit area have been calculated for time intervals of 100 frames ($\approx$ 3.3 s) and then averaged over the duration of the considered sub-session (horizontal lines in the inset of Figure 6.3). These averaged entrainment and deposition rates (identified by crosses in the main plot of Fig. 6.3) allowed the study of the evolution of $E_{bt}$ and $D_{bt}$ over the entire duration of the experiment as shown in Figure 6.3. The good correspondence of entrainment and deposition rates confirms that the bed is essentially in equilibrium throughout the experiment, as also assumed in the development of the model. Both rates fluctuate in time around the averaged values of $E_{bt} = 2.47 \cdot 10^{-7}$ m$^3$/m$^2$s and $D_{bt} = 2.38 \cdot 10^{-7}$ m$^3$/m$^2$s, represented by the horizontal lines in the main plot of Fig. 6.3. The small variability in entrainment and deposition rates (ranging from a minimum of $1{\cdot}10^{-7}$ m$^3$/m$^2$s to a maximum of $4{\cdot}10^{-7}$ m$^3$/m$^2$s) supported the model assumption of a constant entrainment rate in space and time.

An estimation of the total entrainment rate is thus possible by knowing the volumetric entrainment rate of tracers and recalling that $E_{bt} = E_b f_t$, with $f_t$ the tracers' concentration in the active layer. The initial fraction of black spheres located in the stripe in front of camera 4 gives the volumetric tracer concentration, which equalled to 0.089:

$$f_t(t=0) = \frac{n_t\left(4/3\pi\left(\frac{d}{2}\right)^3\right)}{dl_x dl_y s_d(1-\lambda_p)}, \tag{6.7}$$

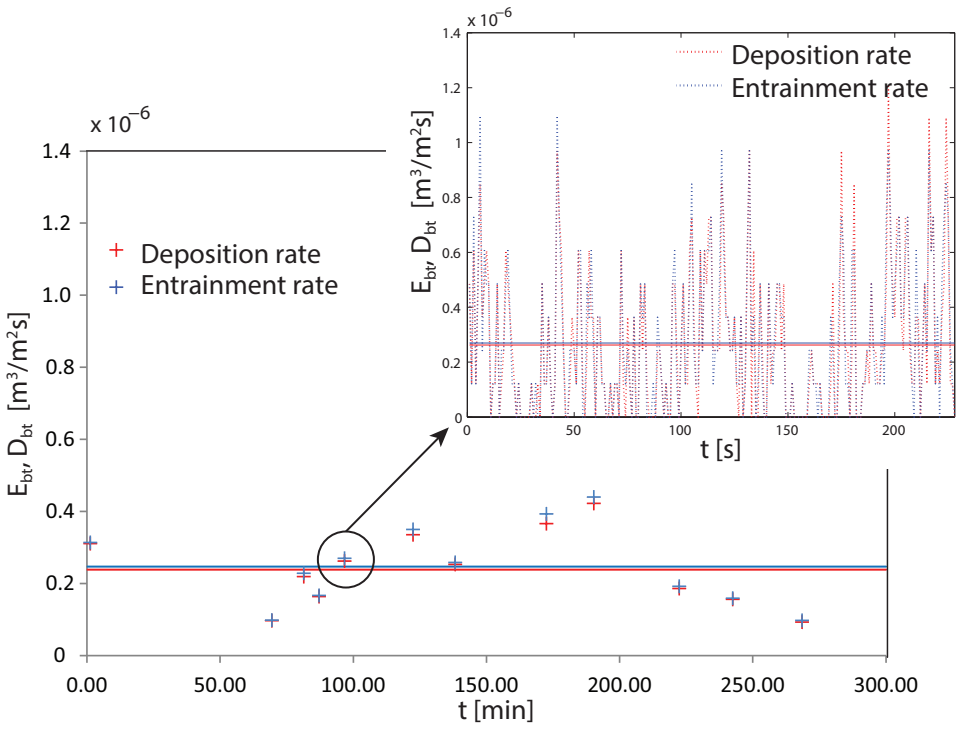


Figure 6.3: Volumetric entrainment and deposition rate of tracers in time. The inset plot offers an example of the trend of the two rates when calculated every 3.3 s for a generic sub-session. The averaged values, which are represented by the horizontal lines in the inset plot, are afterwards reported in the main plot and indicated by crosses. The horizontal line in the main graph reports the averaged rates from the single sub-sessions averaged values (crosses).

with $n_t$ indicating the initial number of tracers (≈200 in total), $dl_x = 60$ mm the longitudinal size of the stripe composed of black spheres, $dl_y = 200$ mm the channel width, and $\lambda_p$ the bed porosity assumed equal to 0.3. $s_d$ denotes the thickness of the sediment layer where the black spheres had been initially mixed with the 10 mm thick transparent sediment deposit (Section 4.4.3 of Chapter 4). Since all the tracers composing the original stripe were eroded and actively contributed to the bed-load transport, this surficial mixed layer corresponds by definition to the active layer. A first estimation of the total entrainment rate provides $E_b = 0.35 \cdot 10^{-5}$ m$^3$/m$^2$s. This value, along with the other input parameters, is presented in Table 6.1.

The evidence of the erosion of the initial stripe, together with the possibility of spotting black particles within the transparent bed deposit, has supported the assessment of the actual active layer thickness. It was indeed observed that particles contributing to the overall transport are located in a surficial layer whose thickness ranges from 2 to 3 times the mean bed diameter $d_{50}$, i.e. $L_a$ = 6.4-9.6 mm, very close to the $s_d$ value of 10 mm of the original eroded stripe. This is although in contrast with the results provided by the active layer formulations reported in Chapter 3, where the thickness of the active layer was either calculated as a function of $d_{50}$, $L_a = 0.5\text{-}0.6d_{50}$ (Nikora et al., 2001, 2002), or scaled to the standard deviation of the bed elevation $\sigma_b$, $L_a = 1.62\sigma_b$ (Wong et al., 2007). The two expressions would produce an active layer thickness of approximately 2 mm, lower than the observed one. This could be a consequence of the duration of the experiment. As shown by Wong et al. (2007) the longer the bed is worked by the competent flow, the larger the volume of moved tracing particles and the thicker the contributing bed-layer would be. If at the beginning of the experiment the exchanging layer was observed to be very shallow (lower than $1d_{50}$), with time its thickness increased reaching a stable value of $2\text{-}3d_{50}$ that was maintained to the end of the 6 hours experiment. Even the

deepest black particles were never recovered further below (Figure 6.4). This would explain why the two tracers' blocks located underneath the bed surface and covered by a layer of about 10 mm transparent material had never been exposed in 6 hours. In the model formulation the active layer was used as calibration parameter and assumed equal to 10 mm at first attempt. The empirical results helped to give though a range of possible thickness values.


Figure 6.4: Images from above the bed that had been worked by 6 hours of competent flow. The submerged tracers are highlighted to give an idea of the covering layer of transparent particles on top of previously mobile tracers. The submerged block of tracers was still covered in transparent particles at the end of the experiment.

## 6.2 Eulerian analysis: concentration of tracers

The cloud of displaced black particles was analysed in order to derive the tracers' concentration along the length of the flume at different times. As for the Lagrangian analysis, tracers originally located in front of camera 4 have been used in this study. Images collected from camera 4, 6 and 8 were processed to evaluate the concentration curves, whilst contribution from camera 10 and 12 was not considered as only few black particles moved further downstream. A preliminary analysis of particles location at different times, as reported in Figure 6.5, showed the expected advective and diffusive behaviour of the tracers' transport. Once the particles are displaced the cloud tends to move downstream and to longitudinally spread occupying further downstream portions of the channel bed.

To derive the concentration curves, the number of tracers $n_{t,i}$ has been recovered in transversal stripes of length $\Delta x$ and the fraction $f_t$ attributed to the stripe $i$ at time $t$ was calculated as follow:

$$f_t\Big(x_i - \Delta x/2 \leq x < x_i + \Delta x/2, t\Big) = \frac{n_{t,i}\left(4/3\pi\left(\frac{d}{2}\right)^3\right)}{\Delta x dl_y s_d(1-\lambda_p)}, \tag{6.8}$$

where $x_i$ represents the longitudinal central coordinate of the strip. In Eq. 6.8 the denominator indicates the volume of the strips with $dl_y$ being the width of the channel and $s_d$ the 10 mm surficial layer thickness. The longitudinal size of the strips over which the concentration is averaged was set to $\Delta x = 80$ mm. This size reduced the fluctuations in tracers' concentration whilst preserving at the same time the characteristic shape of the concentration curves. The fraction of tracers along the channel bed was derived every 20 minutes from the realization of the steady flow conditions to the end of the experiment. Results at 60, 180, 240, and 360 minutes are presented in Figure 6.6. Following the procedure used in the preparation of the initial stripe

of tracers (Chapter 4) it is here considered that the plateau of tracers' concentration is uniform and equal to 0.089. The fraction of tracers at $t = 0$ is spread over only 60 mm, that is a hundredth of the entire flume length, resulting thus in a sort of concentration impulse from which the following curves are generated.

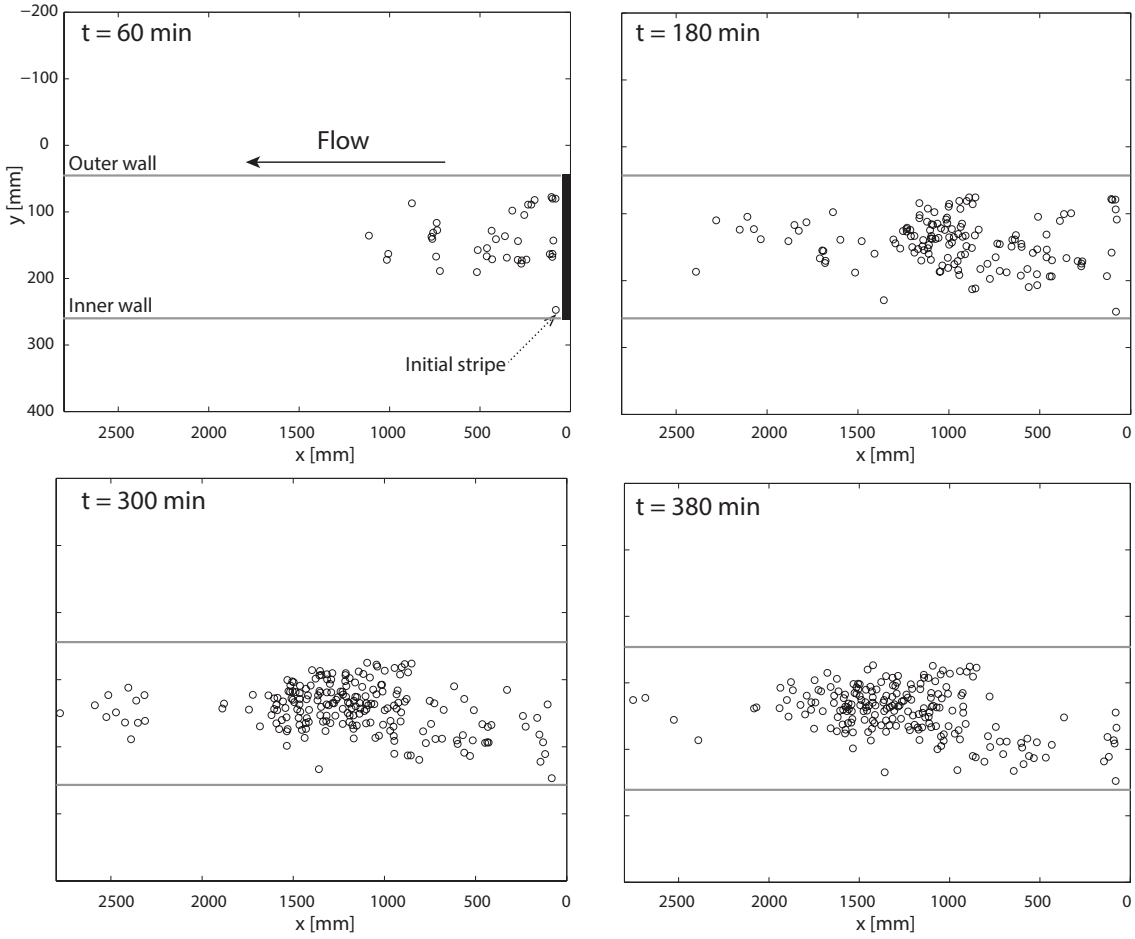


Figure 6.5: Individual tracers' location at different times, i.e. after 60, 180, 300 and 380 minutes. The initial stripe location is indicated by a uniform black rectangle.

To better appreciate the extent of the advective and diffusive flux the initial impulse concentration ($t = 0$, and $t = 60$ min) has been removed from plot in Figure 6.6 so that the following curves could be denoted by a smaller scale on the $y$-axis (Figure 6.7). Initially the black particles form an elongated plume (see 1 hour concentration curve in Figure 6.5 and 6.6). It took approximately 3 hours to observe the bell-shaped curve of tracers' concentration that was instead measured in the previous experiment of Marion (1995) within the first hour. But once it is formed, the evolution of the tracers' fraction in the active layer is consistent with the former trend: the peak in the concentration reduces with time and tends to be levelled while moving downstream. In six hours the centroid of the cloud has travelled 1.5 m, proving that the advection and diffusion are rather restrained in comparison with the results of Marion (1995) experiments. The difference could stem from the dissimilar bed material, in these tests it is almost uniform and sand-free, and from the lower shear stress applied to the bed surface. Even if these two settings act together in limiting the rate and extent of the advective and diffusive nature of the bed-load transport, the granular material used in this experiment allowed for the detailed application of the model.

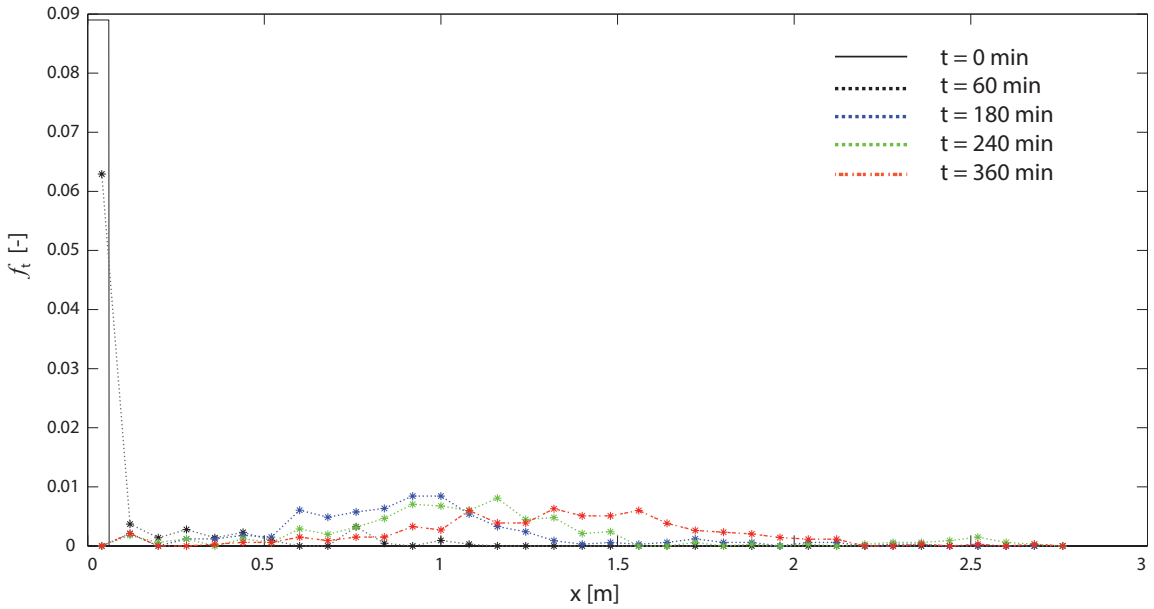


Figure 6.6: Tracers' fraction measured at 0, 60, 180, 240, and 360 minutes from the steady flow conditions.

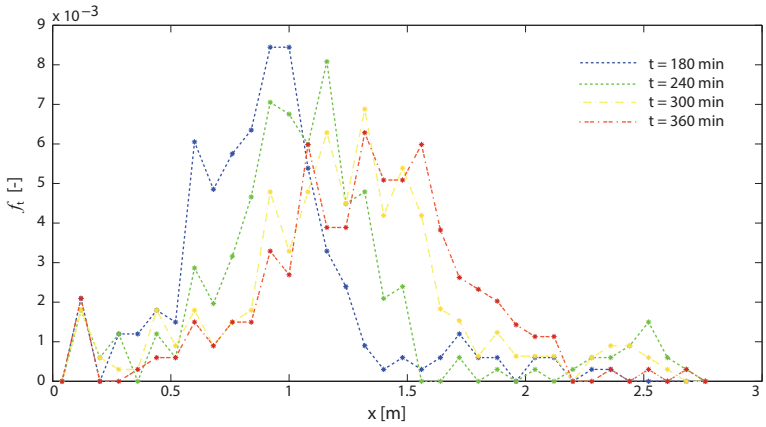


Figure 6.7: The initial concentration for $t = 0$ has been removed here to show a more detailed representation of the tracers' fraction curves at 180, 240, 300 and 360 minutes from the beginning of the steady flow conditions.

## 6.3 Model application and discussion

A finite difference method was applied to discretize Equation 6.2. The solution provided a good preliminary method to test the model and to compare the first results against the measured concentration curves. The discretization grid consisted of longitudinal step $dx = 4$ mm, the size of the tracers, and computing the fraction of tracers every $dt = 0.2$ s. This computational grid is appropriate to describe the step length and the dependent travelling time distributions with sufficient accuracy. It also produced stable results within a reasonable computing time. The input parameters used in the current simulation are reported in Table 6.1. The calibrated variables refer to the volumetric entrainment rate and the active layer thickness so that the best numerical solution was attained for $E_b = 4.15 \cdot 10^{-5}$ m$^3$/m$^2$s and $L_a = 7$ mm. Both values agree well with the empirical estimations from experimental observations reported above.

Figure 6.8 presents the model output of the tracers' fractions for $t = 60$, 120, 180, 240, 300 and 360 minutes. The model results predict the characteristic advection and diffusion observed

Table 6.1: Model input parameters, namely statistics of the step length distribution $(\mu_r, \sigma_r)$, variables to derive the joint distribution of step length and travelling times (maximum step observed $r_{max}$, asymptotic velocity $U_0$, $\alpha_{1,2}$ and $\beta_{1,2}$ for the calculation of the mean and standard deviation of the travelling times distribution), bed parameter (tracers size $d$ and bed porosity $\lambda_p$), and the calibrated parameters obtained by fitting the experimental observations (volumetric total entrainment rate $E_b$ and active layer thickness $L_a$).

| INPUT PARAMETERS | | | | | | | | CALIBRATION PARAMETERS | |
|---|---|---|---|---|---|---|---|---|---|
| $f_s(r)$ | | $f_{\tau_p,r}(\tau_p, r)$ | | | | Bed | | | |
| $\mu_r$ | $\sigma_r$ | $r_{max}$ | $U_0$ | $\alpha$ | $\beta$ | d | $\lambda_p$ | $E_b$ | $L_a$ |
| [mm] | [mm] | [mm] | [mm/s] | [-] | [-] | [mm] | [-] | [m$^3$/m$^2$s] | [mm] |
| 47.91 | 64.24 | 367 | 110 | 0.053($\alpha_1$) | 0.070($\beta_1$) | 4.00 | 0.30 | $4.15 \cdot 10^{-5}$ | 7.00 |
| | | | | 0.012($\alpha_2$) | 0.726($\beta_2$) | | | | |

in the experiment as shown in Figure 6.9. As for the previous plots a more detailed graph is reported for the curves after the first two hours of run (inset of Figure 6.9 and Figure 6.10).

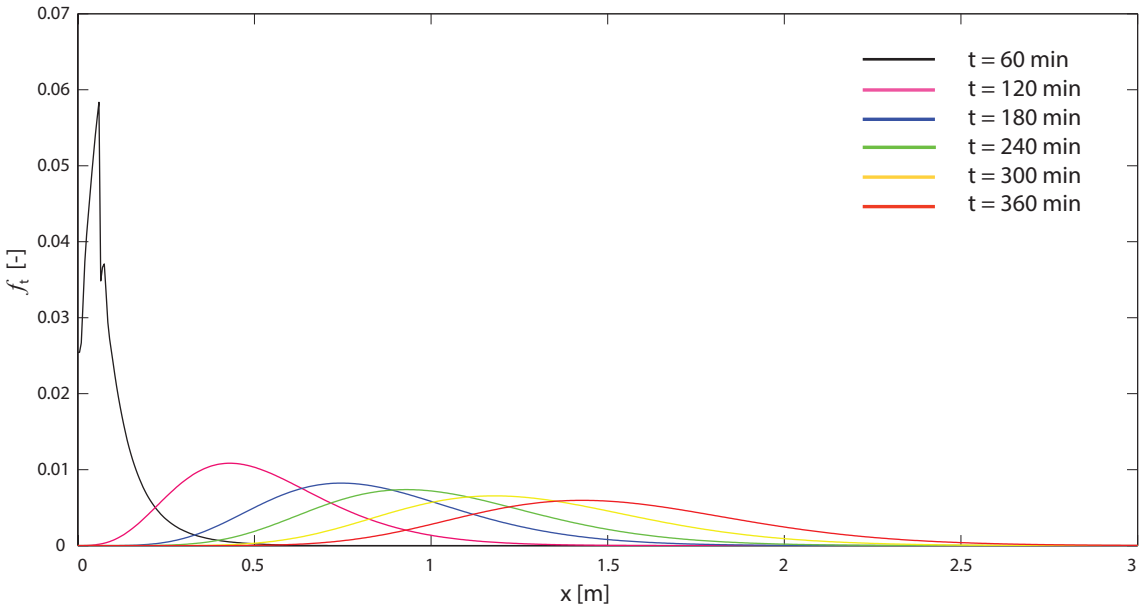


Figure 6.8: Concentration of tracers $f_t$ simulated by the model at every hour from the beginning of the regime conditions.

The model performs poorly in the first two hours of the experiment, generating simulations that do not resemble the measured ones (Fig. 6.9). Within the first two hours it was observed that the black particles located in the initial stripe outnumbered the displaced tracers. The fewer moving beads started advancing downstream by forming an elongated tail in the measured concentration. After three hours all the inserted tracers had left the initial occupied position (for $t = 0$), so that the concentration of tracers over the area initially covered by the stripe became zero. The model seems to catch this trend in the first hour of the experiment but it cannot simulate the distribution of the second hour curve. Its performances greatly improve afterwards by following the observed tracers' fraction at $t = 180$, 240, 300 and 360 minutes (Figure 6.10).

The poor results obtained in the first two hours could find explanation in the variability of the measured volumetric entrainment rate. The model tends to be indeed very sensitive to the entrainment rate parameter. As reported in Figure 6.3, the measured tracers' entrainment rate is lower than the average value for $t < 100$ min. The smaller the rate of the entrained tracers,

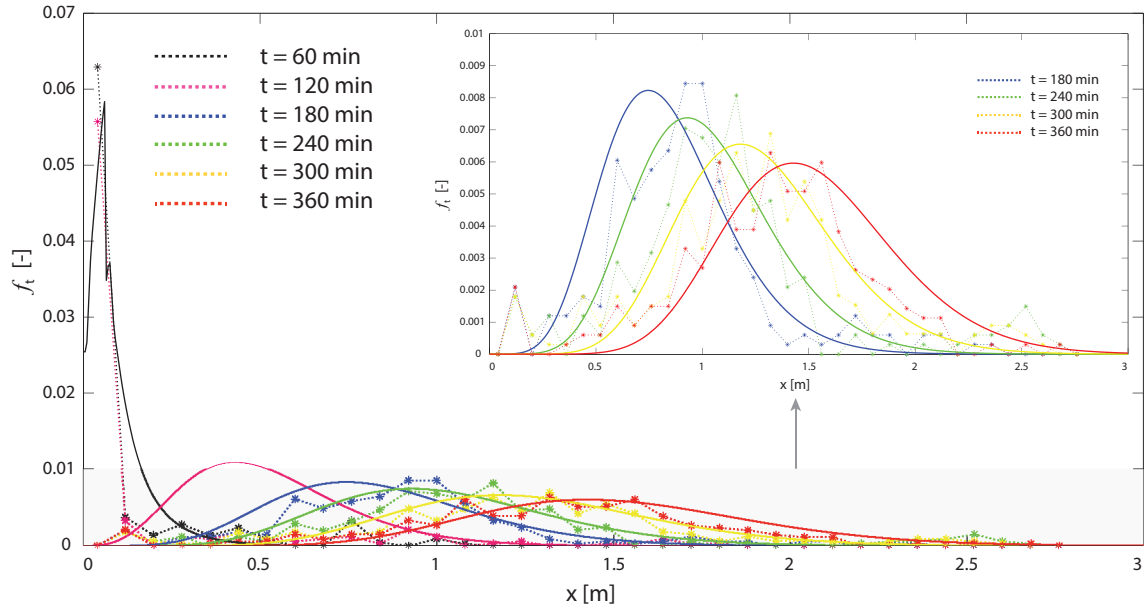


Figure 6.9: Modelled concentration curves (continuous lines) with the respective measured curves (dotted lines) at every hour from the beginning of the steady flow conditions. The 120 minute curve practically overlaps with the 60 minute curves, resulting so difficult to be visualize. The inset reports the tracers fractions, simulated and measured, after the first 2 hours.

the more restrained will be the advective and diffusive character of the concentration curves. The entrainment rate, also lower towards the end of the experiment, may be the reason for the faster moving modelled curve at $t = 360$ min (Figure 6.10, last plot).

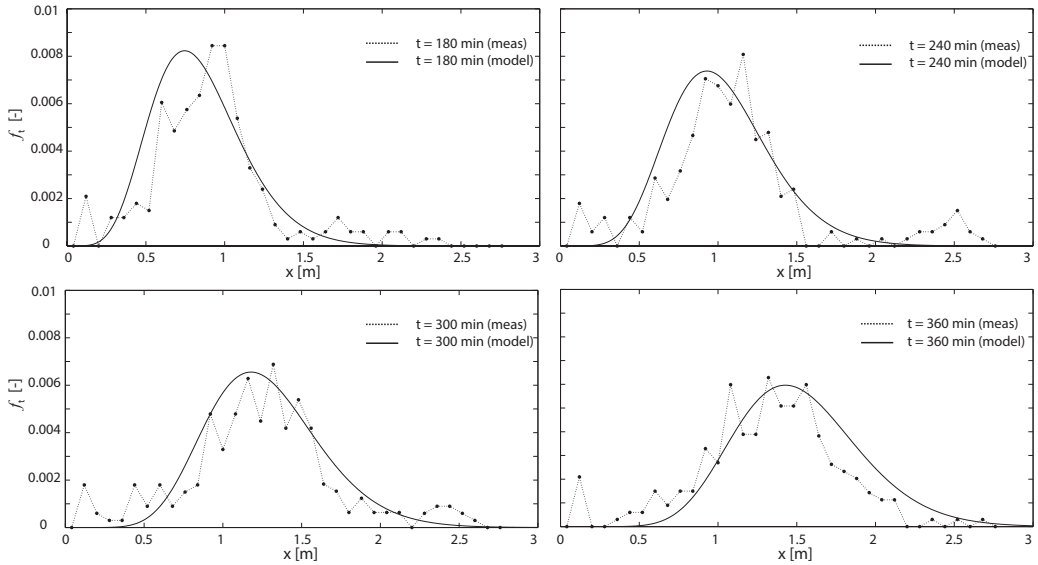


Figure 6.10: Singularly plotted fractions of tracers at $t = 189$, 240, 300 and 360 minutes. The modelled curves are indicated by continuous lines whilst the measured ones are denoted by dotted lines.

The probability of a particle to be entrained can be expressed as a function of the time waited on the bed surface between the last distrainment and the next entrainment event (Ganti et al, 2010). The entrainment rate, here macroscopically determined, appears then as a variable that scales to the particles' resting time. The latest has been shown to distribute according to

two different time scales (Chapter 5) that might identify two resting processes. The formulation as expressed in Equation 6.2 includes the variability of the particles trajectories in terms of travelling distance and time, but not in terms of resting times. Such a limitation could produce discrepancies between the model-described advection and diffusion rates and the observed one.

Despite the initial performance of the model, it is important to highlight its ability in the evaluation of the tracers' fraction evolution after the first two hours (Figure 6.10). The model, as it is formulated in Eq. 6.1, can now incorporate the stochastic information of the single particle's motion into the description of the ensemble group of tracers constituting the moving and spreading plume. The advective and diffusive behaviour resulting from the variability of the particle's step length and travelling time is better approximated now than in the simulations presented in Chapter 3. Similarly to the transport of solutes in rivers, an indication of the plume advective velocity can be obtained by evaluating the first order moment of the concentration curves, also known as the centroid of the cloud:

$$\overline{X}(t) = \frac{\int_x f_t(x,t)dx}{M}, \tag{6.9}$$

with $M$ defining the moment of order zero, that is the area underneath the curves, $M = \int f_t(x,t)dx$. The centroids of the concentrations curves calculated at different times for the experimental and the modelled plumes collapse in a linear relationship with time (Figure 6.11a). Despite the fluctuations of the experimental centroids, the model performs well in simulating the measured advective rate. The same cannot be said for the diffusive rate at first sight of Figure 6.11b. Using again the similarity to the solute transport phenomenon, the second order moment of the concentration curves containing information about the diffusion process in terms of the variance of the curves is so expressed:

$$X^2(t) = \frac{\int_x \left(x - \overline{X}(t)\right)^2 f_t(x,t)dx}{M}. \tag{6.10}$$

$X^2(t)$ indicates the longitudinal spread of the cloud of particles at time $t$ with respect to the location of its centroid. The experimental variance is denoted by a temporal scattered trend, whilst the modelled one evolves linearly with time as reported in Fig. 6.11b. This discrepancy is reduced when the data is plotted in a double-log space (Fig. 6.12).

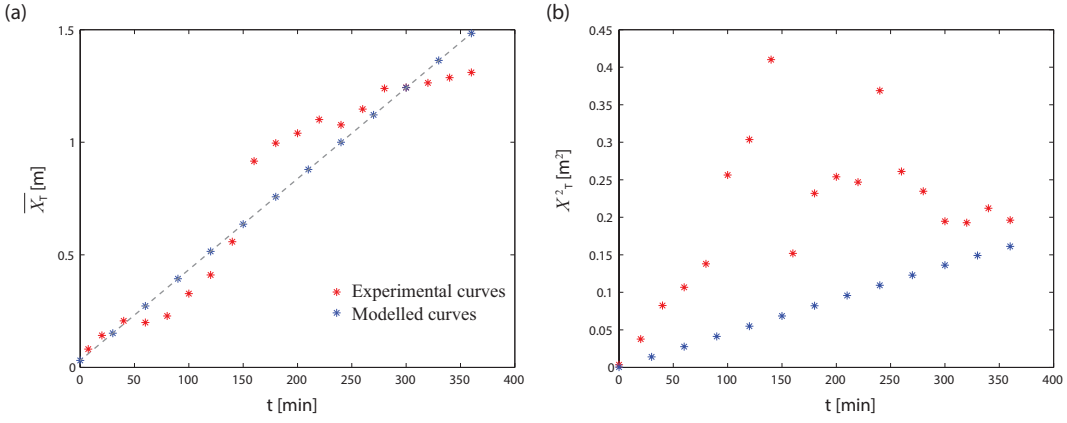


Figure 6.11: Evolution in time of (a) the centroids and (b) variance of the experimental and modelled concentration curves. The dashed grey line in the graph (a) indicates the linear growth of the modelled centroids.

To highlight the dependence of the diffusive rate on time, a dimensionless variance, i.e. $X^2(t)/d^2$, is scaled to the dimensionless time variable, i.e. $tu^*/d$, where $d$ indicates the mean bed diameter $d_{50}$. Similarly to the Lagrangian analysis of single particles' trajectories performed in Chapter 5, the logarithm of the two dimensionless groups should provide information on the growth of the spreading with time in terms of the diffusive scaling coefficient $\gamma_x$, hereafter indicated as $\gamma$ for simplicity:

$$\frac{X^2(t)}{d^2} \propto \left(\frac{tu^*}{d}\right)^{2\gamma} \Rightarrow \log\left(\frac{X^2(t)}{d^2}\right) \propto 2\gamma \left(\frac{tu^*}{d}\right). \tag{6.11}$$

Figure 6.12 presents the result of the analysis. The previous data scatter is reduced in the log-log plot, allowing for a linear fitting of the experimental dimensionless variance. The two interpolations provide close values of the diffusive scaling coefficients, that is $\gamma_E = 0.45$ and $\gamma_M = 0.50$ with subscript $E$ referring to the experimental results and $M$ to the model simulations. The values of dimensionless variance for larger times almost overlap with the model results. In the model the diffusion is normal, that is the spread of the plume grows linearly with time, and so does the experimentally observed diffusion (Figure 6.12). Diffusive regimes will be discusses thoroughly in the following paragraphs.

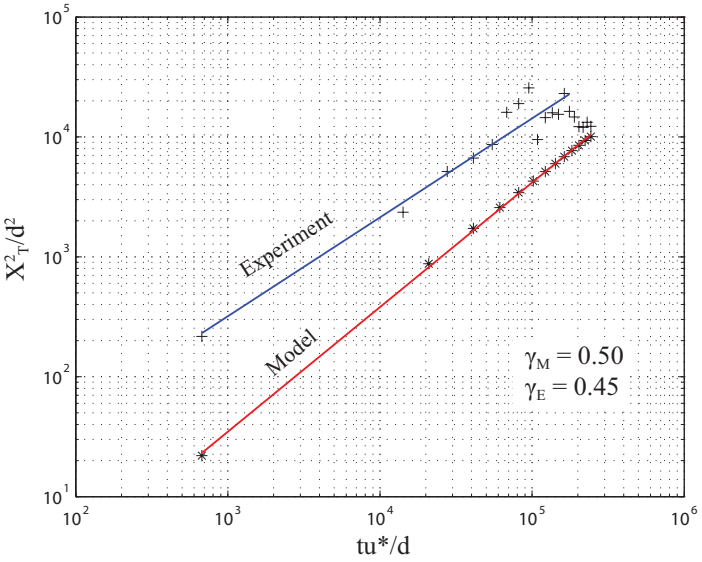


Figure 6.12: Double log-scale plot of the dimensionless variance of the experimental (crosses) and modelled (stars) concentration curves expressed as a function of the dimensionless time parameter. The respective diffusive scaling coefficients are reported too.

It is interesting to notice that the application of the above analysis to the experimental data of Marion (1995) does not produce the same correspondence with the simulations offered by the simplified version of the model (Chapter 3). For the case of gravel transport in bimodal bed (Figure 6.13a), the modelled diffusive coefficient provides a subdiffusive regime ($\gamma_M = 0.42$), contrarily to the experimental one that indicates superdiffusion ($\gamma_E = 0.58$). More remarkable is the difference in the case of sand in trimodal bed (Figure 6.13b) where the superdiffusive scaling coefficient of the experimental curves ($\gamma_E = 0.78$) is largely underestimated by the model, which instead provided a subdiffusive regime ($\gamma_M = 0.35$). The diffusive scaling coefficient derived for the experimental curves of medium sand in the trimodal experiment is remarkably close to the value reported by Bradley et al. (2010) for the reformulated model of Sayre and Hubbell (1965). The authors obtained a superdiffusive sand transport denoted by longitudinal scaling

coefficient ranging from 0.77 to 0.90. The significant difference between the modelled and the experimental growth of the cloud variance could also stem from the lost of tracers mass which is buried in the bed and for tracers that have moved out of the investigated boundary, that is the far end of the flume, and the subsequent arrival of new recirculated tracers from upstream. As a consequence the measured variance lacks the fast moving tracers ahead of the cloud main body but with time it also accounts in the upper part of the flume for new tracers fed back into the channel. The experimental variances so obtained can give an indication of the diffusive processes but the absolute values should be treated carefully.

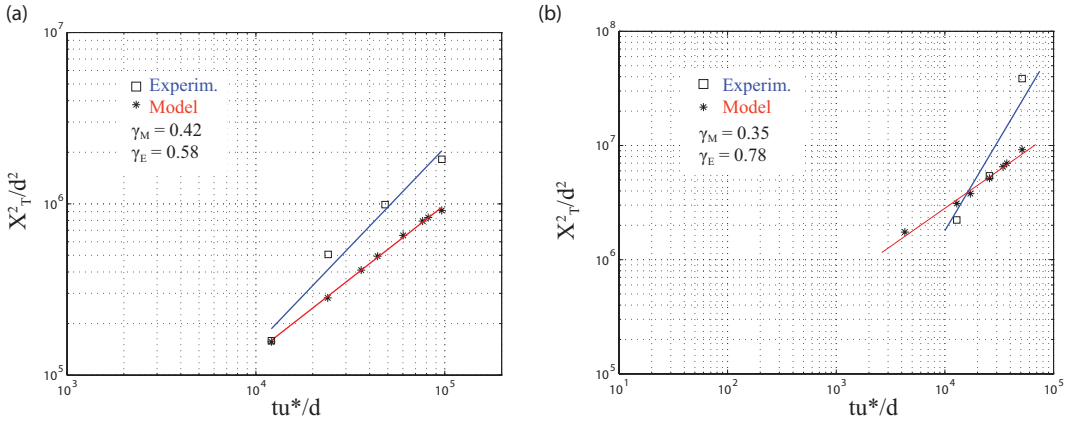


Figure 6.13: Variance of concentration curves in function of the time parameter for (a) the case of gravel transport in bimodal bed and (b) sand transport in trimodal bed from the analysis of the concentrations curves derived from the experimental data of Marion (1995) – squared markers - and the simulations provided by the simplified version of the model – star markers. The modelled and the experimental diffusive scaling coefficients are reported in each graph.

It is then evident that the model formulation including a more general probabilistic description of particles' motion, which means that all the variables defining the grain's trajectories are considered stochastically, better predicts both the advective and the diffusive rate of the tracers transport. The model as expressed in Eq. 6.1 performs well when the measured step length and travelling time resulting from the Lagrangian analysis are incorporated in its computational simulation of the experimental concentration curves. Conversely, the simplified version of the model used in Chapter 3, where the grain's velocity is considered constant, failed in addressing the correct type of diffusive regimes associated to the experimental observations despite the apparently good fitting of the concentration curves, particularly in the case of sand over trimodal bed (for reference Fig. 3.14, Chapter 3).

A closer analysis of the experimental diffusive coefficients $\gamma_E$ obtained from the observed concentration of tracers can give an insight of the role played by the bed roughness in the transport processes, especially in the diffusive rates. The derivation of the variance of the measured concentration curves in time has shown that in the new experiments the diffusion exhibits a nearly normal nature with $\gamma_{\mathrm{E,new}} = 0.45$, whilst the former experiments present a not-pronounced superdiffusion in the case of gravel over bimodal bed, $\gamma_{\mathrm{E,gravel}} = 0.58$, and a high superdiffusion, $\gamma_{\mathrm{E,sand}} = 0.78$, for sand in trimodal sediment. The different diffusive type could constitute a signature of the bed material and composition. While a nearly uniform material results in the classical normal diffusion of particles, the transport of sediment in a graded bed is denoted by superdiffusion. This superdiffusive behaviour appears larger for bed consisting of three mixed-sizes with a larger amount of sand (trimodal bed) than for sediment of just two sizes (bimodal bed).

This observation finds correspondence with the theoretical work of Ganti et al. (2010). The authors demonstrated that the solution of the Exner mass balance equation tends to the normal advection-diffusion equation for thin-tailed distribution of step lengths. Thin-tailed step length distributions are commonly found in uniform bed material as demonstrated in this work. However, the heterogeneity of a mixed-size bed can give origin to heavy-tailed step length distributions, as they depend on both the statistics of the step length for the considered size and the distribution of grain sizes. In this case the equation would generate anomalous diffusion (Ganti et al., 2010; Furbish et al., 2012a).

The first simplified version of the model could not predict the exact anomalous diffusive type as its expression of the step length distribution was incorrectly based on step length statistics derived with Method 1 and because it approximated the solution of the Exner equation by considering constant particles' velocity. On the contrary, with the data recently collected it was possible to derive the complete PDF of step length and travelling time associated to the motion of the tracers. The resulting thin-tailed distributions, once included in the Exner equation, generated normal diffusion solutions, according to the measured tracers' concentration curves.

It is expected that the ability of the more general formulation (Eq. 6.1) in predicting the advective and diffusive behaviour of tracers could find application in the derivation of the stochasticity of particle's trajectories when measured concentration curves are provided. In field and laboratory experiments where the tracing particles' cloud is addressed in terms of concentration curves, it will be possible to estimate the step length distributions as well as the travelling time PDF by a parameters' calibration procedure. The match between the experimentally derived and the modelled curves would be obtained by varying the parameters which define the joint probability of the step length and travelling time, i.e. $\alpha_{1,2}$ and $\beta_{1,2}$. The step length distribution could be derived by a short temporal and spatial Lagrangian analysis of the tracer' trajectories as its incomplete description can now be overcome with the implementation of the statistical Method 2 presented in Chapter 5. The truncated measured step length PDF can be statistically reconstructed and included in the model in the form of thin-tailed distribution for uniform beds or heavy-tailed distribution if combined with the grain-size distribution of graded bed material. The flexibility of the model in considering different types of step length PDFs together with the joint probabilistic description of the tracers' travelling times can be of great use for future river management applications, as further explained in the next chapter.

# Chapter 7

# Conclusions

The study presented here thoroughly investigated the transport of bedload particle so as to attain an accurate description of the variables defining the motion. The experimental evidence gained from the analysis of a former independent experiment (Tregnaghi et al., 2012b) of individual particles tracking have found confirmation with the new series of experiments presented in Chapter 4. The motion of bed-load particles is more appropriately described by random variables, whose spectrum of possible values can only be matched by probabilistic distributions.

Diffusion is a result of the stochastic nature of motion, as proved in the derivation of the diffusive regimes associated to different time scales of particles' trajectories. The preliminary results have although indicated the influence of the sampling window size and time interval in the derivation of reliable statistics of the random variables as well as in the correct assessment of the diffusive regimes (Chapter 2). While the longitudinal ballistic range of diffusion can be detected with a relatively high frequency image acquisition system, and it was demonstrated to take place in the first instant of particles motion after a short superballistic regime, the anomalous diffusive regime associated to the global range suffers from the size of the investigated area and time interval. When the tracking area and the sampling time stop being a limitation, as for the annular flume experiments, a complete derivation of the diffusive regimes can be achieved. The initial longitudinal ballistic regime and the lateral superdiffusion are followed by a subdiffusion denoted by diffusive scaling coefficients similar to the ones reported in literature (Nikora et al., 2002). The absence of an anomalous diffusion associated to the intermediate scale as proposed in the conceptual model is confirmed also by the results of the new experiment. This leads to a dimensionless time boundary between the longitudinal ballistic and the following subdiffusive regime equal to $tu^*/d \approx 12$, well aligned with the previous finding, $tu^*/d \approx 15$ (Nikora et al., 2002) and $tu^*/d \approx 9$ (from analysis of Tregnaghi et al.'s data). Along the lateral direction the transition takes place earlier, at $tu^*/d \approx 5$. Similar characteristic time parameters emerge from different datasets suggesting that the bed-load motion is represented by two time-scales, an initial one associated to the erratic initiation of motion, and a second one characterized by time spent in motion alternated by periods of rest. A mark of the broad variability in the grains' motion is evident in the derivation of the Kurtosis of particles' location, whose great fluctuation indicates the presence of infrequent extreme observations in the particles trajectories.

The spectrum of possible particles' displacement length is then considered in probabilistic terms within the revised Exner mass balance equation to model the advection and diffusion of bed-load tracers in time along the main flow direction (Ganti et al., 2010). To account for the stochasticity of particles' motion the Exner's formula calculates the tracers concentration at a defined location $x$ at time $t$ by incorporating the idea that tracer particles arriving at position $x$ at time $t$ started their random hops $r$ at many different times $(t - \tau_p)$, with $\tau_p$ the travelling

time (Furbish et al., 2012a). The new formulation includes then the joint probability of the step length and the dependent on random variable of the particles' travelling time. The same equation can be expressed also in terms of particles' velocity $v_p$, by considering that $\tau_p = r/v_p$.

A simplified version was used to model a series of experiments on advection and diffusion of bed load particles during long-run flume experiments with graded bed deposits comprised of natural sand and crashed marble gravel (Marion, 1995). The simplified model attributed the stochastic nature of motion only to the step length by describing the variable with a probability density function whose statistics were derived in function of the hydraulic conditions and the bed roughness. Both experimental observations and modelling simulations indicate that bed roughness elements play a major role in dictating the fate of particle motion. For the experimental conditions under investigation, the time scale of tracer diffusion is more than one order of magnitude larger in beds with low sand content compared to the diffusive process occurring for the same type of tracer over beds with higher sand content. The upper layer of the bed deposit is found to be a significant storage zone as grain retention within this zone may explain the long-tailed curves observed during the experiments with finer tracer compared to the size of the bed roughness elements.

An in-deep analysis of the experimental and modelled concentration curves showed some discrepancies in the growth of the tracers' cloud variance, considered here as an indicator of the type of diffusion. While the model provided subdiffusive simulated curves, the experimental ones indicated a superdiffusion whose rate of growth is related to the mixed-sized composition of the bed material. A trimodal bed in case of sand transport resulted in a faster growing variance compared to a bimodal bed. This preliminary conclusion should be treated carefully as the accuracy in the calculation of variance of the experimental curves could be jeopardized by the loss of tracers mass due to burial and fast moving grains leaving the downstream end of the flume, together with the re-seeding of recirculated tracers at the upstream end of the channel.

The experimental limitations faced in the preliminary investigations supported the planning and preparation of a new series of innovative experiments. The study of bed-load sediment transport benefited of the advantages brought by the use of an annular flume. With the continuous closed system of the circular channel it was possible to perform long-run experiments of variable duration (between 6 and 18 hours) under uniform flow conditions with a bed in equilibrium. The transparent bed material consisting of borosilicate glass beads favoured the visualization of the coloured tracing particles within the bed deposit. In doing so, the resulting tracers' concentrations accounted for also the previously lost buried particles and the fast moving ones as the continuous physical system is not limited by a downstream end. The recording system, made of 6 adjacent GoPro cameras, sampled continuously the entire bed circumference at a frequency of 30 Hz, so that the following analysis did not suffer of the sampling window size and the time interval as in the previous experimental investigations. The circular shape of the channel was tackled with a correction algorithm that removed the lens and the channel-shape distortion, so that a Cartesian system could be implemented over a modified straight flume bed. The tracking process that followed helped collecting information on the position of the moving coloured tracers during their motion over the bed deposit. The same images were afterwards processed to obtain the tracers concentrations along the channel at defined times throughout the duration of the experiment.

With the new experiments it was possible to overcome previous limitations both in the experimental methodology and related data collection (Bradley et al., 2010; Lajeunesse et al., 2010; Furbish et al., 2012b; Roseberry et al., 2012), as well as in the theoretical work that follows. The Lagrangian (or particle-based approach) analysis of the newly collected tracers'

trajectories is here no longer subject to the area and temporal sampling characterizing the experiments. As a consequence the derived distributions of the variables defining the bed-load sediment transport are no longer affected by the typical censorship of previous studies. Step length and travelling time have now been derived for a complete dataset of trajectories, showing that an exponential distribution function commonly assumed in past studies (e.g. Sayre and Hubbell, 1965; Nakagawa and Tsujimoto, 1980; Bradley and Tucker, 2012) is not representative of the distributive shape of these broadly-ranging random variables. The new distributions are better addressed by long-tailed probability functions, such as Lognormal and Weibull PDF, that give importance to also the longest and least frequent observations.

The completeness of the new database has also allowed the derivation of a statistically-based method (Method 2) to solve the censorship of truncated experimental data, with particular application to the case of truncated step lengths. As pointed out by several authors (Ganti et al., 2010; Lajeneusee et al., 2010; Furbish et al., 2012b) and also showed in Chapter 2 with the analysis of previous particles' tracking database, the truncation of the step length distribution could give rise to inappropriate fitting distribution functions, underestimated statistics (Roseberry et al., 2012), and eventually inaccurate probabilistic transport models (Bradley et al., 2010; Ganti et al., 2010). With the new method it is possible to compute the un-truncated distribution of step lengths by applying the concept of joint probability to the truncated data of steps and the dependent travelling time or particles' velocity.

The method, that was initially derived for the truncated database of Tregnaghi et al. (2012b) and afterwards validated with the fully described distribution of step length, consists in computing the marginal distribution of the dependent variable (being it the travelling time or the particles velocity) as a function of the marginal distribution of step lengths and the conditional probability of the two variables. The best correspondence between the calculated and the measured marginal distribution of the selected dependent variable provides accurate estimates of the statistics of the un-truncated step length distribution. It is reckoned that favouring the particles' velocity instead of the travelling time would produce more reliable results since the particles' velocity distribution can include also partial trajectories being then less affected by the experimental limitations. If data of particles' tracking are provided over a restrained investigated area, it should be now possible to reconstruct the truncated distribution of step length via implementation of a simple but effective statistical method.

Such information is of great importance in the derivation of the "entrainment flux" probability models (Einstein, 1942; Ganti et al., 2010; Furbish et al., 2012a), and in the "step-resting" dispersive models such as the one proposed by Sayre and Hubbell (1965) and afterwards reformulated by Bradley et al. in 2010. The previous probabilistic formulations contain mathematical simplifications (Ganti et al., 2010; Furbish et al., 2012a) or inaccurate experimental-based variable distributions (Roseberry et al., 2012) that can generate different model solutions to the advection and diffusion of bed-load particles (Bradley et al., 2010; Bradley and Tucker, 2012).

On the contrary, the model here presented in its general form considers the joint probability of step length and travelling time (or particles' velocity), so that particles can arrive in $x$ by starting their jump $r$ from different time $\tau_p$ (or $r/v_p$ in case of particle velocity formulation), which distributes with a probability function of statistics dependent on the step length $r$. This differs from the previous formulation of Ganti et al. (2010), who neglected the time required by a grain to perform a jump and only considered the probability distribution of step length. The governing equation assumed here has not been simplified in a mathematical series expansion where only the first two terms (first and second derivatives of tracers' concentration) are accounted for (Ganti et al., 2010; Furbish et al, 2012a; Roseberry et al., 2012). By neglecting all the higher

terms of the expansion, the revised Exner formulation can be expressed in the form of simple normal advection and diffusion equation (ADE) if step length is assumed thin-tailed distributed, or to the form of fractional advection and diffusion equation (fADE) for heavy tailed step length distribution (Ganti et al., 2010; Furbish et al., 2012a). Here the higher terms, which contain additional information on the advective and diffusive rates that can also reflect the delayed release of buried grains or the periodicity of bedforms in natural beds, are not excluded a priori. In the general formulation both thin and heavy-tailed step length distributions can be included.

Another advantage of the present model is provided by the probabilistic description of the dependent motion parameter ($\tau_p$ or $v_p$), which is denoted by statistic values calculated as a function of the extent of the step $r$. Contrarily to a simple relationship between the travelling time and the step length, as for example the experimentally derived one by Roseberry et al., (2012), i.e. $r \approx \tau_p^{5/3}$, the travelling time distribution are here based on two experimental dataset and turned out to be well described by a distribution function whose statistics are scaled to the step length via power law relationships (or an exponential growth to the an asymptotic velocity value for the case of particles' velocity). As a consequence particles can take different times to compute the same step $r$. Considering averaged values (Bradley et al., 2010) of the particle trajectories variables can lead to misinterpretation of the actual advective and diffusive scale. This is clear in the outputs of the simplified model version. As demonstrated with the analysis of the experimental data, particles move with different velocities, which distribute according to a gamma-like function for each range of steps $r_i$. If this variability is neglected by assuming an average particles' velocity, the modelled variance grows differently in time compared to the experimentally observed one.

When data from a Lagrangian analysis of bed-load particles is provided, even if censorshipped because of the experimental set-up, the general form of the model could fit the curves directly with data rather than choosing values by matching the model outputs to the observed concentration curves. The statistical method proposed here to solve the censorship of observed trajectories can be applied to data collected from experiments with limited investigated area/time interval. In such experiments different bed roughness and hydraulic conditions can be tested in order to clarify their role in the tracked particles' trajectories. By applying the statistical method to the collected truncated-data, it will be possible to reconstruct the PDFs of step length from the related particles' velocity, that constitute the stochastic basis of the general version of the reformulated Exner's equation. The influence that the heterogeneity of different mixed-size material or flow conditions plays on the motion of bedload grains could then be experimentally addressed and statistically incorporated into the reconstructed trajectories variables. Afterwards the distributed random variables (step length, travelling time or particles' velocity) will be included into the probabilistic model for the simulation of the diffusive character of a cloud of particles.

The major role played by the bed roughness was evident in the current study. The relative size of the moving particles and the content of finer material proved to have a different impact on the advective and diffusive extent for respectively the case of coarse and fine sand transport over a trimodal bed, and the case of gravel transport over bimodal and trimodal mixed material. A sign of the roughness influence is also carried by the growth of the clouds variance with time, which indicated a superdiffusive regime. The coarse sand over a bed with higher sand content showed to diffuse faster than in the case of gravel with halved sand fraction in the bed mixture. A preliminary result is presented for the new experiments as well. In this case the smaller variability in particle sizes composing the bed mixture generated a nearly normal diffusion, that could be accurately matched by the model when experimental data is included in the formulation.

A signature of the bed roughness can then be read in the diffusive characteristics of the cloud

of particles. The two bed mixtures and the different sizes of tracers used in the annular flume experiments together with the range of hydraulic conditions applied on the bed would possibly help delineating the influence of these two major factors in sediment transport. However, only experiments involving a wider variability in particle's sizes, as the ones performed by Marion (1995), were used to clarify the relationship of fractional particles' motion and diffusivities. The promising statistical tools presented here though can support future experimental and theoretical investigations by overcoming the censorship of observed data and by including the stochastic nature of motion into probabilistic transport models.

Further study is also required in the assessment of the diffusive regime (Bradley et al., 2010). The global range of trajectories includes many particle' steps and resting times and it was here confirmed to be denoted by subdiffusion ($\gamma_x < 0.5$). In contrast, the concentration curves suggested that the variance of particles' location grows linearly with time in nearly uniform beds ($\gamma_x = 0.5$), or with a superdiffusive character over mixed sediment deposits, respectively $\gamma_x = 0.58$ for gravel in bimodal bed and $\gamma_x = 0.78$ for sand in trimodal bed. The concentration curves fall into the definition of the global regime, as they are formed by particles that spent time travelling and at rest, but they might be characterized by a different time-scale. The derivation of the subdiffusive regime (Chapter 2 and 5) is performed for short time analysis (of the order of few minutes), while the concentration curves are calculated over several minutes or even hours. The curves could then incorporate features of the sediment transport that take place for longer-time bed evolution, such as the formation of bed-forms, the ahead segregation of faster moving grains and the delayed release of trapped grains. The latest, i.e. the subsequent re-mobilisation of trapped grains, have just find confirmation in the analysis of the resting times (Chapter 5) which showed the likelihood for a moving grain to be trapped even for several hours on the bed. These features are promisingly represented in the proposed general model as it solves transport by incorporating the probabilistic data of particles' trajectories, which in turn keeps a record of the hydraulic condition and bed roughness. A further improvement would consist in addressing the temporal evolution of retention and entrainment rate as a function of the particles' probability of rest.

It is important to stress that only when all tracing particles are accounted for in the variance calculation, it is possible to attain reliable scaling diffusive coefficients $\gamma$ and thus a correct assessment of the diffusive regimes. With this regard, the annular flume experiment with transparent bed material proved to satisfy this requirement by avoiding the data collection shortcomings of previous experimental set-ups.

The scientific achievements that have been presented in the current study can find practical application in river restoration and management projects. It should be now possible to assess and predict the movement of a specific size of sediment over the channel bottom by simply focussing on a small group of moving grains of that size over a limited area of the bed. A single water proof camera, as the small GoPro model here used, can be placed parallel to the water surface to capture images of the bed at a sufficiently high frequency. The small cost of such a camera together with its specifications makes it a convenient choice for studying the trajectories of moving bed-load sediment. The following particle tracking would provide valuable information on single grains movement occurring within the camera's field of view. If the observed trajectories result partially determined due to the size of the investigated bed area, a simple statistical solution (Method 2) can be implemented so as to obtain the full stochastic description of moving parameters, e.g. the step length, travelling time or particle velocity, as well as an estimation of the entrainment rate.

The probabilistic description of these Lagrangian variables constitutes the basis of the

advection-diffusion model. The model output would then predict the location of the class of sediment of a determined size along the channel reach in time. This is of particular interest in the assessment of the areas of a river that can be mostly affected by the release and the movement of a polluted group of sediment. Furthermore, the temporal evolution of the predicted concentration curves would provide an indication of the time it would take the sediment to reach further downstream distances, consequently putting at a risk the ecological status of other parts of the water body. The model output can also be interpreted in terms of retention time scale, providing the duration of permanence of grains in a particular location. Such information is essential in the forecast of the future evolution in the status of the river's ecosystems, particularly in the assessment of the future conditions of the benthic community thriving at the interface between sediment and water. Predicting the fate of a contaminated sediment would translate in targeted remediation actions that can take into account not only the spatial scale of the sediment motion but also its temporal evolution.

Besides the environmentally oriented applications of the present research, the method developed here to reconstruct truncated distributions of a group of individual grain trajectories can be easily implemented to similar databases where experimental limitations could jeopardize the representativeness of the results. Research works on granular material movement, such as in studies of landslides, avalanches, mining-related mineral transport, soil-erosional processes, where information on grain movements is fundamental for a thorough analysis of the phenomena, could all benefit from the statistical method of solving truncated motion parameters.

# Appendices

# Appendix A

# Additional material

The additional material comprises the following figures which refer to the analysis of Chapter 2 for the experimental data of Tregnaghi et al. (2012b).

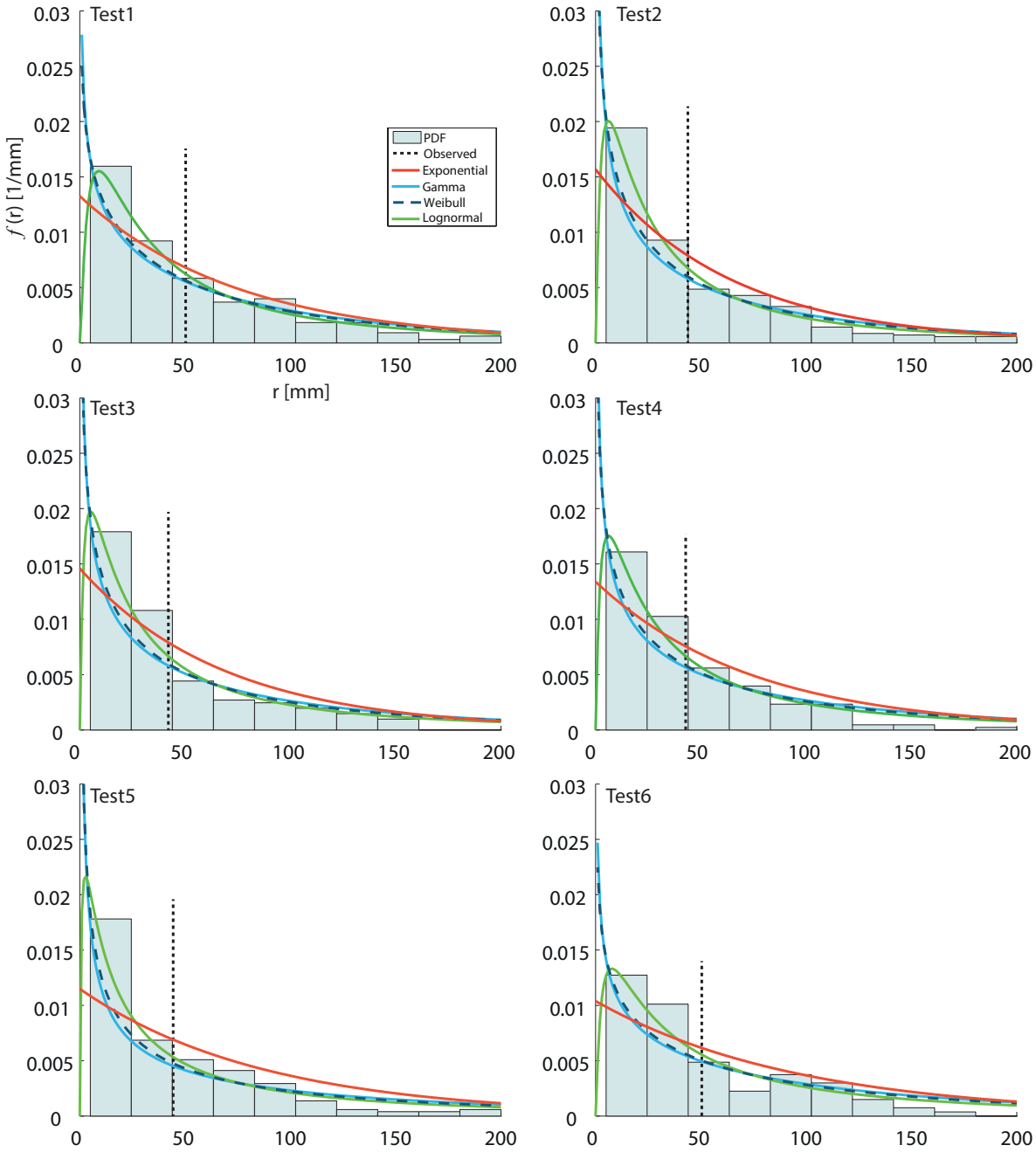


Figure A.1: Step length distributions with the relative fitting model (namely Exponential, Gamma, Weibull and Lognormal) for the six experimental tests. The dashed vertical line indicates the arithmetic mean step length derived for the truncated data.

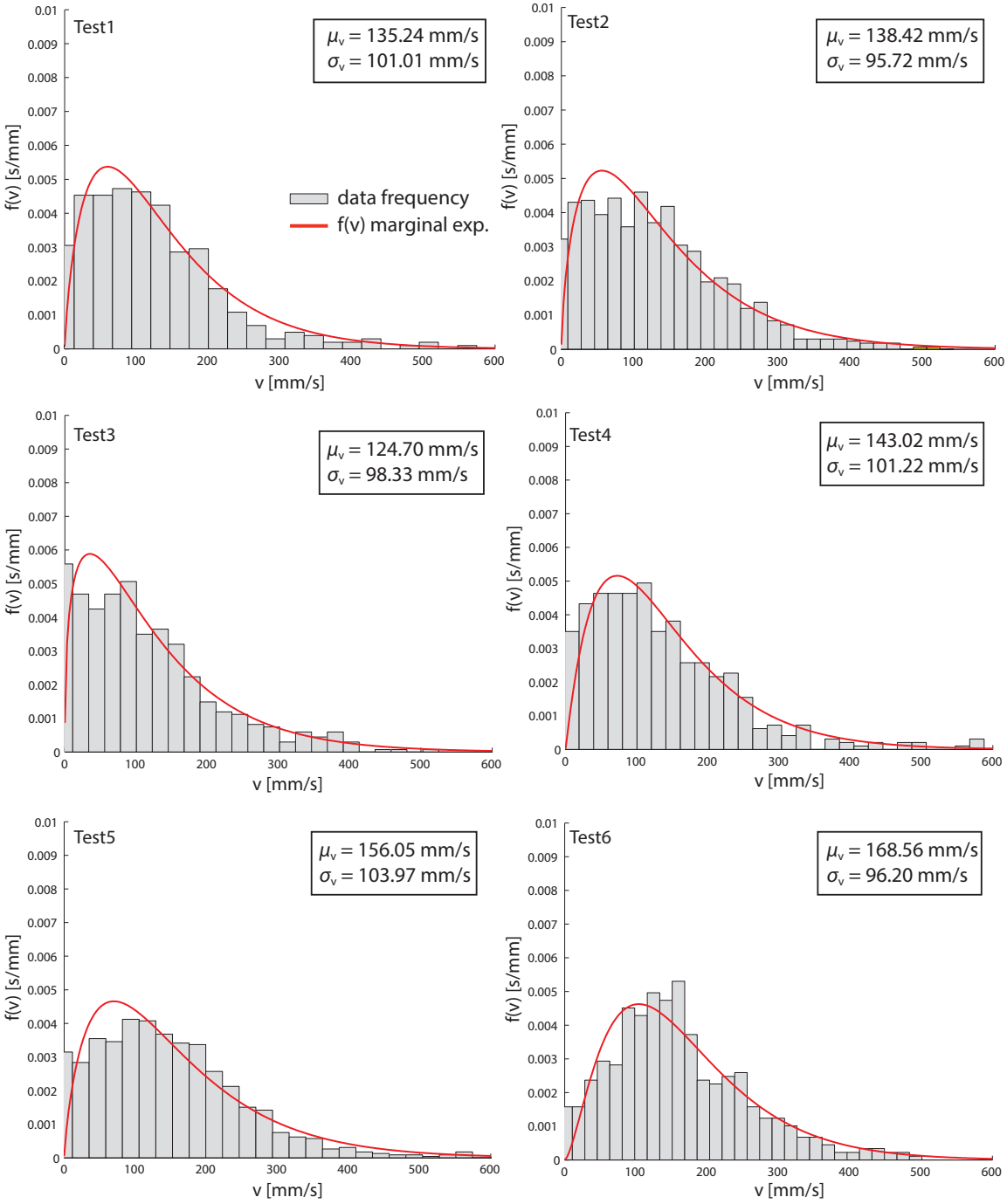


Figure A.2: Particles' velocity frequency distribution together with the fitting gamma-like PDF for the six tests presented in Chapter 2. The mean and standard deviation are reported in each plot.

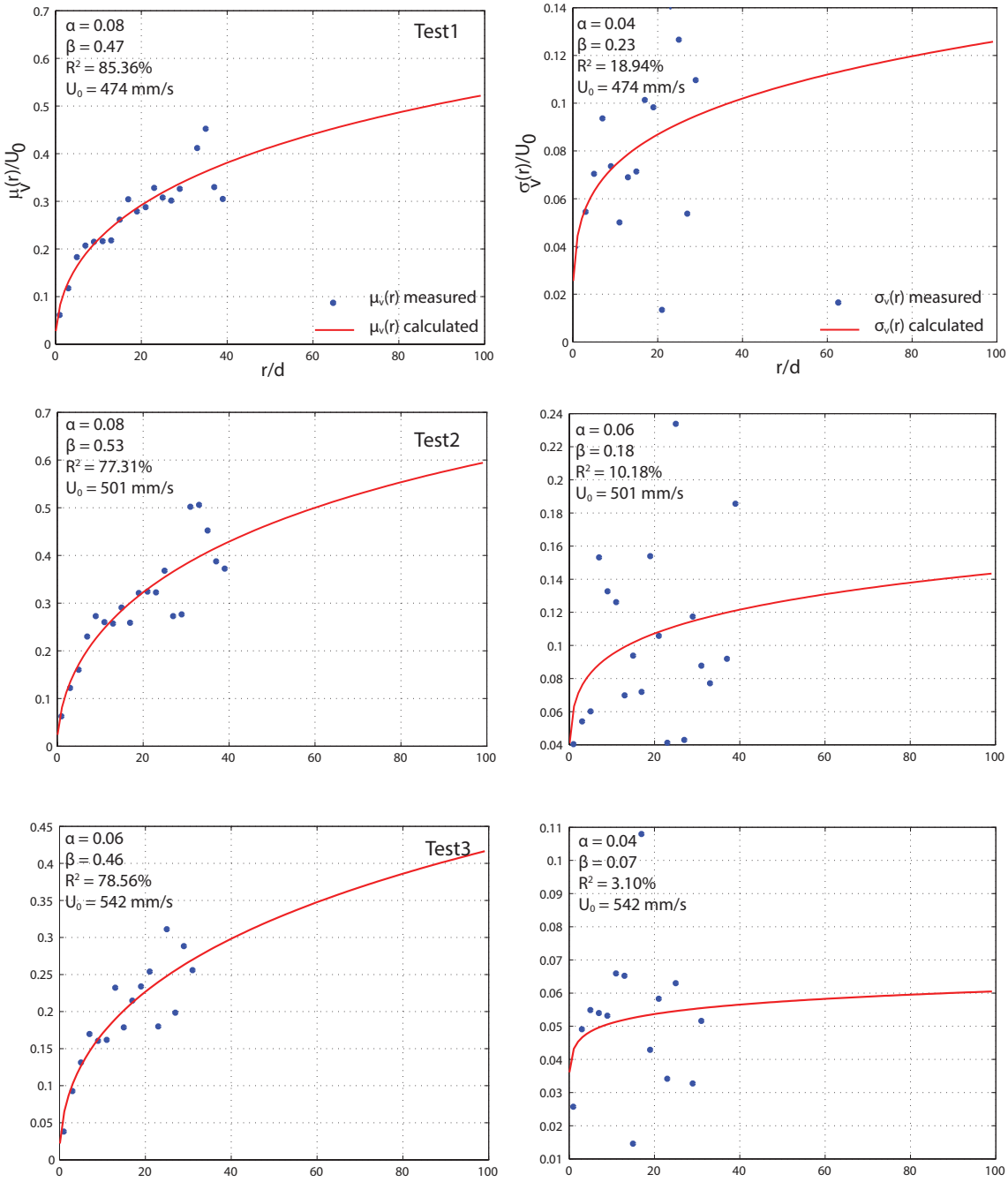


Figure A.3: Mean and standard deviation of the particles' velocity scaled to the dimensionless step length $r/d$ for the experimental tests T1, T2 and T3. The asymptotic value $U_0$ reported in the plots is here calculated with the linear profile at $z_0 \approx 1.0 d_{50}$.

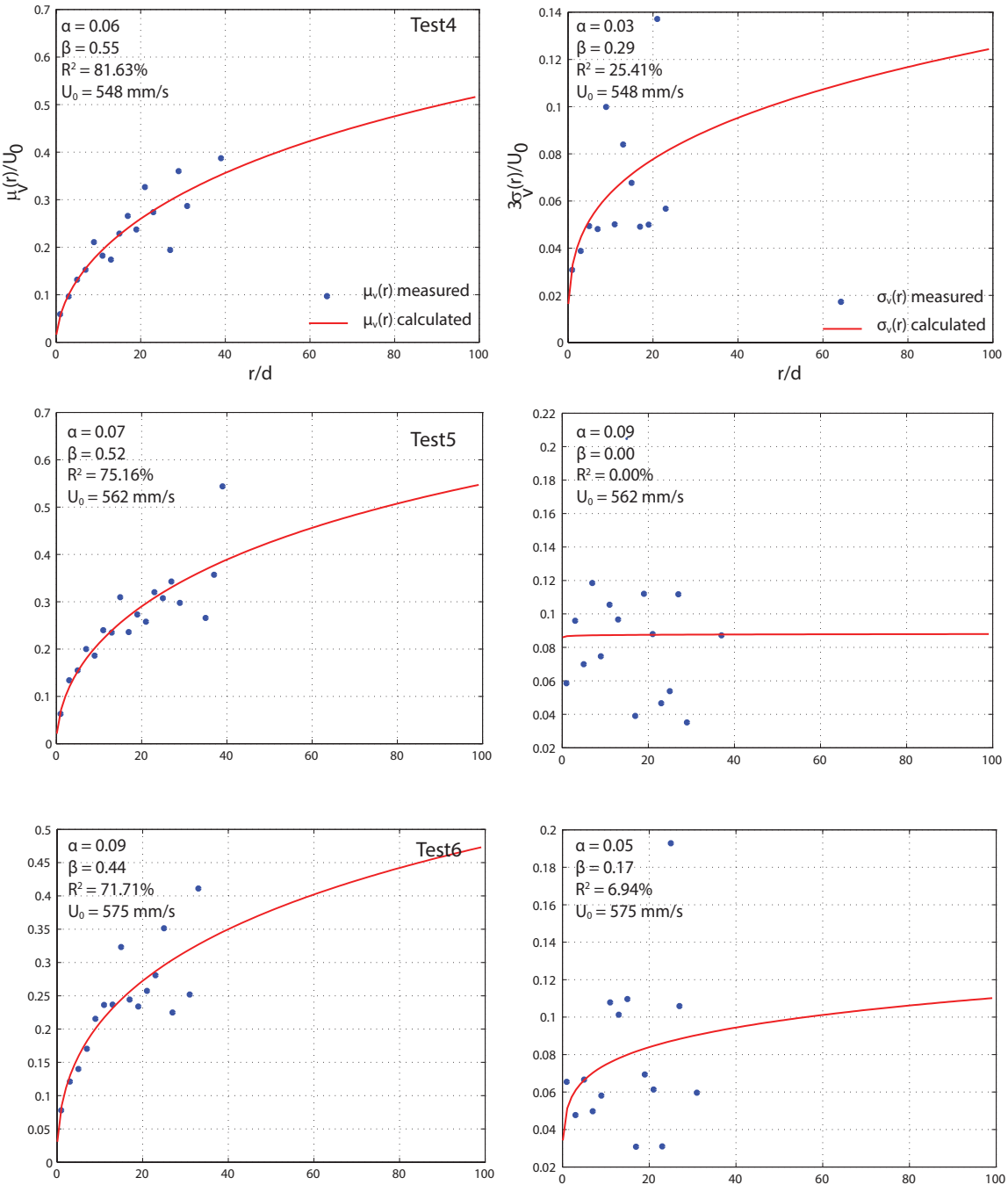


Figure A.4: Mean and standard deviation of the particles' velocity scaled to the dimensionless step length $r/d$ for the experimental tests T4, T5 and T6. The asymptotic value $U_0$ reported in the plots is here calculated with the linear profile at $z_0 \approx 1.0 d_{50}$.

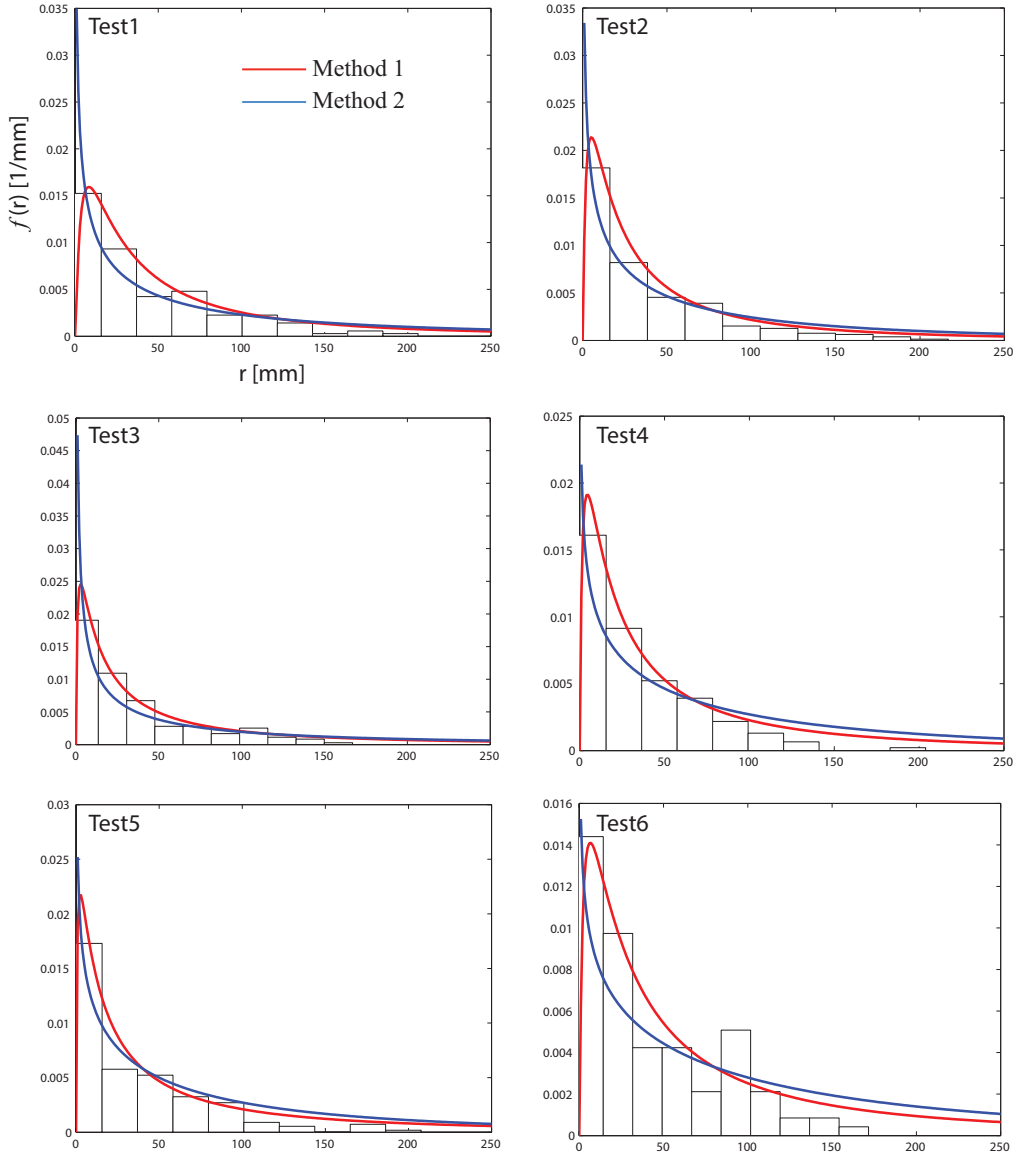


Figure A.5: Probability distributions resulting from the two methods applied to the experimental truncated data. The red line refers to the Lognormal PDF of Method 1, whilst the blue line denotes the Weibull PDF of Method 2.

# References


Abbott, J. E. and Francis, J. R. D. (1977). "Saltating and suspended trajectories of solid grains in a water stream." *Phil. Trans.*, R. Soc. Lond. A 284, 22, 5254.

Aberle, J., Koll, K., and Dittrich, A. (2008). "Form induced stresses over rough gravel-beds." *Acta Geophysica*, vol. 56, no. 3, pp. 584-600, DOI: 10.2478/s11600-008-0018-x.

Achers, P. and White, W. R. (1973). "Sediment transport: a new approach and analysis." *Hydraulics Div. Jour., ASCE*, Vol. 99, No. HY11, pp. 2041-2060.

Bialik, R. J., Nikora, V. I., and Rowinski, P. M. (2012). "3D lagrangian modelling of saltating particles diffusion in turbulent water flow." *Acta Geophysica*, vol. 60, no. 6, pp. 1639-1660, doi: 10.2478/s11600-012-0003-2.

Boano, F., Camporeale, C., Revelli, R., and Ridolfi, L. (2006). "Sinuosity driven hyporheic exchange in meandering rivers." *Geophys. Res. Lett.*, 33, L18406, doi:10.1029/2006GL027630.

Booij, R. (1994). "Measurements of the flow field in a rotating annular flume." *Communications on Hydraulic and Geotechnical Engineering*, Rep. no 94-2 Delft University of Technology, Delft, The Netherlands.

Bosman, J. J., E. V. d. V. and Hulsbergen, C. (1987). "Sediment concentration measurement by transverse suction." *Coastal Engineering, Elsevier.*

Bottacin-Busolin, A., Tait, S. J., Marion, A., Chegini, A., and Tregnaghi, M. (2008). "Probabilistic description of grain resistance from simultaneous flow field and grain motion measurements." *Water Resour. Res.*, 44, W09419, doi:10.1029/2007WR006224.

Bouchaud, J. and Georges, A. (1990). "Anomalous diffusion in disordered media: statistical mechanisms, models and physical applications." *Physics reports*, 195(4), 127–293.

Bradley, D. N. and Tucker, G. E. (2012). "Measuring gravel transport and dispersion in a mountain river using passive radio tracers." *Earth Surf. Process. Landforms*, 37, pp. 1034-1045.

Bradley, D. N., Tucker, G. E., and Benson, D. A. (2010). "Fractional dispersion in a sand bed river." *Journal of Geophysical Research*, 115, pp. 33–52.

Buffington, J. M. (1999). "The legend of A. F. Shields." *Journal of Hydraulic Engineering*, 377.

Campagnol, J., Radice, A., Ballio, F., and Nikora, V. I. (2015). "Particle motion and diffusion at weak bed load: accounting for unsteadiness effects of entrainment and disentrainment." *Journal of Hydralics Research*, 53:5, 633-648, DOI:10.1080/00221686.2015.1085920.

Campagnol, J., Radice, A., Nokes, R., Bulankina, V., Lescova, A., and Ballio, F. (2013). "Lagrangian analysis of bed-load sediment motion: database contribution." *Journal of Hydraulics Research*, 51:5, 589-596, DOI: 10.1080/00221686.2013.812152.

Cantero, M., Mangini, S., Pedocchi, F., Nino, Y., and Garcia, M. (2004). "Analysis of flow characteristics in an annular flume: Implications for erosion and deposition of cohesive sediments." *in World Water and Environmental Resources Congress*, pp. 2610-2619.

Cecchetto, M., Tregnaghi, M., Bottacin-Busolin, A., Tait, S., and Marion, A. (2016). "Statistical description on the role of turbulence and grain interference on particle entrainment from gravel beds." *Journal of Hydraulic Engineering*, doi: 10.1061/(ASCE)HY.1943-7900.0001224.

Celik, A. O., Diplas, P., Dancey, C. L., and Valyrakis, M. (2010). "Impulse and particle dislodgement under turbulent flow conditions." *Phys. Fluids*, 22(4), 046601.

Chegini, A. H. N. and Tait, S. (2011). "Automated measurement of moving grains on bed deposits." *International Journal of Sediment Research*, 26 (2011) 304-317.

Church, M. (2006). "Bed material transport and the morphology of alluvial river channels." *Annu. Rev. Earth Planet. Sci.*, 34:325–54.

Coleman, S. E., Nikora, V. I., and Aberle, J. (2011). "Interpretation of alluvial beds through bed-elevation distribution moments." *Water Resources Research*, 47, W11505, doi:10.1029/2011WR010672.

Cotterle, L. (2015). "Experimental observations of grain step length statistics." *PhD Thesis*, The University of Padova, Italy.

Crane, M. (2002). "Proposed development of sediment quality guidelines under the European Water Framework Directive: a critique." *Toxicology Letters*, 142(2003), 195/206.

Dey, S., Sarkar, S., Bose, S., Tait, S., and Castro-Orgaz, O. (2011). "Wall-wake flows downstream of a sphere placed on a plane rough wall." *Journal of Hydraulic Engineering*, 137(10), 1173–1189.

Diplas, P. (1987). "Bedload transport in gravel-bed streams." *Journal of Hydraulic Engineering*, 113(HY3), 277–292.

Diplas, P., Dancey, C. L., Celik, A. O., Valyrakis, M., Greer, K., and Akar, T. (2008). "The role of impulse on the initiation of particle movement under turbulent flow conditions." *Science*, 322, 717–720.

Diplas, P. and Sutherland, A. J. (1988). "Sampling techniques of gravel sized sediments." *J. Hydraulic Eng., ASCE*, 114(5), 484-501.

Drake, T. G., Shreve, R. L., Dietrich, W. E., Whiting, P., and Leopold, L. B. (1987). "Bed load transport of fine gravel observed by motion-picture photography." *J. Fluid Mech.*, 192, pp. 193-217.

Du Bois, M. P. (1979). "Le Rhone et les rivieres a lit affouillable." *Annals de Ponts et Chaussees*, Section 5 , 18, 141–195. (In French.).

Dwivedi, A., Melville, B., Shamseldin, A., and Guha, T. K. (2011). "Flow structures and hydrodynamic force during sediment entrainment." *Water Resour. Res.*, 47,W01509.

Einstein, H. A. (1942). "Formulas for the transport of bed sediment." *Trans. Am. Soc. Civ. Eng.*, 107, 561–574.

Einstein, H. A. (1950). "The bed-load function for sediment transportation in open channel flows." *Tech. Bull.*, 1026, 78 pp., Soil Conserv. Serv., U.S. Dep. of Agric., Washington, D. C.

Engelund, F. and Eggert, H. (1967). "A monograph on sediment transport in alluvial streams." *Teknisk Vorlag*, Copenhagen, 63p.

Ettema, R. and Mutel, C. F. (2004). "Hans Albert Einstein: Innovation and compromise in formulating sediment transport by rivers." *Journal of Hydraulic Engineering*, Vol. 130, No. 6, doi: 10.1061/(ASCE)0733-9429(2004)130:6(477).

Fenton, J. and Abbott, J. (1977). "Initial movement of grains on a stream bed: The effect of relative protrusion." *Mathematical and Physical Sciences*, Vol. 352, No. 1671, pp. 523-537.

Ferguson, R. I. and Wathen, S. J. (1998). "Tracer-pebble movement along a concave river profile: Virtual velocity in relation to grain size and shear stress." *Water Resour. Res.*, Vol. 34, No. 8, pp. 2031-2038.

Furbish, D. J., Ball, A. E., and Schmeeckle, M. W. (2012c). "A probabilistic description of the bed load sediment flux: 4. Fickian diffusion at low transport rates." *J. Geophys. Res.*, 117, F03034, doi:10.1029/2012JF002356.

Furbish, D. J., Haff, P. K., Roseberry, J. C., and Schmeeckle, M. W. (2012a). "A probabilistic description of the bed load sediment flux: 1. Theory." *J. Geophys. Res.*, 117, F03031, doi:10.1029/2012JF002352.

Furbish, D. J., Roseberry, J. C., and Schmeeckle, M. W. (2012b). "A probabilistic description of the bed load sediment flux: 3. The particle velocity distribution and the diffusive flux." *J. Geophys. Res.*, Vol. 117, F03033, doi:10.1029/2012JF002355.

Ganti, V., Meerschaert, M. M., Foufoula-Georgiou, E., Viparelli, E., and Parker, G. (2010). "Normal and anomalous diffusion of gravel tracer particles in rivers." *J. Geophys. Res.*, 115, F00A12, doi: 10.1029/2008JF001222.

Gharabaghi, B., Inkratas, C., Krishnappan, B. G., and Rudra, R. P. (2007). "Flow characteristics in a rotating circular flume." *The Open Civil Eng. J.*, Vol. 1, pp. 30-36.

Gomez, B. and Church, M. (1989). "An assessment of bedload sediment transport formulae for gravel bed rivers." *Water Resources Research*, VOL. 25, NO. 6, 1161-1186.

Graham, D., James, P. W., Jones, T. E. R., Davies, J. M., and Delo, E. A. (1992). "Measurement and prediction of surface shear stress in annular flume." *J. Hydraul. Eng.*, Vol. 118, No. 9.

Grass, A. J. (1970). "Initial instability of fine sand." *J. Hydraul. Div.*, 96(3), pp. 619-632.

Gronz, O., Hiller, P. H., Wirtz, S., Becker, K., Iserloh, T., Seeger, M., Brings, C., Aberle, J., Casper, M. C., and Ries, J. B. (2016). "Smartstones: A small 9-axis sensor implanted in stones to track their movements." *Catena*, 142 (2016) 245–251.

Hassan, M. A. and Church, M. (1994). "Vertical mixing of coarse particles in gravel bed rivers: a kinematic approach." *Water Resour. Res.*, Vol. 30, No. 4, pp. 1173-1185.

Hassan, M. A. and Church, M. (2000). "Experiments on surface structure and partial sediment transport on a gravel bed." *Water Resour. Res.*, Vol. 36, No. 7, pp. 1885-1895.

Hassan, M. A., Church, M., and Ashworth, P. J. (1992). "Virtual rate and mean distance of travel of individual clasts in gravel-bed channels." *Earth Surface Processes and Landforms*, Vol. 17, pp. 617-327.

Hassan, M. A., Voepel, H., Schumer, R., Parker, G., and Fraccarollo, L. (2013). "Displacement characteristics of coarse fluvial bed sediment." *J. Geophys. Res. Earth Surf.*, 118, 155-165, doi: 10.1029/2012JF002374.

Heathershaw, A. D. and Thorne, P. D. (1985). "Sea-bed noises reveal role of turbulent bursting phenomenon in sediment transport by tidal currents." *Nature*, 316, 339–342, doi:10.1038/316339a0.

Heays, K. G., Friedrich, H., Melville, B. W., M.ASCE, and Nokes, R. (2014). "Quantifying the dynamic evolution of graded gravel beds using particle tracking velocimetry." *Journal of Hydraulic Engineering*, doi: 10.1061/(ASCE)HY.1943-7900.0000850.

Hirano, M. (1971). "On riverbed variation with armouring." *Proc. Jpn, Soc. Civ. Eng.*, 195, 55-65.

Hu, C. (1996). "Bed-load transport. I: Mechanical characteristics." *J. Hydraul. Eng.*, 122, 245–254.

James, P. W., Jones, T. E. R., and Stewart, D. M. (1996). "Numerical and experimental studies of annular flume flow." *Appl. Math. Modelling*, Vol 20, March.

Karelse, M. (1990). "Velocity and bed shear stress measurements in the annular flume." *Rep. Z0159-52*, Delft Hydraulics, Delft, the Netherlands.

Kellerhals, R. and Bray, D. I. (1971). "Sampling procedures for coarse fluvial sedimentss." *J. Hyd. Div., Proc. ASCE*, Vol. 97, No. HY8, pp. 1165-1180.

Kirchner, J. W., Dietrich, W. E., Iseya, F., and Ikeda, H. (1990). "The variability of critical shear stress, friction angle, and grain protrusion in waterworked sediments." *Sedimentology*, 37, 647-672.

Kramer, H. (1932). "Modellgeschiebe und schleppkraft." *Doktor-IngenIngenieurs dissertation*, Technischen Hochschule, Dresden, Germany (in German).

Kramer, H. (1935). "Sand mixtures and sand movement in fluvial models." *Trans., ASCE*, 100(1909), 798–838.

Krishnappan, B. G. (1993). "Rotating circular flume." *Journal of Hydraulic Engineering*, vol. 119, pp. 758-767.

Lajeunesse, E., Devauchelle, O., Houssais, M., and Seizilles, G. (2013). "Tracer dispersion in bedload transport." *Advances in Geosciences*, doi:10.5194/adgeo-37-1-2013.

Lajeunesse, E., Malverti, L., and Charru, F. (2010). "Bed load transport in turbulent flow at the grain scale: Experiments and modeling." *J. Geophys. Res.*, 115, F04001, doi: 1029/2009JF001628.

Marion, A. (1995). "Analisi sperimentale della dinamica verticale dei sedimenti negli alvei fluviali (in Italian)." *Ph.D. thesis*, University of Padova, Padova, Italy.

Marion, A. and Fraccarollo, L. (1997a). "Experimental observation of mobile armouring development." *Water Resour. Res.*, Vol 33, No. 6, pp. 1447-1453.

Marion, A. and Fraccarollo, L. (1997b). "New conversion model for areal sampling of fluvial sediment." *J. of Hydraulic Eng.*, Vol. 123, No. 12, pp. 1148-1151.

Marion, A., Nikora, V., Puijalon, S., Bouma, T., Koll, K., Ballio, F., Tait, S., Zaramella, M., Sukhodolov, A., O'Hare, M., Wharton, G., Aberle, J., Tregnaghi, M., Davies, P., Nepf, H., Parker, G., and Statzner, B. (2014). "Aquatic interfaces: a hydrodynamic and ecological perspective." *J. Hydraul. Eng.*, doi:10.1080/00221686.2014.968887.

McEwan, I., Sorensen, M., Heald, J., Tait, S., Cunningham, G., Goring, D., and Willetts, B. (2004). "Probabilistic modelling of bed-load composition." *J. Hydraul. Eng.*, doi: 10.1061/(ASCE)0733-9429(2004)130:2(129).

Mehta, A. J. and Partheniades, E. (1973a). "Depositional behavior of cohesive sediments." *Techn. Rep. no. 16*, Coastal and Oceanographic Engineering Department, University of Florida, USA.

Mehta, A. J. and Partheniades, E. (1973b). "Effect of physico-chemical properties of fine suspended sediment on the degree of deposition." *Proc. Int. Symp. River Mechanics*, IAHR, Bangkok, Thailand, pp. 465-476.

Meyer-Peter, E. and Muller, R. (1948). "Formulas for bed-load transport." *Proceedings, 3rd Meeting of International Association Hydraulic Resources*, Stockholm, pp. 39-64.

Nakagawa, H. and Tsujimoto, T. (1980). "Sand bed instability due to bed load motion." *J. Hydraul. Div. Am. Soc. Civ. Eng.*, 106(HY12), 2029– 2051.

Nelson, J. M., Shreve, R. L., Mclean, S. R., and Drake, T. G. (1995). "Role of near-bed turbulence structure in bed load transport and bed form mechanics." *Water Resour. Res.*, 31(8), 2071–2086, doi:10.1029/95WR00976.

Nikora, V., Goring, D. G., and Biggs, B. J. F. (1998). "On gravel-bed roughness characterization." *Water Resour. Res.*, Vol. 34, No. 3, pp. 517-527.

Nikora, V., Goring, D. G., McEwan, I., and Griffiths, G. (2001). "Spatially averaged open-channel flow over rough bed." *J. Hydraul. Eng.*, Vol. 127, No. 2.

Nikora, V., Habersack, H., Huber, T., and McEwan, I. (2002). "On bed particle diffusion in gravel bed flows under weak bed load transport." *Water Resour. Res.*, Vol. 38, No. 6, doi: 10.1029/2001WR000513.

Nino, Y. and Garcia, M. H. (1996). "Experiments on particle turbulence interactions in the near wall regions of an open channel flow: Implications for sediment transport." *J. Fluid Mech.*, 326, 285– 319, doi:10.1017/S0022112096008324.

Nokes, R. (2012). "Streams v. 2.00. system theory and design." University of Canterbury, Christchurch, New Zealand.

Paintal, A. S. (1969). "The probabilistic characteristics of bed load transport in alluvial channels." *Ph. D. dissertion*, University of Minnesota. Minneapolis, Minnesota, USA.

Paintal, A. S. (1971). "A stochastic model of bed load transport." *Journal of Hydraulic Research*, 9(4), 527–554.

Papanicolaou, A., Diplas, P., Balakrishnan, M., and Dancey, C. (1999). "Computer vision technique for tracking bed load movement." *Journal of Computing in Civil Engineering*, Vol. 13, No. 2.

Papanicolaou, A., Diplas, P., Dancey, C., and Balakrishnan, M. (2001). "Surface roughness effects in near-bed turbulence: Implications to sediment transport." *J. Eng. Mech.*, 127(3), 211–218, doi:10.1061/(ASCE)0733-9399(2001)127:3(211).

Papanicolaou, A., Diplas, P., Evaggelopoulos, N., and Fotopolous, S. (2002). "Stochastic incipient motion criterion for spheres under various bed packing conditions." *Journal of Hydraulic Research*, 128(4), 369–380, doi:10.1061/(ASCE)0733-9429(2002)128:4(369).

Parker, G., ASCE, M., Paola, C., and Leclair, S. (2000). "Probabilistic Exner sediment continuity equation for mixtures with no active layer." *J. Hydraul. Eng.*

Parker, G., Klingeman, P. C., and McLean, D. G. (1982). "Bedload and size distribution in paved gravel-bed streams." *J. Hydr. Div., ASCE*, 108(4), 544–571.

Partheniades, E. and Kennedy, J. F. (1996). "Depositional behaviour of fine sediment in a turbulent fluid motion." *Proc. 10th Conference on Coastal Engineering*, London, England, vol. 2, pp. 723-742.

Partheniades, E., Kennedy, J. F., Etter, R. J., and Hayer, R. P. (1966). "Investigations of the depositional behavior of fine cohesive sediments in annular rotating channel." *Rep. no 96*, Ralph M. Parsons, Hydrodynamics Laboratory, Massachusetts Institute of Technology, Cambridge, Massachusetts, USA.

Pelosi, A. and Parker, G. (2014). "Morphodynamics of river bed variation with variable bedload step length." *Earth Surface Dynamics*, doi:10.5194/esurf-2-243-2014.

Proffitt, G. T. (1980). "Selective transport and armouring of non-uniform alluvial sediments." *PhD thesis*, Univ. of Canterbury at Christchurch, New Zealand.

Radice, A., Nikora, V., Campagnol, J., and Ballio, F. (2013). "Active interactions between turbulence and bed load: Conceptual picture and experimental evidence." *Water Resour. Res.*, 49, doi:10.1029/2012WR012255.

Ranieri, M. (2005). "Analisi della dispersion di sediment traccianti su letti mobile a granulometria non uniforme." *MSc Thesis*, The University of Padova, Italy, (In Italian).

Roseberry, J. C., Schmeeckle, M. W., and Furbish, D. J. (2012). "A probabilistic description of the bed load sediment flux: 2. Particle activity and motions." *J. Geophys. Res.*, 117, F03032, doi:10.1029/2012JF002353.

Sayre, W. and Hubbell, D. (1965). "Transport and dispersion of labeled bed material, North Loup River, Nebraska." *US Geololgical Survey Professional Paper*, 433.

Schmeeckle, M. W., Nelson, J. M., and Shreve, R. L. (2007). "Forces on stationary particles in near-bed turbulent flows." *J. Geophys. Res.*, 112, F02003, doi:10.1029/2006JF000536.

Schoklitsch, A. (1934). "Der Geschiebetrieb und die Geschie - befracht." *Wasserkraft und Wasserwirtschaft*, 29(4), 37–43 (in German).

Schoklitsch, A. (1950). "Geschiebebewegung in Flussen und an Stauwerken." *Springer-Verlag*, New York (in German).

Sheng, Y. P. (1989). "Consideration of flow in rotating annuli for sediment erosion and deposition studies." *Journal of Coastal Research*, Special Issue No. 5, pp. 207-216.

Shields, A. (1936). "Anwendung der ahnlichkeitsmechanik und turbulenz forschung auf die geschiebebewegung." *Mitteil Preuss Versuchsanst Wasser Erd Schiffsbau*, No. 26, Berlin (in German).

Skafel, M. G. and Krishnappan, B. G. (1999). "Laboratory investigation of depositional characteristics of mud from an inland harbour using a rotating circular flume." *Water, Air and Soil Pollution*, vol. 112,pp. 1-19.

Sutherland, A. J. (1967). "Proposed mechanism for sediment entrainment by turbulent flows." *J. Geophys. Res.*, 72(24), 6183–6194.

Tait, S., Ashley, R., Verhoeven, R., Clemens, F., and Aanen, L. (2003). "Sewer sediment transport studies using an environmentally controlled annular flume." *Water Science and Technology*, Vol 47, No 4, pp. 51–60.

te Slaa, S. (2012). "Calibration report annular flume." *Communications on Hydraulic and Geotechnical Engineering*, ISSN 0169-6548.

Tregnaghi, M., Bottacin-Busolin, A., Marion, A., and Tait, S. (2012a). "Stochastic determination of entrainment risk in uniformly sized sediment beds at low transport stages: 1. Theory." *J. Geophys. Res.*, 117, F04004, doi: 10.1029/2011JF002134.

Tregnaghi, M., Bottacin-Busolin, A., Tait, S., and Marion, A. (2012b). "Stochastic determination of entrainment risk in uniformly sized sediment beds at low transport stages: 2. Experiments." *J. Geophys. Res.*, 117, F04005, doi: 10.1029/2011JF002134.

Valyrakis, M., Diplas, P., Dancey, C. L., Greer, K., and Celik, A. O. (2010). "The role of instantaneous force magnitude and duration on particle entrainment." *J. Geophys. Res.*, 115, F02006.

van Rijn, L. (1984a). "Sediment pick-up function." *J. Hydraul. Eng.*, Vol. 110, No. 10.

van Rijn, L. (1984b). "Sediment transport. I: Bed load transport." *J. Hydraul. Eng.*, 110(10), 1431–1456.

Wiberg, P. L. and Smith, J. D. (1989). "Model for calculating bed load transport of sediment." *Journal of Hydraulic Engineering*, Vol. 115, No. 1.

Wilcock, P. R. (1997). "The components of fractional transport rate." *Water Resour. Res.*, vol. 33, No. 1, 247-258.

Wilcock, P. R., Kenworthy, S. T., and Crowe, J. C. (2001). "Experimental study of the transport of mixed sand and gravel." *Water Resour. Res.*, Vol. 37, No. 12, pp. 3349–3358.

Wilcock, P. R., M.ASCE, and Crowe, J. C. (2002). "Surface-based transport model for mixed-size sediment." *Journal of Hydraulic Engineering*, Vol. 129, No. 2, doi: 10.1061/(ASCE)0733-9429(2003)129:2(120).

Wong, M., Parker, G., DeVries, P., Brown, T. M., and Burges, S. J. (2007). "Experiments on dispersion of tracer stones under lower-regime plane-bed equilibrium bed load transport." *Water Resour. Res.*, 43, W03440, doi: 10.1029/2006WR005172.

Yalin, M. S. (1963). "An expression for bed-load transportation." *ASCE, Journal of the Hydraulics Division*, 89(HY3), 221–250.

Yalin, M. S. (1972). "Mechanics of sediment transport." *Pergamon Press*, New York.

Yang, C. T. (1972). "Unit stream power and sediment transport." *ASCE, Hydraulics Div. Jour.*, Vol. 98, HY10, pp. 1805- 1826.

Yang, C. T. (1984). "Unit stream power equation for gravel." *ASCE, Hydraulics Div. Jour.*, Vol. 110, HY12, pp. 1783-1797.

Yang, C. T. and Sayre, W. W. (1971). "Stochastic model for sand dispersion." *J. Hydr. Eng. Div.-ASCE*, 97(2), 265–288.